

DISSERTATION

---

**Electron Transfer and Solvation  
Dynamics at Solid Cesium-Copper  
Interfaces in Presence of Solvents**

---

Von der Fakultät für Physik  
der Universität Duisburg-Essen  
vorgelegte Dissertation  
zur Erlangung des Grades  
Dr. rer. nat.  
von

**John Thomas**  
aus Vaikom, Indien

Erstgutachter:  
Prof. Dr. Uwe Bovensiepen  
Zweitgutachter:  
Prof. Dr. Karina Morgenstern

Prüfer:  
Prof. Dr. Richard Kramer Campen  
Vorsitzender:  
Prof. Dr. Dietrich Wolf

Tag der Mündlichen Prüfung: 27 September 2022

Duisburg, Deutschland  
March 2023



*Delight thyself also in the Lord;  
and He shall give thee the desires  
of thine heart.... ps 37:4*



Hiermit versichere ich, die vorliegende Dissertation selbstständig, ohne fremde Hilfe und ohne Benutzung anderer als den angegebenen Quellen angefertigt zu haben. Alle aus fremden Werken direkt oder indirekt übernommenen Stellen sind als solche gekennzeichnet. Die vorliegende Dissertation wurde in keinem anderen Promotionsverfahren eingereicht. Mit dieser Arbeit strebe ich die Erlangung des akademischen Grades Doktor der Naturwissenschaften (Dr. rer. nat.) an.

Duisburg, August 2022

---

Ort, Datum

John Thomas

---

(on the line the signature)



# Acknowledgments

It is my pleasure to thank everyone who interacted professionally and personally with me during the Ph. D. study. Although the world witnessed uncertainties during this period in almost every aspect of life due to the outbreak of Covid pandemic at an unprecedented level, it taught us how to tackle several situations in life. I appreciate the University of Duisburg-Essen administration that allowed researchers to carry out works without much restrictions during the pandemic. I also thank the countless people who supported wholeheartedly to bring our life back to normal state where science and life prosper alike.

My sincere thanks to my thesis advisor Prof. Dr. Uwe Bovensiepen who was instrumental in all stages of this journey to attain this degree. I have greatly benefited from his knowledge and scientific advises. He always motivated me to present experimental results and discussions to a higher professional quality. He had worked proactively during the preparation of the manuscripts and the corrections of the thesis. Also, he was very kind enough to support when I faced crisis in administrative matters.

I extend my sincere thanks to Prof. Dr. Karina Morgenstern who was my coadvisor for the thesis. I had several opportunities to discuss about the thesis work with her. As an astute observer, she always suggested novel ideas and additional analysis that enhanced the level of understanding. I am thankful to her for agreeing to become a referee of my thesis.

I enjoyed the discussion with the theoretical collaborators Prof. Dr. Dominic Marx, Dr. Janos Daru, Prof. Dr. Peter Saalfrank, Dr. Christopher Penschke and Prof. Dr. Angelos Michaelides. I thank them for their valuable suggestions and feedbacks. I had learned a lot from Dr. Ping Zhou regarding the optical setup alignments. During the pandemic, he had even spent early mornings and weekends to optimize the laser system for the experiments. I admire his commitment, the level of precision and patience in the work. I convey a big thank to Dr. Ping Zhou for all his support in the past years.

I have undoubtedly learned many things related to ultrahigh vacuum systems and surface preparations from Dr. Cord Bertram with whom I worked the initial two years of Ph. D. He was keen to impart his knowledge and always helpful especially in the difficult stages of the works. I also greatly acknowledge the support from Inga Langguth and Dr. Jayita Patwari for carrying out additional STM experiments.

The laboratory work often encounters the requirement of special mechanical parts. I thank Michael Bieske for his timely support on all issues on mechanical parts. My sincere thanks to Christina Boese who was helpful since the day of joining in the group. She extended her support to diverse issues which include procurement of equipments, visa and scholarship

---

related matters. I thank Roland Kohn for his support on computer related problems.

I would like to thank the past and current members of the photoemission laboratory. I enjoyed a lot working with Yasin and he was kind enough to train me on the routine activities of the photoemission experiments. It was also nice to interact with Ishita, Manuel, Isabella, Samad and Jan. I also acknowledge the support from current members Jayita for her assistance in the laboratory, Florian and Dr. Jayabalan for their invaluable supports on abstract and proof reading of the thesis. Many thanks to senior scientific employs of the group Alex, Klaus and Andrea for their constructive feedbacks whenever I presented my work in the group seminar. I thank all other members of the group for good memories.

The friends and family were an integral part during the study. I thank my parents for their persistent support for my journeys to attain knowledge since childhood. I thank my wife for supporting me in several aspects. I thank my relatives and well-wishers for unwavering supports and encouragements . I had a nice time with the Kerala communities in Duisburg and Essen. Especially, the friendly discussions with Jose uncle, Neelu, Sobin and Annamma aunty. I thank everyone who supported directly and indirectly during this period.

Finally, I thank RESOLV-the cluster of excellence for solvation science- that financially supported me through scholarship and work contract for four years. I greatly acknowledge the financial support from SFB 1242 and University of Duisburg-Essen during the extension time of the Ph.D.

John Thomas  
August 2022



# Abstract

The objective of this thesis is to decipher the fundamental mechanisms during the solvation of alkali in polar and nonpolar solvents on a metal surface. These mechanisms include electrostatic interaction between adsorbates, hydrogen bonding, van der Waals interactions and image charge interactions on the surface. The interplay of such fundamental interactions are decisive for the structure of the alkali-solvent adsorbates at interfaces. In addition, resonant excitation of the alkali results in a coupled alkali-solvent dynamics which in turn increases the lifetime of the excited alkali as well as induce energy transfer to the solvent molecules. This work addresses electronic structure and dynamics of the solvation of  $\text{Cs}^+$  in  $\text{D}_2\text{O}$  and Xe on Cu(111) as a representative solvents with polar and nonpolar behaviour, respectively.

The surface science approaches have enabled the preparation of adsorbates on metal substrates with well-controlled coverages. In the solvation of  $\text{Cs}^+$  in  $\text{D}_2\text{O}$  on Cu(111), the water-water interactions are preferred over water- $\text{Cs}^+$  interactions and that result in a solvation pattern where ions reside at the periphery of the clusters. Such structures exhibit a hybrid alkali-water electronic state and its energy varies as a function of adsorbate coverage ratio. The excited state dynamics of this hybrid state depends on the coordination of the alkali to the solvent molecules.

In the solvation of  $\text{Cs}^+$  in Xe on Cu(111), it is observed that the energy of the Cs 6s state increases with Xe coverage and concomitantly the intensity of the photoemission decreases. This is attributed to the gradual decoupling of the bonding between  $\text{Cs}^+$  and Cu(111). In addition, the lifetime of the excited Cs 6s state has increased significantly upon adsorption of Xe. These properties of the Xe are attributed to the polarization of its charge density by  $\text{Cs}^+$  ions on the surface. Remarkably, no hybrid alkali-Xe state on Cu(111) is observed during the interaction. This suggests a sharp contrast in the solvation of  $\text{Cs}^+$  ions in the polar and the nonpolar solvents.

This work reveals the dominant nature of the cooperative interactions during the solvation of alkali in polar solvents whereas alkali solvation in nonpolar solvent exhibits a competitive nature of the Coulomb and van der Waals interactions on the surface.



# Zusammenfassung

Ziel dieser Arbeit ist es, die grundlegenden Mechanismen bei der Solvatisierung von Alkalimetallen in polaren und unpolaren Lösungsmitteln auf einer Metalloberfläche zu entschlüsseln. Zu diesen Mechanismen gehören elektrostatische Wechselwirkungen zwischen Adsorbaten, Wasserstoffbrückenbindungen, van-der-Waals-Wechselwirkungen und Spiegelladungswechselwirkungen an der Oberfläche. Das Zusammenspiel dieser fundamentalen Wechselwirkungen ist entscheidend für die Struktur der Alkali-Lösungsmittel-Adsorbate an Grenzflächen. Darüber hinaus führt die resonante Anregung der Alkalimetalle zu einer gekoppelten Alkali-Lösungsmittel-Dynamik, die wiederum die Lebensdauer der angeregten Alkalimetalle erhöht und eine Energieübertragung auf die Lösungsmittelmoleküle bewirkt. Diese Arbeit befasst sich mit der elektronischen Struktur und Dynamik der Solvataion von  $\text{Cs}^+$  in  $\text{D}_2\text{O}$  und Xe auf Cu(111) als repräsentative Lösungsmittel mit polarem bzw. unpolarem Verhalten.

Die oberflächenwissenschaftlichen Ansätze haben die Herstellung von Adsorbaten auf Metallsubstraten mit gut kontrollierten Bedeckungen ermöglicht. Bei der Solvataion von  $\text{Cs}^+$  in  $\text{D}_2\text{O}$  auf Cu(111) werden Wasser-Wasser-Wechselwirkungen gegenüber Wasser- $\text{Cs}^+$ -Wechselwirkungen bevorzugt, was zu einem Solvationsmuster führt, bei dem sich die Ionen an der Peripherie der Cluster befinden. Solche Strukturen weisen einen hybriden elektronischen Alkali-Wasser-Zustand auf, dessen Energie in Abhängigkeit vom Adsorbat-Bedeckungsverhältnis variiert. Die Dynamik des angeregten Zustands dieses Hybridzustands hängt von der Koordination des Alkalimetalls mit den Lösungsmittelmolekülen ab.

Bei der Solvataion von  $\text{Cs}^+$  in Xe auf Cu(111) wird beobachtet, dass die Energie des Cs  $6s$ -Zustands mit der Xe-Bedeckung zunimmt und gleichzeitig die Intensität der Photoemission abnimmt. Dies wird auf die allmähliche Entkopplung der Bindung zwischen  $\text{Cs}^+$  und Cu(111) zurückgeführt. Darüber hinaus hat sich die Lebensdauer des angeregten Cs  $6s$ -Zustands durch die Adsorption von Xe deutlich erhöht. Diese Eigenschaften des Xe werden auf die Polarisierung seiner Ladungsdichte durch  $\text{Cs}^+$ -Ionen auf der Oberfläche zurückgeführt. Bemerkenswert ist, dass während der Wechselwirkung kein hybrider Alkali-Xe-Zustand auf Cu(111) beobachtet wird. Dies deutet auf einen scharfen Kontrast bei der Solvataion von  $\text{Cs}^+$ -Ionen in polaren und unpolaren Lösungsmitteln hin.

Diese Arbeit zeigt, dass bei der Solvatisierung von Alkalimetallen in polaren Lösungsmitteln die kooperativen Wechselwirkungen dominieren, während bei der Solvatisierung von Alkalimetallen in unpolaren Lösungsmitteln die Coulomb- und van-der-Waals-Wechselwirkungen auf der Oberfläche miteinander konkurrieren.



# Contents

<b>Abstract</b>	<b>iii</b>
<b>Zusammenfassung</b>	<b>v</b>
<b>List of Figures and Tables</b>	<b>viii</b>
<b>List of Abbreviations and Symbols</b>	<b>xi</b>
<b>1. Introduction</b>	<b>1</b>
<b>2. Background of Investigated Interface Systems</b>	<b>5</b>
2.1. Bulk Solvation of Alkalis . . . . .	6
2.2. Solvation at Charged Interfaces . . . . .	10
2.3. Electronic Structure and Dynamics of Adsorbates at Interfaces . . . . .	14
2.3.1. Chemisorption of Alkalis on Cu(111) Surfaces . . . . .	14
2.3.2. Physisorbed Atoms/Molecules on Metal Surfaces . . . . .	16
2.3.3. Heterogeneous Adsorbates at Interfaces . . . . .	21
2.4. Theoretical Calculations on Investigated Systems . . . . .	26
<b>3. Experimental Methods</b>	<b>29</b>
3.1. Photoemission Spectroscopy . . . . .	29
3.1.1. Theory of Photoemission . . . . .	30
3.1.2. Two-Photon Photoemission Spectroscopy . . . . .	32
3.1.3. Time-resolved 2PPE and Population Dynamics . . . . .	34
3.1.4. Technical Aspects of Photoemission Spectroscopy . . . . .	35
3.1.5. Data Analysis . . . . .	37
3.2. Experimental setup . . . . .	40
3.2.1. Generation of Femtosecond Laser Pulses . . . . .	40
3.2.2. Characterization and Optimization of Laser Pulses . . . . .	43
3.2.3. Ultrahigh Vacuum System (UHV) . . . . .	48
3.3. Surface Preparation and Characterization Under UHV . . . . .	50
3.3.1. Preparation of Cu(111) Surfaces . . . . .	50
3.3.2. Chemisorption of Cs on Cu(111) . . . . .	51
3.3.3. Physisorption of D <sub>2</sub> O Sub-bilayers on Metal . . . . .	52
3.3.4. Adsorption of Multilayers of Xe on Cu(111) . . . . .	53

<b>4. Understanding the Electronic Structure and the Ultrafast Dynamics of Alkali-Water Clusters at Interfaces</b>	<b>55</b>
4.1. Formation of Cs-Water Clusters on Cu(111) . . . . .	55
4.1.1. Evolution of the Electronic Structure of Cs-Water Clusters . . . . .	56
4.1.2. Morphology of Cs-Water Clusters . . . . .	60
4.1.3. Theoretical Investigations on Cs-Water Clusters Using DFT . . . . .	62
4.2. Ultrafast Electron Dynamics of Alkali-Water Clusters at Interfaces . . . . .	64
4.2.1. Ultrafast Solvation Dynamics of Cs-Water Clusters on Cu(111) . . . . .	65
4.2.2. Localized Nature of the Cs-Water Cluster State on Cu(111) . . . . .	69
4.2.3. Temperature Dependence of the Excited State Dynamics of Clusters . . . . .	70
4.2.4. Influence of Xe Overlayer on the Excited Cs-Water State . . . . .	71
4.3. Conclusion . . . . .	73
<b>5. Unveiling the Solvation in Alkali-Noble Gas Adsorbates at Interfaces</b>	<b>75</b>
5.1. Probing the Evolution of Xe-Cs <sup>+</sup> Aggregates on Cu(111) . . . . .	75
5.2. Ultrafast Dynamics of Xe-Cs <sup>+</sup> Aggregates on Cu(111) . . . . .	79
5.2.1. Energy Stabilization and Population Dynamics . . . . .	80
5.2.2. Determination of the Potential Energy Surface . . . . .	83
5.3. Morphology of the Xe-Cs <sup>+</sup> Aggregates . . . . .	84
5.4. Coupled Cluster Calculations on Xe-Cs <sup>+</sup> Adsorbates . . . . .	87
5.5. Xe Double Layer for Decoupling Influence of Substrate . . . . .	89
5.6. Conclusions . . . . .	91
<b>6. Summary</b>	<b>93</b>
<b>A. Optical Bloch Equations</b>	<b>97</b>
<b>B. Error Propagation Method to Determine Error in Adsorbate Coverage Ratio</b>	<b>99</b>
<b>C. Confidence Interval Analysis of Potential Energy Surface</b>	<b>100</b>
<b>Bibliography</b>	<b>103</b>
<b>List of publications</b>	<b>121</b>
<b>Lebenslauf</b>	<b>135</b>

# List of Figures

2-1.	Absorption Spectrum and Dynamics of Na Solvation in THF . . . . .	7
2-2.	Solvation of Cs <sup>+</sup> Ions in Helium Clusters . . . . .	9
2-3.	Schematic of Water Molecules at a Charged Interface . . . . .	10
2-4.	Schematic of a Li <sup>+</sup> -Ion Battery Module . . . . .	12
2-5.	CO <sub>2</sub> Reduction Mechanism at Interface . . . . .	13
2-6.	Nuclear Motion of Cs Atoms on Surface . . . . .	14
2-7.	2PPE Spectra of Alkalis (Li to Cs) on Cu(111) . . . . .	16
2-8.	Energy Level and Potential Energy Surface of Electron Solvation . . . . .	18
2-9.	Dynamical Processes of Electron Solvation at Interface . . . . .	20
2-10.	Electron Solvation in Na <sup>+</sup> Doped Water on Cu(111) . . . . .	22
2-11.	Schematic of Potential Energy Surface of Alkali-Water on Surface . . . . .	23
2-12.	Tr-2PPE of Alkalis(Na, K and Cs)-Water Clusters on Cu(111) . . . . .	24
2-13.	Lifetime of Na <sup>+</sup> /Cu(111) for Various Water Coverages . . . . .	25
2-14.	Alkali Coordination with Water and Change in Surface Properties . . . . .	26
3-1.	Schematic of the 2PPE Excitation Mechanisms . . . . .	32
3-2.	Schematic of the Tr-2PPE Spectroscopy Experiment . . . . .	34
3-3.	Bias Voltage to Compensate Potential Gradients . . . . .	35
3-4.	2PPE Data Acquisition and Signal Processing . . . . .	36
3-5.	2PPE Spectrum of Cu(111) and Cs <sup>+</sup> /Cu(111) with Coadsorbing water . . . . .	37
3-6.	Analysis of Tr-2PPE from D <sub>2</sub> O/Cs <sup>+</sup> /Cu(111) . . . . .	39
3-7.	Schematic of the 2PPE Pump and Probe Experimental Setup . . . . .	41
3-8.	Fluence Profiles of the Pump and Probe laser pulses . . . . .	44
3-9.	Optical Spectrum and Autocorrelation Measurement of Laser Pulses . . . . .	45
3-10.	GVD Compensation of the Pump and Probe Pulses . . . . .	46
3-11.	Schematic of the ultrahigh Vacuum Chamber . . . . .	47
3-12.	Schematic of the Gas System . . . . .	48
3-13.	Design of the Sample Holder . . . . .	49
3-14.	LEED Pattern and 2PPE of a Freshly Prepared Cu(111) . . . . .	50
3-15.	2PPE of Cs <sup>+</sup> /Cu(111) as a Function of Cs Coverages . . . . .	51
3-16.	Calibration and Optimization of D <sub>2</sub> O Coverages . . . . .	52
3-17.	TPD Spectrum of Multilayers of Xe on Cu(111) . . . . .	53
4-1.	Coadsorption of Water on Cs <sup>+</sup> /Cu(111) for Various Cs Coverages . . . . .	57

4-2.	Detailed Analysis of Water Coadsorption on Cs <sup>+</sup> /Cu(111) at 80 K . . . . .	58
4-3.	Compilation of the Water Coadsorption on Cs <sup>+</sup> /Cu(111) Results . . . . .	59
4-4.	STM Images of Cs-Water Clusters on Cu(111) . . . . .	61
4-5.	DFT Calculations on Cs-Water Clusters on Cu(111) . . . . .	63
4-6.	Time-resolved 2PPE of Cs-Water clusters . . . . .	65
4-7.	Energy Stabilization and Population Dynamics of Cs-Water Clusters . . . . .	67
4-8.	Angle-resolved 2PPE of Cs-Water cluster . . . . .	69
4-9.	Temperature Dependent Dynamics of Cs-Water Clusters . . . . .	71
4-10.	Influence of Xe Overlayers on Dynamics of Cs-Water Clusters . . . . .	72
5-1.	2PPE Spectra of Cs <sup>+</sup> /Cu(111) as a Function of Xe Coverage . . . . .	76
5-2.	Work Function and Binding Energy of Xe/Cs <sup>+</sup> /Cu(111) Surface . . . . .	78
5-3.	Cs AR Change as a Function of Xe and Cs Coverages . . . . .	79
5-4.	Tr-2PPE from Cs <sup>+</sup> /Cu(111) for Various Xe Coverage . . . . .	80
5-5.	Population Dynamics of Xe/Cs <sup>+</sup> /Cu(111) . . . . .	81
5-6.	Determination of Potential Energy Surface . . . . .	83
5-7.	Morphology of Xe-Cs <sup>+</sup> Aggregates . . . . .	85
5-8.	STM Images of Bare Cs <sup>+</sup> , Xe and Aggregates on Cu(111) . . . . .	86
5-9.	Coupled Cluster Calculations and Adsorbate Distribution on Surface . . . . .	88
5-10.	Cs Deposition on Xe Double Layer . . . . .	89
5-11.	Stability of Cs Atoms on Xe Double Layer . . . . .	90
C-1.	Confidence Interval Analysis of PES. . . . .	101

## List of Tables

4-1.	Error in the calculation of adsorbate coverage ratio. . . . .	66
4-2.	The excited state lifetime of the adsorbates. . . . .	68



# List of Abbreviations and Symbols

Abbreviation	Denomination
<i>2D</i>	Two-dimensional
<i>2PPE</i>	Two-photon Photoemission
<i>AC</i>	Autocorrelation
<i>AES</i>	Auger Electron Spectroscopy
<i>AOM</i>	Acousto Optic Modulator
<i>AR</i>	Anti-bonding Resonance
<i>BBO</i>	$\beta$ -Barium Borate
<i>BL</i>	Bilayer
<i>CB</i>	Conduction Band
<i>CBS</i>	Complete Basis Set
<i>CCD</i>	Charge Coupled Device
<i>CCSD(T)</i>	Coupled Cluster Single and Double Excitation and the Perturbative Triples
<i>CPA</i>	Chirped pulse amplification
<i>CV</i>	Cyclic Voltametry
<i>CW</i>	Continuous Wave
<i>DFT</i>	Density Functional Theory
<i>DOS</i>	Density of States
$e_s$	Solvated Electron
$eBE$	Electron Binding Energy
<i>EDL</i>	Electric Double Layer
<i>ESCA</i>	Electron Spectroscopy Chemical Analysis
$eTOF$	Electron Time-of-Flight
<i>FWHM</i>	Full Width at Half Maximum
<i>GPiB</i>	General Purpose Interface Bus
<i>GVD</i>	Group Velocity Dispersion
$He_N$	Helium Clusters
$He_NCs^+$	Cs-doped Helium Clusters
<i>IHP</i>	Inner Helmholtz Plane
<i>IPES</i>	Inverse Photoelectron Spectroscopy
<i>KLM</i>	Kerr Lens Mode-locking
<i>LEED</i>	Low Energy Electron Diffraction

## List of Figures

---

<b>Abbreviation</b>	<b>Denomination</b>
---------------------	---------------------

---

<i>M</i>	Cation
<i>MCP</i>	Multi Channel Plates
<i>ML</i>	Monolayer
<i>NMR</i>	Nuclear Magnetic Resonance
<i>OHP</i>	Outer Helmholtz Plane
<i>PES</i>	Potential Energy Surface
<i>pTOF</i>	Position Sensitive Time of Flight
<i>QMS</i>	Quadrupole Mass Spectrometer
<i>SPM</i>	Self-Phase Modelocking
<i>SS</i>	Schocley Surface State
<i>STM</i>	Scanning Tunneling Microscopy
<i>SXPS</i>	Soft X-ray Photoemission Spectroscopy
<i>TCP</i>	Tight Contact Pair
<i>THB</i>	Transient Hole Burning
<i>THF</i>	Tetrahydrofuran
<i>TOF</i>	Time-of-Flight
<i>TPD</i>	Temperature Programmed Desorption
<i>TR – 2PPE</i>	Time-Resolved Two-Photon Photoemission
<i>UHV</i>	Ultra High Vacuum
<i>UPS</i>	Ultraviolet Photoemission Spectroscopy
<i>VB</i>	Valence Band
<i>SXPS</i>	Soft X-ray Photoemission Spectroscopy
<i>XPS</i>	X-ray Photoemission Spectroscopy

<b>Symbol</b>	<b>Denomination</b>
---------------	---------------------

---

$\psi$	Wave Function
$\Phi$	Work Function
$\Theta$	Coverage
$\tau$	Lifetime
$\mu$	Dipolemoment
$\sigma$	Surface Charge Density
$\nu$	Frequency
$\phi$	Scalar Potential
$\omega$	Angular Frequency
$\lambda$	Wavelength

# 1. Introduction

Understanding the solvation of alkalis at interfaces opens up new avenues in fundamental research as well as in technologically important applications. The alkali solvation phenomena are found to occur in diverse contexts and span from the interfaces to the bulk of solvents. The elementary mechanisms of the solvation depend on the polar or the nonpolar nature of the solvents. The alkalis on the surface are model systems for studying the electron transfer processes between the substrate and an adsorbate [1, 2]. In addition, they exhibit nuclear motion normal to the surface upon resonant excitation [3]. In an alkali-solvent system on the surface, resonant excitation results in a coupled alkali-solvent dynamics which increases the lifetime of the excited alkali state and also energy transfer to the solvents [4]. The morphology of the adsorbates at the interfaces is governed by the interplay of cooperation or competition between the elementary mechanisms. Such mechanisms include, but are not limited to, Coulomb interactions, van der Waals interactions, ion-dipole forces and image charge interactions. The focus of this thesis is to disentangle the intricacies of the alkali solvation at the interfaces by utilizing static and time-resolved photoemission studies.

The solvation phenomena have been reported by Humphry Davy more than two centuries ago and he demonstrated that the solvation of potassium grains in ammonia gas turns ammonia into blue colour [5]. Similar effects have been observed in water when it is irradiated with high energy electrons [6]. The characteristic colour change of the solvents is attributed to the absorption of light by solvated species, i.e., the excess electrons in the solvents. The solvated electrons are investigated extensively in bulk water and water clusters [7–10]. Furthermore, the solvation of alkali in polar and nonpolar solvents have gained wide attention due to its fundamental and technological importance. For instance, the solvation of Na in a polar solvent, viz. liquid tetrahydrofuran (THF), is reported in a recent work where the lifetime of the excited state is found to vary as a function of the alkali coordination to solvent molecules [11]. In addition, the formation of solvation shell around Cs ions by nonpolar He clusters is reported in a recent work [12]. Advances in surface science have enabled preparation of adsorbates with diverse properties and well-controlled coverages on a surface. The solvated electrons in ice layers on a metal surfaces are investigated extensively in the recent past decades [13, 14]. The lifetime and dynamics of the solvated electrons are found to be significantly affected upon doping of alkali on ice layers on metal surfaces [15]. Moreover, the energy transfer to the solvent varies for water coadsorbed with Na, K and Cs on Cu(111) and also the formation of a hybrid alkali-water state is observed on the surface [4]. A better understanding on the structure and dynamics of alkali solvation at interfaces would result

in improvements in the operation of electrochemical devices and has the potential for novel applications.

This thesis work addresses the electronic structure and the solvation dynamics of  $\text{Cs}^+$  alkali in  $\text{D}_2\text{O}$  (polar) and Xe (nonpolar) solvents on a Cu(111) surface. The two-photon photoemission (2PPE) technique is employed to study the alkali solvation at interfaces. The technique involves the transient neutralization of the alkali by attachment of an electron from the substrate by ultrashort optical pulses. This initiates the solvation processes at the interfaces and a subsequent laser pulse is used to study the dynamics by the photoemission of the excited state. The evolution of the electronic structure of the adsorbates is studied by 2PPE spectra as a function of the adsorbates coverage. Moreover, the complementary experimental and theoretical approaches (by collaborators) have enriched the understanding on the surface solvation of alkalis. For instance, the 2PPE studies the evolution of the alkali from a neutral state ( $\text{M}^0$ ) whereas the scanning tunneling microscopy (STM) studies the alkali metal ( $\text{M}^+$ ) in an ionized state on the substrate. The adsorbates preparation in 2PPE is performed *vis-à-vis* STM to facilitate nominally identical surfaces in both experiments which has allowed the direct comparison of spectroscopy and morphology results.

The objective of this thesis is to decipher the complex interplay of fundamental interactions during the solvation of alkalis in polar and nonpolar solvents on a surface. The chapter 2 discusses an overview of the solvation of alkalis in bulk (section 2.1) and at interfaces (section 2.2), respectively. A detailed discussion on the 2PPE studies of chemisorbed alkalis, physisorbed atoms/molecules and heterogeneous adsorbates (section 2.3) are presented to understand important works in this area. The last section of the chapter 2 (section 2.4) discusses the DFT studies on hydrated alkalis on Cu(111). The experimental details such as the photoemission spectroscopy, femtosecond laser pulse generation and its characterization, ultrahigh vacuum system, adsorbates preparation and characterization are discussed in chapter 3.

The experimental results of  $\text{Cs}^+$ - $\text{D}_2\text{O}$  and  $\text{Cs}^+$ -Xe on Cu(111) are presented in chapters 4 and 5, respectively. The formation of an alkali-water hybrid state on Cu(111) is reported in a previous work [4]. However, the origin of this state is not explained in that work. As part of the present thesis work, the electronic structure of the  $\text{Cs}^+/\text{Cu}(111)$  is investigated as a function of  $\text{D}_2\text{O}$  coverage for different Cs coverages. The electronic properties of the hybrid state are investigated extensively. The 2PPE results along with morphology and theoretical calculations are presented in section 4.1. It is corroborated that the origin of the hybrid state is due to a peculiar inside-out solvation pattern where  $\text{Cs}^+$  ions reside at the periphery of the water clusters. The properties of the Cs-water clusters such as excited state lifetime, localization, structural phase dependence and solvation site are discussed in section 4.2. It is found that the lifetime of the excited alkali-water clusters on Cu(111) varies as a function of the alkali coordination to solvent molecules. In the case of alkali-nonpolar interaction, i.e.,  $\text{Cs}^+$ -Xe on Cu(111), the energy of the Cs 6s state increases as a function of the Xe coverage (section 5.1) due to the decoupling from the metal substrate. Also, the

---

lifetime of the 6s state has increased substantially (section 5.2). The 2PPE results together with investigations on the morphology (section 5.3) and coupled cluster calculations (section 5.4) show that Xe compensates the repulsive interaction between  $\text{Cs}^+$  ions on the surface due to the polarization of its electron charge density. The efforts to use Xe double layer for decoupling the adsorbates from the metal substrate are promising (section 5.5).

To summarize, the  $\text{Cs}^+$ -water interactions result in the formation of a hybrid state on Cu(111). However, no such hybrid state is observed during  $\text{Cs}^+$ -Xe interactions. This suggests that the 2PPE could differentiate the interaction of alkali with polar and nonpolar solvents. It is also revealed that cooperative interactions are prevalent in the case of surface solvation of alkali in a polar solvent whereas competing interactions are observed in alkali solvation in nonpolar solvents on a surface. By the combination of experimental and theoretical methods, complex interplay of fundamental interactions such as electrostatic interaction between  $\text{Cs}^+$  and solvents, hydrogen bonding, van der Waals interactions and image charge interactions during the surface solvation of alkali have been unveiled. Understanding such elementary mechanisms has important consequences in fundamental science and in technological applications. For instance, the electric double layer concept is crucial in many processes in electrochemistry [16, 17]. This thesis work has addressed electronic structure and charge transfer dynamics at interfaces and it has the potential to influence future developments which include electrochemical cells, photovoltaic cells, energy conversion devices, to name a few.



## 2. Background of Investigated Interface Systems

This chapter discusses several scientific works relevant to the adsorbate systems investigated as part of this thesis work. The first and second section present the general concepts and previous experiments on the ion solvation in bulk and at interfaces, respectively. These sections also discuss the relevance of ion solvation in atmospheric, biological, geological, and technological contexts. The second section emphasizes the concept of electric double layer and its role in solvation at interfaces.

The third section presents an overview of the 2PPE experiments performed on alkali metals, molecules, noble gases, and heterogeneous adsorbates at interfaces. Alkalis at interfaces serve as a model system for studying the charge transfer process between the substrate and an adsorbate due to its partially ionized outermost  $s$  orbital. Cesium (Cs) is considered for the experiments reported on this thesis because of the longer resonance lifetime of its  $6s$  antibonding state on the Cu(111) compared to the intermediate states of Cu(111) and its nuclear motion normal to surface upon resonant excitation. Furthermore, this section discusses the 2PPE spectroscopic studies of physisorbed molecules with an elaborate discussions on adsorbed water which trap electrons at the interfaces. The influence of noble gas adlayers on the lifetime of the image potential states are also addressed in this section. In addition, this section presents an extensive discussion on heterogeneous systems such as alkali-water at interfaces which are relevant to the studies reported in this thesis. The energy stabilization and relaxation dynamics of the alkali-water adsorbates at interfaces are discussed in detail in this section.

The last section discusses the theoretical works performed on the hydration of alkali at Cu(111) surfaces. This is closely associated to the experiments presented in Chapter 4 of this thesis which addresses the formation of a water-induced alkali state and its properties.

## 2.1. Bulk Solvation of Alkalis

The solvation of ions is a ubiquitous phenomenon relevant to many atmospheric, geological, and biological processes [18–25], as well as plethora of technological applications like storage devices, drug design, fuel cells, biomass dissolution etc [26–29]. The ion solvation is extensively investigated in diverse contexts such as at interfaces, in clusters, in molecular cages, and in bulk liquids [30–33]. In general, the solvation phenomena are probed by several experimental and theoretical methods such as neutron diffraction, X-ray scattering and absorption, NMR spectroscopy, electron spin resonance, mass spectroscopy, dielectric relaxation spectroscopy, infrared spectroscopy, fluorescence upconversion, Raman spectroscopy, photoelectron spectroscopy, transient hole burning spectroscopy, nanocalorimetry, scanning tunneling microscopy, density functional theory, coupled cluster calculations, to name a few [11,33–44]. Broadly, the properties that are investigated to understand the ion solvation processes include the nature of the hydration shell structure, solvation free-energy, solvation dynamics, stability of the solvation structures<sup>1</sup>, thermal stability, energy transfer to the solvent, and ion transport [45–47].

The response of solvents in the vicinity of alkalis and halides attracts further attention due to their natural abundance in the planet as well as their diverse roles in living organisms [11, 12, 48–54]. In a recent work, Bragg et al. have reported step by step solvation of Na atoms in a polar solvent, tetrahydrofuran (THF) using ultrafast transient hole burning (THB) spectroscopy and quantum molecular dynamics [11]. They considered Na atoms as a tight-contact pair (TCP) where the valence electron of the sodium is not exclusively associated to the parent atom but also extends significantly into the solvent [55]. As a result, the absorption spectrum of Na in THF peaks at an intermediate wavelength around 870 nm (blue circles) as shown in Fig. 2-1 (a). The absorption peak of gas-phase unsolvated sodium atoms occurs at 590 nm and that of a THF-solvated electron (fully separated Na<sup>+</sup> and e<sup>-</sup>) occurs at 2100 nm [56]. The mixed quantum classical molecular dynamics simulation shows that the absorption peaks around 750 nm (black solid line) and further simulations with consideration of coordination of Na with THF molecules (N=2 to 5) result in blue shift and red shift in the absorption spectrum. The Fig. 2-1(a) shows the simulation of the absorption spectrum for N=3 (blue shift), N=4 (equilibrium state), and N=5 (red shift) in green, orange, and red dashed lines, respectively. A snapshot of the molecular dynamics simulation of the TCP in THF solution is shown in Fig. 2-1 (b) where blue sphere and white isosurface represent Na<sup>+</sup> and electron charge density, respectively. The oxygen site in the THF molecule strongly attracts the electron density of the nearby sodium and results in the displacement of the electron density of the sodium atom. The degree of delocalization of the charge density in sodium is related to the number of THF in its vicinity as shown in the inset of Fig. 2-1 (c). The charge density distortion increases with the number of THF molecules

---

<sup>1</sup>The ions can act as kosmotropes which make the solvent structure or chaotropes which break the solvent structure. These structures accelerate or decelerate the solvation dynamics.



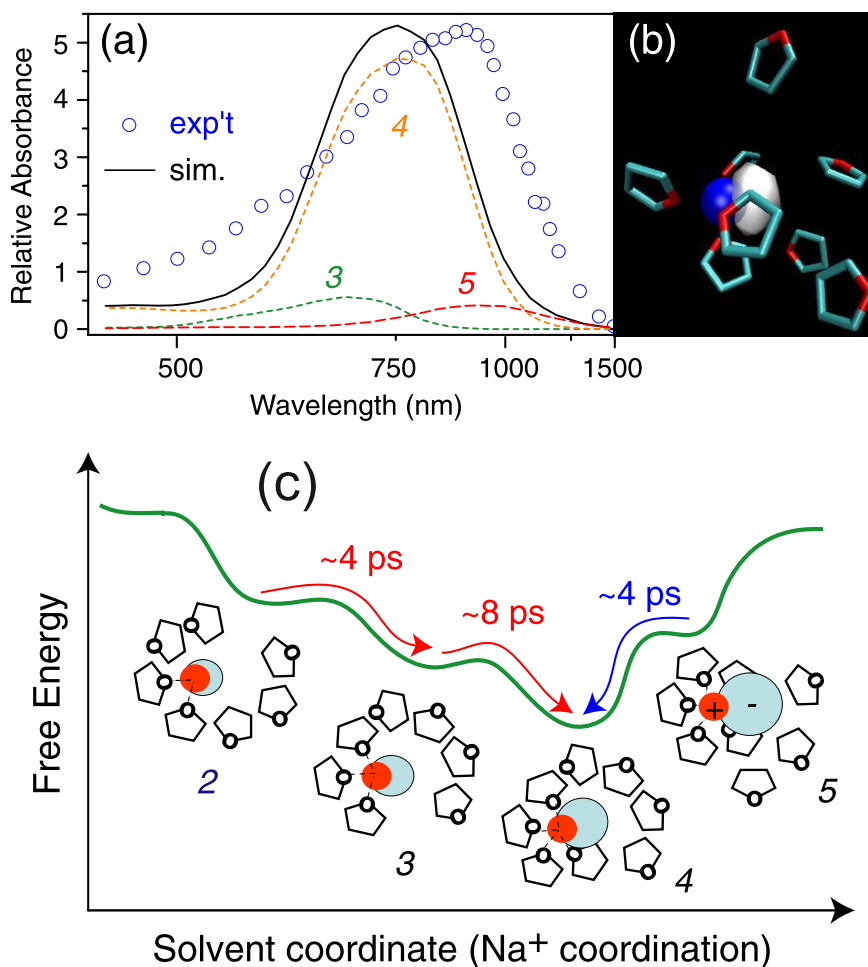


Figure 2-1.: (a) Absorption spectrum of Na in THF at room-temperature. The experimental and simulation of the absorption spectrum are shown in blue circles and black solid lines, respectively. The simulation does not capture the relative population of the coordination motifs of Na with THF. In equilibrium, the solution is dominated by a configuration of Na with four THF (dashed orange line). The motifs with three (dashed green) and five (dashed red) THF molecules are also contributing to the absorption spectrum that result the broadening of the absorption spectrum as observed in the experiments. (b) A snapshot from the molecular dynamics simulations of the Na with its first solvation shell. (c) Schematic of the free-energy of different motifs with the coordination from 2 to 5 THF molecules. The free-energy surface diagram shows that each configuration is distinct in their relaxation time and the degrees of electron displacement (red circles and blue ovals) from Na. Reprinted figure with permission from Bragg, A. et al. Watching the Solvation of Atoms in Liquids One Solvent Molecule at a Time. *Phys. Rev. Lett.*, 104:233005, (2010). DOI: <https://doi.org/10.1103/PhysRevLett.104.233005>. Copyright © 2010 by the American Physical Society. Ref. [11]

( $\text{Na}^+$  and  $\text{e}^-$  are in red and light blue spheres, respectively). At higher solvent coordination, the electron density is pushed away significantly from the  $\text{Na}^+$  and the system responds like a solvated electron (less likely as in the gas-phase). On the other hand, for lower solvent coordination, the electron interacts more with the parent sodium and results in the blue shift of the absorption spectrum. The inhomogeneous broadening of the experimental absorption spectrum in Fig. **2-1** (a) is attributed to coordination of Na with different number of THF molecules [11].

To decipher the role of the solvent coordination on dynamics, ultrafast THB spectroscopy is performed on Na in THF solution [11]. The technique employs three laser pulses in sequence to study the solvation dynamics. The first pulse at 266 nm photoinitiates the electron transfer from  $\text{I}^-$  to  $\text{Na}^+$  to produce the TCPs ( $\text{Na}^+$  and  $\text{e}^-$ ). The TCPs are excited by a second laser pulse (wavelength at 800 nm) at a delay of 0.5 ns after the first pulse. This excitation and associated thermal fluctuations result in a change in the cation-solvent coordination number compared to their equilibrium condition, leading to a transient depletion or bleach of the ground state TCP spectrum. A time-delayed third broadband laser pulse is used to monitor the fluctuations in the absorption spectrum of the TCPs at nonequilibrium. As discussed earlier, the absorption peaks at different wavelengths depending on the cation solvation coordination as shown in the simulations in Fig. **2-1** (a). The ultrafast THB probes the change in the intensity of various absorption peaks due to solvent reorganization as depicted in Fig. **2-1** (c). A distinct change in the relaxation time is observed as a function of the cation-solvent coordination number. This observation by Bragg et al. [11] resembles the dynamics of alkali-water clusters on Cu(111) presented in Chapter 4 in which the excited state dynamics varies as a function of the adsorbate coverage ratio on surface.

The investigations on the interaction of alkali metals and noble gases are of continuing interests due to its fundamental nature and there are several avenues of research yet to be explored. The works in this direction are mainly to study the properties of alkalis in noble gas matrices and electronic polarization and spin effects in alkali-noble gas system [12, 40, 44, 57–60]. In a recent work, Tudela et al. have reported the solvation of  $\text{Cs}^+$  ions in nonpolar  $\text{He}_N$  nanoclusters by experimental and theoretical methods [12]. The experimental procedures for producing Cs-doped helium clusters are discussed elsewhere [61]. Two portions of the mass spectrum after the ionization of the Cs-doped helium clusters is shown in Fig. **2-2** (a). The mass spectrum contains contribution from two species viz. pure He clusters ( $\text{He}_N^+$ ,  $N = 47$  to 59) and Cs-doped He clusters ( $\text{He}_N\text{Cs}^+$ ,  $N = 14$  to 26). Note that pure clusters have an even value of mass per charge where as the doped clusters have an odd value of mass per charge. For the pure He clusters, a satellite peak is observed at 0.1-0.3 amu after every main peak which are indicated with black arrows. This satellite peaks are originating from the metastable decay of cluster ions on their way to the mass spectrometer [62]. For Cs-doped He clusters, the satellite peaks are absent until  $N=16$  and one is prominent only at  $N=26$  as indicated by the red arrow. The relative intensity of the satellite to main peak (not shown here) are analysed further and found that a pronounced change in the ratio

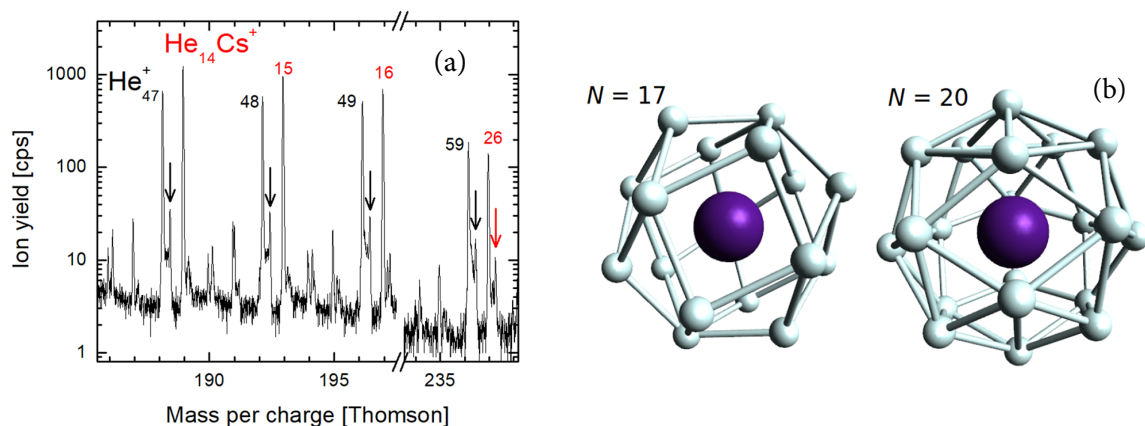


Figure 2-2.: Experimental and theoretical studies on  $\text{Cs}^+$  ion solvation in noble gases. (a) The mass spectrum of pure He clusters ( $\text{He}_N^+$ ,  $N = 47\text{-}59$ ) and Cs-doped He clusters ( $\text{He}_N\text{Cs}^+$ ,  $N = 14\text{-}26$ ). A satellite peak is observed for each pure He cluster (black arrows) and is found prominent only in larger Cs-doped clusters (red arrow). (b) The theoretical model shows an optimum ( $N=17$ ) and close packed ( $N=20$ ) solvation structures which are in agreement with experimental results. Reprinted figure with permission from Tudela, R. P. et al. A Combined Experimental and Theoretical Investigation of  $\text{Cs}^+$  Ions Solvated in  $\text{He}_N$  Clusters. *The Journal of Chemical Physics*, 150:154304, (2019), with the permission of AIP publishing. Ref. [12].

occurs at  $N=17$  and  $N=20$ . This is attributed to the closure of the solvation shell due to the presence of weakly bound He atoms occupying the next solvation layer. These values are closer to the theoretical prediction of the number of He atoms for the solvation of  $\text{Cs}^+$  ions [63]. Furthermore, the theoretical calculations by Tudela et al. [12] have predicted two plausible solvation structures as shown in Fig. 2-2 (b). The  $N=17$  structure corresponds to an optimum packing structure in which He atoms cover the  $\text{Cs}^+$  ion in the most optimum way by providing the lowest association energy per atom. The  $N=20$  structure is interpreted as a maximum packing structure in which the system supports an additional number of atoms with a slight raise of the cluster association energy per atom [64].

The works by Bragg et al. and Tudela et al. have discussed elaborately here as an exemplary case of the bulk solvation of ions in polar and nonpolar solvents, respectively [11, 12]. The interactions of alkalis with polar and nonpolar solvents are fundamentally different as discussed above. The thesis work is specifically addressing the ion solvation in polar and nonpolar solvents at interfaces as discussed in chapters 4 and 5. The following section is devoted to emphasize the importance of interfaces in ion solvation.

## 2.2. Solvation at Charged Interfaces

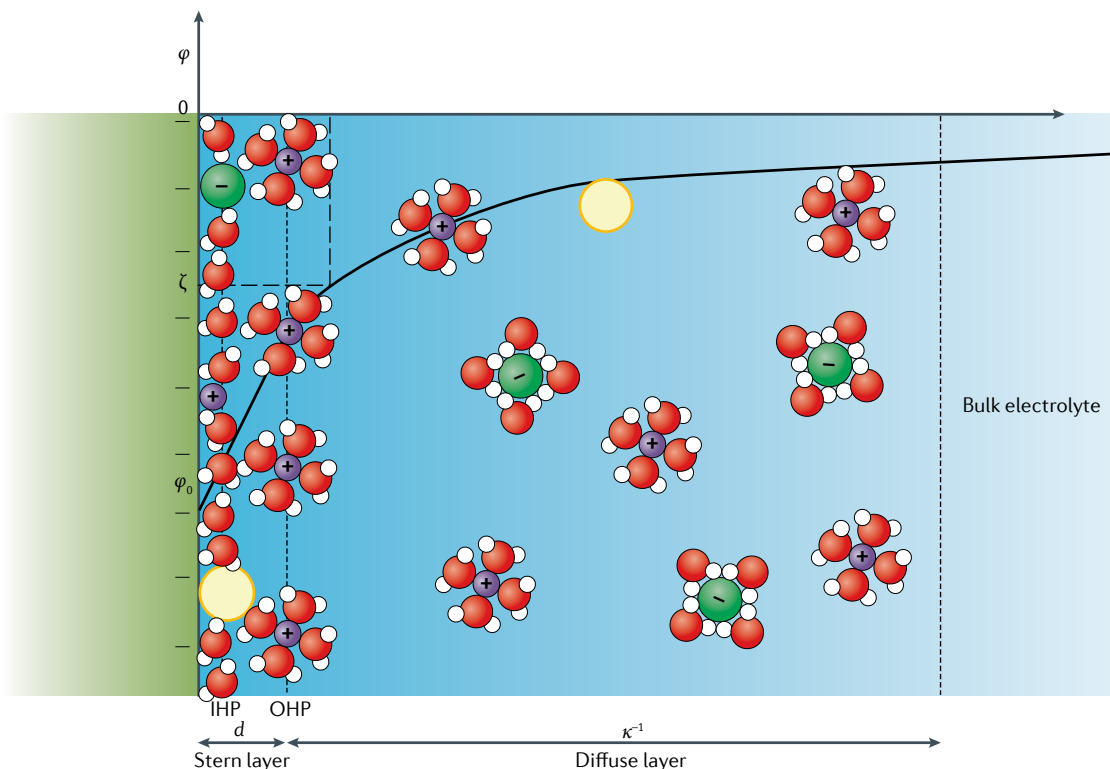


Figure 2-3.: Schematic of the water molecules at a charged interface. The potential  $\phi$  as a function of the distance from the interface is shown as a solid curve. The inner Helmholtz plane (IHP) and the outer Helmholtz plane (OHP) are marked with dashed vertical lines. The extent of Stern layer and diffusive layer (Debye length,  $\kappa^{-1}$ ) are indicated with double headed arrows. The yellow, purple, and green spheres represent neutral species, cations, and anions, respectively. Figure taken from Gonella, G. et al. Water at Charged Interfaces. *Nature Reviews Chemistry*, 5:466–485, (2021), Springer Nature. DOI: <https://doi.org/10.1038/s41570-021-00293-2>. Reproduced with permission from Springer Nature. Ref. [17].

The investigations on the structure and charge transfer dynamics of solvents at a charged interface are gaining more attention because of their fundamental nature and technological importance. For instance, hydrogen oxidation and evolution reaction occurs at electrode-water interfaces in hydrogen fuel cells and electrolyzers [65–67]. Moreover, the surface charges influence the generation of  $\text{H}_2$  from  $\text{H}_2\text{O}$  in metal-oxide based photocatalytic water splitting processes [68–70]. Recently, the role of alkali in promoting the conversion of  $\text{CO}_2$  into  $\text{CH}_4$  at the interface of  $\text{H}_2\text{O}/\text{Cu}(111)$  and the reduction of  $\text{CO}_2$  to  $\text{CO}$  at metal surfaces are investigated theoretically and experimentally, respectively [16, 71].

The efficiency of the aforesaid electrochemical processes are governed by the nature of the

so-called electric double layer (EDL) which defines the molecular-level interactions of the solvent with a charged interface [17]. The investigations on interfacial layers on electrodes date back to the 1850s by Helmholtz in which the charge distribution at the interface between a conductor and an electrolyte are described as a capacitor [72]. Since then, several attempts were made to develop a classical mean-field description of the double layer structure to address diverse scientific problems satisfactorily [73–79].

The schematic of the EDL based on the Gouy-Chapman-Stern model is shown in Fig. **2-3**. The adsorption sites of ions at an interface/electrode are designated as specific adsorption, electrostatic adsorption, and quasispecific adsorption based on their locations [80]. The electrode-electrolyte interface region is enriched by the counter charged ions from the bulk of the solvents and are termed as specific adsorption. The plane containing the specific-adsorption sites is known as inner Helmholtz plane (IHP). The fully solvated ions in the bulk are attracted towards the electrode due to their counter-charge and they get adsorbed on the interface. Such adsorptions are known as the electrostatic adsorption. The quasispecific adsorption refers to the adsorption of cations (anions) mediated by anionic (cationic) species. These cations (anions) do not interact with the electrode directly. The plane containing the electrostatic adsorption sites is known as outer Helmholtz plane (OHP) which is the closest approach of the fully solvated ions. The region between IHP to OHP is known as Stern layer where the potential decreases linearly. The diffuse layer is the region where the potential decay into bulk with a characteristic screening length known as Debye length,  $\kappa^{-1}$ . All length scales are comparable in highly concentrated salt solutions. The properties of the EDL are crucial for solvation and desolvation processes at electrode-electrolyte interfaces. The techniques used for studying the EDL are non-linear optical spectroscopy, photoelectron spectroscopy, atomic force microscopy, Kelvin probe microscopy, to name a few [81–88].

One of the exemplary scenarios of solvation and desolvation can be found in the operation of  $\text{Li}^+$ -ion batteries as schematically shown in Fig. **2-4**. The battery module has a graphite structure and a transition metal oxide which act as anode and cathode, respectively. During the charging phase, the  $\text{Li}^+$  ions are travelling from the anode to the cathode and bulk solvation of ions occurs in the electrolyte. These  $\text{Li}^+$  ions are then desolvated at the interface and are intercalated into the graphite structure. During the discharge process, the  $\text{Li}^+$  are deintercalated and get solvated while travelling from the cathode to the anode where they are stored as metal. The charge transfer processes from the alkali to the metal or vice versa occur at the interface and are decisive for the performance of the battery. The electrons flow only through the circuitry outside of the battery cell. The readers are recommended to refer a few review articles for a discussion on past, current, and future aspects of battery research [90–93]. Earlier, the efforts for the optimization of the performance of batteries were focused mainly on the bulk solvation of ions and that have changed recently to the EDL interface where all electrochemical reactions occur [94–98].

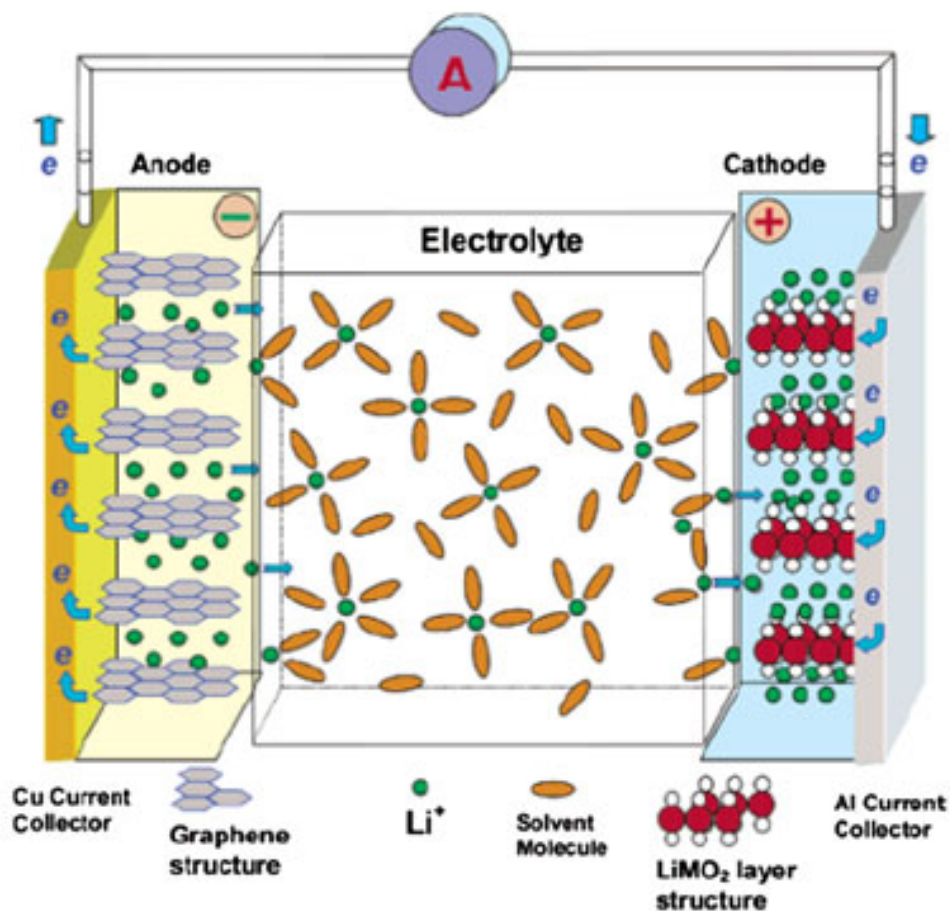


Figure 2-4.: Schematic of a Li<sup>+</sup>-ion battery that utilizes graphene and a transition metal oxide as anode and cathode, respectively. The solvation and desolvation of the Li<sup>+</sup> ions occur at the electrolyte-electrode interfaces during the charging and discharging processes. Reprinted figure with permission from Kang Xu. Nonaqueous Liquid Electrolytes for Lithium-Based Rechargeable Batteries. *Chemical Reviews*, 104(10):4303–4418, (2004). Copyright © 2004 by the American Chemical Society. Ref. [89].

Furthermore, recent investigations show that the presence of the alkali metal ions at interfaces are crucial for electrochemical reactions, although their exact role is under discussion [16, 71]. In a recent work, Monteiro et al. have demonstrated the reduction of CO<sub>2</sub> on noble metal electrodes in the presence of alkali ions experimentally by cyclic voltametry (CV) and scanning electrochemical microscopy techniques [16]. The schematic of a proposed CO<sub>2</sub> reduction mechanism is shown in Fig. 2-5 with relevant chemical reaction pathways. The CO<sub>2</sub> molecule interacts with the substrate to form \*CO<sub>2</sub><sup>-</sup> where \* represents the physisorbed chemical species on the substrate. Then it interacts with the metal cation (M) to form a

$^*\text{CO}_2^- \text{-M}^+$  intermediate compound which in turn react with water molecules to form  $^*\text{COOH} + \text{M}^+ + \text{OH}^-$ . Subsequently,  $^*\text{COOH}$  dissociates to form  $^*\text{CO} + \text{OH}^-$ . Finally,  $\text{CO}(\text{gas})$  is liberated from the substrate. Here, the  $\text{CO}_2$  reduction efficiency varies among different alkali metals. The concentration of alkali metal ions and their ability to interact with negatively charged adsorbates are decisive for the reduction of  $\text{CO}_2$ . For instance, metal cations with a softer hydration shell have a higher concentration at the interface and they exhibit stable coordination with  $\text{CO}_2$  ( $\text{Na}^+$ ,  $\text{K}^+$  and  $\text{Cs}^+$ ). They stabilize easily due to  $\text{M}^+ \text{-O}(\text{CO}_2)$  local interaction. On the other hand, hard hydration shell with  $\text{Li}^+$ , exhibits poor coordination with  $\text{CO}_2$  and thus the stabilization is less efficient [16].

The aforementioned cases of the Li-ion battery and the  $\text{CO}_2$  reduction mechanisms are typical contexts where alkali solvation/desolvation occurs at interfaces. The research carried out in the context of this thesis work addresses fundamental mechanisms at interfaces such as charge injection, charge transfer, energy stabilization, and charge back transfer which are competing processes at an electrolyte/electrode interface. In the experiments reported in this thesis, a model system such as  $\text{Cs}^+/\text{Cu}(111)$  is used as a charged interface, and the solvents such as Xe (nonpolar) and water (polar) are considered for the investigations. The results on the  $\text{D}_2\text{O}/\text{Cs}^+/\text{Cu}(111)$  and  $\text{Xe}/\text{Cs}^+/\text{Cu}(111)$  systems are presented in the chapter 4 and 5, respectively.

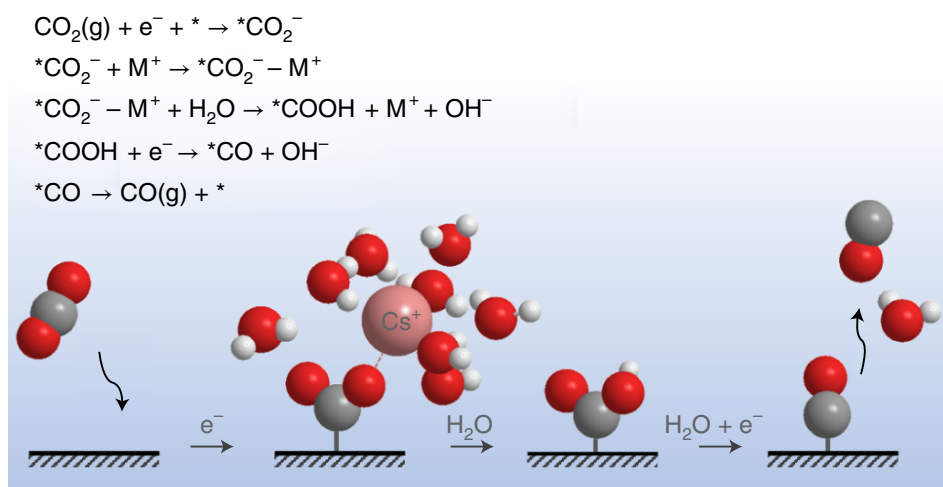


Figure 2-5.: Schematic of a  $\text{CO}_2$  reduction mechanism in presence of a  $\text{Cs}^+$  cation at an interface. The electrochemical reaction pathway is shown in the inset. The oxygen, hydrogen, carbon and cesium atoms are represented as red, white, silver, and pink spheres, respectively. Figure taken from Monteiro, M. C. O. et al. Absence of  $\text{CO}_2$  Electroreduction on Copper, Gold and Silver Electrodes Without Metal Cations in Solution. *Nature Catalysis*, 4:654–662, (2021), Springer Nature. DOI: <https://doi.org/10.1038/s41929-021-00655-5>. Reproduced with permission from Springer Nature. Ref. [16].

## 2.3. Electronic Structure and Dynamics of Adsorbates at Interfaces

This section discusses two-photon photoemission (2PPE) works reported on adsorbates system at interface which are relevant to this thesis work. The first part of this section presents the 2PPE results of alkali metal adsorbates which are extensively investigated as a model systems for more than two decades. The second part of this section discusses 2PPE of physisorbed molecules at interfaces with more emphasis on solvation of electrons. The last part of this section presents heterogeneous adsorbates at interfaces where an elaborate discussion on alkali-water adsorbates at interfaces are presented.

### 2.3.1. Chemisorption of Alkalis on Cu(111) Surfaces

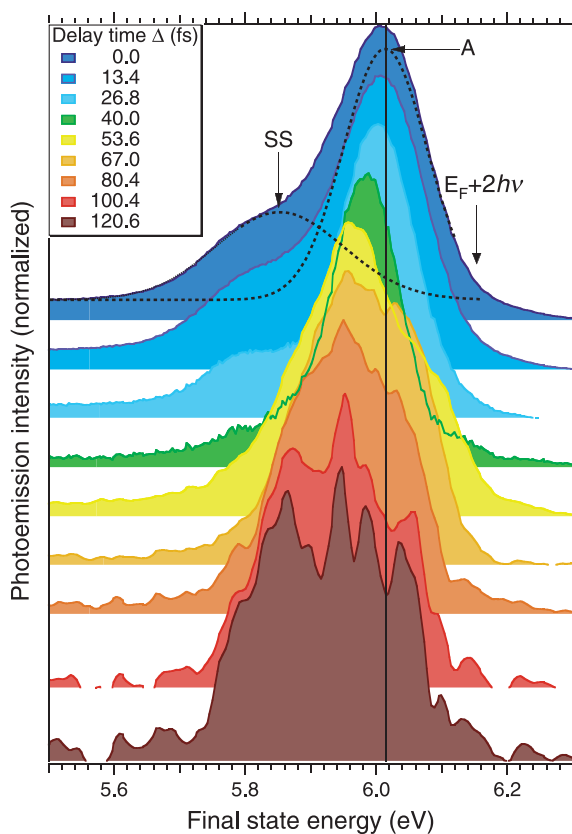


Figure 2-6.: The time-resolved 2PPE spectra of Cs<sup>+</sup>/Cu(111) where pump-probe delays set to an integral number of optical cycles. The dashed lines represent the deconvolution of surface state (SS) and anti-bonding state (A), and the solid line represents the energy of the state A. The complex change in the spectral profiles as a function of time delay originates from the interference effects in the wave packet creation and propagation. Figure taken from Petek, H. et al. Real-Time Observation of Adsorbate Atom Motion Above a Metal Surface. *Science* 288:1402-1404, (2000). Reprinted with permission from AAAS. Ref. [3].

The change in physical and chemical properties of metals upon adsorption of alkalis were reported in the pioneering works by Langmuir in 1923 [99,100]. The adsorption of alkalis and molecules on metals leads to interesting mechanisms such as charge transfer, reduction



in work function, changes in bond energy and molecular orientation, surface reactivity, to name a few. The change in surface properties of metals upon adsorption of alkali metals are reviewed systematically in the literature [101,102]. The 2PPE studies of Cs alkali on Cu(111) are reported by Bauer et al. in which electrons are injected resonantly to the unoccupied 6s orbital from the Cu substrate. The lifetime of the anti-bonding state (Cs 6s) becomes more pronounced than that of an intermediate state when both are excited from the surface state of Cu(111) [1]. Since then, several experimental investigations, see, e.g., [2,3,103,104], and theoretical studies, see, e.g., [105–107], have been performed on the excited states of chemisorbed alkalis on metals as a model system for studying the charge transfer processes at interfaces.

One of the noticeable studies on the Cs/Cu(111) surface is reported by Petek et al. in which the nuclear motion of the Cs ions is observed along the surface normal upon resonant photoexcitation to the 6s orbital [3]. The change in the excited state energy as a function of pump-probe delay is shown in Fig. **2-6** where the energy of the resonance decreases by 0.12 eV over 100 fs after photoexcitation. The excited state has two decay components - a fast  $\leq 15$  fs coherent polarization and a slower energy-dependent, non-exponential decay of the anti-bonding state population. The observed non-exponential decay is attributed to the dissociative motion of Cs atoms on Cu(111). To quantify the nuclear motions on the surface, the time-dependent change in the energy of the excited state is converted to time-dependent changes in the Cu-Cs bond length according to [105] and is fitted to a fourth-order polynomial to get a continuous function of  $R_{\text{Cu-Cs}}(t)$ . This function is differentiated twice to calculate the force acting on the Cs atom as  $F = ma = m\partial^2 R(t)/\partial t^2$  where  $m$  is the mass of the atom. Subsequently, the potential energy surface (PES),  $U$  is determined by integrating the force as,  $U = -\int F \cdot dR$ . The stretching of the Cu-Cs bond is found to be  $\approx 0.35$  Å in 160 fs after the photoexcitation. The photodesorption yield is not substantial since the electronic relaxation back to metal occurs before desorption.

Furthermore, a systematic investigation of the electronic spectra of all alkali metals (Li to Cs) on Cu(111) was performed by Zhao et al. [2]. The Fig. **2-7** shows the influence of the sizes and the ionization potentials of the alkalis on 2PPE spectra as a function of coverage. The work function of the surface decreases with an increase in alkali coverage as indicated by the decrease in energy of the low-energy cut off of the 2PPE spectrum. The alkali adsorption results in the formation of the surface dipoles (dipole moment,  $\mu = 2R_{\text{ads}}$  where  $R_{\text{ads}}$  is the chemisorption distance) and it decreases the work function of the surface. The extent of decrease in work function is related to the surface density ( $\sigma$ ) of alkali atoms as  $\Delta\Phi = 2\pi\mu\sigma$ . Hence, for a given alkali coverage on the surface, the change in the work function is smaller for Li than Cs. In Fig. **2-7**, only the surface state (SS) (red arrows) feature is originating from pure Cu(111) and the anti-bonding resonance, AR, (blue arrows) feature originates from the outermost  $s$  orbital of the alkali. The photoelectron intensity and energy of the AR changes as a function of coverage of the alkali where the maximum intensity of the peak occurs when the AR  $\leftarrow$  SS transition becomes resonant with the photon energy. The alkali

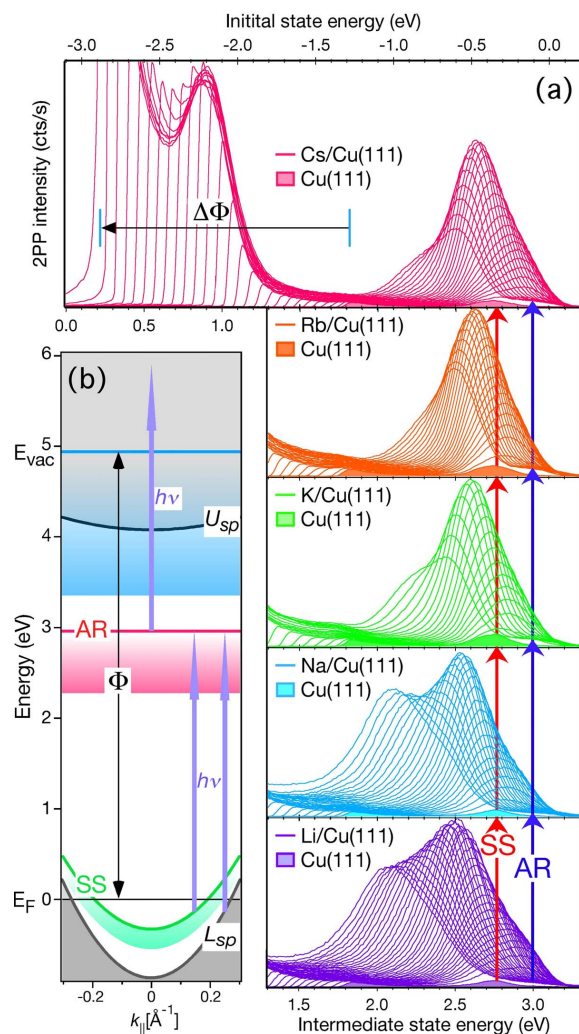


Figure 2-7.: (a) The 2PPE intensity of alkalis (Li to Cs) on Cu(111) is plotted as a function of intermediate state energy (bottom) and initial state energy (top) up to an alkali coverage of 0.1 ML. The Shockley surface state (SS) and anti-bonding resonance (AR) are indicated by red and blue arrows, respectively. (b) The surface-projected band structure as a function of intermediate state energy and electron momentum parallel to the surface ( $k_{\parallel}$ ). A projected band gap exists between the lower ( $L_{sp}$ ) and upper ( $U_{sp}$ )  $sp$  bands. The SS, AR and vacuum level are indicated with green, red and blue lines, respectively. The possible resonant transitions from SS and  $L_{sp}$  to AR at different  $k_{\parallel}$  are marked with vertical arrows. Reprinted figure with permission from Zhao, J. et al. Electronic Potential of a Chemisorption Interface. *Phys. Rev. B*, 78:085419, (2008). DOI: <https://doi.org/10.1103/PhysRevB.78.085419>. Copyright © 2008 by the American Physical Society. Ref. [2].

atoms show significant decrease in ionization potential with increase in atomic size. However, such dependence are not apparent in their binding energy. Remarkably, it is also observed that the width of the AR peak decreases with an increase in atomic radius from Li to Cs as shown in Fig. 2-7. The relatively larger width of the AR of Li (which is adsorbed closer to the surface) is attributed to the shorter lifetime of the electrons that broadens the spectrum according to the energy-time uncertainty relation. This work supported the ionic nature of the interaction during the chemisorption of alkalis where the Coulomb interaction and Pauli exclusion principle are accounted for and excluded the possibility of a covalent interactions where valence electrons occupy the orbitals shared by the adsorbate and the substrate [2].

### 2.3.2. Physisorbed Atoms/Molecules on Metal Surfaces

Two-Photon Photoemission (2PPE) Spectroscopy of physisorbed atoms/molecules have been extensively investigated for more than two decades for noble gases to complex organic molecules adsorbed on diverse noble metal surfaces [13, 108–116]. The efforts were intended

to understand (1) the behaviour of the excess electrons in polar or non-polar molecular environments, (2) the influence of adlayers on the electronic properties of the metal surfaces, and (3) the solvation of molecules in the presence of ions.

The properties of solvated electrons is a subject of continuing interests in the scientific community over a long time. The properties of the solvated electrons such as cavity-forming or non-cavity forming structures, adiabatic or non-adiabatic relaxation mechanisms, existence of long-lived surface electron, and accurate values for electron binding energy (eBE) are still under debate [7–10, 117–121]. In the context of surface science experiments, self-trapping of electrons at the interface as a result of small polarons is reported by Ge et al. by using time and angle-resolved 2PPE techniques [108]. In their work, a n-heptane bilayer is adsorbed on a Ag(111) substrate and its influence studied on the well-known image potential states on metals [122, 123]. The image potential states are unoccupied intermediate states bound with respect to the vacuum level of the metal with energies similar to hydrogen atoms. These states are delocalized on the surface. The alkane layers with their negative electron affinity decouples image potential states further away from the surface. Upon excitation of the electrons to the image potential states, the electrons try to stabilize their energy by locally altering the dielectric properties of the molecular environment. As a result, the excited state becomes more localized with longer lifetime than the delocalized state. The angle and time-resolved 2PPE experiments provide insights into the evolution of the state from a delocalized to localized state in which  $E$  vs.  $k_{\parallel}$  changes from dispersive to flat. This kind of mechanism is analogous to the electron transfer processes proposed by Marcus in 1956 [124] and such processes are ubiquitous in Chemistry and Biology [125].

Furthermore, image potential states and changes in their properties with adlayers of noble gas atoms or simple molecules have been investigated extensively in the past decades [109–112, 126–129]. There are several studies on the effect of noble gases (Ar, Kr, and Xe) on the image potential states of the Cu(100) [112, 126, 127]. It is reported that the lifetime of the image states increases up to 10 ps for an Ar coverage for 5 ML [126] due to its negative electron affinity. In contrast, decoupling of the image states on Cu(100) is less prominent for Kr and Xe because of their positive electron affinity [112]. In another study, image potential states of the Ag(111) and Cu(111) with a monolayer of Ar are investigated and it is found that the properties of the image potential states are significantly different on both surfaces [129]. On Ag(111) surface, the lifetime of the  $n = 1$  state increases to 6 ps for a coverage of 4 ML Ar whereas on Cu(111), the lifetime does not exceed 3 ps up to a coverage of 10 ML of Ar. To sum up, the lifetime of the image potential states on metals are significantly affected by the electron affinity of the adsorbates and also depend on the crystallographic orientation of the surface. In this thesis work, D<sub>2</sub>O and Xe are utilized as solvents for ion solvation. A discussion of the spectroscopy of these adsorbates on Cu(111) is presented as follows.

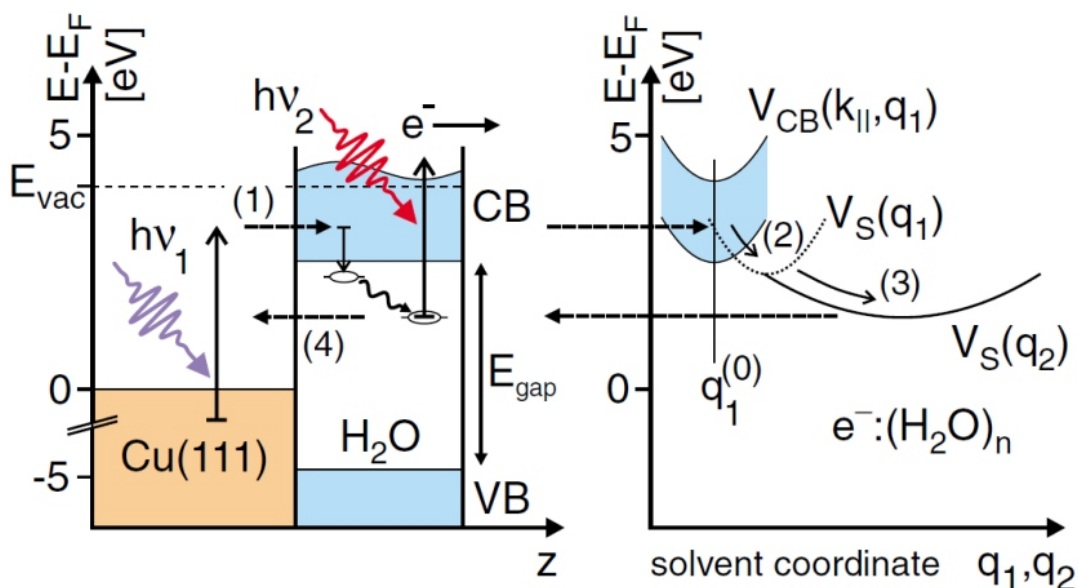


Figure 2-8.: The energy level diagram for the electron solvation in water (left) and its potential energy surface as a function of solvent coordinates (right). The surface solvation process involves electron transfer (step-1), localization (step-2), solvation (step-3), and back transfer (step-4) as marked in the diagrams. Reprinted figure with permission from Gahl, C. et al. Ultrafast Dynamics of Electron Localization and Solvation in Ice Layers on Cu(111). *Phys. Rev. Lett.*, 89:107402,(2002). DOI: <https://doi.org/10.1103/PhysRevLett.89.107402>. Copyright © 2002 by the American Physical Society. Ref. [13].

**D<sub>2</sub>O on Cu(111):** Ultrafast dynamics of electron localization and solvation in ultra thin layers of ice on Cu(111) are reported by Gahl et al. in their study [13]. The elementary steps in the electron solvation process are described as shown in Fig. 2-8. Direct excitation of electrons from the valence band (VB) to the conduction band (CB) of the ice layers is not possible (in the linear absorption regime) with the pump laser energy of  $\approx 4$  eV due to the large bandgap of the ice (8.2 eV). The electrons are injected to the CB of the ice layers from the metal substrate (*step-1*) since there is an overlap of wave functions of CB of ice and photoexcited electrons. In addition to the back-transfer to the substrate, the delocalized electrons can find specific sites on ice where it can localize (*step-2*) by reconfiguring the solvent molecules (fluctuations in bond angles or uncompensated hydrogen bonds) as shown in the right panel of Fig. 2-8. The localization results in time-dependent flattening of the dispersion curve which occurs  $\approx 100$  fs after photoexcitation. Electrons are stabilized further in the ice layers over a period of a few picoseconds duration (*step-3*) similar to the self-trapping phenomena discussed in [108]. This shifting of the binding energy of the trapped state due to the rearrangement of the water molecules represents the solvation of the electrons. As shown in the right panel of Fig. 2-8, a one-dimensional potential energy surface is plotted as a function of a hypothetical solvation coordinate,  $q_i$ . The potential of the

system changes from a highly delocalized state ( $q_1$ ) to a localized state ( $q_2$ ) upon solvation. Finally, the back transfer of electrons to the metal substrate (*step-4*) leads to the decay of the population from solvated state. In fact, a back-transfer process is observed at all times (*step 1 – 3*) and it becomes prominent only in the last step. The solvation process occurs faster at lower coverages ( $\Theta \leq 2$  BL) due to less-rigid coordination of solvent molecules than for higher coverages ( $\Theta \geq 3$  BL) [13].

Furthermore, ice structures are known to exhibit crystalline and amorphous structure at substrate temperatures  $T \geq 140$  K and  $T \leq 110$  K, respectively [130]. The 2PPE spectroscopy of the amorphous and crystalline structure of ice layers shows a change in the work function by  $\approx 400$  meV upon phase transition [131]. The dynamics of the solvated electrons vary during the structural phase transition [132]. Further efforts to explore the structure and electron solvation dynamics, identification of the electron solvation site, and binding energy of the solvated state in water clusters on Cu(111) are reported in several works [14, 113, 133, 134]. In ref. [113], the low-temperature STM studies show that the amorphous ice structures can be porous or compact at temperatures of 85 K and 120 K, respectively. The 2PPE studies of these structures have revealed that the solvated electrons in the porous ice structures are loosely bound and they decay faster (30 % faster) than in compact structures. The longer lifetime in compact ice structures is attributed to the higher density of D<sub>2</sub>O molecules underneath the solvated electrons.

As discussed above, the electron solvation can occur in crystalline or amorphous ice (porous or compact) structures or in the wetting layers. Xe overlayers can be used to identify the solvation sites in different ice structures, since Xe is highly polarizable. It can strongly interact with localized solvated state if the solvation site is on the surface. The experiments show that in both amorphous porous and amorphous compact structures of water clusters the solvated electron peak shifts more than 400 meV to higher energies which indicates that the ice-vacuum interface is the favourable location for solvated electrons [113, 134]. In the case of wetting layers of water on Cu(111), the Xe overlayer has no effect on the binding energy and stabilization rate of the solvated electron state because Xe is not interacting with the bulk solvated state [133]. In addition, the stabilization rate of  $0.22$  eV ps<sup>-1</sup> is found in the three types of water structures (porous, compact, and multilayer). However, the dynamic response or the population decay of the three structures are significantly different and it is proposed that solvated electrons reside on the edge of the amorphous water cluster [134]. A comprehensive review on different aspects of the electron solvation in amorphous water structures is presented in ref. [135].

In a recent work [14], the elementary steps during the ‘birth’ of the solvated state electrons are investigated with a better time-resolution than previous studies [13, 113, 133]. The schematic of the processes associated with the solvation and the relaxation dynamics of the system are shown in Fig. **2-9**. The electrons are excited from the SS state of Cu(111) to the delocalized CB of water clusters and they relax to the CB minimum around 800 meV below the excitation at a rate of 4 meV/fs. The localization of the electrons occur within 22 fs

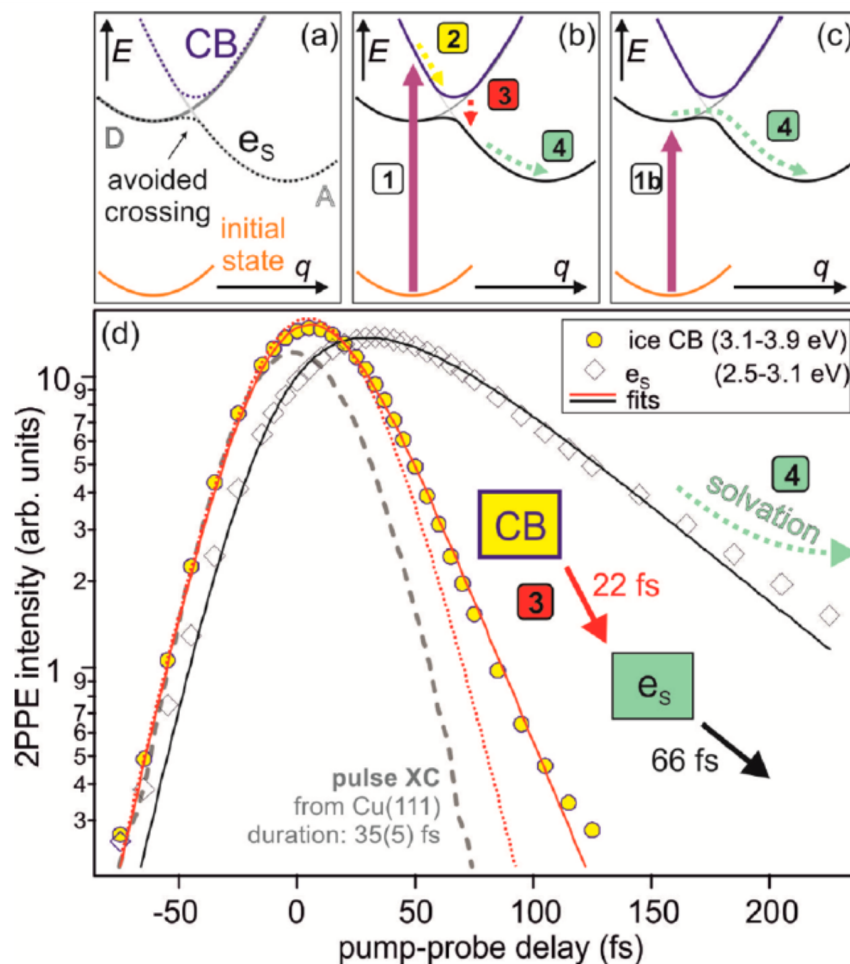


Figure 2-9.: (a) Marcus representation of potential energy surface (PES) for conduction band of ice (CB) and trapped state of electrons ( $e_s$ ). (b) Charge transfer from metal to CB of ice (1), relaxation to CB minimum (2), vertical transition to  $e_s$ (3), and relaxation to potential minima (4). (c) Direct excitation to  $e_s$  and subsequent relaxation. (d) Energy-integrated, time-resolved 2PPE intensity of CB (circles) and  $e_s$  (diamonds) fitted by rate equation models (solid lines). Comparison of indirect excitation and direct excitation to  $e_s$  are shown in solid and dotted red lines. Reprinted figure from Stähler, J. et al. Real-Time Measurement of the Vertical Binding Energy During the Birth of a Solvated Electron. *Journal of the American Chemical Society*, 137:3520–3524, (2015). DOI: <https://doi.org/10.1021/ja511571y>. Article licensed under Creative Commons Attribution 4.0 International Public License. Ref. [14].

with a gain of several hundreds of meV of binding energy. This energy dissipation results the high-frequency vibrations of the molecular environment. Finally, the solvated state resides a few hundreds of fs before the electrons decay back to the metal substrate. In addition to the indirect excitation to the solvated state via CB of ice, direct excitation to the solvated state from the Cu  $sp$  is also observed. This indicates that the trapping sites are pre-existing

before the onset of the electron solvation [14].

**Xe on Cu(111):** The ultrafast electron dynamics of image potential states upon adsorption of a monolayer of Xe on Cu(111) is reported by Wolf et al. [109]. It is observed that the lifetime of the  $n = 1$  and  $n = 2$  image potential states of the Cu(111) has increased from 18 fs to 75 fs and from 17 fs to 40 fs, respectively. Furthermore, the lifetime of the  $n = 1$  image potential states are enhanced up to 1.6 ps by the adsorption of a monolayer of  $N_2$  which decouples the state further away from substrate due to its negative electron affinity [110]. The influence of adlayers on the femtosecond dynamics of image potential states of metal surfaces are reviewed in a publication for more details [136]. As part of this thesis work, the solvation of  $Cs^+$  ions by Xe on Cu(111) is investigated which exploits the local polarization of the electron cloud of Xe in the vicinity of alkali ions. Similar investigations of alkali-noble gas adsorbates at interfaces are not investigated extensively.

### 2.3.3. Heterogeneous Adsorbates at Interfaces

The heterogeneous surfaces are used as model systems for several phenomena that occur in nature as well as fundamental processes of technological importance [4, 15, 16, 24, 25, 90, 137]. The 2PPE spectroscopy of alkali and water on Cu(111) interfaces is one of the topics investigated as part of the thesis work. Hence, this section is intended to cover the important works that have been reported earlier [4, 15].

**Alkali-water interactions on Cu(111):** The solvated electron species at ice-metal interfaces have a lifetime of a few hundred femtoseconds to minutes in bulk or on the interfaces [132, 138]. The energy stabilization and population dynamics of the solvated electrons at interfaces are strongly influenced by the presence of alkali ions [4, 15]. The comparison of the time-resolved 2PPE spectra of ice layer (left) and Na-doped ice layer (right) on Cu(111) is shown in the Fig. 2-10. For a coverage of 5 BL  $D_2O$  on Cu(111), the solvated electrons feature appears at  $E-E_F = 2.90$  eV and the peak shifts to the lower energy with increasing time delay. The peak intensity decreases nonexponentially with lifetime of  $\tau_1 = 140$  fs for time-delay  $< 300$  fs and  $\tau_2 = 320$  fs for higher pump-probe delay. The solvated electron peak shifts to  $E-E_F = 2.60$  eV upon adsorption of 0.08 ML Na onto 5 BL  $D_2O$ , as shown in the right panel of Fig. 2-10, and also there is substantial increase in the lifetime of the solvated electrons (note that the difference in the x-axis of the left and right panel figures). For  $Na^+$ -doped ice layers, the solvated electron state has a longer lifetime up to 20 ps with three distinct decay regimes. The relaxation times of the solvated state are determined as  $\tau_1 = (110 \pm 10)$  fs,  $\tau_2 = (880 \pm 50)$  fs and  $\tau_3 = (9.60 \pm 5)$  ps. These relaxation times are found to vary as a function of the  $Na^+$  coverage [15].

In a recent work, Meyer et al. have investigated ultrafast solvation dynamics of alkalis (Na, K and Cs) on Cu(111) coadsorbed with  $D_2O$  [4]. A Marcus type conceptual energy diagram for solvated  $Na^+/Cu(111)$  is shown in Fig. 2-11 and it is applicable to other alkalis too. The solvation coordinate (bottom axis) is not a real coordinate but rather conceptual in

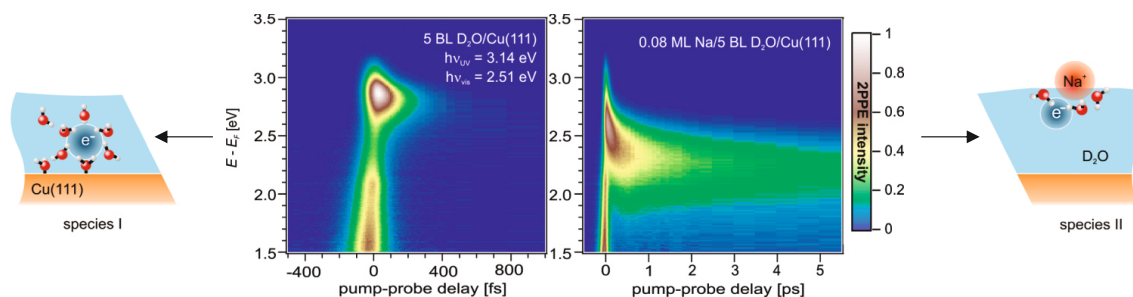


Figure 2-10.: Left panel: False colour representation of 2PPE intensity from 5 BL D<sub>2</sub>O/Cu(111) as a function of intermediate state energy and pump-probe delay, and the schematic of the electron solvation indicated as species I. The peak at  $E - E_F = 2.9$  eV originates from the solvated electrons in a water film. Right panel: False colour representation of 2PPE intensity from 0.08 ML Na on 5 BL D<sub>2</sub>O/Cu(111) and the schematic of the electron-alkali complex at the interface is indicated as species II. The peak at  $E - E_F = 2.6$  eV results from the electron solvation in the presence of Na ions. The spectra are recorded as cross-correlation measurements with pump and probe pulses with photon energies at 3.14 eV and 2.51 eV, respectively. Reprinted figure with permission from Meyer, M. et al. *Ultrafast Dynamics at the Na/D<sub>2</sub>O/Cu(111) Interface: Electron Solvation in Ice Layers and Na+-Mediated Surface Solvation. The Journal of Physical Chemistry C*, 115:204-209, (2011). DOI: <https://doi.org/10.1021/jp107253g>. Copyright © 2011 by the American Chemical Society. Ref. [15].

nature and it represents the coordination/configuration of water molecules in the solvation structure. The ground state of the adsorbate system is in a solvated state and it is represented as  $2p^6 \text{Na}^+$  (aq.). The excited state  $3s \text{Na}$  (aq.) is attained by the charge transfer from the metal to adsorbate by the pump pulse and it is a vertical transition along the solvation coordinate axis. Note that the solvation coordinates are different for the minima of the ground and excited state. The excited state evolves to the bottom of the potential along the solvation coordinate to gain energy and results in the rearrangement of the solvent molecules. The relaxation dynamics of the system is captured by photoemission from the excited state by using a time-delayed probe pulse. The kinetic energy of the photoemitted electrons are measured in a time-of-flight spectrometer.

The time-resolved 2PPE spectra of the hydrated alkalis are shown in Fig. 2-12 that exhibit three common features for the investigated alkalis (Na, K, and Cs). They are (1) an energy state which occurs a few 100 meV below the binding energy of the alkali due to water-alkali hybrid formation, (2) considerably large energetic stabilization by transferring energy to the solvent molecules upon relaxation, and (3) an excited state lifetime of a few 100 fs which is significantly longer than that of bare alkali on the surface. All these aspects are discussed as follows.

Firstly, as shown in Fig. 2-12, the antibonding feature of the surface splits into two states



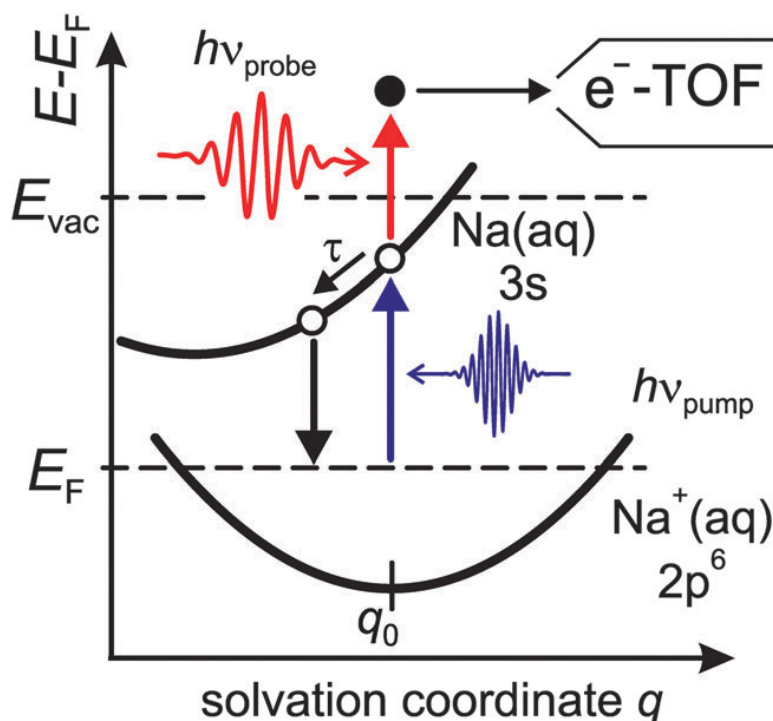


Figure 2-11.: The schematic of the potential energy diagram of  $\text{Na}^+/\text{Cu}(111)$  coadsorbed with  $\text{D}_2\text{O}$ . The ground state is represented as  $2p^6 \text{Na}^+(\text{aq.})$  and is at its minimum near the equilibrium solvation coordinate  $q_0$ . The excited state,  $3s \text{Na}(\text{aq.})$  is attained by the excitation of electrons from the metal substrate to the alkali using optical pulses. The excited adsorbate system relaxes in a time  $\tau$  and its dynamics is captured using a probe pulse. Reprinted figure from Meyer, M. et al. Ultrafast Electron Dynamics at Water Covered Alkali Adatoms Adsorbed on  $\text{Cu}(111)$ . *Phys. Chem. Chem. Phys.*, 17:8441–8448, (2015). DOI: <https://doi.org/10.1039/C4CP05356G>. The article is licensed under a Creative Commons Attribution 3.0 Unported Licence. Ref. [4].

for K and Cs on  $\text{Cu}(111)$  after the adsorption of water. The high-energy peak (at 2.7 eV for K and 2.8 eV for Cs) originates from bare alkalis on the substrate and the low-energy peak (at 2.1 eV for K and 2.55 eV for Cs) originates from the formation of the alkali-water hybrid structures on  $\text{Cu}(111)$ .

Secondly, the energy of the alkali-water hybrid state decreases with respect to the Fermi level as a function of time delay which indicates an increase in the binding energy of the state. The energy stabilization for all the investigated alkalis is in the range of 200-300 meV that occurs within 200 fs after photoexcitation. The extent of energy stabilization is determined by the population decay rate of the excited state and coupling of the excited electron back to the metal substrate. The concept of energy stabilization is explained in the Fig. 2-11 where the time-dependent increase in binding energy results in the solvent rearrangement.

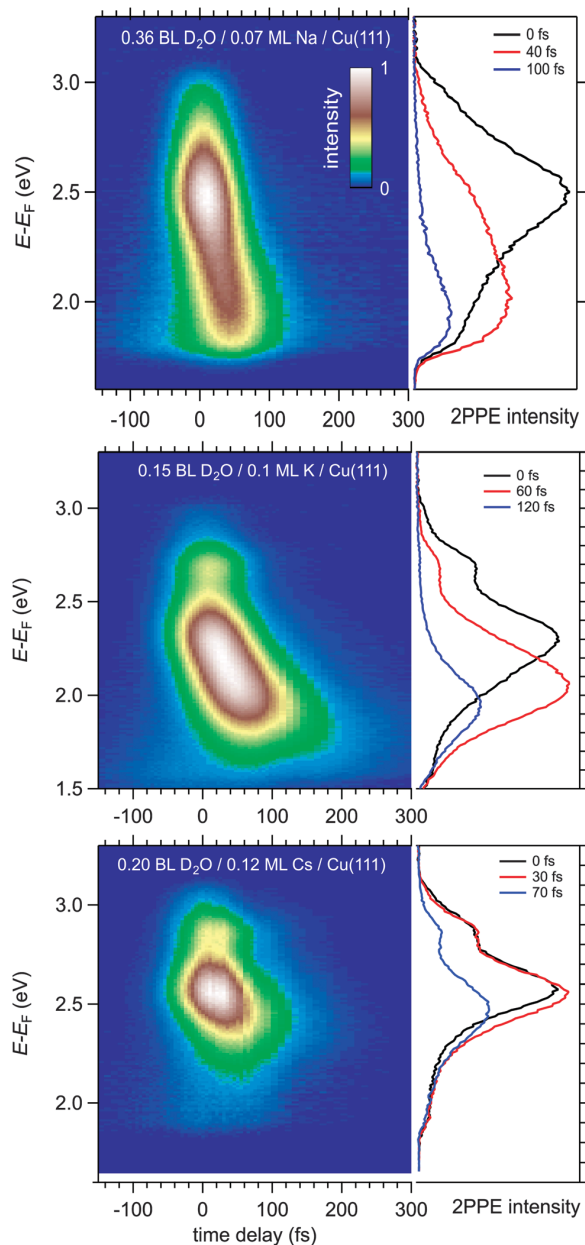


Figure 2-12.: The false colour intensity of time-resolved 2PPE from alkali (Na, K and Cs)-water clusters on Cu(111) is plotted as a function of the intermediate state energy (left) and the pump-probe time delays (bottom). The spectra at specific time-delay are shown in the right panel. The spectra exhibit two prominent features; a short-lived alkali resonance (at higher energy of the spectrum) and of water-induced state (a few 100 meV below the alkali resonance) are clearly distinguishable for K and Cs. The energy stabilization, the rate of change of the excited state energy has been found to be decreased from Na to Cs. Reprinted figure from Meyer, M. et al. Ultrafast Electron Dynamics at Water Covered Alkali Adatoms Adsorbed on Cu(111). *Phys. Chem. Chem. Phys.*, 17:8441–8448, (2015). DOI: <https://doi.org/10.1039/C4CP05356G>. The article is licensed under a Creative Commons Attribution 3.0 Unported Licence. Ref. [4].

The time-dependent change in the excited state potential energy surface along the solvation coordinate  $q$  and the transient increase of the binding energy is attributed to the response of the solvent after the excitation. The stabilization rate (in  $\text{eV ps}^{-1}$ ) for the water-alkali hybrid is determined as 2.1, 1.7 and 1.1 for Na, K and Cs, respectively. The  $\text{Na}^+$  ions are solvated by rigid and well aligned arrangements of water molecules which will respond and gain energy faster upon optical excitation than Cs with its weaker alkali-water interaction.

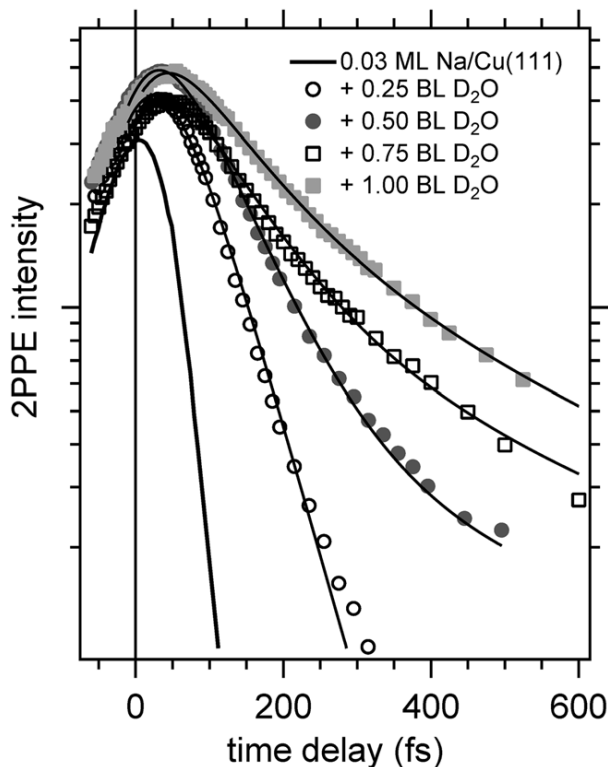


Figure **2-13**.: Time-resolved 2PPE intensity from Na/Cu(111) as a function of water coverage. The lifetime of the Na<sup>+</sup>-water hybrid structure increases with water coverage. A solid line is shown for bare Na<sup>+</sup> on Cu(111) to indicate the laser pulse profile and the markers with solid lines represent the fit to the data by the convolution of a bi-exponential and the laser pulse correlation. Reprinted figure from Meyer, M. et al. Ultrafast Electron Dynamics at Water Covered Alkali Adatoms Adsorbed on Cu(111). *Phys. Chem. Chem. Phys.*, 17:8441–8448, (2015). DOI: <https://doi.org/10.1039/C4CP05356G>. The article is licensed under a Creative Commons Attribution 3.0 Unported Licence. Ref. [4].

Finally, the energy-integrated 2PPE intensity as a function of pump-probe time delay is shown in Fig. **2-13** for different Na-water hybrids on Cu(111). For bare alkali, the dynamics fit to the convolution of laser pulse profile and single exponential decay is consistent with previous observations [1, 2, 106]. However, upon increasing the coverage of the water on Na/Cu(111), the relaxation dynamics changes significantly and it follows a non-exponential decay similar to solvated electrons in amorphous solid water films [13]. The data shown in Fig. **2-13** are fitted better with a bi-exponential decay function. At lower coverage of water on Na/Cu(111), the dynamics of the system resembles the bare alkali on Cu(111). At a water coverage almost an order higher than that of Na, the relaxation dynamics changes substantially due to the onset of the pure electron solvation dynamics which competes with the excited state of the solvated alkali and hence results in a complex relaxation mechanism. It is known that the transient neutralization of the chemisorbed alkali by optical excitation leads to the nuclear motion along the surface normal [3]. So, such excitation in presence of solvent molecules undoubtedly results a coupled alkali-water mode of adsorbate dynamics. A detailed theoretical study on the dynamics of alkali-water clusters on Cu(111) was published recently [43] and it is discussed in the section 2.4.

## 2.4. Theoretical Calculations on Investigated Systems

This section briefly discusses the theoretical works relevant to the experiments performed as part of this thesis work. The thesis work focuses on the interaction between alkali (Cs) and polar ( $D_2O$ ) and non-polar (Xe) solvents on Cu(111). These adsorbates/surface systems represent model systems where a solvent encounters a charged interface. There are many theoretical and 2PPE experimental works on alkali-water systems at interfaces [4, 15, 24, 25, 43, 139]. Although, the interactions of alkalis with noble gases are investigated theoretically and experimentally in the bulk [12, 40, 44, 57–60], their interactions at interfaces were not addressed extensively until recently [44]. The following discussion is based on the theoretical results on the hydration of alkali (Na, K and Cs) on Cu(111) which is related to the work reported in this thesis [43].

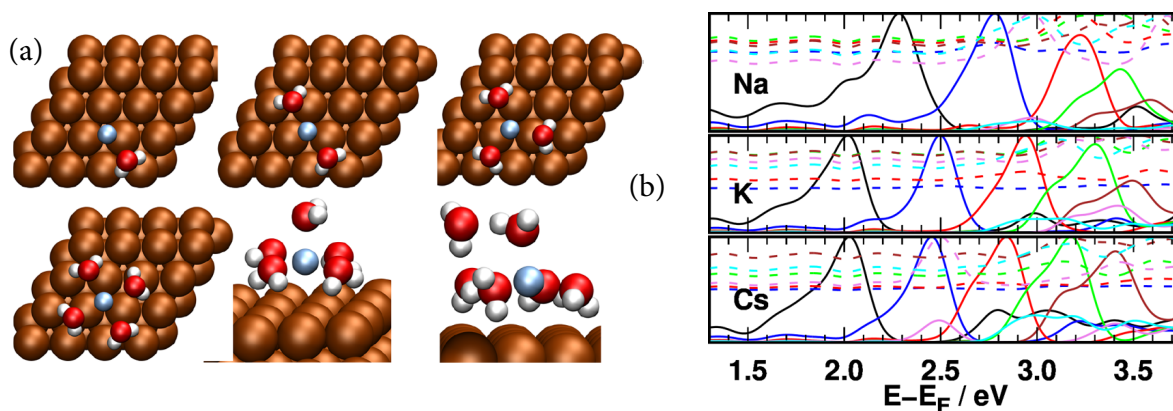


Figure 2-14.: DFT calculations on hydration of Na on Cu(111): (a) Optimized hydration structures of alkali by up to 6 water molecules. The Cu, H, O and Na atoms are shown in orange, white, red, and silver spheres respectively. The fifth water molecule is bonded to Na axially and the sixth water molecule forms a hydrogen bond with the fifth water molecule. (b) The electronic density of states (DOS in  $eV^{-1}$ ) projected on the s orbital of alkali atoms (solid lines on bottom) and valence of orbitals of the water molecules (dashed lines on top). The black, blue, red, green, brown, violet, and cyan lines represent the consecutive addition of water molecules from 0 to 6 molecules. Reprinted figure with permission from Alejandro Pérez Paz and Angel Rubio. Hydrated Alkali Atoms on Copper(111): A Density Functional Theory Study. *The Journal of Physical Chemistry C*, 125(7):3868–3879, (2021). Copyright © 2021 by the American Chemical Society. Ref. [43].

**Alkali Hydration on Cu(111):** Theoretical investigations on the hydration of alkalis/Cu(111) have been performed recently by Paz et al. [43] which is based on the previous experimental results [4]. They have reported the structure, surface charge properties, work function, and density of states (DOS) of hydrated alkalis on Cu(111) as a function of the

water coverages. The relaxed state cluster coordinations between an alkali and up to six water molecules are shown in Fig. **2-14** (a). The water molecules form a linear, trigonal pyramidal, tetragonal pyramidal, and square pyramidal as their coordination number increases from  $n = 2, 3, 4,$  and  $5,$  respectively. The alkali-water clusters are found to be in a quasi  $C_n v$  symmetry for  $n = 2-4$  water molecules. For  $n = 5,$  four water molecules remains in the equatorial plane and the fifth water molecule occupies the axial position close to the alkali. This reduces the work function of the surface because the new dipole points in opposite direction compared to the dipoles of the remaining water molecules. For coordination numbers  $n = \geq 6,$  the water molecules do not interact with the alkali atom, but it forms a hydrogen bond with the axial water molecule and there is the possibility of the formation of the second hydration shell [43].

In addition, the influence of the water molecules on the DOS of the unoccupied  $s$  orbital of the alkalis are shown in Fig. **2-14** (b). The energy of the outermost  $s$  orbital with respect to the Fermi level is at 2.3 eV for Na and 2 eV for K and Cs. The energy of the  $s$  orbital increases as a function of the water coverage due to the interaction between  $\sigma^*$  state and water states which is in agreement with previous 2PPE works [4,140]. At complete hydration, it is observed that the alkali detaches from the substrate and hence recovers the resonance energy at  $\sim 2.5$  eV (for Cs). This is confirmed by computing the DOS spectrum of an isolated alkali-water cluster in the absence of a substrate that reproduces the alkali peak at  $\sim 2.5$  eV [43]. Furthermore, the dashed lines in Fig. **2-14** (b) shows Kohn-Sham electronic state projections of orbitals as a function of water molecules in which DOS is distributed to alkali and water states. This indicates that the excited electrons can reside not only on the parent alkali  $s$  orbital but also on the water states. The increase in water coverage increases the availability of water states which further spread the alkali  $s$  orbital. As a result, the probability of resonant photoemission decreases [43].

The calculations in Paz et al. [43] are very relevant to the investigations performed as part of this thesis work. The increase in the work function of the alkali-covered surface and the upshift of the  $\sigma^*$  antibonding state are in agreement with the results discussed in chapter 4 of the thesis. However, the solvation structure and the interpretation for the origin of the new state are different in our studies.



## 3. Experimental Methods

In this chapter, experimental details of the static two-photon photoemission (2PPE) and time-resolved 2PPE (tr-2PPE) spectroscopy experiments on polar and non-polar solvents co-adsorbed with  $\text{Cs}^+$  on Cu(111) are presented. The first section discusses the fundamentals of the photoemission spectroscopy, excitation mechanisms in 2PPE, tr-2PPE and population dynamics, technical aspects of photoemission spectroscopy, data acquisition and analysis. The experimental details such as the principle of ultrashort pulse generation, characterization and optimization of laser pulses, and ultrahigh vacuum (UHV) system are described in the second section. In the last section, preparation of the Cu(111) surfaces and its characterization, and the preparation and characterization of adsorbates such as Cs, Xe and  $\text{D}_2\text{O}$  on Cu(111) are also described.

### 3.1. Photoemission Spectroscopy

The photoemission spectroscopy is based on the well-known photoelectric effect where the photoelectrons are emitted when photons with suitable energy are incident on a surface [141]. It is an attractive tool for investigating surface sensitive phenomena because the photoemitted electrons have short mean free path in the range of 3-50 Å for a wide range of electron energies from 5 eV to 5000 eV [142]. The incident photon energy ( $h\nu$ ) and kinetic energy ( $E_{kin}$ ) of the photoemitted electrons are related by:

$$h\nu = \Phi + E_{kin} + (E_i - E_F), \quad (3-1)$$

where  $\Phi$ ,  $E_i$ , and  $E_F$  are work function, initial state energy, and Fermi energy, respectively. Depending on the range of the energy of the incident photons, photoemission occurs from core level or valence bands. Hence, it is classified into three regions as ultraviolet photoemission (UPS, 5 to 100 eV), soft X-ray photoemission (SXPS, 100 to 1000 eV) and X-ray photoemission (XPS, > 1000 eV). Using the UPS (valence band photoemission), one can determine the electronic dispersion curves  $E(\vec{k})$  of the solid surfaces by angle-resolved photoemission, and Photoionization of core levels are observed in the case of SXPS and XPS (core level photoemission). The core level energy states are the chemical *fingerprint* of the surface under investigation and hence, the technique is often termed as ESCA (Electron Spectroscopy Chemical Analysis) [143]. There are significant differences in the treatment of valence and core level photoemission spectra.

### 3.1.1. Theory of Photoemission

The basic theory of photoemission with more emphasis on valence band photoemission along with one-step and three-step photoemission models are presented in this section. These contents are adopted from the text book, ‘Photoelectron Spectroscopy, Principles and Applications’ by Stefan Hüfner [143].

An important concern in the theory of photoemission spectroscopy is the influence of non-interacting electrons ( $V = 0$ ) and interacting electrons ( $V \neq 0$ ). In the case of non-interacting electron system, the spectrum has a single peak corresponding to a transition. In contrast, in an interacting electron system, the spectrum has a main peak and the so-called satellite peaks due to core hole potential interaction with valence electrons. In both cases, the centre of gravity of the spectra is equal to the so-called Koopman’s binding energy  $E_B = -\epsilon_k$ , the energy of the line in the non-interacting case.

In photoemission experiments, the generation of photocurrent is due to the transition from an initial state ( $\psi_i$ ) to a final state ( $\psi_f$ ) by a optical field having the vector potential  $\mathbf{A}$ . Considering a small perturbation  $\delta$  we can express the transition probability  $\omega$  per unit time for an N-electron system according to Fermi’s Golden rule as:

$$\omega \propto \frac{2\pi}{\hbar} |\langle \psi_f | \Delta | \psi_i \rangle|^2 \delta(E_f - E_i - \hbar\omega). \quad (3-2)$$

The perturbation,  $\Delta$  is given as:

$$\Delta = \frac{e}{2mc} (\mathbf{A} \cdot \mathbf{p} + \mathbf{p} \cdot \mathbf{A}) - e\phi + \frac{e^2}{2mc^2} \mathbf{A} \cdot \mathbf{A}, \quad (3-3)$$

where  $\mathbf{A}$  and  $\phi$  are vector and scalar potentials and  $\mathbf{p}$  is the momentum operator ( $\mathbf{p} = -i\hbar\nabla$ ). Considering gauge  $\phi = 0$ , neglect photon-photon interaction ( $\mathbf{A} \cdot \mathbf{A} = 0$ ) and commutation between  $\mathbf{A}$  and  $\mathbf{p}$ , the perturbation term reduces as

$$\Delta = \frac{e}{mc} \mathbf{A} \cdot \mathbf{p}. \quad (3-4)$$

Hence, the commutation relation becomes

$$\langle \psi_f | \mathbf{A} \cdot \mathbf{p} | \psi_i \rangle \propto \langle \psi_f | \mathbf{A} \nabla \cdot \mathbf{V} | \psi_i \rangle \propto \langle \psi_f | \mathbf{A} \cdot \mathbf{r} | \psi_i \rangle \quad (3-5)$$

and the unperturbed Hamiltonian (in the absence of electromagnetic field) is given as:

$$H = \frac{\mathbf{p}^2}{2m} + V(r). \quad (3-6)$$

**Valence band photoemission:** In the scope of this thesis work, all experiments were performed in a domain where the photoemission is resulting from valence band electrons. A detailed discussion on the theory of photoemission is available in [143]. In contrast to the theory of core-level photoemission, valence band photoemission theory incorporates (1) the



wave vector dependence of photoemission and (2) the response of the surface from which photoemission occurs. The photocurrent from a crystalline solid surface is the result of several factors and can be expressed as:

$$I(E, \hbar\omega) \propto \sum_{i,f} \underbrace{\frac{\text{Im} \sum(k_i)}{(E - E^0(k_i) - \text{Re} \sum(k_i))^2 + (\text{Im} \sum(k_i))^2}}_{\text{Term I}} \cdot \underbrace{\frac{|\tilde{M}_{i,f}|^2}{(k_{i\perp}^{(1)} - k_{f\perp}^{(1)})^2 + (k_{f\perp}^{(2)})^2}}_{\text{Term II}} \cdot \underbrace{\delta(k_{i\parallel} - k_{f\parallel} + G_{\parallel})}_{\text{Term III}} \cdot \underbrace{\delta(k_i - k_f + G)}_{\text{Term IV}} \cdot \underbrace{\delta(E^1(k_f) - E^1(k_i) - \hbar\omega)}_{\text{Term V}} \cdot \underbrace{\delta(E - E^1(k_f) + \phi)}_{\text{Term VI}} \cdot \underbrace{f(E, T)}_{\text{Term VII}}. \quad (3-7)$$

A brief description of the different terms in the equation of photocurrent is as follows. The **Term I** represents the electron-electron interactions as a result of the photoexcitation of electrons. In the **Term II**, numerator ( $|\tilde{M}_{i,f}|^2$ ) indicates a contribution from the transition matrix element and the denominator shows a complex wave vector perpendicular to the surface because of the fact that photoexcited electrons have an inelastic mean free path of a few tens of Ångströms and its amplitude decays normal to the surface. The **Term III** and **Term IV** indicate momentum conservation where the periodicity of the Bloch function with respect to the reciprocal lattice vector,  $\mathbf{G}$  is considered. The momentum conservation parallel to the surface is shown explicitly in **Term III** because of the Fresnel equations. The **Term V** represents the conservation of energy in the photoexcitation process. The **Term VI** indicates that only photoelectrons with energy above the vacuum level  $\phi$  are detected in the photoemission experiments. Finally, the **Term VII** represents electron distribution in the material using the Fermi distribution function. In the context of formulating the theory of photoemission, three-step and one-step models of photoemission are considered. A brief explanation of these models are given below.

**Three-Step model of photoemission:** The photoemission processes can be divided into three steps as (1) transition of the electron from an initial state to a final state with energy and momentum conservation (2) propagation of the photoexcited electron to the surface where damping of electron wave function occurs and (3) emission of the electron from the solid into the free continuum states which requires the conservation of the parallel component of the momentum [143]. The three-step model of photoemission is considered for formulating the theory in the equation 3-7.

**One-Step model of photoemission:** In the one-step model, a Bloch wave electron is excited to a final state in vacuum that propagates into the spectrometer but decays away from the surface into the solid [143]. The photoemission intensity in the one-step model is calculated by modifying the Fermi Golden rule (equation 3-2) with suitable initial and final state and the dipole operator for the interaction between an electron and incoming light field.

### 3.1.2. Two-Photon Photoemission Spectroscopy

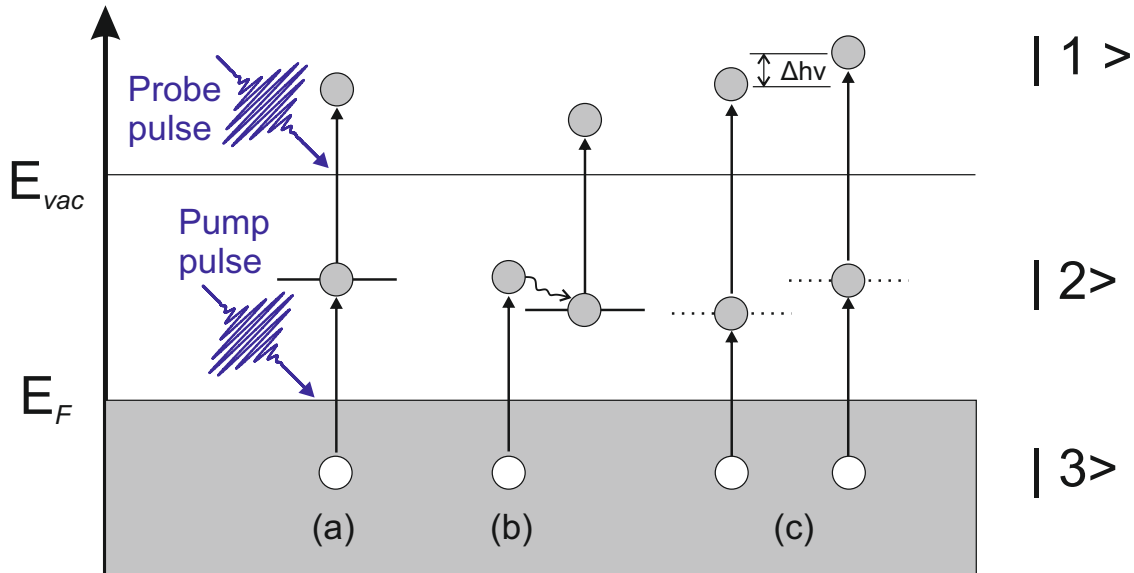


Figure 3-1.: Schematic of the 2PPE excitation mechanisms involving initial ( $|3\rangle$ ), intermediate ( $|2\rangle$ ) and final ( $|1\rangle$ ) states. The excitation processes can be classified as (a) resonant excitation, (b) non-resonant excitation, and (c) photoemission via virtual intermediate states. In the case of photoemission via virtual intermediate states, the final energy of the electron varies with the change in photon energy as indicated by  $\Delta h\nu$  in (c). Please note that the states are indicated here as sharp states ( $|i\rangle$ ) for the sake of representation.

The photoemission results from one-photon absorption is a direct transition from an initial state to a final state and the momentum of the electron is conserved during the process. The energy and momentum distribution of the electrons enable the determination of the electronic dispersion curves  $E(\vec{k})$  as well as the information about the occupied states in the solid. Details of the unoccupied bands can be investigated using Inverse PhotoEmission Spectroscopy (IPES) where incident electrons populate the unoccupied state and photons are generated due to Bremsstrahlung emission processes. However, it has low energy resolution (around 1 eV), small cross-section, and also limitations to address the dynamics of the e-h recombination processes [143, 144]. In two-photon photoemission spectroscopy (2PPE), the first photon excites an electron from the occupied state to an intermediate state (real or virtual state) and it is then photoemitted from the surface by the second photon. The 2PPE technique has the advantage of probing the unoccupied intermediate states that lie between the Fermi level  $E_F$  (in metal) or valence band maximum (in semiconductors) and the vacuum level  $E_{vac}$  with better energy resolution [122, 145–147]. The schematic of different excitation mechanisms in 2PPE is shown in Fig. 3-1 where the initial state, the intermediate state, and the final state are represented as  $|3\rangle$ ,  $|2\rangle$  and  $|1\rangle$ , respectively.

**Resonant excitation:** The first photon excites electron from an initial state to an unoccupied intermediate state and the second photon emits electron from the surface simultaneously. The photoemission process becomes resonant when the energy of the first photon matches with the energy difference between the initial and intermediate state as shown in Fig. 3-1 (a). The intensity of photoemission is stronger in resonant processes compared to the non-resonant processes.

**Non-resonant excitation:** An electron is excited to an intermediate state by the first photon which is then relaxed to a real intermediate state via interband or intraband scattering and subsequently a second photon is used for the photoemission from the intermediate state as shown in Fig. 3-1 (b).

**Photoemission via virtual intermediate states:** In presence of an intense optical field, absorption of two photons of same energy or different energy occurs simultaneously due to the transient second-order polarization of the material. Here, the first photon excites electron to a virtual intermediate state as shown in Fig. 3-1 (c). In contrast, the intermediate state is a real state in resonant photoexcitation process. The type of excitation mechanism can be differentiated by tuning the photon energy of the excitation. The energy of the photoemission via virtual state varies as a function of the photon energy used for excitation.

**Energy scaling:** In 2PPE experiments, the photoemission intensity is measured as a function of the kinetic energy using a time-of-flight spectrometer. Rescaling of the kinetic energy axis is essential for interpreting the energy levels observed in the spectrum which originate as a result of physical or chemical interactions of the adsorbates with the substrate. The commonly used energy references are *initial state energy* ( $E_i - E_F$ ), *intermediate state energy* ( $E - E_F$ ), *binding energy* ( $E - E_{vac}$ ) and *final state energy* ( $E_{fin} - E_F$ ). The occupied energy levels in the substrate can be meaningfully described using the *initial state energy* representation. For instance, the occupied states such as Shockley surface state and *d*-band of Cu(111) are observed below the Fermi level at 0.4 eV and 2 eV, respectively. The *intermediate state energy* is suitable for representing real energy levels that exist between vacuum level and Fermi level. The unoccupied Cs 6s state of the chemisorbed Cs<sup>+</sup>/Cu(111) due to *anti-bonding* is described using the *intermediate state energy*. The change in the energy due to the adsorption of molecules at interfaces or the image potential states can be well described in terms of the *binding energy* with respect to the vacuum level. Furthermore, the *final state energy* representation is used where the absorption of photons excites bound electrons in the material into a final state above the vacuum level. The 2PPE experiments provide access to the dynamics of the unoccupied intermediate states and the proper selection of the energy reference is required for a meaningful interpretation of the data.

### 3.1.3. Time-resolved 2PPE and Population Dynamics

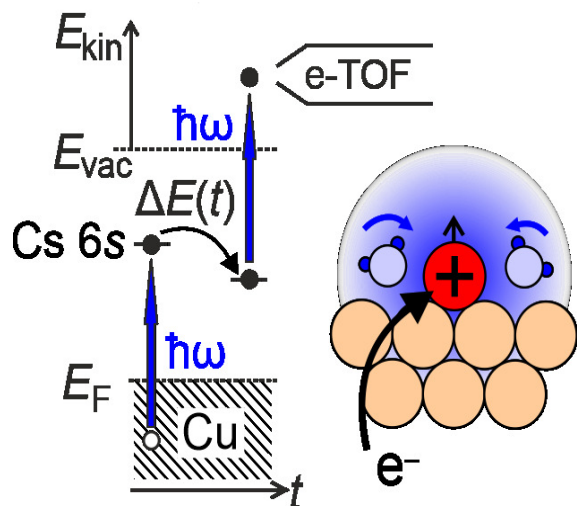


Figure 3-2.: Schematic of the tr-2PPE spectroscopy experiment and a cartoon of the solvation dynamics are shown. The electron attachment to the unoccupied Cs 6s state from the Cu substrate by pump pulse (bold vertical arrow), energy transfer to the solvents during relaxation and the excitation to the final state by probe pulse (bold vertical arrow) are depicted. The cartoon shows the electron attachment to the  $\text{Cs}^+$  ion core (black curly arrow) and subsequent dynamics of the solvent in the vicinity of the ion.

relaxation dynamics of the solvent depends on the polarity and the coverage of the adsorbates on the surface.

In general, the population at different energy states are described by optical Bloch equations. These are a set of coupled differential equations which give the population of a state as a function of population in other states (initial, intermediate, and final) and their plausible decay rates. A detailed description of optical Bloch equations and its implementation in the context of the time-resolved 2PPE can be found in several works [145, 146, 149–151]. The mathematical treatment of determining the population dynamics using optical Bloch equations is presented in Appendix A. In this thesis work, the decay of the excited state is fitted with a mathematical function which is the convolution of a linear exponential decay and

The time-resolved 2PPE technique enables the investigation of the lifetime of photoexcited electrons in materials, electron-phonon coupling, surface exciton formation, magnon emission, and so on [148]. The schematic of the time-resolved 2PPE experiment and a cartoon of the dynamic process are shown in Fig. 3-2. The experiment can be performed as either auto-correlation (same photon energy for pump and probe laser pulses) or cross-correlation (different photon energies for pump and probe laser pulses) measurements. In this thesis work, time-resolved auto-correlation 2PPE is performed on Xe and  $\text{D}_2\text{O}$  coadsorbed on  $\text{Cs}^+/\text{Cu}(111)$  using 3.1 eV femtosecond laser pulses. In the pump-probe experiment, the pump pulse populates the Cs 6s state by attaching an electron from the metal substrate which triggers the dynamics of the solvents (Xe or  $\text{D}_2\text{O}$ ) due to the transient change in the charge state of the Cs atoms. A time-delayed probe laser pulse is used for photoemission of the excited state to study the solvation dynamics on the surface. The energy of the photoemitted electrons are analysed using a time-of-flight (TOF) spectrometer. The

a Gaussian function. The procedure to determine the lifetime is discussed in the section 3.1.5.

### 3.1.4. Technical Aspects of Photoemission Spectroscopy

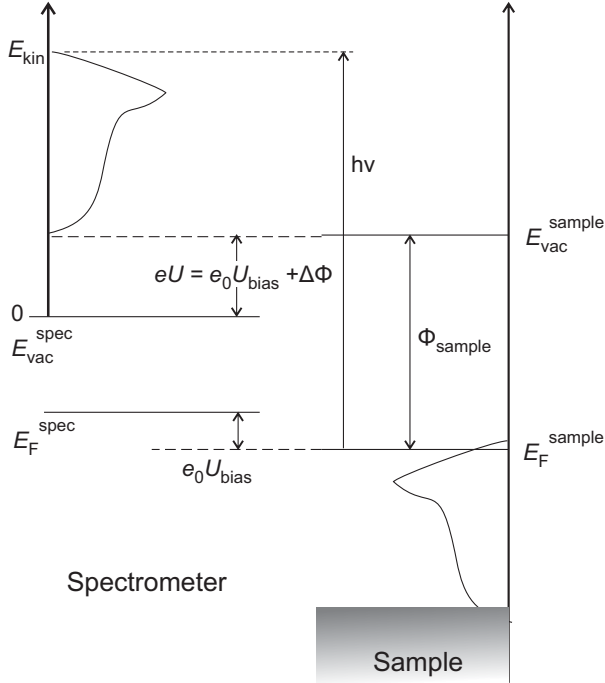


Figure 3-3.: Applying a bias voltage to compensate the difference in work function between sample and spectrometer.

A brief description of the data acquisition and signal processing is presented in this section. Detailed information can be found in previous thesis works [152–155].

The TOF spectrometer has a field-free tube of length 297 mm and is grounded. The entrance aperture of the TOF has a diameter of 1.5 mm and the multi-channel plates (MCP) are situated on its back side for the detection of electrons. It has an acceptance angle of  $\pm 3.8^\circ$  for the incoming photoelectrons. The TOF spectrometer is coated with graphite to ensure a uniform work function ( $\Phi_{\text{TOF}}=4.45$  eV) for the detector. The work function of the sample and spectrometer are slightly different and hence the low-energy cut off region of the electronic spectrum cannot be detected in the spectrometer. A bias voltage is applied to the sample to facilitate the detection of the entire spectrum as shown in the schematic Fig. 3-3. The kinetic energy of the photoemitted electrons is related to the TOF as:

$$E_{kin} = \frac{m_e}{2} \left( \frac{L}{t} \right)^2 = 2.4828 \left( \frac{L^2}{t^2} \right) eV \text{ ns}^2 \text{ mm}^{-2}, \quad (3-8)$$

where  $m_e$  is the mass of the electron,  $L$  is the length of the TOF spectrometer and  $t$  is the time of travel of the electrons from surface. The flight time of the electrons is measured with a precision of the order of sub-nanoseconds where higher kinetic energy electrons take relatively shorter time to reach the detector than those with lower kinetic energy. The photoemitted electrons have to overcome the potential barrier ( $e_0U$ ) due to the difference in the work function between the surface and the spectrometer ( $\Delta\Phi$ ). Hence, a bias voltage ( $U_{bias}$ ) is applied between sample and spectrometer to detect the complete spectrum of the electrons as given below:

$$e_0U = \Delta\Phi + e_0U_{bias}. \quad (3-9)$$

The acceleration of electrons due to the bias voltage is possible till the tip of the spectrometer due to the variation of the potential. However, the electrons travel around 297 mm through

the field-free tube of the spectrometer at constant velocity. Hence, the short acceleration of the electrons by this bias potential can be ignored [156]. The kinetic energy of the photoemitted electrons (equation 3-8) in presence of the bias voltage can be expressed as:

$$E_{kin} = \frac{m_e}{2} \left( \frac{L}{t_m - t_0} \right)^2 - e_0U, \quad (3-10)$$

where the actual flight time ‘ $t$ ’ differs from the measured time,  $t_m$  by a constant  $t_0$  due to the difference in the ‘start’ signal in the electronics. The value of  $t_0$  is determined by recording spectra at different bias voltages.

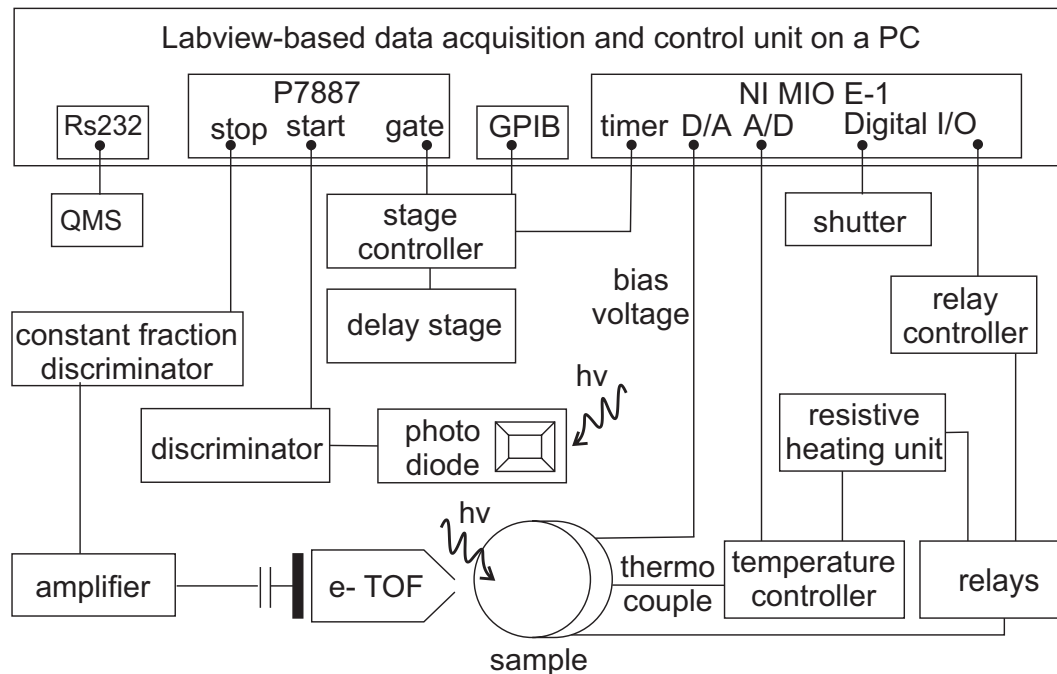


Figure 3-4.: Schematic of the 2PPE data acquisition and signal processing unit.

**Data Acquisition and Processing:** The key challenge in the data acquisition and signal processing is the precise measurement of the time-of-flight of electrons originating from different states of the surface under investigation. A schematic of the electron detection and signal processing unit is shown in Fig. 3-4. The TOF is the time interval between *start-pulse* which is generated from the femtosecond laser and *stop-pulse* which is coupled out of the MCP electron detector by a condenser. Both signals are coupled to discriminators for smoothing out fluctuations and producing negative pulses. Finally, these signals are processed by *time-to-digital* card in the computer which can detect time differences with an accuracy of 0.25 ns without dead time between events. The detectors can handle multi-hit events upto a maximum rate of  $10^6$  cts/s. The detected electrons TOF information is sorted into 8192 bins. The computer is also equipped with a multi-function measurement card that has several signal processing options such as A/D and D/A converters, counters, and logical

and programmable channels. In the conversion of TOF to kinetic energy,  $t \rightarrow E$ , the count of electrons  $N(t)$  is converted to  $N(E)$  as follows:

$$\frac{dN}{dE} = \frac{dN}{dt} \left| \frac{dE}{dt} \right|^{-1} = \frac{dN}{dt} \frac{t^3}{m_e L^2}. \quad (3-11)$$

For time-resolved measurements, a stage controller is used to change the optical path length between pump and probe via a GPIB (general purpose interface bus) port. Temperature dependent measurements are performed using the relays connected to the sample surface. The data acquisition is performed with the help of the *LabView* environment.

### 3.1.5. Data Analysis

In this section, the data analysis for a 2PPE spectrum and 2D false colour 2PPE spectra (in static 2PPE and time-resolved 2PPE) are discussed to get an overview of the analysis methods employed in the thesis. *Igor Pro 6.x* and *Igor Pro 8.x* software packages are used for the analysis.

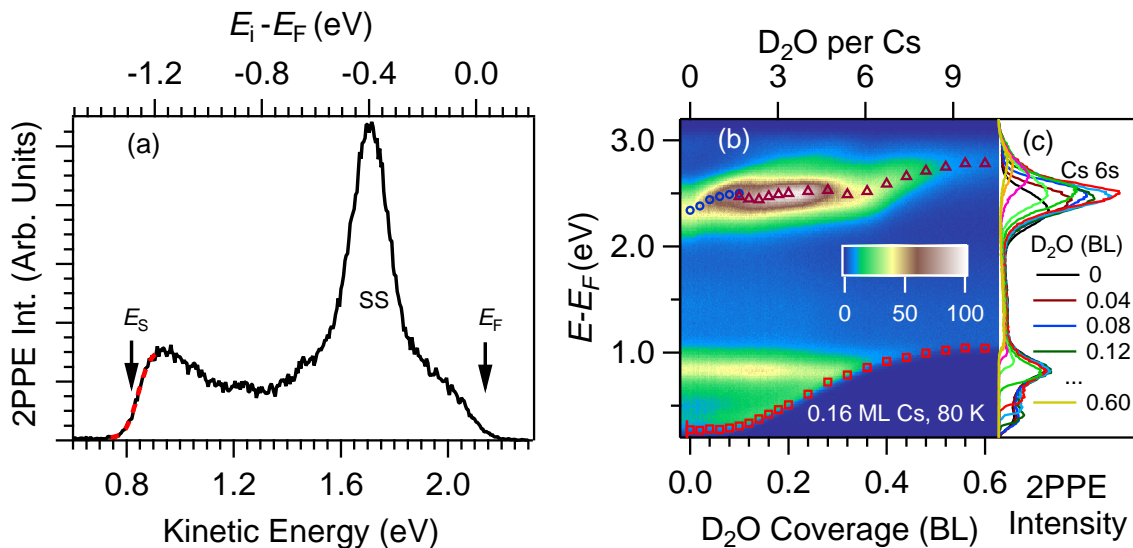


Figure 3-5.: (a) Static 2PPE intensity from Cu(111) plotted as a function of kinetic energy (bottom) and initial state energy (top) with fit on the low-energy cut off (red dashed line), (b) false color 2PPE of Cs/Cu(111) while adsorbing  $D_2O$  marked with Cs 6s state (blue circles), water-induced state (red triangles), and change in work function (red squares), and (c) spectrum extracted for specific water coverages from panel (b).

**Static 2PPE:** Static 2PPE spectrum of Cu(111) surface using 3.1 eV is shown in the Fig. 3-5 (a). The spectrum has three distinct features such as Fermi-edge  $E_F$  (highest energy electrons emitted from the Fermi-level), surface state SS, and secondary edge  $E_s$

(electrons that just overcome the potential barrier). The bandwidth of the laser pulse is taken into consideration while determining the Fermi-edge of the spectrum (a discussion on the relationship between bandwidth and pulse duration of the laser pulse width can be found in section 3.2.2). A sharp and prominent SS indicates the quality of the surface because irregular surfaces result in broadening of the peak due to the scattering of electrons. Finally, determining the secondary edge or low-energy cut off is decisive for calculating the work function of the surface. The intensity of the background secondary electrons is described by a Heaviside step function and exponential decay as:

$$I(E) = \begin{cases} A e^{\frac{\Phi-E}{d}} & \text{for } E \geq \Phi. \\ 0 & \text{for } E < \Phi, \end{cases} \quad (3-12)$$

where  $\Phi$ ,  $A$ , and  $d$  are the work function, the amplitude, and decay constant of the background secondary electrons, respectively. The secondary electrons lose their energy due to electron-phonon and electron-electron scattering while leaving the surface. In the detector, the cut off of the spectrum is broadened due to the finite resolution of the spectrometer. So, a convolution of the step function and a Gaussian (with a width parameter  $w$  that is related to the resolution of the spectrometer) which gives an Error function of the form as follows [157]:

$$I'(E) = I_0 + A' \operatorname{erf}\left(\frac{\Phi - E}{\sqrt{2}w}\right), \quad (3-13)$$

where  $I_0$  and  $A'$  are the background intensity and amplitude of the function, respectively. The fit of the secondary cut off of the spectrum is shown in Fig. **3-5** (a) as a red dashed line. The low-energy cut off and  $w$  are determined as 0.84 eV and 37 meV, respectively.

**2D static 2PPE:** In order to understand the change in electronic structure of the surface during adsorption, static 2PPE spectra are recorded while adsorbing solvents on Cu(111). The Fig. **3-5** (b) shows a false colour representation of the change in static 2PPE intensity from Cs/Cu(111) as a function of intermediate state energy and D<sub>2</sub>O coverages. The spectra at specific coverages are shown in the panel (c). The spectral peaks are determined manually as shown in blue circles and red triangles. The change in secondary edge of the spectra is shown in red squares and is analogous to the change in work function which is determined by fitting the low-energy cut off with an error function as described earlier. Finally, a top axis is introduced as ‘D<sub>2</sub>O per Cs atom’ which is evaluated by taking the ratio of D<sub>2</sub>O coverage and Cs coverage. The methods of determining the D<sub>2</sub>O and Cs coverages are described under the surface preparation section later in this chapter. The quantitative analysis of the energy states and their evolution are described in detail in Chapters 4 and 5.

**tr-2PPE:** Time-resolved 2PPE involves recording photoemission spectra with an additional parameter  $\Delta T$ , the pump-probe time delay. Analysis of such spectra give valuable information on energy transfer rates in the excited system, population dynamics or relaxation dynamics, nuclear motion, and so on [3, 4, 44]. The schematic of the time-resolved 2PPE is



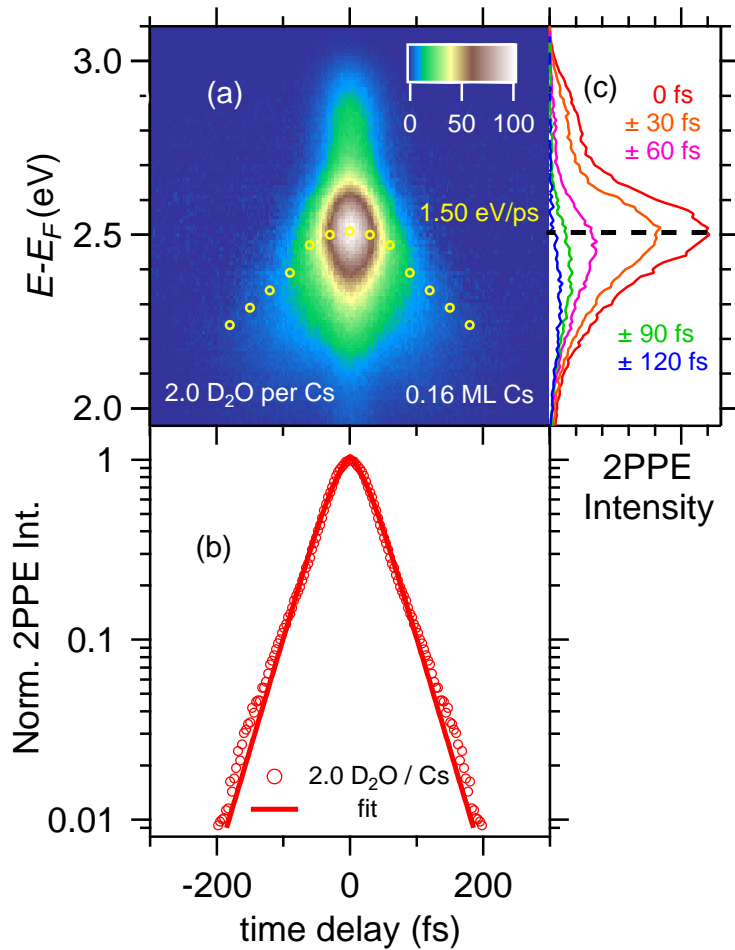


Figure 3-6.: Time-resolved 2PPE intensity (a) in false colour as a function of intermediate energy (left) and time delay (bottom) for 2 D<sub>2</sub>O per Cs<sup>+</sup>. The peaks are marked with yellow circles. (b) Normalized 2PPE intensity (red circles) integrated for an energy window in panel (a) from 2 eV to 3 eV as a function of time delay and fit of the data (solid red line). (c) Spectra at specific time delay extracted from the panel (a). A black dashed line at zero delay is drawn to show the shift of the spectral weight to lower energies with increasing time delay.

shown in the inset of Fig. 3-6. The pump pulse excite an electron from the metal substrate to the intermediate Cs 6s state and a subsequent time-delayed probe pulse photoemits electron. The relaxation rate and energy transfer rate of the excited state depend on the type of solvent and coverage. A typical tr-2PPE spectra for D<sub>2</sub>O/Cs/Cu(111) surface is shown in Fig. 3-6 (a). The energy of the Cs 6s state (yellow circles) for time delays  $\leq 100$  fs is determined by manually finding the peak. For higher time delays, for which the peaks become broadened and less intense, we considered the spectral weight for accurate determination of the peak energy by evaluating  $I(E_i) \times E_i / \sum I_i$ . The analysis of the change in Cs 6s peak energy as a function of time-delay is useful for the determination of potential energy surfaces (PES) [3, 44, 105] and is adopted in the work on the Xe/Cs/Cu(111) system in Chapter 5. The spectra at specific time delays are shown in Fig. 3-6 (c) where the intensity and energy of the peak vary as a function of time delay. Furthermore, the excited state population decay dynamics of the D<sub>2</sub>O/Cs/Cu(111) system is shown in Fig. 3-6 (b) where the excited state 2PPE intensity is integrated over the energy window from 2 eV to 3 eV (red circles) plotted as a function of pump-probe delay. As mentioned previously, a convolution of Gaussian and

exponential decay function is used to fit the data rather than optical Bloch equations. The time-resolved 2PPE measurement is performed in auto-correlation mode where the pump and probe pulses are of same photon energy. The intensity of the 2PPE from the intermediate state can be expressed as:

$$I_{AC}(t) = \iint dt' dt'' I_1(t') I_2(t'' - \Delta t) R(t'' - t'), \quad (3-14)$$

where  $I_1$  and  $I_2$  are the intensity of the pump and probe laser pulses and  $R(t)$  is the response function of the intermediate state. The decay of the intermediate state population  $N(\Delta t)$  is modelled using an exponential decay of the form:

$$N(\Delta t) = N_0 \exp\left[-\frac{\Delta t}{\tau}\right], \quad (3-15)$$

where  $N_0$  and  $\tau$  are the initial population and the decay rate of the intermediate state. The convolution of the equation 3-14 and equation 3-15 results into a mathematical expression of the form:

$$I(t) = \frac{1}{2} e^{-\tau\left(t - \frac{T_p^2}{2}\right)} \left[ 1 + \operatorname{erf}\left(\frac{(t - T_p^2\tau)}{\sqrt{2}T_p}\right) \right], \quad (3-16)$$

where  $T_p$  is the FWHM of the Gaussian pulse. The fit of the population dynamics according to equation 3-16 is shown in Fig. **3-6** (b) as red solid line which gives an excited state lifetime of  $(35 \pm 3)$  fs. All the time-resolved data discussed in the thesis are fitted with equation 3-16.

## 3.2. Experimental setup

### 3.2.1. Generation of Femtosecond Laser Pulses

Femtosecond lasers are indispensable parts of the nonlinear pump-probe photoemission experiments to investigate ultrafast dynamics. The schematic of the experimental setup employed in the thesis work is shown in Fig. **3-7**. The femtosecond laser pulses are produced by a commercial system from *Coherent Inc.* that consists of an Oscillator (*Micra-5*, *Coherent Inc.*) and a regenerative amplifier (*RegA 9000*). Both oscillator and amplifier are optically pumped by a CW solid state laser system (*Verdi V-18*) operating at 532 nm. The oscillator employs Kerr lens mode-locking in conjunction with intracavity prism pair to generate low-noise, large-bandwidth, and high-peak power laser pulses [158]. The active medium of the oscillator is a Titanium:sapphire crystal capable of producing mode-locked femtosecond laser pulses with a bandwidth exceeding 100 nm at the central wavelength around 800 nm. The mode-locked power of the oscillator is 450 mW at a repetition rate of 76 MHz that corresponds to 6 nJ energy per pulse.

The working principle of the oscillator is based on Kerr lens mode-locking (KLM) where the interplay of Kerr lens effect and self-phase modulation (SPM) lead to the generation of

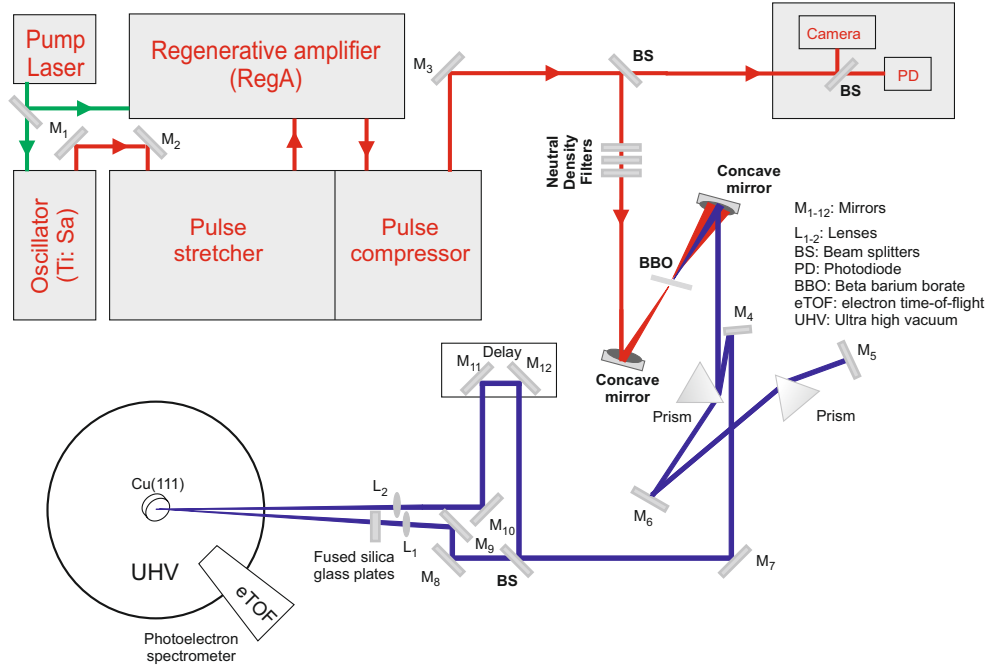


Figure 3-7.: Schematic of the 2PPE femtosecond pump-probe experimental setup employed for auto-correlation measurements using photon energy of 3.1 eV. See text for the details.

a stable train of femtosecond laser pulses. The oscillator cavity supports the oscillation of several longitudinal modes which are out of phase with a frequency separation of  $\Delta\nu$  given by:

$$\Delta\nu = \frac{c}{2L}, \quad (3-17)$$

where  $c$  and  $L$  are speed of light and cavity length. In a laser system, these modes are oscillating independently without any phase relationship to other modes. These modes can be made to oscillate with locked-phase by means of active optical components such as electro and acousto optic modulators or passively by self-locking of modes or by using saturable absorbers. Once several modes are phase-locked, the laser operation changes from continuous wave to pulsed mode. These pulses are generated due to the constructive interference of several modes and are separated in time by  $\tau$  as:

$$\tau = 2L/c. \quad (3-18)$$

These pulses occur at a frequency equal to the mode spacing of the laser,  $\Delta\nu$ . If  $n$  is the number of phase-locked modes, then the mode-locked bandwidth is  $n\Delta\nu$ . The larger the mode-locked bandwidth, the shorter the duration of the laser pulse. The bandwidth and the pulse duration are related by the relationship as:

$$\Delta t = \frac{k}{n\Delta\nu}, \quad (3-19)$$

where the factor  $k$  is the ‘time-bandwidth product’ and its value depends on the profile of the laser pulse. For example, the value of  $k$  for Gaussian and  $\text{sech}^2$  pulse profiles are 0.414 and 0.315, respectively [159]. The laser medium exhibits an intensity dependent refractive index effect known as optical Kerr effect and can be expressed as:

$$n(\omega, I) = n_0(\omega) + n_2I, \quad (3-20)$$

where  $n_0$  is the linear refractive index and  $n_2$  is the intensity-dependent refractive index. A laser beam with a Gaussian spatial profile experiences non-uniform refractive index as it passes through the lasing medium. The centre of the laser beam experiences higher refractive index than the periphery that results into self-focusing of the laser beam inside the laser medium. As a result, strong intensity maxima of the laser cavity will be focused more tightly than the weaker intensity part of the beam. By placing an aperture inside the laser cavity, one can favor certain modes of oscillations and suppress other modes. A rapid transient change in the optical path length of the laser cavity is required for initiating the mode-locking. As a result of the rapidly changing intensity  $I(t)$ , the change in refractive index occurs as a function of time as  $n = n_0 + n_2I(t)$ . This results in a rapid change of the phase of the pulse as a function of time. This self-phase modulation broadens the spectrum of the wave and hence shortens its duration. A pair of prisms are used inside the cavity to compensate group velocity dispersion (GVD) of the laser pulses. The combined effect of the KLM and the SPM lead to the generation of a quasi-soliton like pulse of femtosecond time duration [160].

In most of the ultrafast laser experiments, amplified laser pulses are required for the generation of sufficient intensity of photoelectrons for the detection. Chirped pulse amplification (CPA) is the technique widely used for the amplification of femtosecond laser pulses and its invention was awarded the nobel prize in physics recently [161,162]. The technique involves mainly three steps: (1) stretching of the laser pulse, (2) amplification of the stretched pulse and (3) compression of the amplified laser pulse. The CPA provides the amplification of laser pulses from a few nJ to several mJ energy. In order to amplify the femtosecond laser pulses, the laser pulses are stretched to picosecond duration by using a pair of prisms or gratings. Otherwise, the high peak power of the laser pulses will lead to a damage of the active medium and optical elements of the amplifier. The active medium of the amplifier (Ti:sa) and an acousto-optic modulator (AOM), which serves as a Q-switch, are placed between two totally reflective cavity mirrors. The active medium of the amplifier is a Titanium:sapphire crystal which is also pumped by a part of the pump laser for the oscillator. The stretched femtosecond laser pulses from the oscillator are seeded to the amplifier via a Faraday isolator which prevents the reflected beam to travel back to the oscillator. The acousto-optic cavity dumper reduces the repetition of the oscillator pulses from MHz to KHz range, thereby allowing selected laser pulses to make several round trips and extract maximum energy from the amplifying medium before it is deflected out of the resonator by a cavity dumper [159,163,164]. The output of the amplifier has an energy of a few  $\mu\text{J}$  with

250 KHz repetition rate and a central wavelength at 800 nm. Finally, laser pulses from the amplifier are compressed down to 45 fs using a pair of holographic gratings [165]. The output of the laser system is continuously monitored using a photodiode, camera, and spectrometer as shown in Fig. 3-7.

As part of the thesis work, laser pulses with a photon energy of 3.1 eV are generated from a BBO crystal by frequency doubling the fundamental of the amplified laser pulse. The frequency doubled laser pulses are compressed again by using a pair of prisms. The laser beam is subsequently split into pump and probe laser beams. The probe beam is allowed to pass through a delay stage to capture the ultrafast dynamics of the surface under investigation. Fused silica glass plates are introduced into one of the beam paths to produce identical pulses for the experiments. Both beams are focused onto the Cu(111) substrate positioned inside the UHV chamber using convex lenses of focal length  $\sim 60$  cm. The total optical path length of the experimental setup is around 8 meters from the exit of the amplifier to the sample under investigation. The optimization and characterization methods of the laser pulses are described in the following section.

### 3.2.2. Characterization and Optimization of Laser Pulses

In order to perform experiments in a consistent manner, laser pulse parameters have to be set to optimum values. Since, the laser performance might vary as a result of change in the temperature or humidity in the laboratory, significant attention is given to the optimization and characterization of (1) the focal spot profiles of the pump and probe laser pulses, (2) the optical spectrum of the laser pulses, and (3) the pulse duration and compensation of the GVD laser pulses. A brief account of these experimental aspects are discussed in the following paragraphs.

**Characterization of focal spots:** Since the laser pulses are travelling a few meters in the experimental setup through various reflective and dispersive optical components, they suffer non-uniform spatial intensity distributions. In order to characterize the focal spots of both beams, a flip mirror is placed in front of the window for the optical coupling to the chamber and a CCD camera (DMK21AU04, The Imaging Source, Inc.) is placed exactly at a distance equal to the sample distance from the flip mirror so that one can reproduce focal spots outside the chamber which are identical to that on the sample. The optimizations of the focal spots of the laser beams are mainly done by fine adjustments of the mirror,  $M_5$  and the orientation of the prism in front of that mirror. The focal spots of the pump and the probe laser beams are shown in Fig. 3-8 (a, b) as a false colour map. The vertical and horizontal line profile of the fluence distribution of the pump and the probe are shown in Fig. 3-8 (c, d). The fluence profiles in the horizontal and vertical profiles are fitted with a Gaussian function. The spot sizes are 37  $\mu\text{m}$  and 46  $\mu\text{m}$  for the pump laser along the horizontal and vertical directions, respectively. Similarly, spot sizes of the probe laser are 35  $\mu\text{m}$  and 42  $\mu\text{m}$  along the horizontal and vertical directions, respectively. The theoretical

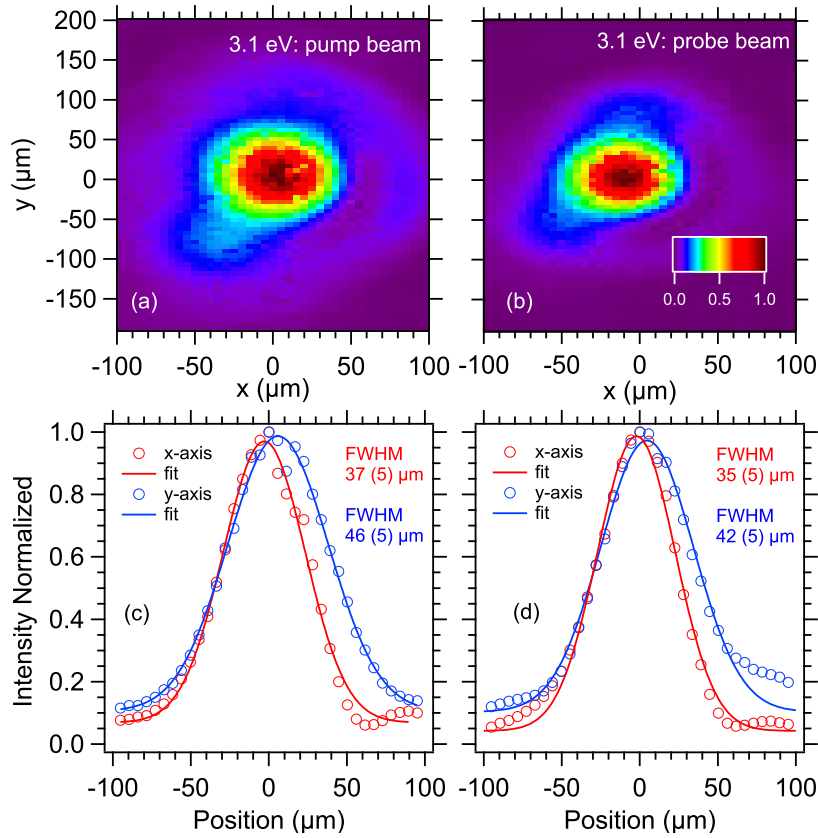


Figure 3-8.: False colourmap of the intensity of focal spot profiles of the pump and probe laser beams are shown in panels (a) and (b). The vertical and horizontal intensity profiles of the pump and probe laser beams are shown in panel (c) and (d), respectively (circular markers). The intensity profiles are fitted with a Gaussian (solid lines) to determine the spot size of the laser beams.

limit of the spot size ( $2w_0$ ) for a light beam of wavelength  $\lambda$  with beam size of  $D$  on a lens of focal length  $f$  is given by the equation:

$$2w_0 = \frac{4M^2\lambda f}{\pi D} \quad (3-21)$$

Upon substitution of reasonable values from the experimental setup, the spot size is estimated to be around 32 μm which is close to the values determined from the fit of the focal spot profiles of the pump and probe laser pulses. The spot size values are necessary for the determination of the laser fluence on the surface which is in the range of 1-5 mJ/cm<sup>2</sup> in our experiments. A high laser fluence will generate a larger current of photoemitted electrons which might lead to space-charge effects and hence distort the electronic spectrum. Such effects are minimized by increasing the focal spot size and/or decreasing the energy of the laser pulses.

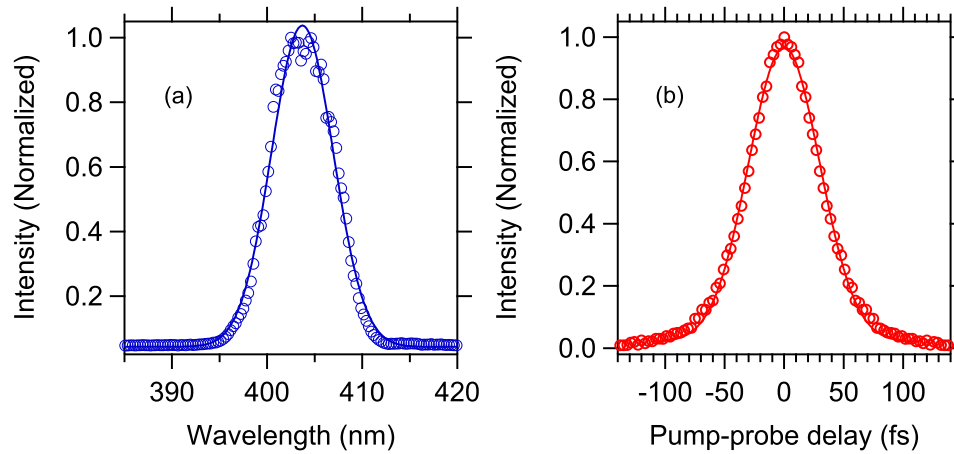


Figure 3-9.: (a) Optical spectrum of the 3.1 eV laser pulse used for the measurements and (b) auto-correlation signal of the highest energy electrons (hot electrons) as a function of pump-probe delay. The data points (circular markers) in panel (a) and (b) are fitted (solid line) with Gaussian functions to determine spectral width and pulse duration, respectively.

**Optical spectrum of the laser:** The maintenance of the photon energy of the laser pulses throughout the experiments is important because slight variations in alignment of the setup can drift the photon energy of the pulse and affect the results. The optical spectrum of the laser pulse is continuously monitored by using a fibre optic spectrometer (*HR4000CG – UV – NIR*, Ocean Optics) and optimization is done by changing injection and ejection settings of the amplifier and the orientation of the BBO crystal (which generates the 404 nm by frequency doubling) to maintain the photon energy at 3.1 eV. The optical spectrum of the laser is shown in Fig. 3-9 (a) and a Gaussian function is used to fit the spectrum. The central wavelength and full width at half maximum (FWHM) of the laser beam are 404 nm and 8 nm, respectively.

**Pulse duration measurement:** The intensity of the photoemission depends on the duration of the laser pulses. The optimization of the laser pulse duration is performed by jointly adjusting the injection and the ejection of the laser pulses in the amplifier and the compressor for the fundamental and the second harmonic frequency. It is inconvenient and challenging the measurement of the pulse duration of the 404 nm (3.1 eV) pulses by second harmonic generation in a frequency resolved optical gating device.

As discussed in the section 3.1.5, the time-resolved 2PPE spectrum from Cu(111) is considered here for the determination of the pulse duration. The electrons from the highest intermediate state energy are analysed where the lifetime of the electrons is scaled with  $\tau \sim \frac{1}{(E-E_F)^2}$ . These electrons fairly represent the profile of the laser pulse because the intermediate state for high-energy electrons is a virtual state with an infinitesimal short lifetime. The measurements are done in the experiment in an auto-correlation mode where both pump and probe pulses have same energy and the response function of the intermediate state can

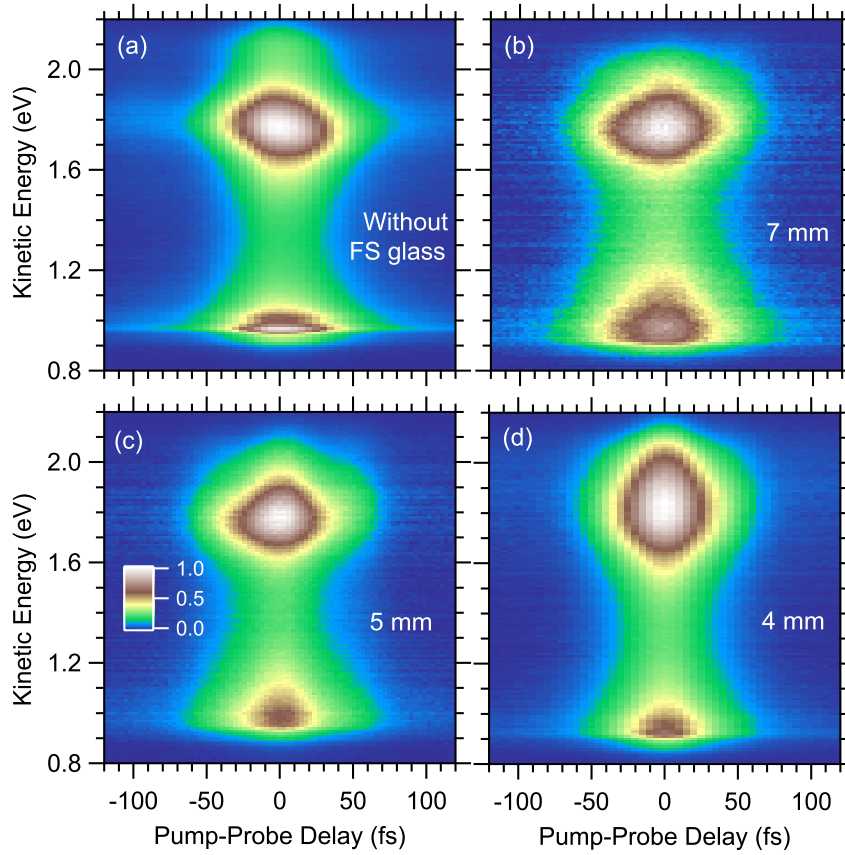


Figure 3-10.: False colour 2PPE intensity from Cu(111) surface as a function of kinetic energy (eV) and pump-probe time delay. (a) Without any dispersion compensation optical component. (b-d) Improving the symmetry of the spectra with respect to time-zero by the insertion of a fused silica glass plate for the compensation of GVD in the optical paths. The thickness of the glass plate is indicated in the corresponding panel.

be approximated by a  $\delta$  function. Hence, the equation 3-14 can be expressed as:

$$I_{AC}(t) = \int dt' I_1(t) I_2(t - t'). \quad (3-22)$$

The auto-correlation of a Gaussian pulse profile of the form  $I(t) = \exp\left[-\left(\frac{2\sqrt{\ln 2}t}{\Delta\tau_{pulse}}\right)^2\right]$  can be expressed as:

$$A^{(2)}(\tau) = \exp\left[-\left(\frac{2\sqrt{\ln 2}\tau}{\Delta\tau_{AC}}\right)^2\right], \quad (3-23)$$

where  $\Delta\tau_{pulse}$  and  $\Delta\tau_{AC}$  are the FWHM of the femtosecond laser pulse and the auto-correlation function, respectively and are related by the expression [159]:

$$\Delta\tau_{AC} = 1.41\Delta\tau_{pulse}. \quad (3-24)$$



The normalized energy integrated 2PPE intensity as a function of the pump-probe delay for electrons in the highest intermediate state is shown in the Fig. 3-9 (b). A Gaussian fit on the data points provides the FWHM of the auto-correlation function as 43 fs. By assuming a transform-limited pulse shape, the pulse duration of the femtosecond laser pulses in the experiments is calculated according to equation 3-24 as  $(32 \pm 3)$  fs.

In addition, the optimization of pulse shape is required for producing symmetric time-resolved data. The asymmetry originates from the difference in GVD for the pump and the probe as they propagate through different optical path lengths in the setup. For instance, in a beam splitter, the transmitted and reflected beams travel unequal optical path length and hence they exhibit unequal GVD. In addition, the number of optical components are different for pump and probe beam paths due to the time-delay stage in the setup. Ideally, both optical paths length should be identical to obtain symmetric autocorrelation traces. To compensate the difference in GVD between the pump and probe beam path, a fused silica glass plate is inserted into the beamline where the optical path length is shorter. The GVD values of the fused silica and N-BK7 (beam splitter) at 400 nm are considered for determining the dispersion compensation [159,166]. The effect of different GVD on the time-resolved spectra is shown in Fig. 3-10. The spectra are asymmetric with respect to time-zero without any dispersion compensation and show better symmetry when the thickness of the glass plate varies as shown in panel (b-d).

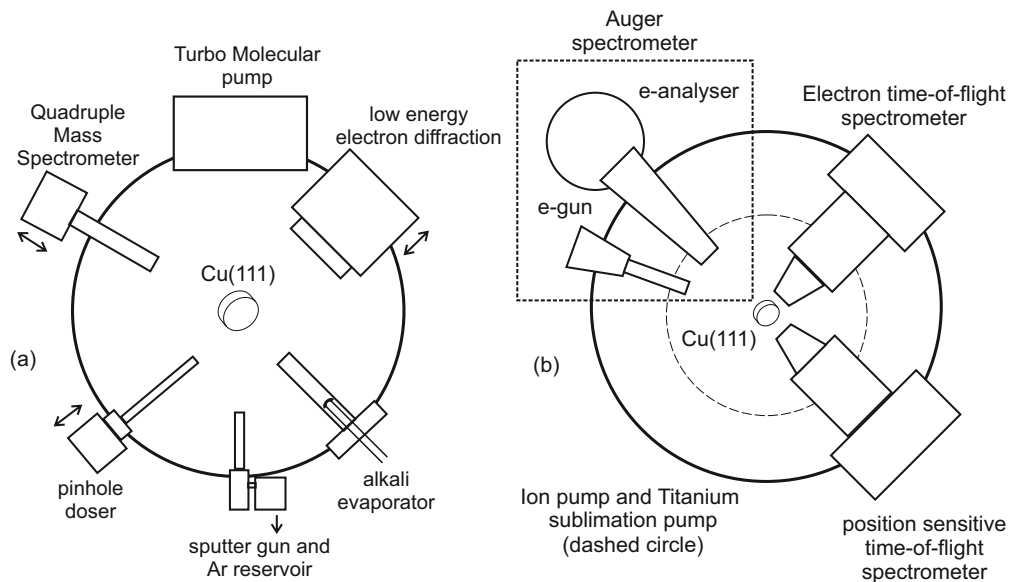


Figure 3-11.: Schematic of the Ultrahigh vacuum chamber which is separated into a preparation chamber (a) and spectrometer chamber (b). See text for the details of the instruments available in the chamber for surface preparation and analysis.

### 3.2.3. Ultrahigh Vacuum System (UHV)

All measurements are performed in an UHV chamber with a base pressure  $< 2 \times 10^{-10}$  mbar and at cryogenic temperature  $T = 30\text{ K}$  or  $80\text{ K}$ . A simple schematic of the chamber is shown in Fig. 3-11. A gate valve is used to separate the chamber as (a) preparation chamber and (b) spectrometer chamber. The ultrahigh vacuum is produced by a turbo molecular pump (HiPace 700, Pfeiffer) and is connected to a pre-turbo pump (Pfeiffer) and a membrane pump (Vacuubrand) to generate necessary pre-vacuum for the main turbo pump. After pumping down the chamber to a pressure  $< 1 \times 10^{-8}$  mbar, a bake-out procedure at  $T \approx 100^\circ\text{ C}$  has to be carried-out to eliminate residual water molecules in the chamber and hence to obtain pressure of the order of  $1 \times 10^{-10}$  mbar.

The preparation chamber is equipped with several thermal evaporators which can be used for deposition of alkalis, earth alkalis, and lead depending on the requirements. The working of these evaporators are based on resistive heating of the desired material that is encapsulated inside a cartridge. The Cs cartridges were procured from SAES Getters for the experiments. Noble gases and different molecules for the experiments are introduced into the preparation chamber via a pinhole doser with a diameter of  $50\ \mu\text{m}$ .

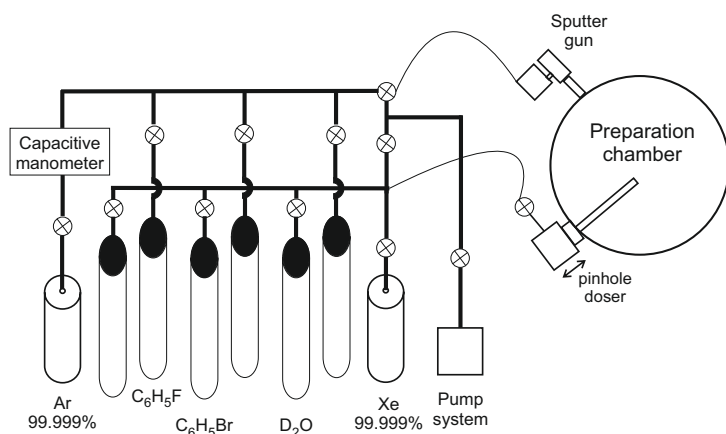


Figure 3-12.: Schematic of the gas system attached to the preparation chamber with several adsorbates for a wide range of experiments.

The adsorbates are introduced controllably to the preparation chamber with the help of a gas system as shown in Fig. 3-12. The gas system is always pumped with a turbo pump (HiCube Eco, Pfeiffer) and a capacitive manometer (Baratron, MKS instruments) is used for measuring the pressure (base pressure of  $2.5 \times 10^{-3}$  mbar without adsorbates). Several adsorbates in gas phase and liquid phase are attached to the gas system for different experiments. In the scope of this thesis work, commercially available D<sub>2</sub>O (Deuterium Oxide,

Sigma Aldrich) and Xe (Xenon 4.0, Westfalen) are utilized as solvents for the experiments. The adsorbates are buffered into the gas system up to a pressure  $< 1$  mbar and introduced into the preparation chamber via a pinhole doser or leak valve. In addition, the sputtering system (SPECS) in the preparation chamber produces high energy Ar ions for cleaning the surface by bombardment. Furthermore, the preparation chamber has a low-energy electron diffraction (LEED) system (SPECS surface nano analysis, GmbH) for checking the long-range uniformity of the Cu(111) surface. In addition, a quadrupole mass spectrometer

(QMS) (MKS instruments) which is capable of identifying masses from 1 amu to 200 amu is used for monitoring the residual gas in the chamber. With the help of an optional attachment for temperature reading, the QMS is also used for characterization of adsorbates by temperature-programmed desorption (TPD).

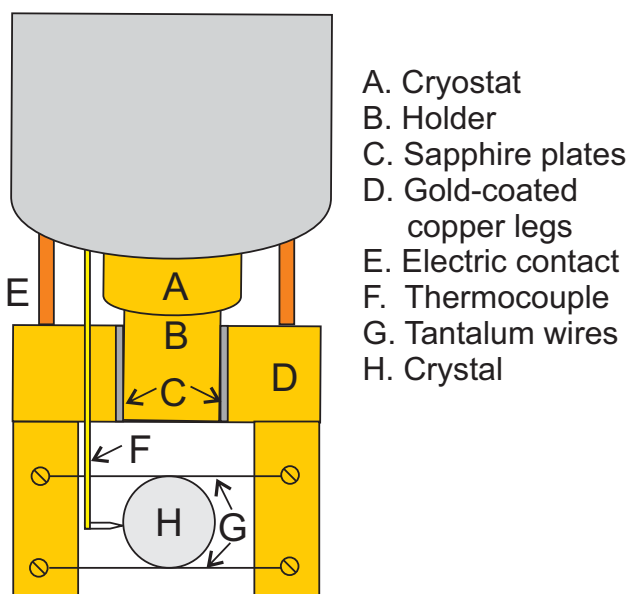


Figure 3-13.: Design of the sample holder and the lower part of the cryostat that are attached to the manipulator.

The spectrometer chamber (lower part of the chamber) is equipped with Auger Electron Spectrometer (AES), photoelectron time-of-flight spectrometer (eTOF), and position sensitive time-of-flight spectrometer (pTOF). The AES is based on the analysis of the energy of the secondary electrons emitted from the surface [167]. The AES technique can be used for quantitative analysis of the composition of the surfaces because the energy of the secondary electrons from the core level is unique for every atoms (not to be confused with the electrons at the secondary edge in 2PPE). The eTOF and pTOF analyse the kinetic energy and angle of the photoemitted electrons, respectively. In the thesis work, all experiments are performed with eTOF spectrometer to study the ultrafast solvation dynamics.

A motor controlled three dimensional manipulator is used for the transportation of the sample between preparation chamber and spectrometer chamber. The sample can be positioned 400 mm vertically and  $\pm 12.5$  mm laterally. In addition, we can rotate the sample approximately  $\pm 20^\circ$  to study the angular dependence of the photoemission. A cryostat (CryoVac) on the manipulator is capable of cooling the sample surface down to 25 K - 30 K. All the measurements were performed at cryogenic temperature using either liquid  $N_2$  or liquid He. The schematic of the sample holder is shown in Fig. 3-13. The Cu(111) crystal (A) is placed between two Tantalum wires (B) of thickness 0.4 mm which are mounted to gold-coated copper legs (D). The copper legs are attached to a holder (E) with sapphire glass plates (C) as a spacer for electrical insulation. The holder is connected to the cryostat (F). In addition, metallic contacts are made to the sample (H) for heating or applying bias voltage. A Type-K thermocouple is attached to the sample for determining its temperature.

### 3.3. Surface Preparation and Characterization Under UHV

To achieve high purity of adsorbates on the surface and a surface free of any residual gases, experiments are performed under Ultrahigh Vacuum conditions. Alkali and solvents are adsorbed on a freshly prepared Cu(111) surface for the experiments. In this section, the preparation of Cu(111) surfaces, preparation of adsorbates, such as Cs, Xe and D<sub>2</sub>O on Cu(111), and their characterization are presented.

#### 3.3.1. Preparation of Cu(111) Surfaces

The preparation of the single crystalline Cu(111) surfaces with crystallographic quality and free of irregularities such as steps or terraces are essential for performing experiments. The Cu(111) surface is prepared by several sputtering-annealing cycles. Commercially available Ar gas (Argon 5.0, Westfalen) is introduced into the preparation chamber via a variable leak valve and maintaining the chamber pressure of  $\sim 2 \times 10^{-5}$  mbar. The Ar is ionised by the sputter gun and bombarded to the substrate with an energy of 1.5 keV for 10 – 20 minutes while maintaining the sample current of  $(1.0 \pm 0.3)$   $\mu$ A. The depth of removal of the substrate depends on the type of sputtering gas and the energy of the ions. The sputtered surface is subsequently annealed at a temperature of 500 – 600 K to minimize the irregularities by mobilizing atoms. Normally, around 20 cycles of sputtering and annealing are performed on a surface introduced into the chamber first time for measurement and a single cycle of sputtering-annealing is sufficient for cleaning the surface in between the measurements.

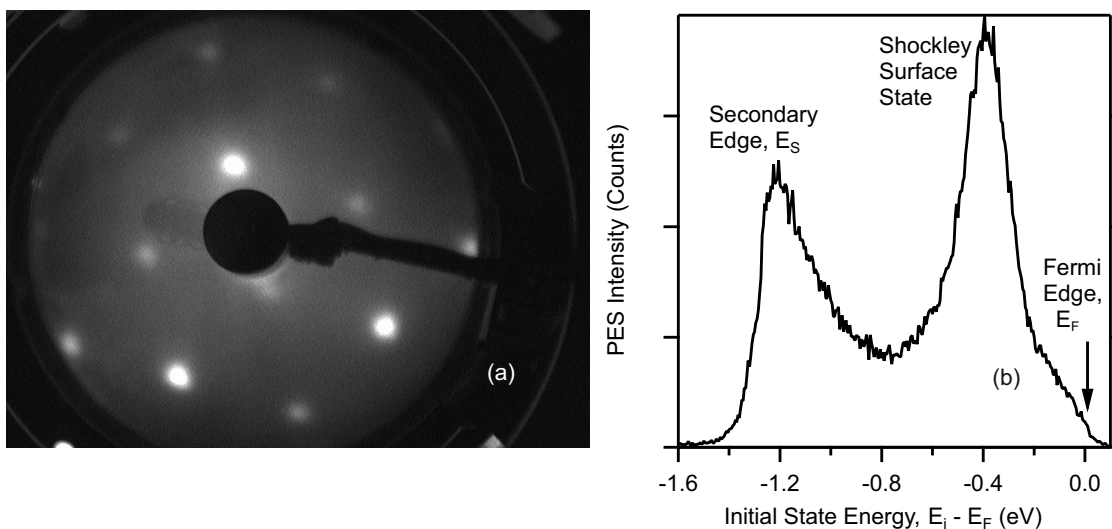


Figure 3-14.: The LEED pattern of the freshly prepared Cu(111) recorded with an electron energy of 250 eV in panel (a) and 2PPE from a Cu(111) surface with spectral features in panel (b).

(LEED) and 2PPE. A LEED is usually performed at the beginning of the measurement period to understand the long-range quality of the surface since the probing electron beam size is of the order of millimeters. The LEED pattern of a freshly prepared Cu(111) is shown in Fig. 3-14 (a). The hexagonal diffraction pattern originates from the (111) surface of the copper substrate. The sharpness, uniform intensity, and periodicity of the pattern are a measure of the crystallographic quality of the surface. Furthermore, more systematic characterization of the surface is performed using 2PPE where we continuously monitor the width of the Shockley surface state and intensity of the photoemission at the secondary edge of the spectrum after every sputter-annealing cycles. A 2PPE spectrum of a freshly prepared surface is shown in Fig. 3-14 (b) with the spectroscopic features marked. The sputtering and annealing parameters are optimized in such a direction to obtain less-intense secondary edge and reduced width for the Schotkly surface as we progress surface preparation. For instance, two different surface quality can be inferred from the 2PPE spectra shown in the Fig. 3-14 (b) and the left panel of Fig. 3-5.

### 3.3.2. Chemisorption of Cs on Cu(111)

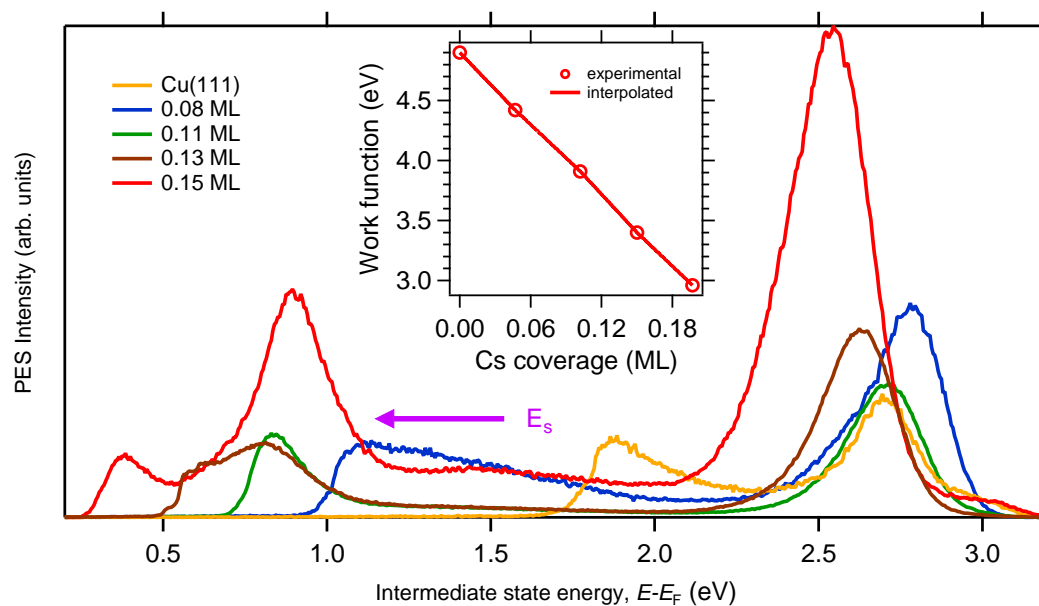


Figure 3-15.: 2PPE intensity as a function of intermediate state energy plotted for different Cs coverages. The inset shows the calibration graph (obtained from [168]) for Cs coverages in the range of the experiments.

The Cs alkalis are chemisorbed on freshly prepared Cu(111) at  $T > 200$  K from an alkali cartridge. The Cs cartridge (SAES Getters) is mounted on a home-built resistive evaporator for alkali deposition. The rate of ejection of the alkali from cartridges is observed to be not steady and varies over time. Depending on the coverage, we deposit Cs for a duration of

5 – 45 minutes and determine its coverage using 2PPE. The 2PPE intensity is plotted as a function of intermediate state energy for different Cs coverages as shown in Fig. **3-15**. The work function of the Cu(111) decreases upon chemisorption of Cs and as a result the width of kinetic energy increases. This decrease in the work function of the surface is attributed to the formation of surface dipoles that lower the energy barrier for an electron to emit from the surface. The calibration of Cs coverages on Cu(111) is shown in the inset of Fig. **3-15** and can be found elsewhere [168,169]. In the experiments discussed in the thesis, coverages up to 0.2 ML are prepared for experiments because above this coverage, the work function reduces below the photon energy and that results in direct photoemission.

### 3.3.3. Physisorption of D<sub>2</sub>O Sub-bilayers on Metal

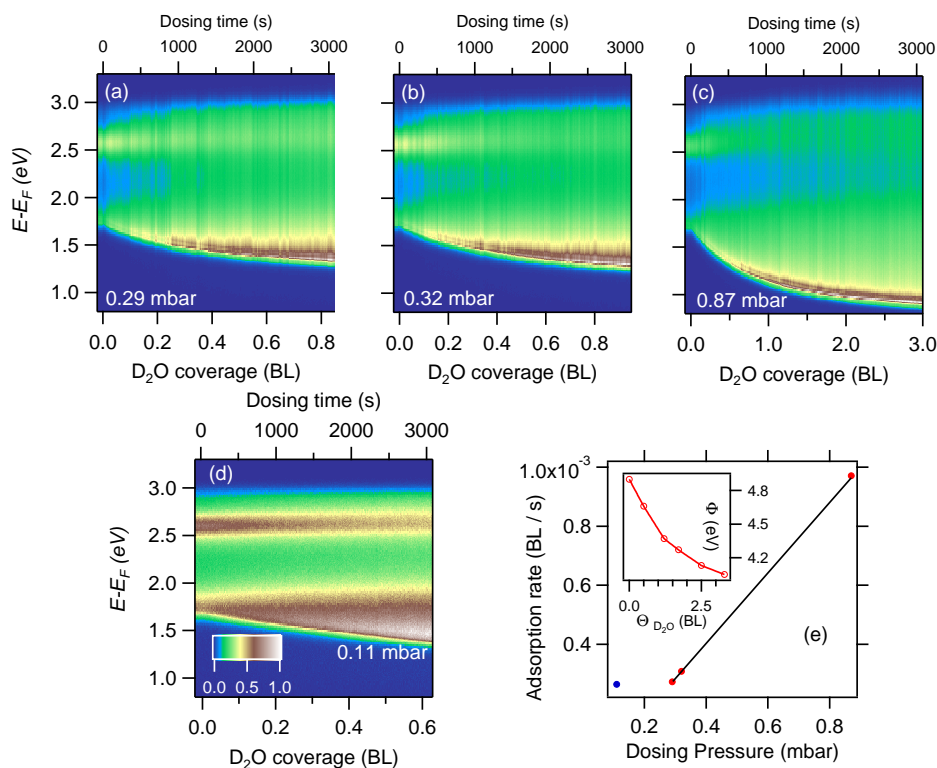


Figure **3-16**.: False colourmap of intensity of 2PPE plotted as a function of intermediate state energy and D<sub>2</sub>O coverage for different dosing pressures from panels (a)-(d). The inset of panel (e) shows the calibration of D<sub>2</sub>O coverage according to [170] and main panel shows the determination of adsorption rates for different gas system pressures during dosing.

The D<sub>2</sub>O molecules are buffered to the gas system and is then adsorbed onto the Cu(111) either by directly placing it in front of the pinhole doser or while recording TOF spectra. The experiments with D<sub>2</sub>O are performed at a sample temperature of 30 K and 80 K. The 2PPE of the surface is analysed for determining the coverage of D<sub>2</sub>O. The Fig. **3-16** shows

the false color representation of the photoemission spectra of Cu(111) while adsorbing D<sub>2</sub>O for different gas system pressures. The work function of the surface decreases as result of the adsorption of D<sub>2</sub>O due to the formation of surface dipoles. In the first set of experiments, only the upper part of the gas system is used and the results are shown in Fig. 3-16 (a,c). The decrease in work function becomes faster as we increase the gas system pressure. To maintain a steady adsorption, both upper and lower parts of the gas system are used and at a pressure of 0.1 mbar as shown in panel (d) of Fig. 3-16. The D<sub>2</sub>O coverage on Cu(111) is calibrated according to [170, 171] and is presented in the inset of panel (e) of Fig. 3-16. The adsorption rate for different dosing pressures are plotted in Fig. 3-16 (e) for upper part of gas system (red data points) and full gas system (blue data point). It is found that the adsorption of D<sub>2</sub>O is linear. However, to achieve a better consistency during deposition, we use both upper and lower part of the gas system.

### 3.3.4. Adsorption of Multilayers of Xe on Cu(111)

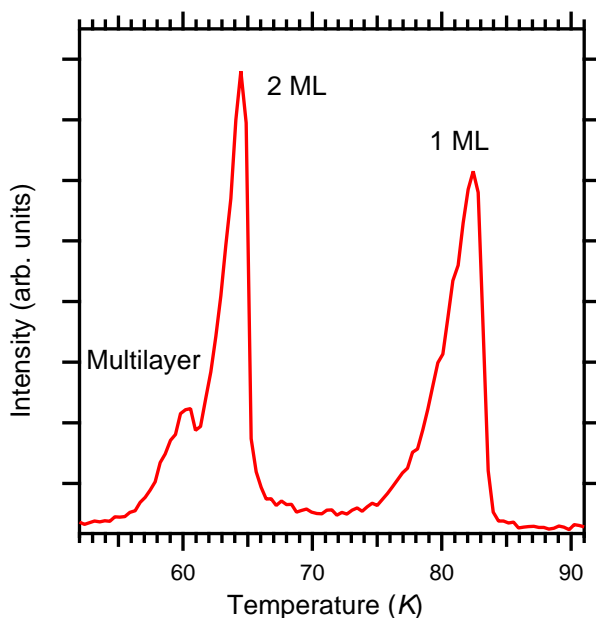


Figure 3-17.: TPD spectrum of multilayers of Xe on Cu(111). The surface is heated at  $\sim 1$  K/s. The characteristic desorption energy are marked and calibrated according to [110].

In order to perform experiments with Xe as a solvent or an intermediate layer for decoupling, the surface has to be cooled down with liquid-He. The cryostat in the manipulator is capable of cooling the surface down to 30 K and adsorption of multiple layers of Xe occurs well above this temperature [110]. After the adsorption of Xe, TPD is performed to characterize the coverage of Xe/Cu(111). The Cu(111) surface is heated at a rate of  $\sim 1$  K/s. A typical TPD of Xe is shown in Fig. 3-17 where the peaks at 82 K, 64 K and 60 K correspond to first monolayer, second monolayer and multilayers of Xe. By varying the dosing pressure and the duration of adsorption, Xe layers of desired coverages are prepared for the experiments.





# 4. Understanding the Electronic Structure and the Ultrafast Dynamics of Alkali-Water Clusters at Interfaces

In this chapter, a systematic investigation of the electronic structure and the ultrafast electron transfer processes in the Cs-water clusters at interfaces are presented. In the first section, discussions on the results of static 2PPE experiments on chemisorbed  $\text{Cs}^+/\text{Cu}(111)$  while adsorbing  $\text{D}_2\text{O}$  are presented. Similar experiments had been performed as part of the Ph. D. thesis work of Michael Meyer, former graduate in our research group. The formation of a novel state with a few 100 meV lower energy than the Cs 6s state was observed while adsorbing water on alkali/Cu(111). The origin of this state was explained as the alkali-water hybrid state and further insights on the electronic properties and the structural information of the alkali-water cluster was not clear [4, 169]. The DFT calculation on hydrated alkali (Na, K or Cs) on Cu(111) was reported recently based on the experimental observations in Meyer et al. and attempted to explain the origin of the novel alkali-water cluster state [4, 43]. In this chapter, the first section presents the 2PPE experiments in conjunction with STM and DFT calculations which shed light on the origin of the alkali-water state and its properties. In the second section, time-resolved 2PPE experiments are presented for various adsorbate coverages to understand the energy transfer to the solvent and population dynamics of the excited Cs-water cluster state. More properties of the Cs-water clusters are investigated using angle-resolved 2PPE experiments, temperature-dependent measurements, and Xe overlayers to understand the confinement or delocalization, influence of structure on dynamics, and the location of solvation site, respectively.

## 4.1. Formation of Cs-Water Clusters on Cu(111)

To understand the formation of Cs-water clusters, experiments are performed by varying Cs and water coverages to observe the changes in the electronic structure as a result of water adsorption on  $\text{Cs}^+/\text{Cu}(111)$ . The energy of the unoccupied Cs 6s state and the Cs-water cluster state as a function of water coverage is analysed for more insights. In addition, our findings are confirmed by complementary experimental (STM by research group of Morgenstern, Ruhr University of Bochum) and theoretical (DFT by research group of Saalfrank,

University of Potsdam and research group of Michaelides, University of Cambridge) results from our collaborators.

### 4.1.1. Evolution of the Electronic Structure of Cs-Water Clusters

In order to understand the coverage-dependent change in the electronic structure of solvated alkali, 2PPE spectra of the  $\text{Cs}^+/\text{Cu}(111)$  are recorded while adsorbing the  $\text{D}_2\text{O}$ . The schematic of the 2PPE process and representative data acquired with photon energy of 3.1 eV are shown in Fig. 4-1. First a photon attaches an electron from the substrate to the unoccupied Cs 6s state, a second photon photoemits the electron from that excited adsorbate state, and the kinetic energy of the photoemitted electrons are analysed using a TOF spectrometer as shown in Fig. 4-1 (a). False colour representation of the 2PPE intensity for different coverages of  $\text{Cs}^+/\text{Cu}(111)$  as a function of intermediate state energy and water coverage at 80 K are shown in Fig. 4-1 (b-d). The notable spectroscopic features in the false colour spectra are Cs 6s state, Cs-water cluster state, and low-energy cut off or secondary edge. The coverage of Cs and water are determined with respect to a  $2 \times 2$  and  $\sqrt{3} \times \sqrt{3}$  superstructures on Cu(111), respectively, as described in the chapter 3 on experimental methods. The average number of  $\text{D}_2\text{O}$  per  $\text{Cs}^+$  is determined by calculating the ratio of the individual adsorbate coverages with respect to the Cu(111) surface. The energy  $E-E_F$  of the Cs 6s state (denoted as state A here onwards) decreases with increasing Cs coverage consistent with previous work [2]. The variation in the energy of this state while adsorbing water are marked with blue circles. The Cs-water state (denoted as state B here onwards) appears for a water coverage of above  $\approx 0.1$  BL and is marked with red circles. In addition, the change in the low-energy cut off of the spectra which is analogous to the change in the work function of the surface are indicated with yellow circles. Individual spectrum for specific coverages of water are shown in the right panel of the figures (b) to (d). It is obvious from the panels (b) to (d) of Fig. 4-1 that the energies of the states A and B change differently as a function of the water coverages and an analysis of the energy of these states with reference to a proper energy scale is required for better understanding their behaviour.

The energy of the states A and B for different coverages of  $\text{Cs}^+/\text{Cu}(111)$  as function of the excited state energy and the water coverage at 25 K and 80 K are shown in Fig. 4-2. The measurements at 25 K and 80 K are indicated with ‘open’ markers and ‘solid’ markers in the figures, respectively. The energy references with respect to Fermi level ( $E-E_F$ ) and vacuum level ( $E-E_{\text{vac}}$ ) are taken into considerations in the analysis. The former is used for describing chemisorbed systems and the latter is used for physisorbed systems on metal substrates. In the absence of water, the energy of the state A decreases with increase in Cs coverage for both energy references as shown in Fig. 4-2 (a, c). Upon adsorption of water, the energy of the state A with respect to  $E_F$  increases with the coverage of water (panel a) and the rate of the increase in energy is not same for different coverages of  $\text{Cs}^+/\text{Cu}(111)$ . The change in the binding energy of the state A with respect to the vacuum level as a function of water

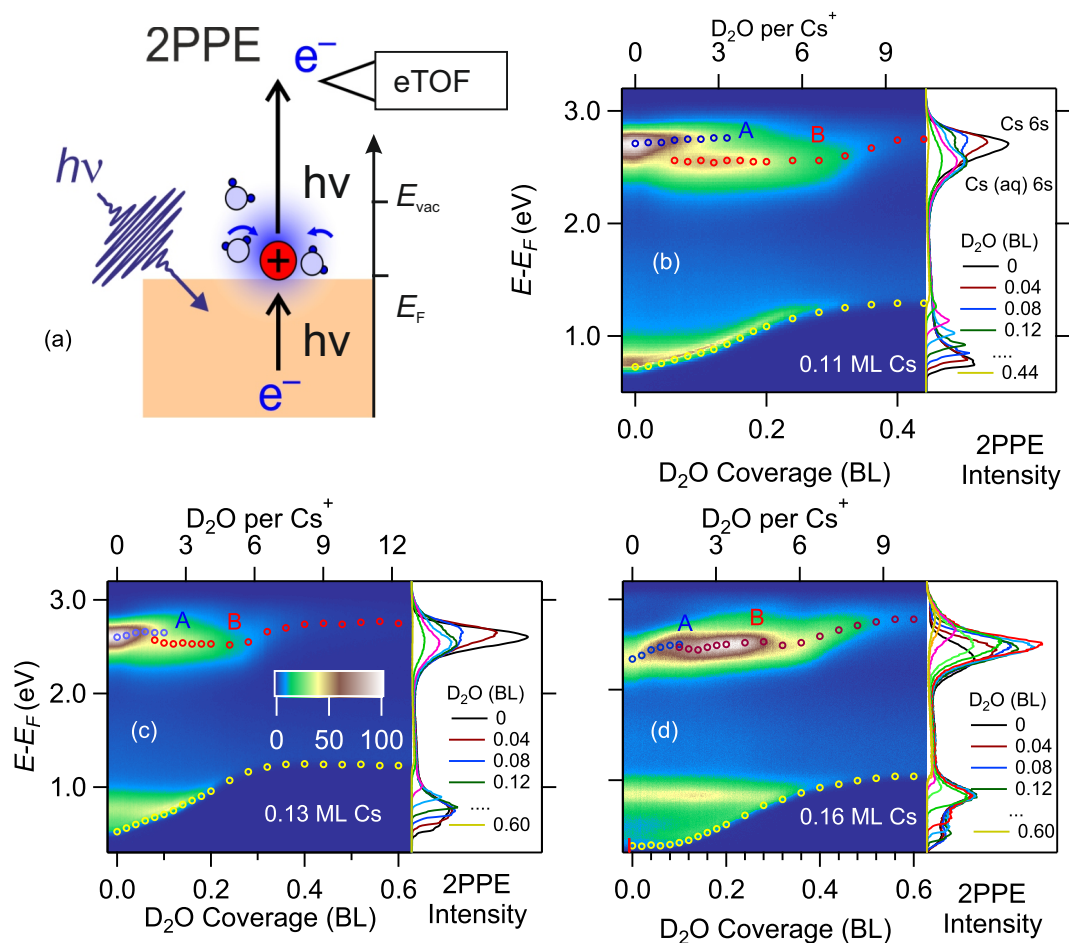


Figure 4-1.: (a) Schematic of the static 2PPE experiment where two-photon photoemission of electrons occurs from  $Cs^+/Cu(111)$  while adsorbing water. (b-d) False colour representation of 2PPE intensity for different coverages  $Cs^+/Cu(111)$  as a function of intermediate state energy,  $E-E_F$  (left axis) and water coverage (bottom axis). The spectra at specific water coverages are shown in the right panel of (b-d). The water coverage in bilayer (bottom axis) is determined according to [169] and average number of water molecules per  $Cs^+$  is indicated (top axis). The energy of the Cs 6s state (state A) and its variation as a function of water adsorption are marked with blue circles. The intensity of the water-dressed Cs 6s state decreases and vanishes around 3  $D_2O$  per  $Cs^+$ . The new Cs-water cluster state observed at a coverage above 2  $D_2O$  per  $Cs^+$  occurs due to the agglomeration of  $Cs^+$  in water and are indicated with red circles. The change in the low energy cut off the spectra are indicated with yellow circles and is analogous to the change in the work function. All measurements are performed at a temperature of 80 K.

coverage is very small as shown in the panel (c). This indicates that the decoupling of the state A is more sensitive to the changes with reference to the Fermi level than the vacuum level. Similarly, the energy of the state B with respect to the Fermi level and the vacuum

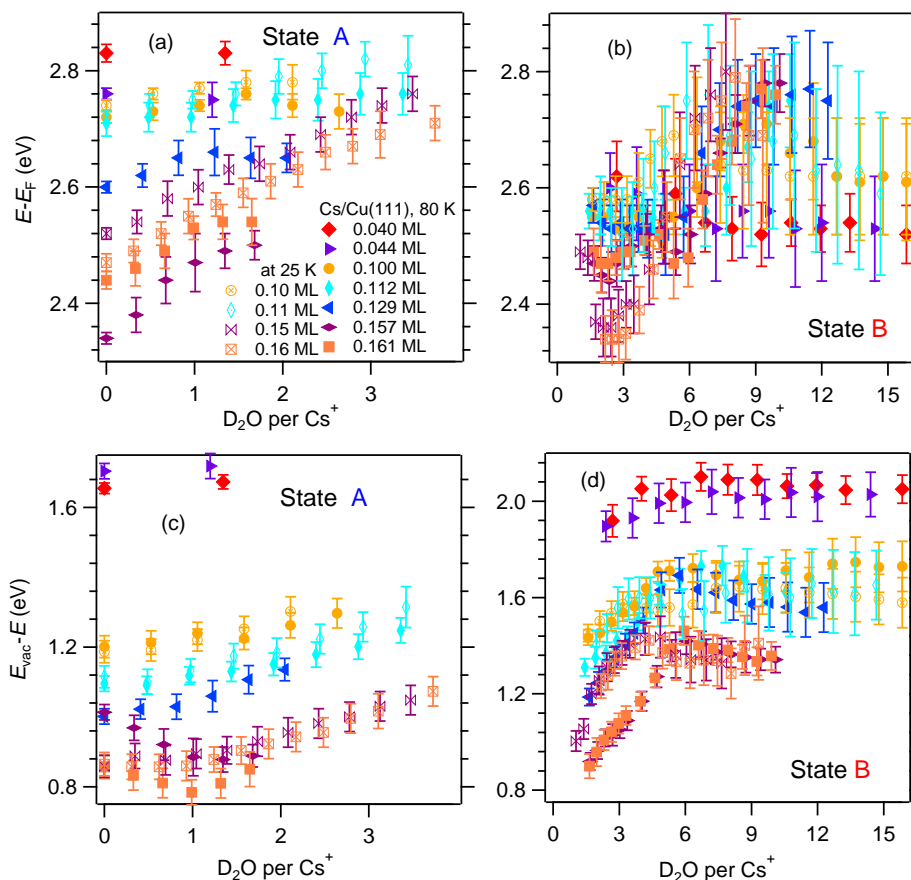


Figure 4-2.: Detailed analysis of the states A and B as a function of water coverage on Cs<sup>+</sup>/Cu(111). (a-b) The change in the intermediate state energy,  $E - E_F$  as a function of water coverage for the state A and Cs-water cluster state B for different Cs coverages. (c-d) The change in the binding energy with respect to vacuum level as a function of the water coverage for the state A and state B for different Cs coverages. The measurements are performed at a substrate temperature of 25 K and 80 K and are represented with open and solid markers, respectively.

level are shown in Fig. 4-2 (b, d). It is clear from panel (b) that the state B does not show any Cs<sup>+</sup> coverage dependence as the data sets overlap each other. Hence, the energy of the state B is independent on the coverage of the Cs<sup>+</sup> and overall, the energy of the state B increases with water coverage up to  $\approx 10$  D<sub>2</sub>O per Cs<sup>+</sup>. In contrast, the change in the energy of the state B with respect to the vacuum level depends on the Cs coverage and is varying only up to  $\approx 5$  D<sub>2</sub>O per Cs<sup>+</sup>. The state B does not change at higher adsorbate coverages. Hence, the energy reference with respect to the Fermi level is considered for interpreting the scientific aspect of the investigation. In addition, the nearest Cs coverage are averaged from Fig. 4-2 for the upcoming discussion.

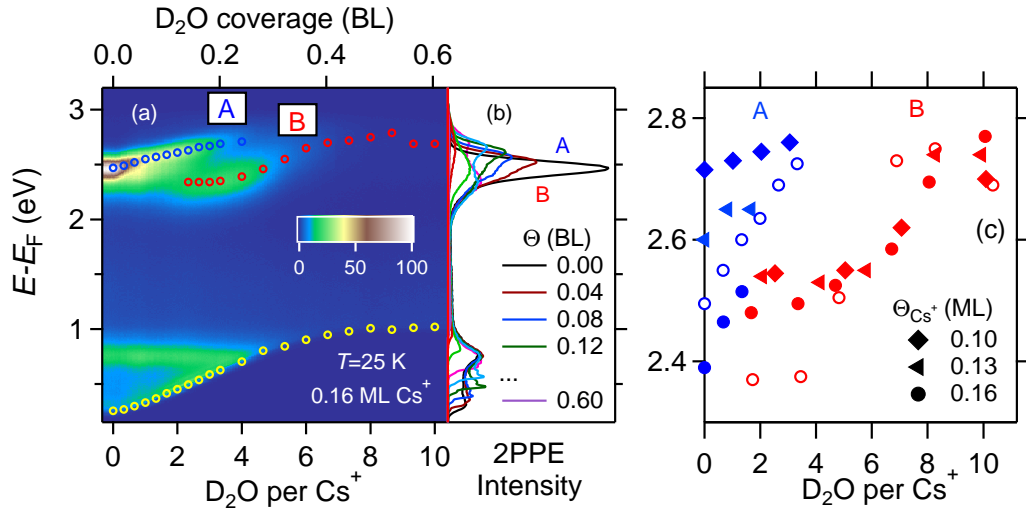


Figure 4-3.: (a) False colour 2PPE intensity of  $Cs^+/Cu(111)$  while adsorbing  $D_2O$  at 25 K as a function of the intermediate state energy,  $E-E_F$  (left), and  $D_2O$  coverage. The  $D_2O$  coverage is given as the number of  $D_2O$  per  $Cs^+$  (bottom axis) and as in bilayers (top axis), according to [172]. The change in the Cs 6s state (state A) with water coverage is indicated with blue circles and it diminishes around 4  $D_2O$  per  $Cs^+$ . The new state B, appearing around 2  $D_2O$  per  $Cs^+$ , is indicated with red circles. The state at energy 0.75 eV originates from the d-band of Cu(111). The change in the energy of the secondary cut off is indicated with yellow circles and is analogous to the change in the work function as a function of water coverage. (b) The spectra extracted at different water coverages from the panel (a) for better clarity. The compilation of the analysis of the energy of the states A and B for different  $Cs^+$  coverages are shown in panel (c). The open circles refer to the measurements at 25 K and solid circles refer to the measurements at 80 K. Reprinted figure with permission from Penschke, C. et al. Hydration at Highly Crowded Interfaces. *Phys. Rev. Lett.*, 130:106202, (2023). DOI: <https://doi.org/10.1103/PhysRevLett.130.106202>. Copyright © 2023 by the American Physical Society. Ref. [140].

In experiments conducted at 80 K, the states A and B are broader and are sometimes overlap each other. A few measurements are performed at 25 K which provide well-distinguishable sharp features. The false colour 2PPE intensity from  $Cs^+/Cu(111)$  while adsorbing  $D_2O$  at 25 K is shown in the Fig. 4-3 (a). In the absence of water, the peaks at energy  $E-E_F=2.47$  eV and 0.75 eV are originated from the state A and the occupied d-band of the Cu(111), respectively. Upon adsorption of the water, the energy of the state A increases by 240 meV from 2.47 eV to 2.71 eV as marked with blue circles in panel (a) and intensity of the photoemission decreases gradually and disappear around  $\approx 4$   $D_2O$  per  $Cs^+$ . The d-band of the Cu(111) is unaffected initially but disappears when the work function of the surface becomes greater than the energy for 2PPE from the d-band. The state B which evolves at an energy

of  $E-E_F=2.34$  eV and its energy increases with water coverage as indicated with red circles. The Fig. 4-3 (b) shows the extracted spectra for a different coverages of water for the ease of comparison. The state B is not visible in our experiments with Xe as a solvent [44] which will be discussed in the chapter 5. In addition, Fig. 4-3 (c) shows the compilation of analysis of state A and B (panels (a) and (b) of the Fig. 4-2) where the nearest Cs coverages data from experiments at 80 K are averaged for better clarity. The change in the energy of the state A due to adsorption of water depends on the coverage of the  $\text{Cs}^+/\text{Cu}(111)$ . However, the energy of the state B is not directly depending on the coverage of  $\text{Cs}^+$  and it increases around 300 meV as a function of the adsorbate coverage ratio. Slight changes in the energy of the states A and B are observed in the experiments at 25 K and 80 K. However, the overall trend in the change in the energy as a function of water coverage is similar in both cases. Specifically, we can see for both at 25 K and 80 K that the energy of the state B is nearly constant below 4  $\text{D}_2\text{O}$  per  $\text{Cs}^+$  and above 7  $\text{D}_2\text{O}$  per  $\text{Cs}^+$ . There is a sharp transition of the energy of the state B at 5 to 7  $\text{D}_2\text{O}$  per  $\text{Cs}^+$ . This is attributed to the major structural rearrangement of the adsorbates on the surface with increase in the coverage of the water and will be addressed in the section 4.1.2 and 4.1.3. There are discrepancies in the energy of the state B for 25 K and 80 K data which arise due to the inhomogeneous distribution of the adsorbates (both adsorbates are at sublayer coverages) on the surface. More insights on the morphology of the Cs-water clusters are revealed in STM experiments and will be discussed in the next section.

### 4.1.2. Morphology of Cs-Water Clusters

This section is about the STM experiments performed by Cord Bertram in the research group of Karina Morgenstern at the Physical Chemistry I, Ruhr University of Bochum. The results discussed here are part of the published work by Penschke et al [140]. The 2PPE technique provides the electronic structural information of the adsorbates from a probing region of size of a few tens of microns and the STM provides the morphology of the adsorbates with atomic scale resolution. A discussion on morphology is presented here to demonstrate the link between the electronic structure and the morphology of the adsorbates at interfaces.

The STM studies on  $\text{Cs}^+/\text{Cu}(111)$  surfaces which are partially solvated and completely solvated with different adsorbate coverages are shown in Fig. 4-4. The bare  $\text{Cs}^+$  ions are arranged periodically as a  $6 \times 6$  superstructure on  $\text{Cu}(111)$  with a separation of  $(1.55 \pm 0.07)$  nm for a coverage of 0.2 ML as shown in the inset of Fig. 4-4(a). This periodic arrangement is due to the long-range Coulomb interaction between  $\text{Cs}^+$  ions and is consistent with previous observations [173]. The striped appearance of  $\text{Cs}^+$  is due to their motion during the imaging. In a partially water covered  $\text{Cs}^+/\text{Cu}(111)$ , the region with bare  $\text{Cs}^+$  ions are well-periodic and the remaining water-covered  $\text{Cs}^+$  ions are less-periodic due to the presence of water molecules which screen the repulsion between  $\text{Cs}^+$  ions. The hexagonal distribution of  $\text{Cs}^+$  ions become broader upon adsorption of water from an area of  $(0.34 \pm 0.08)$   $\text{nm}^2$  to 60

( $0.83 \pm 0.09$ )  $\text{nm}^2$  and also its height increases from 125 pm to 170 pm as plotted as a line profile in Fig. 4-4(b). This indicates that each ion is attached with one water molecule and the hexagonal distribution is not affected significantly and hence the Coulomb repulsion still persists. So, there is a coexistence of two morphological forms of adsorbates while gradually progressing the solvation. Surprisingly, this is analogous to the observation in the 2PPE experiments discussed in the previous section where two states (state A and B) are observed as a function of the water coverage. The energy of the state A increases and its intensity diminishes with water coverage. The state B evolves at a later stage of solvation and there is coexistence of state A and B at intermediate water coverage in the experiments. The origin of state A is due to bare  $\text{Cs}^+$  ions on the surface and origin of the state B is attributed to hydrated-alkali structures at the interface.

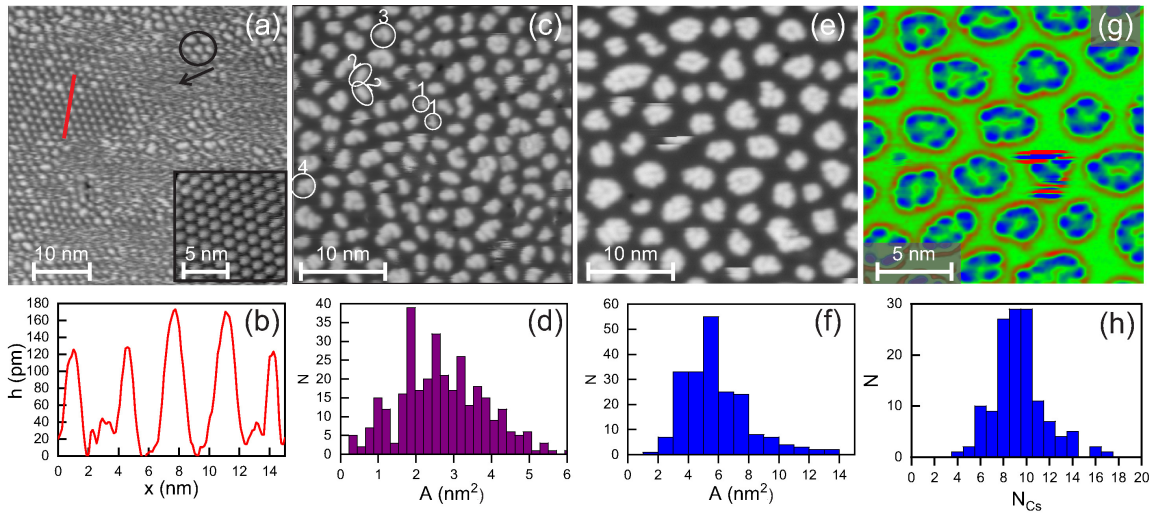


Figure 4-4.: STM images of Cs-water clusters on Cu(111). (a) Partially solvated  $\text{Cs}^+$  ions on Cu(111) where diffusive regions are covered by water and periodic pattern is found for bare  $\text{Cs}^+$ . The inset of the panel (a) shows the bare  $\text{Cs}^+$  on Cu(111). The panel (b) shows line profile of a partially covered region where water covered ions show increase in apparent height. (c) Fully solvated  $\text{Cs}^+$  ions with a coverage of 10  $\text{D}_2\text{O}$  per  $\text{Cs}^+$  and area histogram of the cluster in panel (d) at a temperature of 7 K. (e, f) The change in the structure of Cs-water clusters and its area histogram after annealing at 50 K. (g, h) Laplace-filtered image of the panel (e) for enhancing the visibility of  $\text{Cs}^+$  ions at the periphery and histogram showing the distribution of  $\text{Cs}^+$  ions on the surface. The STM imaging parameters are: (a) -250 mV, 10 pA (c) 53 mV, 7.5 pA (e) 40 mV, 7.5 pA and (g) 100 mV, 10 pA. Reprinted figure with permission from Penschke, C. et al. Hydration at Highly Crowded Interfaces. *Phys. Rev. Lett.*, 130:106202, (2023). DOI: <https://doi.org/10.1103/PhysRevLett.130.106202>. Copyright © 2023 by the American Physical Society. Ref. [140].

At higher coverages of water, all the  $\text{Cs}^+$  ions are fully solvated as shown in Fig. 4-4 (c). The decrease in the number of individual clusters compared to partially solvated surface

(panel a) indicates the presence of multiple  $\text{Cs}^+$  ions in a cluster and is estimated around four to five. The effective distance between the  $\text{Cs}^+$  on Cu(111) has been reduced after adsorption of water since it screens the repulsion between ions. The Cs-water clusters are also appearing as ellipsoids as marked in the Fig. 4-4 (c) and their sizes suggest a coverage of 10  $\text{D}_2\text{O}$  per  $\text{Cs}^+$  as reported earlier [174]. The area histogram of the solvated clusters are shown in the Fig. 4-4 (d) and ellipsoids structures are more prominent shapes for this adsorbates coverage.

In order to prepare a nominally identical surface with 2PPE experiments, the surface is annealed to 50 K as shown in the Fig. 4-4 (e). The annealing results in increased mobility of the adsorbates and formation of larger clusters due to the coalesce of smaller clusters. The area distribution of the Cs-water clusters has increased by a factor of two after annealing as shown in Fig. 4-4 (f). The large Cs-water clusters have random shape and  $\text{Cs}^+$  ions are located at the perimeter. The visibility of these ions are enhanced by Laplace filtering the image as shown in Fig. 4-4 (g). The number of  $\text{Cs}^+$  ions in the cluster are determined as shown in the histogram in Fig. 4-4 (h) where the majority of the clusters consist of 8-10  $\text{Cs}^+$  ions per cluster. To summarize, the STM studies shed light into a formation of a novel solvation structure where ions are situated at the perimeter of the cluster instead of at the centre in a conventional picture of the solvation model. In addition, STM provides a convincing explanation of the two states A and B in 2PPE which originate from bare and completely solvated  $\text{Cs}^+$  on the Cu(111). More insights on the electronic structure and morphological aspects of the Cs-water clusters are revealed by DFT calculations and will be discussed in the following section.

### 4.1.3. Theoretical Investigations on Cs-Water Clusters Using DFT

This section is about the DFT calculations performed by Christopher Penschke and Peter Saalfrank at University of Potsdam along with Angelos Michaelides, Cambridge University. The results discussed here are part of the published work by Penschke et al. and more technical details can be found in the article [140]. These results are presented here to facilitate the link between observations in STM and 2PPE experiments.

The most prominent spectroscopic features in 2PPE experiments are the states termed A and B in Fig. 4-3 (a). The DFT calculations provide a scenario to explain their origin as a function of water coverage and are presented in Fig. 4-5. The calculation of the density of states (DOS) after the adsorption of  $n(\text{H}_2\text{O})$  on a single Cs on Cu(111) where  $n$  varies from 0 to 6 are shown in Fig. 4-5 (a). The DOS for Cu,  $\text{H}_2\text{O}$ , and Cs are shown in brown, red, and blue, respectively. The energy of the Cs 6s (state A) increases with the coverage of the water up to 4  $\text{D}_2\text{O}$  per  $\text{Cs}^+$  akin to the observation in the 2PPE experiments shown in Fig. 4-3 (a). However, the calculations do not show the appearance of the new state (state B) upon increasing the coverage of water. The change in the work function upon adsorption of water is observed in theory (This result is not shown in the thesis and please



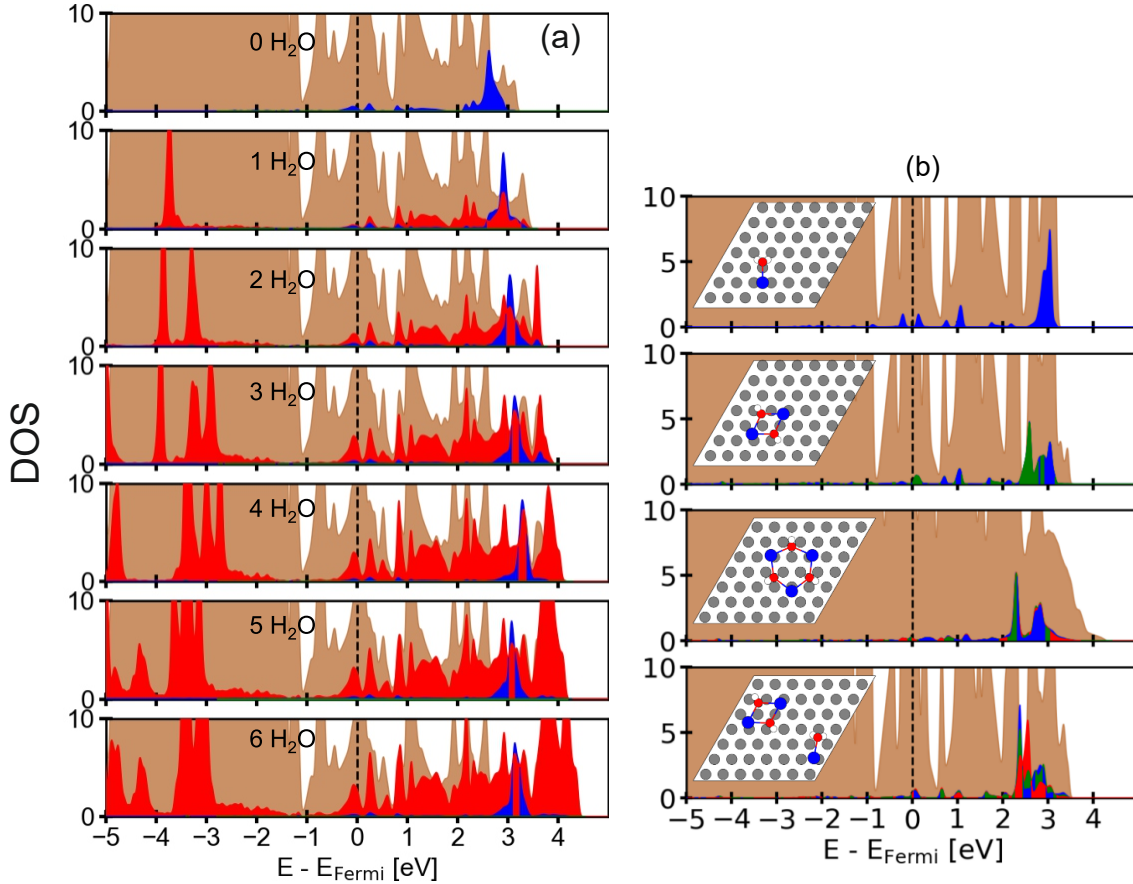


Figure 4-5.: DFT calculations on different composition of Cs<sup>+</sup> and water clusters on Cu(111). Panel (a): DOS calculations for Cu(111) (brown), cesium (blue) and water (red). The energy of the unoccupied Cs 6s state increases with water coverage of around 4 H<sub>2</sub>O. Panel (b): The electronic DOS of Cs-water clusters on Cu(111) with different Cs<sup>+</sup> ions configurations (blue, green and red). The inset of each panel shows corresponding structural configurations (Cs atoms: grey, Cs atoms: blue, O atoms: red and H atoms: white). The energy of the unoccupied Cs 6s state found to be decreasing when Cs-water forms various structures due to agglomeration of Cs<sup>+</sup> ions inside a water cluster. Reprinted figure with permission from Penschke, C. et al. Hydration at Highly Crowded Interfaces. *Phys. Rev. Lett.*, 130:106202, (2023). DOI: <https://doi.org/10.1103/PhysRevLett.130.106202>. Copyright © 2023 by the American Physical Society. Ref. [140].

refer [140]) which is in agreement to 2PPE results in Fig. 4-3 (a) where the change in work function is manifested as the change in the low-energy cut off. The calculations also show that for a given water coverage, the energy of the state A decreases if we increase the local coverage of the Cs<sup>+</sup> ions [140]. The increase in energy of the Cs 6s state as a function of the water coverage is attributed to the decoupling of the state from the Fermi level as a result of

the overlapping of the DOS of water molecules (red colour) as shown in Fig. 4-5 (a). More details of this calculations can be found in the article by Penschke et al. [140].

To understand the formation of the state B in 2PPE, STM results in section 4.1.2 are considered for potential models for structural calculations. The STM shows Cs-water clusters on Cu(111) with Cs<sup>+</sup> ions at the periphery for higher coverages of water. It is not computationally feasible for considering the large Cs-water clusters similar to STM for theoretical calculations. This requires sampling of large unit cell size and vast phase space. Hence, different combinations of a few Cs<sup>+</sup> ions and water molecules are considered in the DFT calculations. The electronic DOS calculations for different configuration of Cs<sup>+</sup> ions and water molecules on Cu(111) are shown in Fig. 4-5 (b). The inset of the figures show the arrangement of Cu, Cs, O and H atoms on the surface which are represented in grey, blue, red and white circles, respectively in the corresponding DOS calculations. Even though the ratio of water molecules to Cs<sup>+</sup> ions is one, the energy of unoccupied Cs 6s state has found to decrease as a result of structural modifications as shown in blue, green and red (from top to bottom) in the main panel of Fig. 4-5 (b). This is attributed to the alkali-water interaction in water clusters on the surface that results in the increase of local coverage of the Cs<sup>+</sup> ions and hence the evolution of the state B as shown in Fig. 4-3 (a). For different configurations, the pattern where Cs<sup>+</sup> ions at the periphery are found to be stable is similar to the observations in STM results as presented in Fig. 4-4. This novel solvation pattern arises because the water-water interactions due to hydrogen bonding is stronger than Cs<sup>+</sup>-water interactions on the Cu metal surface.

## 4.2. Ultrafast Electron Dynamics of Alkali-Water Clusters at Interfaces

Understanding the ultrafast solvation dynamics of alkali-solvents at interfaces are important due to their relevance in electrochemistry and catalysis [16, 80, 175]. As part of the thesis work, time-resolved 2PPE experiments are performed on Cs-water clusters adsorbed on Cu(111) with a coverage ratio of up to around 7 D<sub>2</sub>O per Cs<sup>+</sup>. The energy stabilization and population dynamics of the adsorbate system are analysed for understanding the solvation processes. The charged species are confined spatially by solvent molecules during solvation and hence their energy states are localized. Angle-resolved 2PPE measurements are performed to understand the degree of localization of the Cs-water cluster. Moreover, the temperature dependence of the dynamics of the Cs-water cluster state is investigated to understand the influence of solvent structure on dynamics since the water can form amorphous or crystalline structures depending on the substrate temperature. In addition, Xe overlayer experiments are performed to analyse the surface or interface sites of the solvated state and its population dynamics.

## 4.2.1. Ultrafast Solvation Dynamics of Cs-Water Clusters on Cu(111)

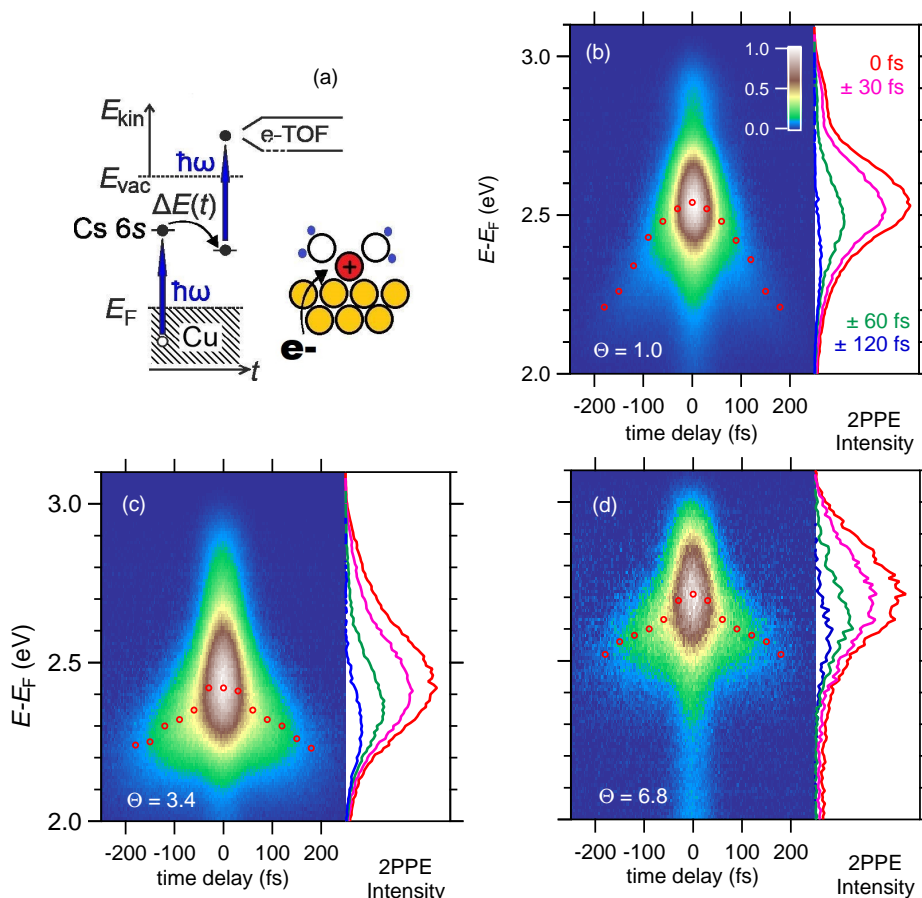


Figure 4-6.: (a) The schematic of the time-resolved 2PPE experiment shows the pump laser pulse attaches an electron to  $\text{Cs}^+$  and a time-delayed probe laser photoemits electron from the Cu(111) surface which is covered with  $\text{Cs}^+$  and  $\text{D}_2\text{O}$ . The kinetic energy of the photoemitted electrons are analysed by a TOF spectrometer. The photon energy used for the auto-correlation measurement is at 3.1 eV. Panels (b) to (d) show the time-resolved spectra measured for increasing water coverages as the number of  $\text{D}_2\text{O}$  per  $\text{Cs}^+$  ( $\Theta$ ). Note that the energy of the excited state changes with water coverage which is consistent with the observation in Fig. 4-3 (a). The change in the energy of the excited state as a function of the time delay is indicated with red circles. The spectra at specific pump-probe delay are shown in the right panels of (b)-(d).

The static 2PPE spectroscopy technique discussed in the previous section provides insights into the electronic structure of the Cs-water clusters as a function of the water coverage. The excited state dynamics of the adsorbates on Cu(111) is studied by time-resolved auto-correlation experiment and is shown in Fig. 4-6(a). These measurements probe the ultrafast

charge transfer dynamics which includes the electron attachment, solvation dynamics, and the electron back transfer to the substrate. Here, the first laser pulse attaches an electron to unoccupied Cs 6s from the Cu substrate to trigger the dynamics of the solvent molecules in the vicinity of the ion due to transient change in the charge state. A time-delayed second laser pulse is used for the photoemission from the excited state and the kinetic energy of the electrons is analysed using a TOF spectrometer. The surface preparation and the coverage determination of the adsorbates are performed as discussed in the chapter 3 on experimental methods. The time-resolved experiments are performed for a Cs coverage of above 0.1 ML where Cs ions form a stable periodic arrangement [173] which allows varying the water coverage continuously by adsorption and desorption without altering the Cs coverage. Fig. 4-6(b-d) shows the time-resolved 2PPE of Cs-water clusters of different adsorbate coverage on Cu(111) and their right panel shows the spectra at specific time delays. It is clear from figures that the energy of the excited state varies with the adsorbate coverage ratio and is consistent with the experimental observation in Fig. 4-3 (a).

The time-resolved 2PPE spectra of the Cs-water clusters provide insights into the energy transfer to the solvent molecules and the population dynamics. In an alkali-water cluster in equilibrium, the charge density of the alkali is shared by the metal substrate and the oxygen atom of the water molecules. The electron attachment to the alkali by resonant excitation redistributes the charge density. As a result, the solvent molecules minimize their energy by librational or vibrational or orientational responses. A time-delayed second pulse probes the dynamics of the alkali-water adsorbates on the surface. The energy of the excited state electrons decreases while transferring energy to the solvent. In addition, the lifetime of the excited state depends on the coverage of solvent which reduces the back transfer of electrons to the metal substrate.

Coverage ratio	1.0	1.4	2.0	3.4	3.5	6.8
Error	0.1	0.1	0.1	0.2	0.2	0.4

Table 4-1.: Error in the calculation of adsorbate coverage ratio.

The energy transfer to the solvent and population dynamics for different adsorbates coverage ratio are shown in Fig. 4-7. It is clear from the figures that the adsorbate ratio is relevant in the dynamics of the excited Cs-water clusters. The error in the adsorbate coverage ratio is determined by error propagation method as discussed in the Appendix B and they are given in Table 4-1. Based on the similarities in dynamics as observed in Fig. 4-7, the adsorbate ratio is grouped into three for the sake of discussion. They are no water coverage, intermediate coverages and higher coverages which correspond to bare Cs<sup>+</sup>, 1 to 2 D<sub>2</sub>O per Cs<sup>+</sup> and 3.4 to 6.8 D<sub>2</sub>O per Cs<sup>+</sup> on /Cu(111), respectively. (To remind the reader that the adsorbate ratio is the average number of adsorbates on the surface.) As shown in the Fig. 4-7 (a), the energy transfer is smaller in bare Cs<sup>+</sup>/Cu(111) compared to the

intermediate and higher adsorbate coverages. For bare  $\text{Cs}^+/\text{Cu}(111)$ , the change in energy is attributed to the nuclear motion of the Cs atoms normal to the surface [3]. The energy transfer becomes significant upon adsorption of water on  $\text{Cs}^+/\text{Cu}(111)$ . Noticeably, the energy transfer is higher for intermediate coverages ( $\approx 340$  meV) than higher coverages ( $\approx 250$  meV). This is attributed to the fact that at intermediate adsorbate coverages water is less rigid and hence dissipate more energy than higher adsorbate coverages where the water-water bonding becomes stronger due to the hydrogen bonding as discussed in DFT calculations in the section 4.1.3 and also in [140]. The molecular mechanisms in liquid water have been investigated earlier and the potential mechanisms are OH stretch, OH bend, and librations with a lifetime of 200 fs, 170 fs, and sub-100 fs, respectively [176,177]. The excited state lifetimes of Cs-water clusters reported in this thesis are sub-100 fs (See the discussion on population dynamics in the next paragraph.). This suggests that the dominant mechanisms during the energy transfer to the solvent in Cs-water clusters are librations of the water molecules as well as nuclear motion of Cs atoms.

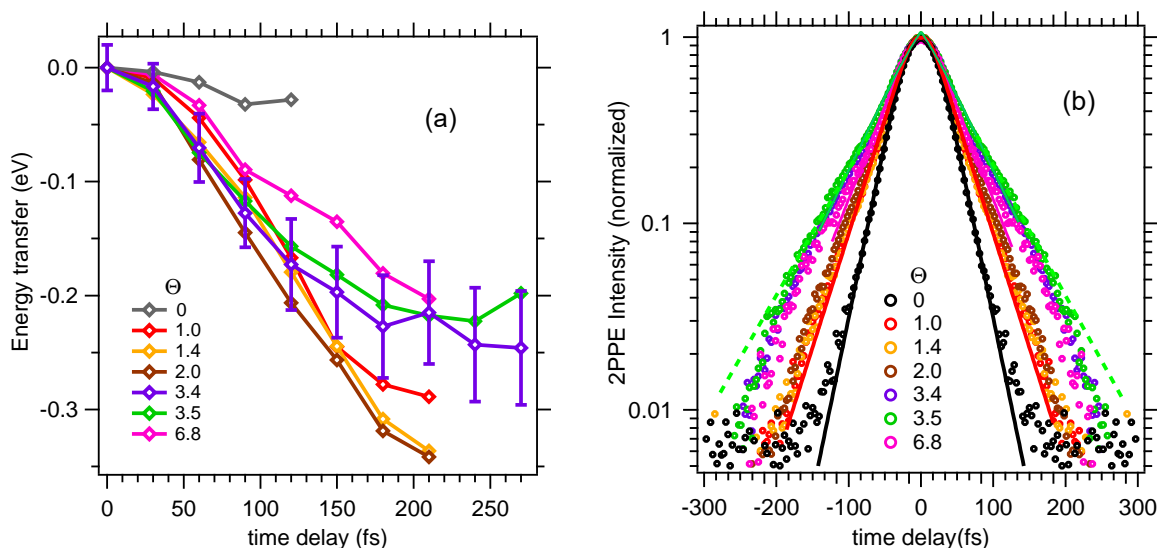


Figure 4-7.: The change in the energy of the excited state as a function of the time delay provides the energy transfer dynamics of the solvent ( $\text{D}_2\text{O}$ ) -solute (Cs) system as shown in panel (a). The energy transfer increases upon adsorption of water and it is larger at intermediate adsorbate coverages than higher adsorbate coverages. The change in the energy-integrated normalized 2PPE intensity of the excited state as a function of the time delay provides population dynamics of the adsorbates as shown in panel (b). The data corresponding to bare  $\text{Cs}^+$  and intermediate coverages ( $\Theta \leq 2$   $\text{D}_2\text{O}$  per  $\text{Cs}^+$ ) are fitted with the convolution of the Gaussian and exponential decay for the entire dynamic range. The higher adsorbate coverages ( $\Theta > 2$   $\text{D}_2\text{O}$  per  $\text{Cs}^+$ ) data deviate from single exponential decay as shown with green dashed line. See text for detailed discussion.

The population dynamics of Cs-water clusters for different adsorbate coverages is shown in Fig. 4-7 (b). The excited state lifetime of the Cs-water cluster increases with the adsorbates coverage ratio for the normalized 2PPE intensity above  $\approx 0.1$ . However, below the 2PPE intensity of 0.1, the relaxation rate of the adsorbates is nearly same as bare  $\text{Cs}^+/\text{Cu}(111)$ . For higher adsorbate coverages, the decay time changes slightly around the 2PPE intensity of 0.1 and hence the data cannot be fitted accurately in the entire dynamic range (i.e. from 2PPE intensity of 0.005 to 1) with a convolution of single exponential decay function and Gaussian function. A bi-exponential decay fit gives large error due to the small difference in the decay time of the two mechanisms [178]. As shown in Fig. 4-7 (b), the lifetime of the excited state of the Cs-water clusters has increased significantly upon adsorption of water. The intermediate adsorbate coverages are fitted up to a 2PPE intensity of 0.01 and higher water coverage data are fitted up to an intensity of 0.1. A dashed green line is drawn on the higher coverage to show the apparent deviation of the decay time at longer delays. The lifetime for the nonoverlapping data in Fig. 4-7 (b) are tabulated in Table 4-2.

$\text{D}_2\text{O} / \text{Cs}^+$	bare $\text{Cs}^+$	1.0	3.5	6.8
Lifetime (fs)	$23 \pm 3$	$31 \pm 3$	$55 \pm 5$	$43 \pm 4$

Table 4-2.: The excited state lifetime of the adsorbates.

We can see that the lifetime of the excited state is increased from 23 fs to 55 fs and then decreases to 43 fs which correspond to adsorbate coverages from bare  $\text{Cs}^+$  to 3.5  $\text{D}_2\text{O}$  per  $\text{Cs}^+$  and then to 6.8  $\text{D}_2\text{O}$  per  $\text{Cs}^+$ , respectively. This implies that the water screens the Cs excited state from metal substrate by decoupling its wave function. The calculations of the lifetime of the excited Cs-water cluster state for different adsorbate coverage ratio are under consideration with the support of theory collaborators. However, it is plausible to propose a mechanism analogous to the alkali solvation in bulk. As discussed in section 2.1, Bragg et al. have reported the correlation between excited state lifetime and alkali coordination number for  $\text{Na}^+$  in THF [11]. The charge density of the  $\text{Na}^+$  is attracted by oxygen site of the THF and it distorts as a function of the number of THF attached to the  $\text{Na}^+$ . The excited state lifetime of the  $\text{Na}^+(\text{THF})_N$  changes as N changes from 2 to 5. This is analogous to the observation in Fig. 4-7 (b). The Cs charge density is initially shared by the metal substrate and oxygen site of water in equilibrium. The resonant excitation results the increase in the charge density towards oxygen sites and as a result nonequilibrium molecular responses occur. The response time vary as a function of the number of water molecules attached to the  $\text{Cs}^+$ . In the final stage, the population decays back to the metal substrate through the Cs atoms irrespective of the adsorbate coverage ratio. This suggests that the similar decay trends for 2PPE intensity below 0.1 are originated from identical decay mechanisms for all adsorbate coverages.

## 4.2.2. Localized Nature of the Cs-Water Cluster State on Cu(111)

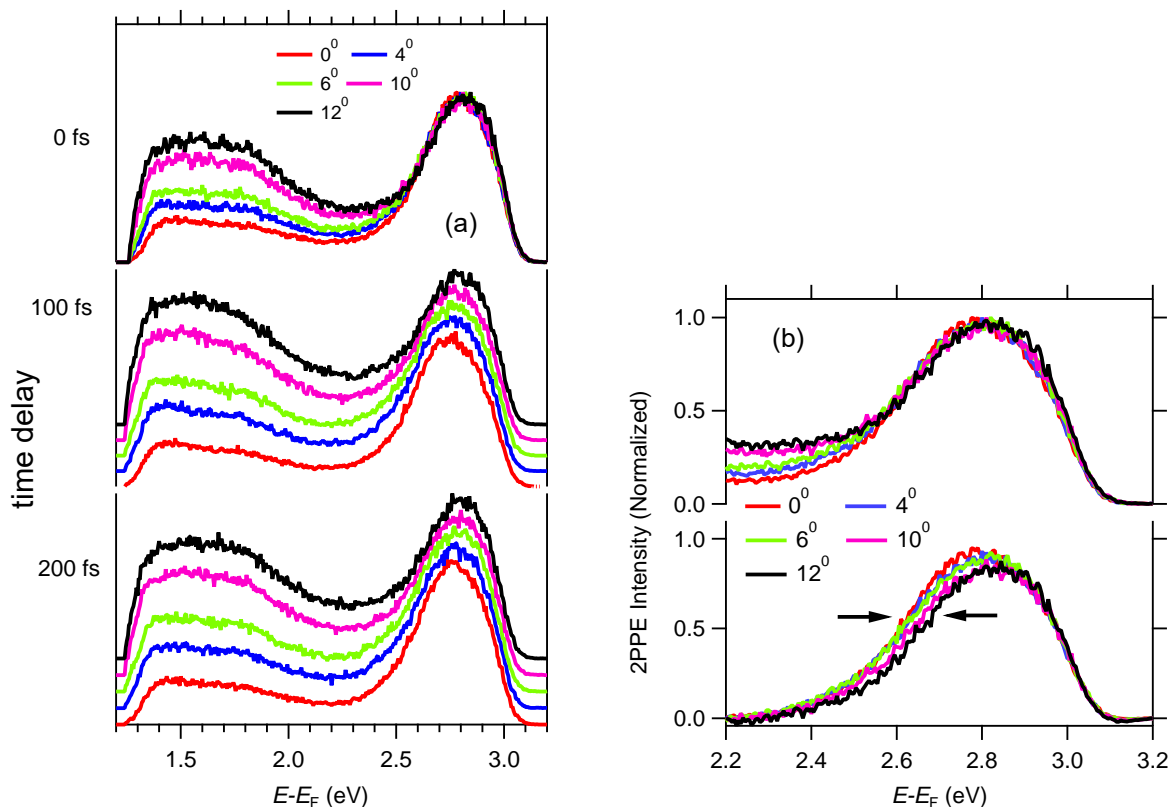


Figure 4-8.: The angle-resolved photoemission spectra of Cs-water clusters on Cu(111) at an adsorbate coverage of 3.4  $D_2O$  per  $Cs^+$ . Panel (a) shows the spectra recorded for photoemission angles from  $0^\circ$  to  $12^\circ$  for a pump-probe delay from 0 fs to 200 fs. The spectra are normalized with respect to state B and plotted without y-offset (zero delay) and with y-offset (100 fs and 200 fs). Panel (b) shows the role of non-uniform background on the energy of the peak. The top panel is plotted without background subtraction of 0 fs delay data and bottom panel is plotted after subtracting a linearly decreasing background in the same energy window from 2.2 eV to 3.2 eV. Due to the asymmetric nature of the peak, the spectral weight of the peak has to be taken into consideration to determine the centre of the peak. The peak energy of the Cs-water cluster has increased by 30 meV and FWHM of the peak has decreased by 50 meV for photoemission angles from  $0^\circ$  to  $12^\circ$ .

The solvated electron or ionic states are ideally localized states as the solvation processes are associated with the confinement of charge by solvent molecules. The localization property of the interfacial state trapped electrons are first reported by Ge et al. where angle-resolved femtosecond 2PPE experiments are performed on n-alkane layers on Ag(111) [108]. The first laser pulse excites electrons from the metal substrate into the unoccupied interfacial states

and a time-delayed second laser pulse ejects the excited state electrons into the vacuum where the kinetic energy of electrons is measured at various angles.

In a set of experiments, D<sub>2</sub>O-Cs clusters are prepared on Cu(111) at a coverage ratio of 3.4 D<sub>2</sub>O per Cs<sup>+</sup> and static 2PPE spectra are recorded for different photoemission angles and for pump-probe time delays from 0 fs to 200 fs with an interval of 50 fs. The angle and time-dependent spectra for the solvated state are shown in Fig. 4-8 (a). The peak corresponding to the state B ( $E-E_F = 2.8$  eV) is normalized for all the angles from 0° to 12°. Consistence with previous observations in Fig. 4-7 (a), the energy of the Cs-water cluster decreases as a function of the time delay. It is apparent from the zero delay data that the background on the low energy region of the peak increases with increase in the photoemission angle. To scrutinize the role of the background signal on the peak energy value, the background of the zero delay data is subtracted as shown in Fig. 4-8 (b). The top panel shows the data with background from 2.2 eV to 3.2 eV and the bottom panel shows the same data after subtracting a linearly decreasing background in the same energy range. The FWHM of the peak has decreased by around 50 meV with increase in the angle of photoemission. Due to the asymmetric nature of the peak, the energy of the peak is determined by considering the spectral weight of the peak. The peak energy of the Cs-water cluster has increased by 30 meV from 1.56 eV to 1.59 eV when the photoemission angle increases from 0° to 12°. This indicates that the solvated state is localized to a larger extend and the slight increase in the peak energy is attributed to the inhomogeneous nature of the adsorbates on Cu(111) and the re-organization of the clusters at 80 K which is observed in STM measurements.

### 4.2.3. Temperature Dependence of the Excited State Dynamics of Clusters

It is well known that ultrathin water layers have amorphous ( $T \leq 110$  K) or crystalline ( $T \geq 140$  K) structures depending on the substrate temperatures [130]. There are several investigations on the properties of solvated electrons in amorphous and crystalline water structures [113,131]. The 2PPE spectroscopy of the amorphous and crystalline structure of ice layers shows a change in the work function by  $\approx 400$  meV due to the phase transition. However, no significant change in the dynamics of the solvated electrons are observed in water on Cu(111) [131]. In contrast, a structural dependence on the dynamics is reported for the solvated electrons in water/Ru(001) [132]. Depending on the temperature of the substrate, the amorphous water cluster can be in the form of a porous or compact structure [113]. As part of the thesis, the temperature dependence of the ultrafast electron dynamics of Cs-water clusters is investigated for understanding the structural dependence of solvents in Cs<sup>+</sup> ion solvation. The Cs ions are chemisorbed at surface temperature of around 200 K and water is co-adsorbed at a surface temperature of 28 K. The LHe supply for cooling is disconnected and allowed the surface to warm-up gradually during the acquisition of the



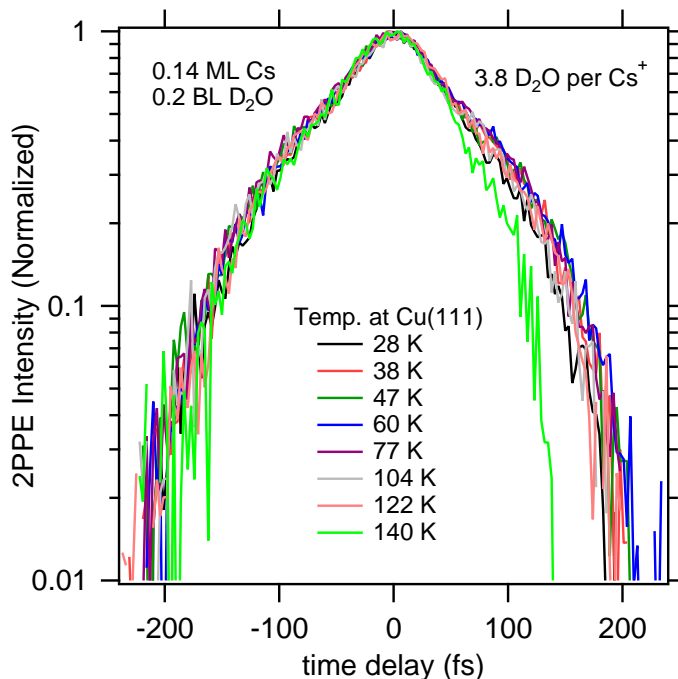


Figure 4-9.: Energy-integrated normalized 2PPE intensity of the excited state for an adsorbate coverage ratio of 3.8 D<sub>2</sub>O per Cs<sup>+</sup> as a function of the pump-probe time delay acquired at different temperatures. The time-resolved 2PPE spectra is recorded continuously for a specific time while allowing the substrate to heat up without any cryogenic support. The temperatures at the starting and the end of the measurements are averaged to obtain the surface temperature for a time-resolved data.

data. The temperatures in the beginning and end of the time-resolved data acquisition (5 scans for each data set) are noted and averaged for estimating the measurement temperature. The average temperature of the Cu(111) substrate is increased from 28 K to 187 K during the measurement. The energy-integrated normalized 2PPE intensity is plotted as a function of time delay for different substrate temperatures as shown in Fig. 4-9. The intensity of the photoemission becomes asymmetric for both positive and negative time delay of a single scan from 140 K and above. It is clear from Fig. 4-9 that the electron dynamics of the excited Cs-water cluster is weakly affected by the structural modification of the water till 122 K. It is reported that ice can form amorphous porous or amorphous compact structures on a surface as a function of the temperature [113].

#### 4.2.4. Influence of Xe Overlayer on the Excited Cs-Water State

Electron solvation is an extensively investigated phenomena and there are controversial reports on the properties of solvated electrons such as locations, binding energy and so on in the bulk water [7–10, 117–121]. In surface science experiments, the structure of the water

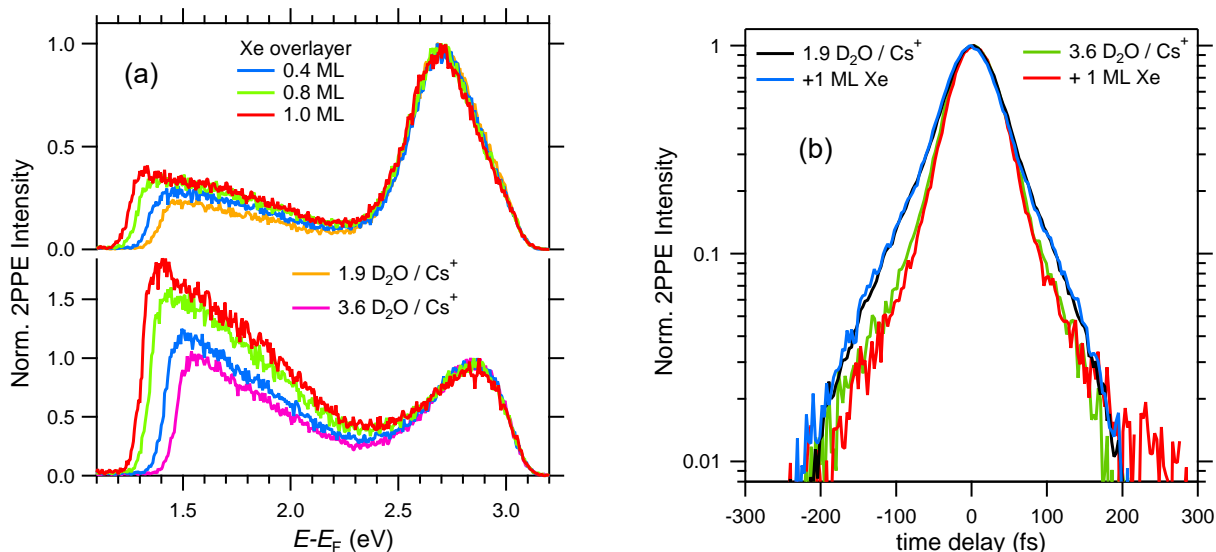


Figure 4-10.: Influence of Xe overlayers on the electronic structure and population dynamics of Cs-water clusters on Cu(111). Panel (a): 2PPE intensity from Cs-water cluster at coverage of 1.9  $D_2O$  per  $Cs^+$  (Top panel - orange trace) and 3.6  $D_2O$  per  $Cs^+$  (Bottom panel - magenta trace) with subsequent adsorption of Xe overlayers at a coverage of 0.4 ML (blue), 0.8 ML (green) and 1.0 ML (red). Panel (b): Comparison of the energy-integrated normalized 2PPE intensity as a function of pump-probe delay for Cs-water clusters of coverage ratio 1.9  $D_2O$  per  $Cs^+$  and 3.6  $D_2O$  per  $Cs^+$  with Xe overlayer and without Xe overlayer. The slight asymmetric appearance of the data with respect to time-zero is due to small difference in the intensity of two laser pulses.

depends on the temperature of the substrate. The water clusters can be in crystalline or compact amorphous or porous amorphous as discussed in the previous section. To understand the location of solvated electrons, Xe is coadsorbed as an overlayer over the ice water clusters to identify the solvation sites [113, 133, 134]. The solvated electrons interact with the Xe since it is highly polarizable and the interaction can be strong or weak depending on the location of solvated electrons. In experiments to identify solvated electrons location for ice clusters, the peak shifts around 400 meV after adsorption of Xe overlayers in both amorphous structures [113]. In layers of ice, the Xe overlayer had no influence on the binding energy and stabilization rate of solvated electrons [133].

In the thesis, Xe overlayer experiments are performed to understand the characteristics of the energy state for ion solvation. The energy change and population dynamics of the Cs-water clusters upon Xe adsorption are investigated in the experiments as shown in Fig. 4-10. Cs-water clusters are prepared at adsorbate coverage ratio of 1.9 and 3.6  $D_2O$  per  $Cs^+$  and Xe is adsorbed over the clusters. The 2PPE spectra are recorded at Xe coverages of 0.4 ML, 0.8 ML and 1 ML as indicated in Fig. 4-10 (a). It is observed that the energy of the

excited Cs-water cluster states at 2.70 eV and 2.85 eV does not change as a function of Xe coverages. However, the work function of the surface decreases with increase in Xe coverages (observed as the shift in the low-energy cut off of the spectra). In addition, time-resolved pump-probe experiments are performed with and without Xe overlayer on Cs-water clusters at a coverage ratio of 1.9 and 3.6 D<sub>2</sub>O per Cs<sup>+</sup> as shown in Fig. 4-10 (b). It is clear that the population dynamics of the Cs-water clusters is not significantly affected by the adsorption of Xe overlayer. This is attributed to the fact that water-water or Cs-water interactions in the cluster is stronger than the interaction of Xe with the cluster. The decrease in the work function of the surface upon the adsorption of Xe overlayer also suggests that Xe is interacting mainly with the metal substrate than the Cs-water cluster.

### 4.3. Conclusion

The efforts to understand the electronic structure of the interaction between alkali and water on Cu(111) has begun more than a decade ago [4, 15, 169]. The formation of water-induced alkali state (state B) was interpreted initially assigned to an alkali-water hybrid structure [4, 169]. Very recently, DFT calculations of the alkali (Na, K, Cs)-water structures on Cu(111) are reported based on the previous 2PPE experimental results [43]. Although this work considered a completely different alkali-water structure with different coordination number for the alkali ion, it explains the increase in the energy of the state A with water coverage satisfactorily. However, this work interprets the origin of the state B as a result of detachment of alkali from Cu surface upon complete hydration. As part of this thesis work, interaction of alkali-water on Cu(111) are investigated extensively for different coverages of Cs<sup>+</sup> ions and D<sub>2</sub>O. The evolution of the energy states A and B are analysed systematically to understand their properties. The STM experiments by collaborators has revealed an unusual solvation pattern of alkali on surface where they preferably situated at the periphery of the water clusters. The STM results also explains the simultaneous occurrence of states A and B in 2PPE experiments. Furthermore, DFT calculations performed by our collaborators support the observations in both 2PPE and STM. The calculations show that (1) the increase in the energy of the state A with water coverage, (2) the origin of the new state as a result of novel solvation pattern, and (3) the preference of Cs<sup>+</sup> ions to reside at the periphery of the water clusters. The 2PPE, STM and DFT have synergistically explained the intricacies associated with alkali solvation on a metal surface.

Investigation of ultrafast electron dynamics of alkali-solvent systems are key to understand several fundamental processes in nature and also for designing energy storage devices where solvation-desolvation of alkalis at interfaces are crucial. In time-resolved 2PPE experiments, the energy transfer and population dynamics of Cs-water clusters for various adsorbate coverages are investigated systematically. The energy transfer from solute to solvent increases substantially upon solvation of water and our results show that at low adsorbate coverages, the energy transfer is higher than that of higher adsorbate coverages. This is attributed to

the fact that the water molecules are less-rigid at lower coverages than at higher coverages that dissipates its energy by molecular level responses. At normalized 2PPE intensity above 0.1, the decay time increases from 23 fs to 55 fs and then decreases to 43 fs for an adsorbate coverage from zero to 3.5 D<sub>2</sub>O per Cs<sup>+</sup> and 6.8 D<sub>2</sub>O per Cs<sup>+</sup>, respectively. In contrast, the decay time does not vary significantly as a function of adsorbate coverage in the normalized 2PPE intensity below 0.1. We plan to perform theoretical studies to understand the coverage-dependent dynamics of the adsorbates to gain more insights on the coverage dependent dynamics of the adsorbate.

To characterize the features of the excited Cs-water cluster (state B), experiments are performed for angle-resolved photoemission, temperature dependence and Xe overlayers. The analysis of the angle-resolved data shows that the peak energy increases by 30 meV and FWHM decreases by 50 meV for the state B when the photoemission angle increases from 0° to 12°. This is due to the inhomogenous nature of the surface and also increased mobility at the measurement temperature. The investigation on the temperature dependence of the ultrafast dynamics show that the dynamics is not affected significantly as a function of temperature. As part of the thesis work, experiments are performed to understand the response of the state B of the Cs-water clusters with Xe overlayer. It is found that the work function of the surface decreases with Xe coverage and there is no noticeable shift in the energy of the state B. This decrease in work function is due to the interaction of Xe with the Cu(111). Furthermore, the population dynamics of the state B is not affected significantly by the Xe overlayer.

# 5. Unveiling the Solvation in Alkali-Noble Gas Adsorbates at Interfaces

This chapter presents the interaction of  $\text{Cs}^+$  and Xe - an exemplary system - at the Cu(111) surface. The solvation of alkali in non-polar solvents is one of the barely researched areas and it provides valuable information on the nature of fundamental forces - Coulomb and van der Waals - prevailing during the solvation. The section 1.1 presents the surface electronic structure of the adsorbates during the evolution of Xe- $\text{Cs}^+$  aggregates on Cu(111). The section 1.2 discusses the ultrafast electron dynamics of the excited alkali state in the aggregates and associated energy transfer due to the transient polarization of the electron cloud of Xe atoms. The comparison of the potential energy surfaces (PES) of  $\text{Cs}^+$ /Cu(111) in presence and absence of Xe is also presented in this section. The section 1.3 discusses the STM investigation on the morphology of Xe- $\text{Cs}^+$  aggregates on Cu(111) by the research group of Karina Morgenstern, Ruhr University of Bochum. The stability of the aggregates and the nature of the interaction are studied by performing coupled cluster calculations and charge density difference analysis by the research group of Dominic Marx, Ruhr University of Bochum and are presented in section 1.4. Finally, the section 1.5 discusses the results of the experiments for adopting Xe double layer as an intermediate layer to negate the substrate effects.

## 5.1. Probing the Evolution of Xe- $\text{Cs}^+$ Aggregates on Cu(111)

In order to understand the interaction between  $\text{Cs}^+$  ions and Xe atoms, the 2PPE spectra of the  $\text{Cs}^+$ /Cu(111) are recorded while adsorbing Xe on the surface and are shown in Fig. 5-1. The schematic of the static 2PPE process is shown in the right panel where the first photon excites an electron to the unoccupied Cs 6s state from the Cu(111) and a second photon emits that electron simultaneously. The kinetic energy of the photoemitted electrons are analysed in a TOF spectrometer. In one-colour 2PPE, the work function of the surface  $\Phi$  is given by the difference between twice the photon energy and the width of the 2PPE spectrum  $\Delta E$  which is the difference between high-energy and low-energy cut off.

The high-energy cut off is determined by the photon energy  $2h\nu$  plus  $E_F$  and is independent of the changes on the surface. The electrons at the low-energy cut off ( $E_s$ ) which have energies just to overcome the work function of the surface and  $E_s$  varies in response to the changes on the surface. Mathematically, the work function can be expressed as,

$$\Phi = 2h\nu - \Delta E = 2h\nu - (E_F - E_s). \quad (5-1)$$

Hence, the change in work function while adsorbing Xe is manifested as the change in the low energy cut off of the 2PPE spectra.

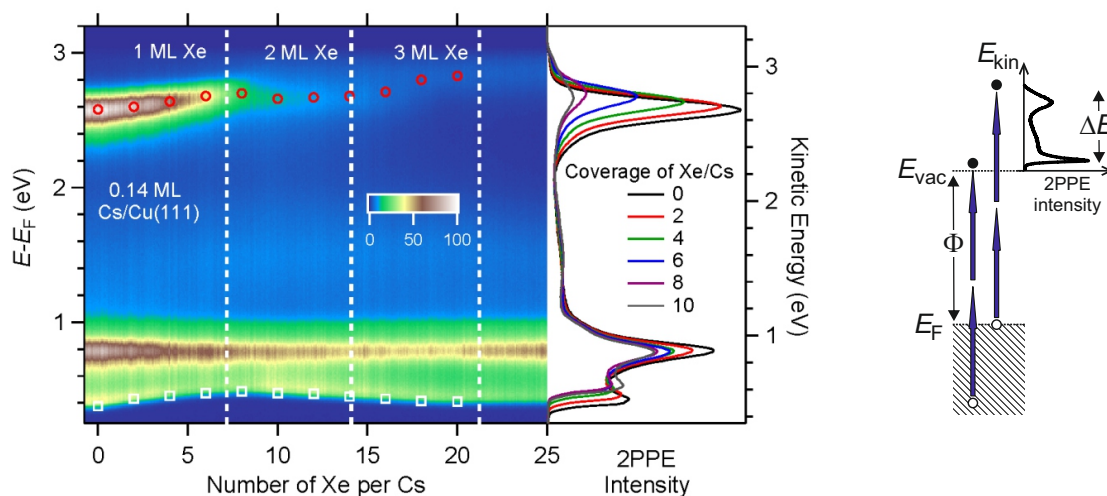


Figure 5-1.: False colour representation of the 2PPE intensity for 0.14 ML  $\text{Cs}^+/\text{Cu}(111)$  as a function of the intermediate state energy and Xe coverage per Cs (left panel) and spectra at specific Xe per Cs coverages (centre panel). The coverage values for first, second, and third Xe ML are indicated with vertical white dashed lines in the left panel. The coverage ratio of Xe to Cs is given as the number of Xe per Cs in the abscissa. The peaks at  $E - E_F = 2.58$  eV and  $E - E_F = 0.80$  eV originate from the Cs 6s state and Cu 3d band, respectively. The scheme of the one-colour static 2PPE spectroscopy measurements is shown in the right panel where the first photon excites an electron to an intermediate state and subsequently a second photon photoemits that electron. The kinetic energy of the photoemitted electrons are measured in a time-of-flight spectrometer. The experiments are performed with a photon energy of 3.1 eV and temperature at  $T = 30$  K. Reprinted figure with permission from Thomas, J. et al. Competition between Coulomb and van der Waals Interactions in Xe- $\text{Cs}^+$  Aggregates on Cu(111) Surfaces. *Phys. Rev. Lett.*, 127:266802, (2021). DOI: <https://doi.org/10.1103/PhysRevLett.127.266802>. Copyright © 2021 by the American Physical Society. Ref. [44].

The  $\text{Cs}^+$  ions are chemisorbed on freshly prepared Cu(111) from a commercial Cs getter source (SAES getters) at a temperature  $T = 200$  K. As a result, the work function of the

surface is reduced due to the formation of surface dipoles. Subsequently, Xe is physisorbed onto the surface at a background pressure of  $1 \times 10^{-8}$  mbar and temperature  $T = 30$  K. The coverage of the Cs<sup>+</sup> ions and Xe are determined according to [168] and [110], respectively, and a detailed discussion on coverage determination can be found in chapter 3. The false colour 2PPE intensity from 0.14 ML Cs<sup>+</sup>/Cu(111) as a function of intermediate state energy  $E-E_F$  eV (left axis) and Xe coverages (bottom) is shown in the left panel of Fig. 5-1. The Xe coverage in terms of ‘number of Xe per Cs’ is determined by calculating the ratio of the coverages (note that this is the average coverage of the adsorbate over a probing region which is the focal spot size of the laser beam that spans a few tens of microns. The surface has inhomogeneous distribution of adsorbates). The coverage in terms of Xe layers are marked with vertical white dashed lines. The spectra at specific Xe coverages are shown in the centre panel of the Fig. 5-1. The peak at  $E-E_F=2.58$  eV originates from Cs 6s state and it increases by 120 meV up to 1 ML of Xe and then remains nearly constant for higher coverages. Also, the 2PPE intensity of the Cs 6s state decreases as a function of the Xe coverage. The peak at  $E-E_F=0.80$  eV originates from the Cu *3d* band and it does not change as a function of the Xe coverage. The change in the work function of the surface is analogous to the change in the low energy cut off of the photoemission spectra which are marked as white squares in the left panel of Fig. 5-1. The work function of the surface increases by 100 meV up to a coverage  $\Theta=(1.0 \pm 0.2)$  ML and it decreases for higher coverages.

To understand the nature of interaction between the Cs<sup>+</sup> ions and the Xe atoms, the change in work function and the binding energy of the Cs 6s state are analysed as a function of the Xe coverage and is shown in Fig. 5-2. The increase in work function by 100 meV at sub-ML Xe coverage is due to the screening of the Cs<sup>+</sup> ions by Xe and the corresponding modification of the surface dipole. The binding energy with respect to  $E_{vac}$  for the Cs 6s state does not change significantly in the coverage of  $\Theta < (1.5 \pm 0.2)$  ML and it decreases for  $\Theta > (2.0 \pm 0.2)$  ML. It is shown in Fig. 5-1 that the energy of the Cs 6s state  $E-E_F$  increases up to Xe coverage of  $\Theta = (1.0 \pm 0.2)$  ML which is due to the decrease in binding of the Cs to Cu(111) upon the electron transfer. As shown in the Fig. 5-2, both energies have different trends up to  $\Theta = (1.0 \pm 0.2)$  ML and the Cs 6s state is bound more to the metal substrate. But, both energies decrease for higher coverages which indicate the repulsion of the electron wave function ( $\Psi_{6s}$ ) from the substrate as a result of the interaction of the Xe with Cs<sup>+</sup>/Cu(111). The temporal evolution of the  $\Psi_{6s}$  at ultrafast time-scale in Xe-Cs<sup>+</sup> aggregates is discussed in the section 5.2.

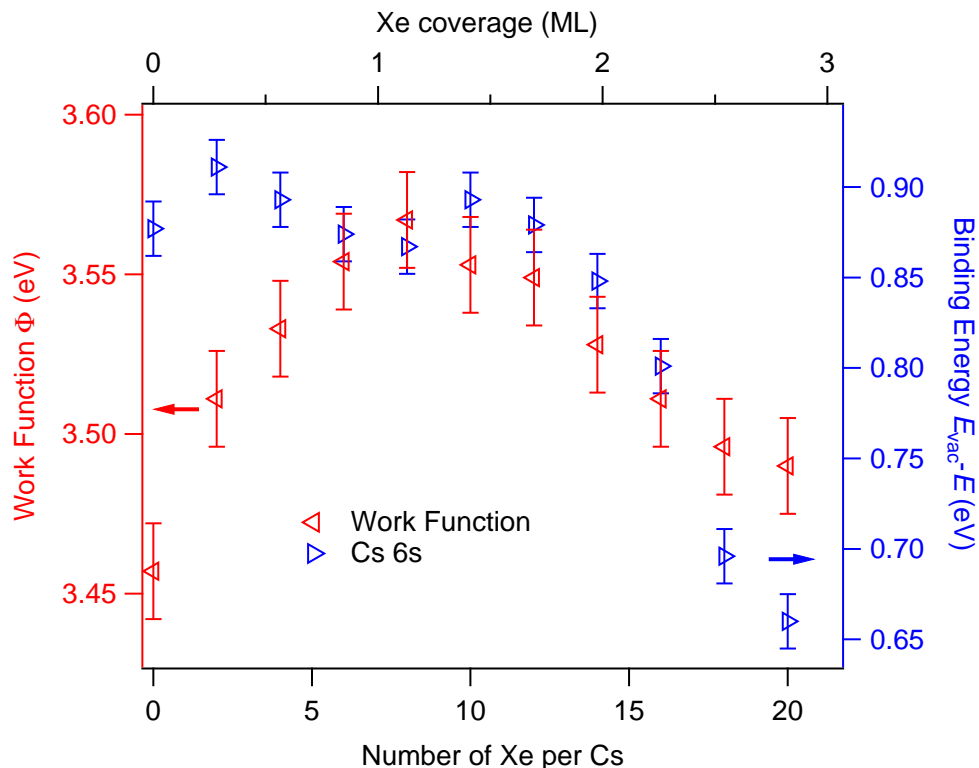


Figure 5-2.: The work function (left axis) and the binding energy with respect to vacuum level of Cs 6s state (right axis) for Cs<sup>+</sup>/Cu(111) are plotted as a function of the coverage ratio, Xe per Cs (bottom axis) and Xe in ML (top axis). Reprinted figure with permission from Thomas, J. et al. Competition between Coulomb and van der Waals Interactions in Xe-Cs<sup>+</sup> Aggregates on Cu(111) Surfaces. *Phys. Rev. Lett.*, 127:266802, (2021). DOI: <https://doi.org/10.1103/PhysRevLett.127.266802>. Copyright © 2021 by the American Physical Society. Ref. [44].

Furthermore, coadsorption of Xe atoms on Cs<sup>+</sup>/Cu(111) is performed for several  $\Theta_{Cs}$  and the analysis of the change in the Cs 6s state ( $E - E_F$ ) as a function of Xe coverage is shown for a few representative data in Fig. 5-3 (a). Consistent with previous works, the energy of the Cs 6s state decreases with increase in Cs coverage [2, 140] and also the work function of the surface (not shown here) decreases with increase in Cs coverage up to 0.2 ML [168, 169]. The energy of the Cs 6s state, marked with solid circles, increases linearly with Xe coverages for all  $\Theta_{Cs}$  and is fitted with a linear function (solid line). The change in the Cs 6s state energy per Xe is larger for higher value of  $\Theta_{Cs}$  than lower  $\Theta_{Cs}$ . The change in Cs 6s energy per Xe which is the slope of the linear fit function is plotted as a function of the coverage of Cs<sup>+</sup> ions as shown in Fig. 5-3 (b). It is observed that up to  $\Theta_{Cs}$  of 0.11 ML,  $\Delta E$  per Xe for the Cs 6s state is almost independent of the  $\Theta_{Cs}$ . But, it increases linearly above 0.11 ML Cs<sup>+</sup> which implies that the interaction of Cs<sup>+</sup> ions and Xe atoms becomes more pronounced at higher Cs coverages where the repulsion between Cs<sup>+</sup> ions are significant. This increase in the  $\Delta E$



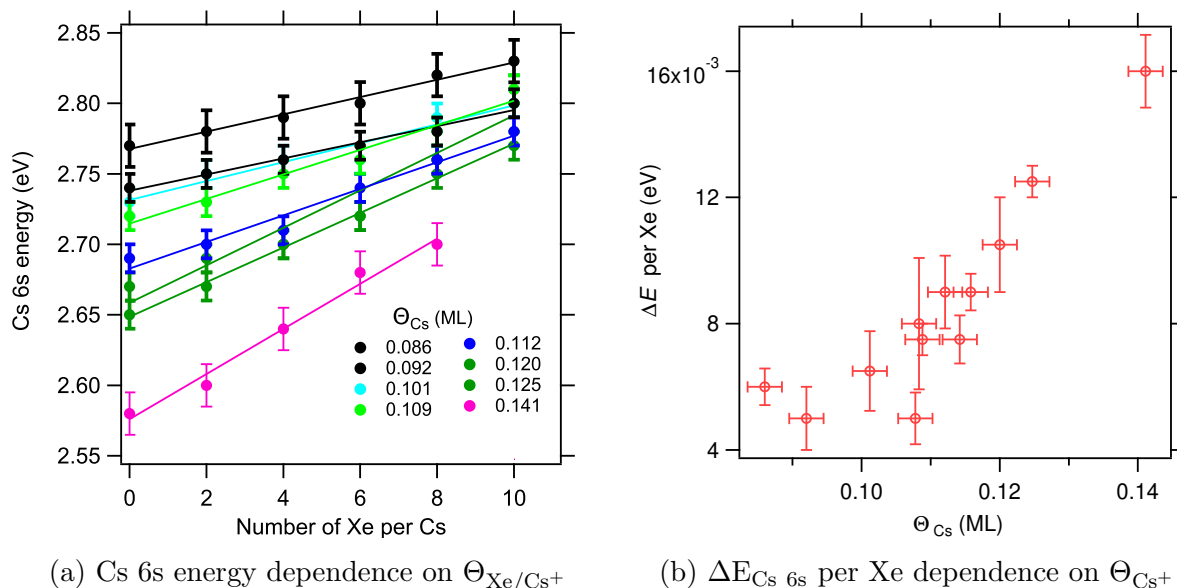


Figure 5-3.: (a) The energy of the Cs 6s state as a function of the coverage ratio,  $\Theta_{\text{Xe}/\text{Cs}^+}$  (solid circles) and the linear fit of the data (solid lines). Note that the slope of the lines increases with the coverage of Cs<sup>+</sup>. (b) The slope of the fits i.e.  $\Delta E$  of Cs 6s per Xe/Cs<sup>+</sup> is plotted as a function of  $\Theta_{\text{Cs}^+}$ . The energy does not change for the Cs<sup>+</sup> coverage below 0.11 ML and increases linearly for higher coverages. This is pointing towards a prominent role of Coulomb interaction at higher coverages.

per Xe for Cs 6s state at higher Cs coverages is commensurate to the increase in the work function of the surface upon adsorption of Xe as discussed in the context of Fig. 5-2 where a transition of the energy reference from the Fermi level to the vacuum energy is observed.

## 5.2. Ultrafast Dynamics of Xe-Cs<sup>+</sup> Aggregates on Cu(111)

The chemisorbed Cs<sup>+</sup>/Cu(111) surface serves as a model system for understanding the electron dynamics of excited states of the alkalis on metal surface [1, 3, 107]. The dynamics in the alkali is initiated by resonant excitation of an electron from the metal substrate to the unoccupied alkali state by the pump pulse which transiently populates the excited state. The energy transfer to the solvent via molecular re-organization or electronic polarization occurs when the excited state relaxes to the ground state. The dynamics of the system is analysed by photoemission from the excited state using a probe pulse. In this section, the results of the excited state dynamics of Cs<sup>+</sup>/Cu(111) in presence of a non-polar solvent Xe are discussed. The lifetime and energy stabilization of the excited Cs 6s state are evaluated and subsequently the potential energy surface as a function of the distance between the ion core to the Cu substrate on Cs<sup>+</sup>/Cu(111) is determined before and after the adsorption of Xe atoms.

### 5.2.1. Energy Stabilization and Population Dynamics

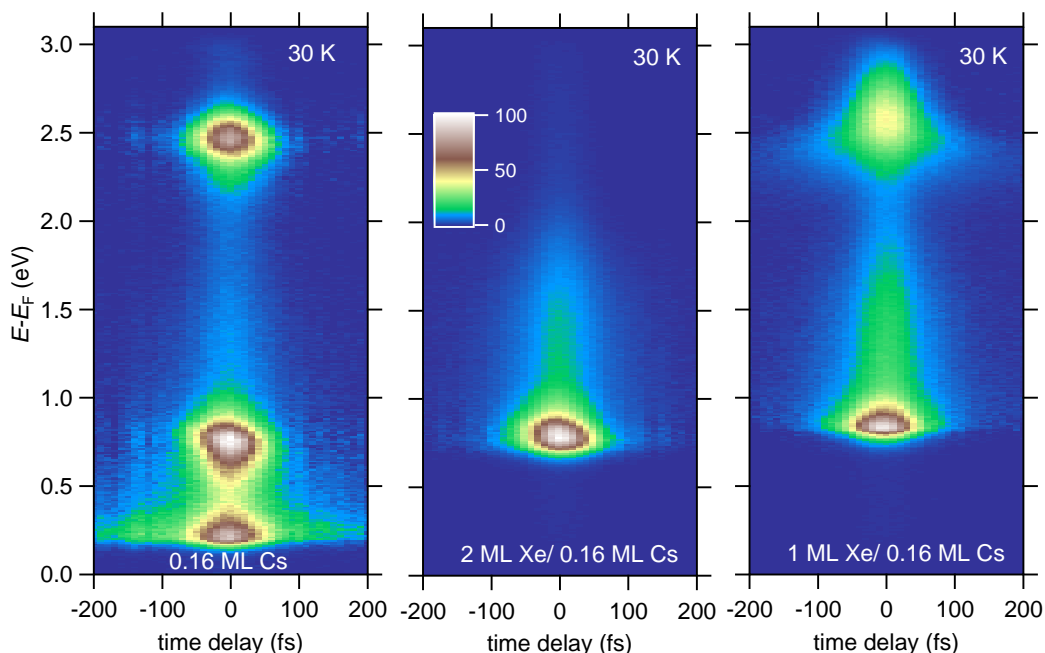


Figure 5-4.: Time-resolved 2PPE intensity in false colour as a function of intermediate energy  $E-E_F$  and time delay for (Left) 0.16 ML  $\text{Cs}^+/\text{Cu}(111)$ , (Centre) 2 ML Xe on 0.16 ML  $\text{Cs}^+/\text{Cu}(111)$  and (Right) 1 ML Xe on 0.16 ML  $\text{Cs}^+/\text{Cu}(111)$ . The measurements are performed in the autocorrelation with photon energy of 3.1 eV. Well-ordered layers of Xe are prepared according to [110].

To understand the interaction of Xe atoms with  $\text{Cs}^+$  ions at the interface, well-ordered layers of Xe are adsorbed on  $\text{Cs}^+/\text{Cu}(111)$  and time-resolved 2PPE spectra are recorded at different adsorbate coverages as shown in Fig. 5-4. The  $\text{Cs}^+$  ions are chemisorbed on  $\text{Cu}(111)$  at  $T = 200\text{ K}$  and subsequently cooled to  $T = 30\text{ K}$  for recording the time-resolved 2PPE spectra as shown in the left panel of Fig. 5-4. The peak at  $E-E_F = 2.46\text{ eV}$  and  $E-E_F = 0.75\text{ eV}$  are originating from the Cs 6s state and Cu 3d band, respectively. The peak at  $E-E_F = 0.23\text{ eV}$  arises from the secondary electrons which have energies just to overcome the work function of the surface. Since the Xe multilayers show distinguishable desorption peaks in TPD, desorption/adsorption and annealing of Xe layers at specific temperature result in the formation of well-ordered layers. The Xe layers are prepared with the assistance of the TPD technique as discussed in [110]. The centre panel of the Fig. 5-4 shows the time-resolved 2PPE spectra of 2 ML Xe on  $\text{Cs}^+/\text{Cu}(111)$  where only the Cu 3d band is prominent. The right panel of the Fig. 5-4 shows the time-resolved 2PPE spectra of 1 ML Xe on  $\text{Cs}^+/\text{Cu}(111)$  which is prepared by the desorption of the second monolayer. The peak at  $E-E_F = 2.55\text{ eV}$  originates from the Cs 6s state of the Xe- $\text{Cs}^+$  aggregates. In a nutshell, the evolution of

the electronic structure of Cs<sup>+</sup>/Cu(111) as a function of Xe layers is shown in Fig. 5-4 from the left panel to the right panel where the work function of the surface has increased upon adsorption of Xe and the appearance (disappearance) of an upshifted Cs 6s peak at  $\sim 1$  ML (at 2 ML) is also observed. Furthermore, the lifetime and energy stabilization of the Cs 6s state are significantly larger after the adsorption of Xe layers than that of bare Cs<sup>+</sup>/Cu(111). A quantitative analysis of this excited Cs 6s state in the Xe-Cs<sup>+</sup> aggregate is discussed in detail as follows.

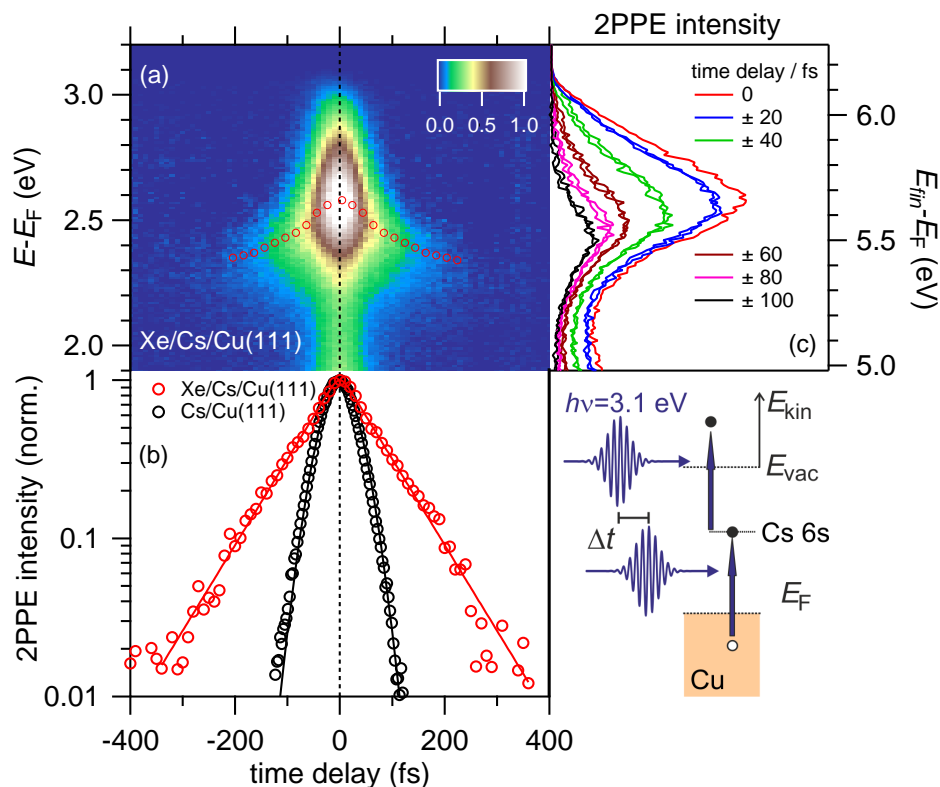


Figure 5-5.: Time-resolved 2PPE intensity (a) in false colour as a function of intermediate energy (left), final state energy (right) and time delay for 1 ML Xe on 0.16 ML Cs/Cu(111), (b) comparison of bare Cs/Cu(111) (black circles) and 1 ML Xe on Cs/Cu(111) (red circles) and (c) spectra at specific time delays. Reprinted figure with permission from Thomas, J. et al. Competition between Coulomb and van der Waals Interactions in Xe-Cs<sup>+</sup> Aggregates on Cu(111) Surfaces. *Phys. Rev. Lett.*, 127:266802, (2021). DOI: <https://doi.org/10.1103/PhysRevLett.127.266802>. Copyright © 2021 by the American Physical Society. Ref. [44].

To remind the reader, the time-resolved 2PPE experiment is shown schematically in the inset of Fig. 5-5. The pump pulse resonantly excites an electron to the unoccupied Cs 6s state and a time-delayed probe pulse photoemits electrons from the intermediate state. The energy of the photoemitted electrons are analyzed by a time-of-flight spectrometer as a function of

pump-probe time delay. The time-resolved 2PPE autocorrelation intensity measurement of 0.16 ML Cs<sup>+</sup>/Cu(111) with 1 ML Xe overlayer is shown in Fig. 5-5 (a) and the spectra at specific time delays are shown in the panel (c). Consistent with the observation in Fig. 5-1 that the energy of the Cs 6s state increases as a function of the Xe coverage up to 1 ML, the energy of the Cs 6s state in the Xe - Cs<sup>+</sup> aggregates occurs at  $E-E_F = 2.6$  eV at time-zero and relaxes to lower energy as a function of the pump-probe time delay due to the propagation of the nuclear wave packet [3]. It is observed that the Xe has dual impact on the excited state of the Cs 6s antibonding orbital i.e. on the population dynamics and energy transfer dynamics.

First, the lifetime  $\tau$  of the excited Cs 6s state increases to 80 fs on the Xe-covered surface compared to 13 fs for bare Cs<sup>+</sup> ions on Cu(111) as shown in Fig. 5-5 (b). This substantial increase in  $\tau$  indicates a significant reduction in the overlap of the  $\Psi_{6s}$  wave function with Cu(111) surface state [106]. Note that the convolution of a single exponential decay and Gaussian is used for fitting the time-resolved experiments in this thesis. However, the optical Bloch equations model which takes account of both elastic and inelastic contributions to the lifetime is reported earlier [1,106]. Hence, the determination of lifetime is numerically smaller in this thesis than in previous reports. The enhancement in the lifetime upon adsorption of Xe is attributed to the repulsion of the Cs wave function  $\Psi_{6s}$  from the substrate by the electron cloud of the Xe atoms. Similar effects have been reported earlier for the image potential states of metal surfaces which are attracted/repelled from the surface depending on the electron affinity of the fully covered adsorbate gases [109–111]. However, in the context of this work, electrons are excited to a localized alkali state which is solvated by Xe atoms. Secondly, the change in the energy of the excited Cs 6s state as a function of pump-probe delay provides insights into the energy transfer dynamics which is shown as red circles in Fig. 5-5 (a). As discussed in the Chapter 2, a Marcus type solvation picture is helpful to understand the electron transfer processes in the solvation processes. The excitation to neutral alkali state and the subsequent relaxation of the Cs 6s state transfers energy to the solvent medium. The energy transfer has different influences depending on the nature of solvents. It can be molecular vibrations, librational motions, or reorganization in the case of polar molecules. The non-polar atomic solvent like Xe respond to charge transfer by transient polarization effects in its electron cloud which are in the vicinity of Cs<sup>+</sup> ions. The energy transfer dynamics also depends on the type of the alkali chemisorbed on the metal. Meyer et al. have reported different energy stabilization dynamics for Na, K, and Cs [4]. This is further confirmed in a recent theoretical work where Paz et al. have shown that the partial charge distribution of the alkali/Cu(111) is different for Na than K and Cs [43] and that it influences the charge transfer dynamics at the interfaces. Hence, the polarization effects on the Xe atoms due to the energy transfer in the alkali/metal interface is influenced by the type of alkali. To understand the influence of Xe on the excited state Cs 6s state, the potential energy surface (PES) of Cs<sup>+</sup>/Cu(111) in the absence and presence of Xe is simulated according to [3] and is discussed in the next section.

## 5.2.2. Determination of the Potential Energy Surface

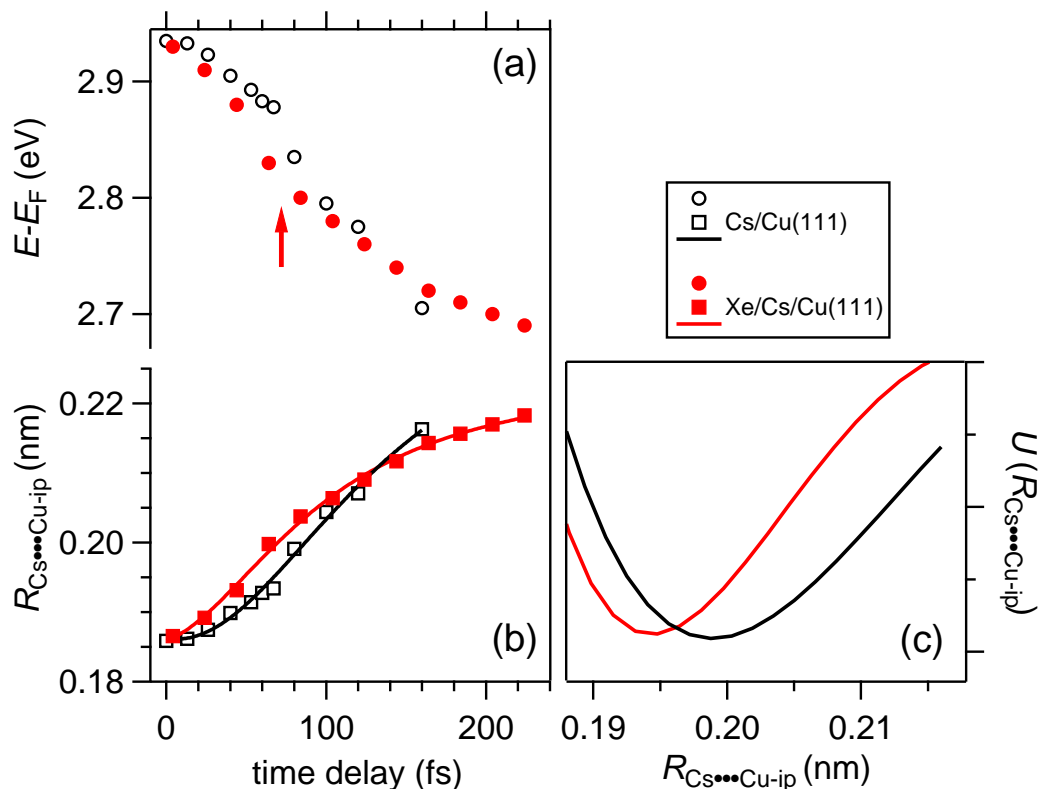


Figure 5-6.: In panel (a) the time-dependent intermediate state energy is plotted for Xe/Cs<sup>+</sup>/Cu(111) as reported in Fig. 5-5 and for bare Cs<sup>+</sup>/Cu(111) using data from [3]. The respective distances  $R_{\text{Cs}\dots\text{Cu-ip}}$  and the ground state potential energy surface  $U(R_{\text{Cs}\dots\text{Cu-ip}})$  are determined with and without coadsorbed Xe, indicated in red and black, see panels b and c, respectively. Note that there is no accurate information regarding the absolute energy difference between the two potentials in (c). Reprinted figure with permission from Thomas, J. et al. Competition between Coulomb and van der Waals Interactions in Xe-Cs<sup>+</sup> Aggregates on Cu(111) Surfaces. *Phys. Rev. Lett.*, 127:266802, (2021). DOI: <https://doi.org/10.1103/PhysRevLett.127.266802>. Copyright © 2021 by the American Physical Society. Ref. [44].

The ground state (ionic state) energy of the alkali valence  $s$  orbital state as a function of the distance  $R_{\text{Cs}\dots\text{Cu-ip}}$  from the substrate is evaluated in a previous study [105] and the method of determination of the excited state (neutral) of an alkali on metal is discussed in several works [179, 180]. Petek et al. have implemented these methods to determine the potential energy surface of the excited and ground state of Cs<sup>+</sup>/Cu(111) in a later work [3]. Similar methodology is adopted in our recent study to calculate the ground state potential in the presence of Xe atoms [44]. The comparison of the change in the ground Cs 6s

state energy as a function of the pump-probe time delay for Cs<sup>+</sup>/Cu(111) and Xe covered Cs<sup>+</sup>/Cu(111) are shown in Fig. 5-6 (a). The transient energy gain of around 0.24 eV is found in both cases and the energy stabilization rate is different for both cases. The conversion of the ground state energy to the distance between the Cs<sup>+</sup> and the image plane of the Cu(111) ( $R_{Cs...Cu-ip}$ ) has been performed as discussed elsewhere [3, 105] and is plotted as a function of pump-probe delay in Fig. 5-6 (b) where the data is fitted with an analytical function. We have made an assumption that the energy to distance  $R_{Cs...Cu-ip}$  conversion is the same for both systems because Xe has no major effect on the Cs 6s state energy. The Xe/Cs<sup>+</sup>/Cu(111) data shows an inflection point at  $\Delta t = 70$  fs (see the red arrow in panel (a)) and is not prominent for Cs<sup>+</sup>/Cu(111) surface. Again the inflection point is appearing for the Xe/Cs/Cu(111) data in panel (b) for higher time delays. The analytical function for the fit in Fig. 5-6 (b) is differentiated twice to obtain the acceleration of the Cs<sup>+</sup> ion core as  $a = \frac{\partial R^2}{\partial t^2}$ . Using the acceleration, one can obtain the force acting on the Cs<sup>+</sup> ion core  $F = ma$ , which is further integrated as a function of the  $R_{Cs...Cu-ip}$  to obtain the ground state potential as  $U(R_{Cs...Cu-ip}) = -\int F \cdot dR_{Cs...Cu-ip}$ . The simulated potential energy surface for Cs<sup>+</sup>/Cu(111) with and without Xe overlayer is shown in Fig. 5-6 (c). The minimum of the potential  $U$  along the surface normal shifts by 4.0 pm toward the Cu(111) after the adsorption of the Xe. Furthermore, the confidence interval analysis of the potential energy curve is calculated which shows that the minima are not overlapping and hence, the shift of the PES is not within the error of the fitting. The method adopted for the calculation of confidence interval analysis is presented in the Appendix C. It is realistic that the adsorption of Xe on Cs<sup>+</sup>/Cu(111) compensates for the repulsive interaction between neighbouring Cs<sup>+</sup> and promotes the binding of the Cs<sup>+</sup> ions along the surface normal. To understand the morphology of Xe-Cs<sup>+</sup> aggregates at different adsorbate coverages and the fundamental interactions between adsorbates and their interactions with the substrate, complementary STM investigations and coupled cluster calculations are performed by our collaborators and are discussed in the following sections.

### 5.3. Morphology of the Xe-Cs<sup>+</sup> Aggregates

This section presents the STM experiments initially performed by C. Bertram and additional measurements by J. Patwari and I. Langguth at the research laboratory of Karina Morgenstern, Ruhr University Bochum. The 2PPE experiments study the properties of the aggregates over a probing region of  $\sim 40$   $\mu\text{m}$  and Cs atoms in the aggregate are in the excited state (neutral charge). The 2PPE experiments do not provide enough photoemission signal when the  $\Theta_{Cs} < 0.01$  ML. On the other hand, the STM probes the morphology of the aggregates at atomic resolution and the Cs atoms are in the ground state (charged state). A discussion on the morphology of Xe-Cs<sup>+</sup> aggregates is adopted in this thesis from a joint publication to provide the link between electronic structure and morphology of the aggregates which gives a comprehensive picture of the alkali-noble gas interactions [44].

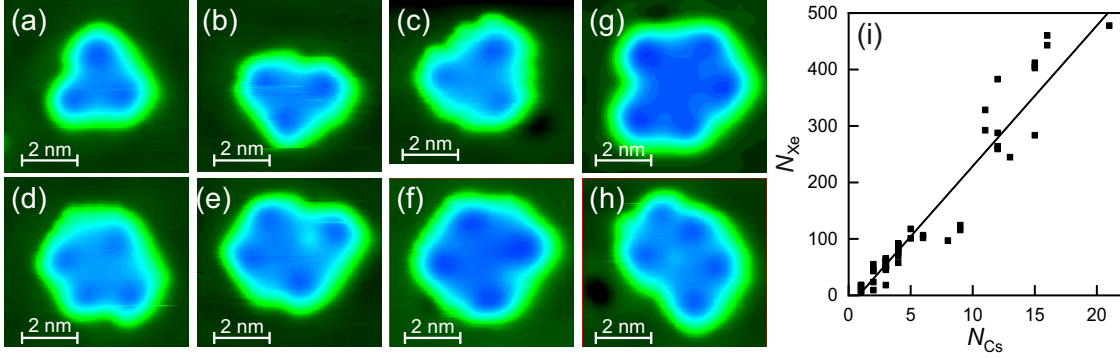


Figure 5-7.: Xe-Cs<sup>+</sup> aggregates with different number of Cs<sup>+</sup> on false color scale; (a-c) 3 Cs<sup>+</sup>; (d-f) 4 Cs<sup>+</sup>; (g,h) 5 Cs<sup>+</sup>; ( tunneling parameters: 10 pA, -500 mV). The number of Xe atoms and ratio of numbers Xe to Cs<sup>+</sup> in these aggregates are (a) 52 Xe, 17 Xe/Cs<sup>+</sup>; (b) 54 Xe, 18 Xe/Cs<sup>+</sup>; (c) 69 Xe, 23 Xe/Cs<sup>+</sup>; (d) 75 Xe, 19 Xe/Cs<sup>+</sup>; (e) 84 Xe, 21 Xe/Cs<sup>+</sup>; (f) 90 Xe, 23 Xe/Cs<sup>+</sup>; (g) 100 Xe, 20 Xe/Cs<sup>+</sup>; (h) 94 Xe, 19 Xe/Cs<sup>+</sup>. Panel (i) provides an overview of the numbers of Xe atoms  $N_{Xe}$  and Cs<sup>+</sup> ions  $N_{Cs}$  in the analyzed aggregates. Reprinted figure with permission from Thomas, J. et al. Competition between Coulomb and van der Waals Interactions in Xe-Cs<sup>+</sup> Aggregates on Cu(111) Surfaces. *Phys. Rev. Lett.*, 127:266802, (2021). DOI: <https://doi.org/10.1103/PhysRevLett.127.266802>. Copyright © 2021 by the American Physical Society. Ref. [44].

The Cu(111) surfaces are prepared by sputter-anneal cycles and subsequently Cs<sup>+</sup> are deposited from a commercial Cs dispenser at  $T = 200$  K and Xe deposition at  $T = 8$  K. The Xe-Cs<sup>+</sup> aggregates on Cu(111) for a wide range of adsorbate coverages are investigated as shown in Fig. 5-7 (a-h) and Fig. 5-8 (a-e). For lower coverages, all Cs<sup>+</sup> (dark blue circles) are situated at the periphery of the aggregates for smaller aggregates as shown in Fig. 5-7 (a-h). These aggregates do not show any specific orientation on the Cu(111). For the case of three Cs<sup>+</sup> per aggregate (panel a-c), ions are placed equidistantly in the aggregate. However, aggregates form a random shapes while increasing the coverages of the adsorbates. The relative number of the Xe and Cs<sup>+</sup> in the analysed STM images are shown in Fig. 5-7 (i). Understanding the morphology of the large aggregates is important because of their nominally identical nature to the adsorbate preparation in 2PPE which requires higher coverage of adsorbates for better signal. The key observations in the STM experiments are shown in Fig. 5-8. The STM images of  $7 \times 10^{-4}$  ML Cs and 1 ML Xe on Cu(111) are shown in Fig. 5-8 (a) and on its inset, respectively. The Cs<sup>+</sup> ions are partially mobile and appear as stripped in the STM images. The morphology of a Xe-Cs<sup>+</sup> aggregate is shown in Fig. 5-8 (b, c). The Cs<sup>+</sup> ions in the aggregate are arranged preferably on the borders of the aggregate and rarely on the interior of the aggregate. The flat part of the aggregate consists mainly Xe and they resemble to the R30<sup>0</sup> -  $\sqrt{3} \times \sqrt{3}$  hexagonal superstructure shown in the inset of Fig. 5-8 (a) for pure Xe on Cu(111). To obtain better contrast of the aggregate, the Laplace-filtered image of the panel (b) is shown in the Fig. 5-8 (c). This reveal two

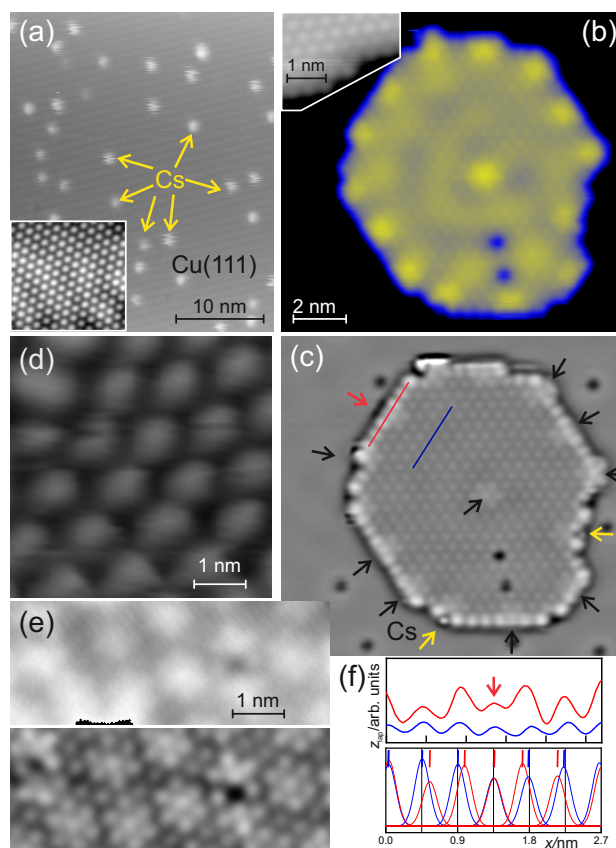


Figure 5-8.: STM images (a) of Cs<sup>+</sup>/Cu(111), -500 mV, 10 pA, and (b) of a Xe-Cs<sup>+</sup> aggregate on Cu(111) using a false-color scale, 10 pA, -25 mV. Insets in (a,b) show 1 ML Xe/Cu(111), recorded at 1.2 nA, 100 mV on a wetting ML and at an aggregate perimeter, 44 pA, 7 mV, respectively. (c) Laplace-filtered image of (b). The Xe:Cs<sup>+</sup> ratio in (b,c) is 40:1. (d) 0.16 ML Cs<sup>+</sup>/Cu(111), 10 pA, 250 mV; (e) Original (top) and Laplace-filtered image (bottom) of 1 ML Xe on top of 0.16 ML Cs<sup>+</sup>/Cu(111), 89 pA, 250 mV, (f) apparent height profiles (top) and their Gaussian fits with maxima marked (bottom) in panel (c) in identical colors. Reprinted figure with permission from Thomas, J. et al. Competition between Coulomb and van der Waals Interactions in Xe-Cs<sup>+</sup> Aggregates on Cu(111) Surfaces. *Phys. Rev. Lett.*, 127:266802, (2021). DOI: <https://doi.org/10.1103/PhysRevLett.127.266802>. Copyright © 2021 by the American Physical Society. Ref. [44].

types of Xe-Cs<sup>+</sup> coordination which are marked by yellow and black arrows. In the first type (yellow arrows), a small feature with the size of Cs<sup>+</sup> ions are laterally covered by Xe atoms and the apparent height of the Xe atoms are larger compared to other Xe atoms. In the second type (black arrows), the lateral size of all features is similar. These two types of Xe-Cs<sup>+</sup> coordination represent 2D solvation of Cs<sup>+</sup> ions in noble gases. The formation of fully solvated Cs<sup>+</sup> ions by a Xe heptamer is marked at the centre of the Laplace filtered image. At a coverage of 0.16 ML Cs (Cs<sup>+</sup> ions are uniformly spaced due to mutual Coulomb



repulsion) and 1 ML Xe on top of the ions on Cu(111), the Xe heptamers become the dominant species of solvation on the surface as shown in the raw (top) and Laplace filtered (bottom) images of Fig. 5-8 (e). Note that the spacing between heptamers become more visible due to the attractive interaction alkali ion and noble gas atoms. The growth of Xe layer follows a carpetlike mode [181, 182] over the Cs<sup>+</sup> ions because of the larger size of Xe ( $r_{Xe}=216$  pm vs  $r_{Cs^+}=174$  pm) and a physisorption distance of 360 pm [183] which is higher than the chemisorption distance of Cs<sup>+</sup> of 301 pm [184]. The height profiles of pure Xe (blue line) and Xe-Cs<sup>+</sup> (red line) are plotted in Fig. 5-8 (f). For pure Xe layer, the Xe atoms are arranged regularly with a separation of 0.45 nm and it is shortened by around 50 pm in the case of Xe-Cs<sup>+</sup> indicated by red arrow in the top panel. The bottom panel of Fig. 5-8 (f) shows a Gaussian fit of the both pattern which clearly shows the difference in the distance between adjacent Xe atoms in pure layer and in aggregates. The similar effect observes for Cs<sup>+</sup> ions solvated by Xe heptamers as shown in Fig. 5-8 (e).

The STM results discussed in this section poses further scientific questions such as how strong is the interaction between an alkali ion and noble gases, why an aggregate with multiple Cs<sup>+</sup> ions does not fragment into smaller units due to Coulomb repulsion of ions, and so on. To address these aspects coupled cluster calculations are performed and is discussed in the following section 5.4.

## 5.4. Coupled Cluster Calculations on Xe-Cs<sup>+</sup> Adsorbates

This section presents the Coupled cluster calculations performed by J. Daru at the theoretical chemistry group of Dominic Marx, Ruhr University Bochum. The calculations on the attractive/repulsive interactions between the constituents in the aggregates and their interactions with the substrate are essential for understanding the reason behind the formation of Xe-Cs<sup>+</sup> aggregates and their stability. A discussion from our joint publication is presented here to gain more insights on the solvation of alkali in noble gases at the interface [44].

The calculations aim to determine (i) the attractive interaction between Xe-Cs<sup>+</sup> and (ii) the repulsive interaction between Cs<sup>+</sup> ions in the absence and presence of the substrate. The calculations are supported by the STM results discussed in section 5.3. The presence of an ion induces electronic polarization on noble gas atoms [12] and a charge density difference analysis is performed to understand the degree of the electronic polarization as shown in the inset of Fig. 5-9 (a). A linear combination of Xe-Cs<sup>+</sup>-Xe are plotted where the yellow spheres represent the nucleus of Xe and blue sphere represents the nucleus of Cs<sup>+</sup>. The accumulation of the charge density is depicted in blue and the depletion of the charge density in red colour. The charge density is more concentrated on the vicinity of the Cs<sup>+</sup> ion due to the attractive interaction between Xe and Cs<sup>+</sup>. Furthermore, the attractive interaction in Xe-Cs<sup>+</sup> and Cs<sup>+</sup>-Xe-Cs<sup>+</sup> arrangement is plotted in the inset of Fig. 5-9 (a) which shows a minimum of 150 meV for an interatomic distance of 0.4 nm. This distance is in agreement with the STM results shown in Fig. 5-8 (f).

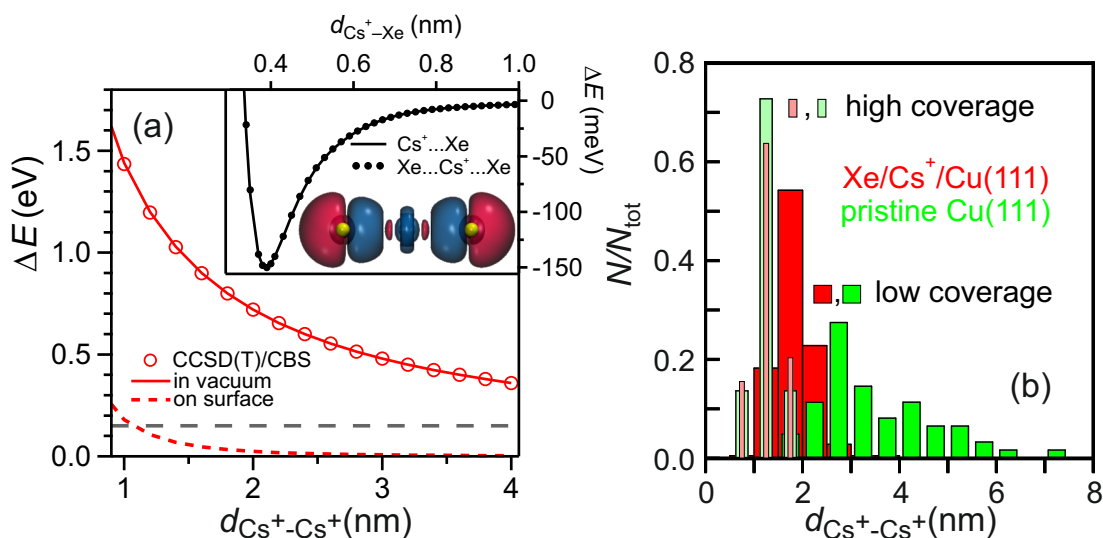


Figure 5-9.:  $\text{Cs}^+-\text{Cs}^+$  distances in  $\text{Xe}-\text{Cs}^+$  aggregates: (a) Repulsive interactions between two  $\text{Cs}^+$  without (solid line) and with contact to a metal (red dashed line) as a function of the  $\text{Cs}^+-\text{Cs}^+$  distance. Circles represent the CCSD(T)/CBS reference. Inset: Attractive interactions between  $\text{Cs}^+$  and one/two Xe atoms per Xe obtained from CCSD(T)/CBS calculations as a function of  $\text{Cs}^+-\text{Xe}$  (equi)distance; the resulting attraction of 150 meV per nearest-neighbor Xe atom provides the gray dashed line in the main panel. The blue/red isosurfaces of the charge density difference visualize charge accumulation/depletion of  $\text{Xe}-\text{Cs}^+-\text{Xe}$  at the optimized equidistance of 0.39 nm. Xe cores are shown in yellow colour. (b) Nearest-neighbor distance histogram of  $\text{Cs}^+$  on  $\text{Cu}(111)$  in green and in  $\text{Xe}-\text{Cs}^+$  aggregates in red normalized to the number of distances  $N_{\text{tot}}$  in STM images for  $\Theta_{\text{Cs}^+} = 7 \cdot 10^{-4}$  ML (low) and 0.16 ML (high). Reprinted figure with permission from Thomas, J. et al. Competition between Coulomb and van der Waals Interactions in  $\text{Xe}-\text{Cs}^+$  Aggregates on  $\text{Cu}(111)$  Surfaces. *Phys. Rev. Lett.*, 127:266802, (2021). DOI: <https://doi.org/10.1103/PhysRevLett.127.266802>. Copyright © 2021 by the American Physical Society. Ref. [44].

In addition, the repulsive interaction between  $\text{Cs}^+$  ions are calculated in vacuum (red open circles and solid line) and on a substrate (red dashed line) as shown in the main panel of Fig. 5-9 (a). The metal substrate plays a prominent role on the repulsion between  $\text{Cs}^+$  ions since it reduces the repulsion up to 1 eV in the range of 1-2 nm separation of the ions. Moreover, the nearest neighbour distances for bare  $\text{Cs}^+$  ions ( $d_{\text{Cs}^+-\text{Cs}^+}$ ) on copper and that of aggregates on copper are determined and is shown as a histogram in Fig. 5-9 (b). In the low coverage ( $7 \times 10^{-4}$  ML in dark green),  $\text{Cs}^+$  ions have a broad distribution in the range of 2-7 nm centred around 4 nm compared to high coverage (0.16 ML in light green). Upon the adsorption of Xe, the distribution of  $\text{Cs}^+$  ions shrink and the mean of the distribution occurs around 1.7 nm. In the higher coverage regime, the Coulomb repulsion between  $\text{Cs}^+$

ions is stronger than the attractive interaction in Xe-Cs<sup>+</sup>. Hence, the distribution of Cs<sup>+</sup> ions are not altered significantly while Xe grows in carpetlike growth over the Cs<sup>+</sup> ions. But, nearest neighbour distance of the Xe is affected by Cs<sup>+</sup> ions as discussed in Fig. 5-8 (f).

## 5.5. Xe Double Layer for Decoupling Influence of Substrate

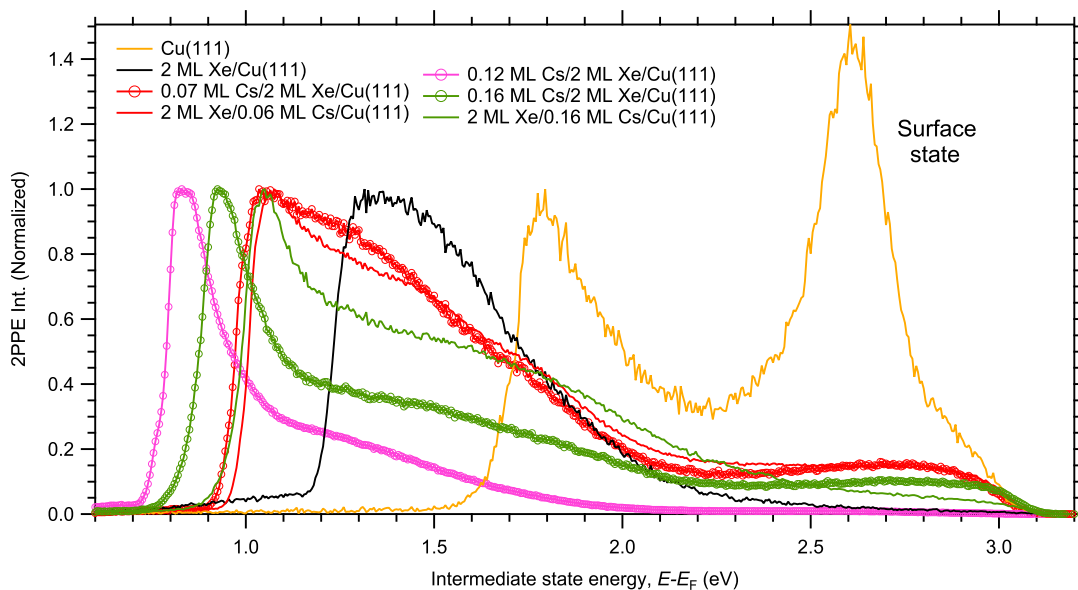


Figure 5-10.: The static 2PPE spectra for various adsorbates on Cu(111). The work function change is the pronounced effect and hence the spectra are normalized with a low-energy cut off. The spectrum for bare Cu(111) is shown in orange colour as a reference. The work function decreases upon adsorption of 2 ML Xe on Cu(111) (black trace). The surfaces with Cs<sup>+</sup> ions above Xe double layer are represented as 'solid line + circles' with different colours for clarity and the flipped configurations are shown as a solid line with same colour.

In the previous sections, all discussions are focused on the response of Xe as a solvent in Xe-Cs<sup>+</sup> aggregates at interfaces. This section presents results of the 2PPE experiments to investigate the effectiveness of Xe as a decoupling layer where it physically isolates adsorbates from the metal substrate. Such decoupling layers are fundamentally interesting because (i) it reduces the electron back transfer rate to the substrate in time-resolved experiments and hence increases the lifetime of excited adsorbate states and (ii) reduces the background 2PPE signal contribution from the substrate. In a recent study, an ultra thin oxide layer is used for decoupling the adsorbates from the substrate which offers suppression of the background signal in photoemission orbital tomography experiments [185]. As part of this thesis work, experiments are performed to explore whether a double layer of Xe is sufficient to act as a decoupling layer or not. The observations from these experiments are discussed as follows.

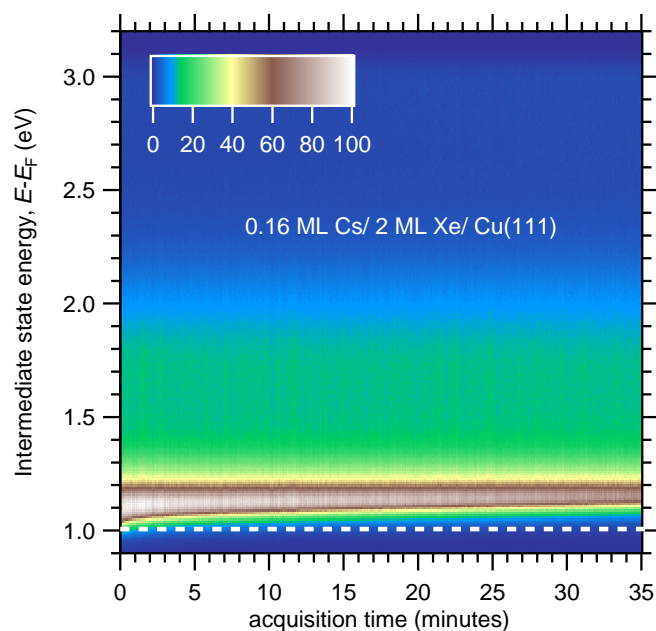


Figure 5-11.: Static 2PPE intensity from 0.16 ML Cs doped over 2 ML Xe/Cu(111) as a function of intermediate state energy and acquisition time. The work function change which is analogous to the change in low-energy cut off the spectra are indicated with a white horizontal dashed line for guidance to the eyes. The experiment is performed at 25 K.

the flipped configuration (represented by solid line) i.e. Cs<sup>+</sup> ions covered by 2 ML Xe shows a relatively higher work function than the corresponding top-doped configuration. It is also noticed that the 2PPE spectra of 0.07 ML Cs and 2 ML Xe in both configurations (red traces) are nearly identical which questions the stability of the Cs<sup>+</sup> ions on top of the Xe double layer.

To scrutinize this concern, 0.16 ML Cs<sup>+</sup> ions are doped on to the top of 2 ML Xe/Cu(111) and continuously recorded static 2PPE spectra over a duration of 35 minutes as shown in Fig. 5-11. It is observed that the work function of the surface increases by around 100 meV over the duration of data acquisition. This indicates a gradual modification on the surface potentially due to the penetration of Cs<sup>+</sup> ions into the Xe layers. It is also appropriate to give general remarks on the adsorbate preparation at this moment. In experiments with chemisorbed Cs<sup>+</sup>/Cu(111), the Cs ions are deposited around at  $T = 200$  K to avoid coadsorption of residual materials from the evaporator. In the case of Xe layers on Cu(111), the desorption temperature occurs at 82 K and 64 K for the first and second mono-layers, respectively. Hence, the deposition of Cs<sup>+</sup> ions have to be carried out at a temperature below

The static 2PPE spectra using 3.1 eV photon energy for different adsorbate configurations are shown in Fig. 5-10. The work function of the surface changes upon adsorption of adsorbates and results in pronounced changes in the low-energy cut off (normalized for better clarity) of the spectra. The work function of the surface Cu(111) surface (orange trace) decreases by 0.48 eV upon adsorption of 2 ML Xe on Cu(111) (black trace). The spectra for Xe double layer doped with 0.07 ML, 0.12 ML and 0.16 ML coverages of Cs<sup>+</sup> ions are shown as solid line + open circles in red, magenta and green, respectively. The work function of the surface drops as a result of the Cs<sup>+</sup> ions doping on the top of the Xe double layers and is found to be not linear where the decrease is more for 0.12 ML Cs<sup>+</sup> ions than 0.16 ML Cs<sup>+</sup> ions. Furthermore,

64 K which might lead to adsorption of residual materials from the evaporator. Overall, it is possible to dope Cs<sup>+</sup> ions on top of the Xe double layer. But, the purity and long-term stability of the adsorbates on the double layer are not clear at this moment.

## 5.6. Conclusions

In combination of 2PPE, STM, and coupled cluster calculations, the fundamental interactions between Xe and Cs on Cu(111) are investigated. The 2PPE probes the interaction of neutral Cs atoms whereas STM probes the charged Cs<sup>+</sup> state interactions. The STM measurements are performed for lower and higher adsorbate coverages. However, the 2PPE measurements are performed relatively higher Cs<sup>+</sup> coverage for obtaining better photoemission intensity.

The static 2PPE results show that the energy of the Cs 6s state increases by 120 meV with respect to Fermi level up to 1 ML Xe coverage which indicates the gradual decoupling of the energy state from the substrate. From the compilation of all experiments, it is found that there is negligible change in the Cs 6s energy per Xe atom for lower Cs<sup>+</sup> coverages and it increases linearly for higher Cs<sup>+</sup> coverages. The time-resolved 2PPE results show that Xe acts as a solvent which mediates an attractive interaction between Cs<sup>+</sup> ions on the surface by screening the Coulomb repulsion and enhances the binding of the Cs<sup>+</sup> ions to the Cu(111) substrate. In addition, Xe increases the lifetime of the Cs 6s state around six-fold by repelling its wave function  $\Psi_{6s}$  (decoupling from the surface) from the surface. These properties of Xe originate due to the transient polarization of the electron cloud induced by charge state of the cations.

The formation of Xe-Cs<sup>+</sup> aggregates at lower adsorbate coverages is observed in STM where Xe-Xe neighbouring distance has reduced in presence of Cs<sup>+</sup> ions. Furthermore, Xe forms heptamer structure around Cs<sup>+</sup> ions for higher adsorbate coverages which resembles to a 2D solvation structure. In addition, Coupled cluster calculations based on the STM results corroborate our observations. The effective repulsion between Cs<sup>+</sup> ions in vacuum decreases considerably in presence of a metal substrate due to the presence of image charge interactions. Upon adsorption of Xe on Cs<sup>+</sup>/Cu(111), the repulsion between Cs<sup>+</sup> ions become weaker than the attractive interaction between Xe and Cs<sup>+</sup>. Furthermore, the charge density difference analysis shows that the accumulation of the charge cloud of Xe toward the Cs<sup>+</sup> ion core. Furthermore, it is demonstrated that the Xe double layer can act as a decoupling layer. The work function of the 2 ML Xe/Cu(111) surface decreases upon doping of the Cs<sup>+</sup> ions and it is observed that the change in work function is not monotonically as a function of Cs coverage. Moreover, further characterizations are required to obtain the purity of the surface and long-term stability of the dopants to reside on the surface without penetration to the substrate.



## 6. Summary

This thesis work aims at understanding the elementary mechanisms and their interplay during the solvation of alkali in polar and nonpolar solvents on a metal surface. These mechanisms include, but are not limited to, (1) ion-dipole forces in which the alkali ion interact with the polar molecules, (2) hydrogen bonding between polar molecules, (3) van der Waals interactions in nonpolar molecules, (4) Pauli repulsion, and (5) image charge interactions between adsorbates and metal substrate. These interactions are either cooperative or competitive during the solvation and they are decisive for the morphology of adsorbates. In addition, the alkalis transfer the valence electron to the metal substrate upon chemisorption which offers an opportunity to study the charge transfer between alkali and substrate upon resonant excitation by optical pulses. It is known that such charge transfer between alkalis and the substrate are associated with nuclear motion normal to the surface. The charge transfer process becomes complex when the alkali is solvated by polar or nonpolar solvents. In such a scenario, the resonant excitation results a coupled nuclear-solvent motion at ultrafast time scale and concomitant decoupling of the excited state from the substrate. The dynamics of the adsorbate system vary as a function of the coordination of the alkali to solvent molecules. Insights on heterogeneous charge transfer processes at interfaces are important for the development of optoelectronic devices, electrochemical cells and energy conversion applications.

Two-photon photoemission (2PPE) spectroscopy is employed to investigate the alkali-solvent interaction at interfaces. The technique involves the excitation of electrons to the unoccupied  $s$  orbital of the alkali by a laser pulse which drives the alkali-solvent system to a nonequilibrium state. The dynamics of the solvation of the adsorbates on the surface is probed by time-resolved 2PPE in which a subsequent laser pulse photoemits the electron from the excited alkali-solvent state on the surface. Also, the evolution of the electronic structure of the adsorbates on surface can be studied using 2PPE as a function of the adsorbate coverages. Furthermore, the 2PPE can be employed for investigation of the localization property of the excited state, structural phase transition and solvation sites at interfaces. The complementary scanning tunneling microscopy (STM) and theoretical methods (by our collaborators) have added a new dimension to the understandings on solvation at interfaces. The 2PPE investigates the solvation of an alkali which is excited to a transient neutral state ( $M^0$ ) whereas STM studies the solvation of an alkali in ionized state ( $M^+$ ). The performances of these techniques are different at lower and higher adsorbate coverages on the surface. The theoretical methods such as coupled cluster calculations and DFT have supported the

experimental observations and also facilitated the understandings on the surface solvation of alkalis.

The interaction of  $\text{Cs}^+$ - $\text{D}_2\text{O}$  and  $\text{Cs}^+$ -Xe on Cu(111) are investigated using 2PPE as part of this thesis work. The surface science approaches have facilitated the preparation of alkalis and solvents on a metal substrate with well-controlled coverages. The frequency-doubled laser pulses from a Ti:sapphire laser operating at a central wavelength around 800 nm are employed for 2PPE experiments. The time-resolved autocorrelation experiments are performed to understand the energy transfer to the solvent and population dynamics of the excited state of the alkali-solvent adsorbates. Furthermore, 2PPE is utilized for probing the evolution of the electronic structure of the  $\text{Cs}^+/\text{Cu}(111)$  as a function of water and Xe coverages. The adsorbates preparation in 2PPE is performed *vis-à-vis* STM to facilitate the preparation of nominally identical surfaces. This strategy has enabled a direct comparison of the spectroscopy results and the corresponding morphology of the adsorbates. Furthermore, coupled cluster calculations (for Xe- $\text{Cs}^+/\text{Cu}(111)$ ) and DFT (for  $\text{D}_2\text{O}-\text{Cs}^+/\text{Cu}(111)$ ) have accounted the morphology of adsorbates into consideration for the determination of electronic and structural properties of alkali-solvent interactions on surface.

The investigations on the interaction of  $\text{Cs}^+$  and  $\text{D}_2\text{O}$  on Cu(111) have resulted into novel insights on alkali solvation at interfaces. The formation of a hybrid alkali-water state is observed during the interaction of alkali and water on Cu(111) in a previous work (Meyer et al., 2015). As part of this thesis work, the properties of this state have investigated extensively by 2PPE spectroscopy. The Cs 6s feature (termed as state A) and water-induced alkali state (termed as state B) exhibit different behaviour as a function of solvent coverages. It is observed that the energy of the state B increases due to structural modification of the Cs-water clusters. The simultaneous occurrence of states A and B in 2PPE are explained by STM as the presence of partially solvated alkali ions and bare alkali ions on the surface. The STM of Cs-water clusters on the surface show an unusual inside-out solvation pattern where ions are found at the periphery of the cluster. The DFT studies have accounted this unusual solvation pattern by calculation of different properties of the adsorbates and it has corroborated the experimental observations. The formation of inside-out pattern is attributed to the preference of the water-water interactions over the alkali-water interactions on the surface. In addition, the time-resolved 2PPE studies of Cs-water clusters show that the energy transfer to the solvent and the population dynamics change as a function of the alkali coordination to the solvent molecules. In our studies on  $\text{Cs}^+$  and Xe on Cu(111), it is observed that the energy of the unoccupied Cs 6s state (state A) increases linearly with respect to Fermi level while adsorbing Xe. This indicates that the bonding of the Cs to the substrate becomes weaker as a result of Xe adsorption. Moreover, the lifetime of the Cs 6s state has increased around six-fold due to the repulsion of its wave function by Xe charge density. These properties of Xe are attributed to the transient polarization of its electron cloud by the alkali ions. Remarkably, there is no formation of a hybrid state of alkali with Xe aggregates on surface. This is a strong indication that 2PPE can differentiate the



---

interaction of alkali with polar and nonpolar solvents. The STM results show that  $\text{Cs}^+$ - $\text{Cs}^+$  separation on Cu(111) is reduced in presence of Xe atoms at lower coverages and also the formation of Xe heptamer structures are observed around  $\text{Cs}^+$  ions for higher coverages. The coupled cluster calculations show that the interaction between  $\text{Cs}^+$  and Xe is stronger than the repulsion between  $\text{Cs}^+$  ions in the aggregates on Cu(111). Hence, Xe can compensate the repulsive interaction between  $\text{Cs}^+$  ions on the surface. To sum up, the solvation of alkali ions on surface is fundamentally different in polar and nonpolar solvents. Hydrogen bonds and electrostatic interactions to substrate are prevalent in the former and Coulomb interactions is favoured over van der Waals interactions in the latter. The 2PPE technique along with STM and theoretical methods have synergistically provided novel insights on the alkali solvation at interfaces.

Understanding the alkali solvation at interfaces has several impacts which include the development of electrochemical cells, photovoltaic cells and electrocatalytic reduction for the sustainable production of chemicals and fuels. The researches in these area rely on the electric double layer model for the description of interfacial processes. However, the surface science approaches provide insights at a fundamental level on the morphology and heterogeneous charge transfer at interfaces. Such approaches have the potential to improve the present electric double layer model for interface chemistry. There are several future directions to be explored in the area of ion solvation at interfaces. One of the pathways is to extend the studies to earth alkali metals to tune the local adsorbate-metal interactions. So far, the thesis work has considered only water molecules and Xe noble gas. The ion solvation in larger molecules such as ammonia or tetrahydrofuran would offer additional opportunities to understand the influence of solvent structure and ion coordination on ultrafast surface dynamics. Furthermore, the noble gases exhibit different electron affinity and experiments to other noble gases offers additional opportunities to study their interaction with alkalis.



# A. Optical Bloch Equations

In order to study the population in different energy states, optical Bloch equations are employed. These are set of coupled differential equations giving decay rate of a state as a function of population in other states (initial, intermediate and final) and their plausible decay rates. A detailed description of optical equations and its implementation in the context of time-resolved 2PPE can be found in several works [145, 146, 149–151]. A naive picture on the origin of optical Bloch equations in a three-level system is presented as follows. The wave function at any time is the superposition of the eigenfunctions of the three levels which are normalized and orthogonal:

$$\Psi(\vec{r}, t) = C_1(t) \cdot \Psi_1(\vec{r}, t) + C_2(t) \cdot \Psi_2(\vec{r}, t) + C_3(t) \cdot \Psi_3(\vec{r}, t). \quad (\text{A-1})$$

The probability of the transition of an electron in any state depends on the expectation value of that state and can be expressed as density matrix as:

$$\hat{\rho} = \begin{pmatrix} \rho_{11} & \rho_{12} & \rho_{13} \\ \rho_{21} & \rho_{22} & \rho_{23} \\ \rho_{31} & \rho_{32} & \rho_{33} \end{pmatrix}. \quad (\text{A-2})$$

The diagonal elements of  $\hat{\rho}$  describe the probability that the system is in state  $|i\rangle$  with decay time of  $T_1^i$ . The off-diagonal elements give the probability of the optically induced coherence between two different states decaying with  $T_2^{ij}$  ( $i, j = 1, 2$  and  $3$ ). According to Liouville-von Neumann theorem, the equations of motion of the density matrix can be expressed as,

$$\frac{d}{dt}\hat{\rho} = \frac{-i}{\hbar}[\hat{H}, \hat{\rho}] + \frac{d}{dt}\hat{\rho}_{diss}, \quad (\text{A-3})$$

where  $\hat{H} = \hat{H}_0(t) + \hat{H}_I(t)$ . The  $\hat{H}_0$  and  $\hat{H}_I$  are the time-independent contribution and incident light field induced contribution to the Hamiltonian respectively. The strength of the optical transition between the states and the polarization dependence of the incident optical field are introduced by an additional value,  $\phi_{ij}(t) = \frac{1}{\hbar}\vec{\mu}_{ij} \cdot \vec{E}(t)$ , which describes the polarization dependence ( $\mu_{ij}$  and  $E(t)$  are the transition dipole moment and electric field respectively). We get a set of 9 coupled differential equations upon evaluating the Liouville-von Neumann equations as given below [150]:

$$\frac{d}{dt}\rho_{11} = -i\phi_{12} \cdot (\rho_{21} - \rho_{12}) + \frac{d}{dt}\rho_{11}^{diss}, \quad (\text{A-4a})$$

$$\frac{d}{dt}\rho_{12} = -i(\phi_{12} \cdot (\rho_{22} - \rho_{11}) - \phi_{23} \cdot \rho_{13}) + i(\omega_1 - \omega_2) \cdot \rho_{12} + \frac{d}{dt}\rho_{12}^{diss}, \quad (\text{A-4b})$$

$$\frac{d}{dt}\rho_{13} = -i(\phi_{12} \cdot \rho_{23} - \phi_{23} \cdot \rho_{12}) + i(\omega_1 - \omega_3) \cdot \rho_{13} + \frac{d}{dt}\rho_{13}^{diss}, \quad (\text{A-4c})$$

$$\frac{d}{dt}\rho_{22} = -i(\phi_{12} \cdot (\rho_{12} - \rho_{21}) + \phi_{23} \cdot (\rho_{32} - \rho_{23})) + \frac{d}{dt}\rho_{22}^{diss}, \quad (\text{A-4d})$$

$$\frac{d}{dt}\rho_{23} = -i(\phi_{23} \cdot (\rho_{33} - \rho_{22}) + \phi_{12} \cdot \rho_{13}) + i(\omega_2 - \omega_3) \cdot \rho_{23} + \frac{d}{dt}\rho_{23}^{diss}, \quad (\text{A-4e})$$

$$\frac{d}{dt}\rho_{33} = -i\phi_{23} \cdot (\rho_{23} - \rho_{32}) + \frac{d}{dt}\rho_{33}^{diss}, \quad \text{and} \quad (\text{A-4f})$$

$$\frac{d}{dt}\rho_{ij} = \frac{d}{dt}\rho_{ij}^*, i \neq j. \quad i \text{ or } j = 1, 2 \text{ or } 3 \quad (\text{A-4g})$$

The set of equations given under A-4 are known as optical Bloch equations (OBE). To study the population dynamics of different energy states, these equations have to be solved numerically as a function of time delay between pump and probe laser pulses.

## B. Error Propagation Method to Determine Error in Adsorbate Coverage Ratio

Let  $\Theta$  and  $\Delta\Theta$  be the adsorbate coverage ratio and the error in its determination, respectively. Let the errors in the measured coverage of Cs ( $\Theta_{Cs}$ ) and ice ( $\Theta_{D_2O}$ ) on Cu(111) be  $\Delta\Theta_{Cs}$  and  $\Delta\Theta_{D_2O}$ , respectively. The adsorbate coverage ratio can be expressed as:

$$\Theta(\Theta_{Cs}, \Theta_{D_2O}) = \frac{\Theta_{D_2O}}{\Theta_{Cs}}. \quad (B-1)$$

Now, the error in the determination of  $\Theta$  can be expressed using the error propagation of the measured quantities as:

$$\Delta\Theta = \frac{\partial\Theta(\Theta_{D_2O}, \Theta_{Cs})}{\partial\Theta_{D_2O}}\Delta\Theta_{D_2O} + \frac{\partial\Theta(\Theta_{D_2O}, \Theta_{Cs})}{\partial\Theta_{Cs}}\Delta\Theta_{Cs}. \quad (B-2)$$

Use partial derivative of equation B-1 in equation B-2, we get:

$$\Delta\Theta = \frac{1}{\Theta_{Cs}}\Delta\Theta_{D_2O} + \frac{\Theta_{D_2O}}{\Theta_{Cs}^2}\Delta\Theta_{Cs}. \quad (B-3)$$

The equation B-3 gives the error in the determination of the adsorbate coverage ratio as a function of the coverage of the individual adsorbates and error in its determination. The adsorbate coverage ratio and the corresponding error in its determination are tabulated in chapter 4-1.

## C. Confidence Interval Analysis of Potential Energy Surface

As discussed in the section 5.2, the PES is simulated for  $\text{Cs}^+/\text{Cu}(111)$  and  $\text{Xe}/\text{Cs}^+/\text{Cu}(111)$  based on the previous works [3,105]. The minima of the PES for both surfaces are separated by around 4 pm as shown in the Fig. 5-6 (c). The question arises whether both minima overlap if the errors in the determination of energy are taken into consideration. In order to address this concern, errors in the Cs 6s energy for different time delay are determined for 1 ML  $\text{Xe}/\text{Cs}^+/\text{Cu}(111)$  as shown in the Fig. C-1 (a).

The conversion of ground state Cs 6s energy to the distance of  $\text{Cs}^+$  from surface is shown in Fig. C-1 (b). Since the energy scales linearly with the distance from Cu image plane, considering only upper or lower bound errors in the energy simply shift the PES vertically up or down. So, two cases are considered for determining the confidence interval of the fit of the original data. In the case I, lower error bound of the energy is considered up to 100 fs time delay and upper error bound for above 100 fs time delay (green data points and fits). In the case II, upper error bound of the energy is considered upto 100 fs time delay and lower error bound for above 100 fs time delay (blue data points and fits). The fitted analytical function is processed further as discussed in the main text according to [3,44]. The PES of the 1 ML  $\text{Xe}/\text{Cs}^+/\text{Cu}(111)$  for different cases in panel (b) is shown in the Fig. C-1 (c). The minima are distinguishable and a separation of 1.5 pm is found which is smaller than separation of the PES minima in the Fig. 5-6 (c). Hence, observation of the shift of PES upon adsorption of Xe is reliable.

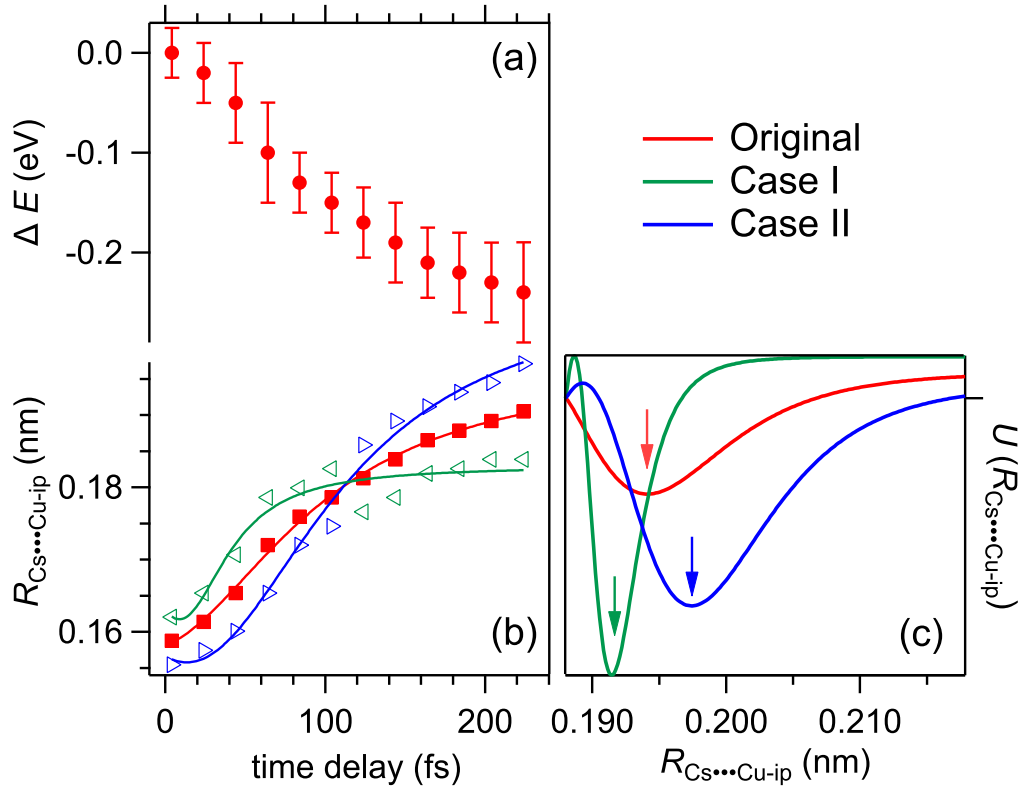


Figure C-1.: (a) The change in the energy of the Cs 6s state of the Xe-Cs<sup>+</sup> aggregates as a function of time delay is shown with error bars. The lower (L) and upper (H) bound error in the energy are considered along with the original data for energy to distance conversion in panel (b). The panel (c) shows the PES determined for the original energy (red) and that with maximum errors (green and blue). The minima of the red and blue are separated by around 1.5 pm. See text for detailed description of the analysis.





# Bibliography

- [1] M. Bauer, S. Pawlik, and M. Aeschlimann. Resonance Lifetime and Energy of an Excited Cs State on Cu(111). *Phys. Rev. B*, 55:10040–10043, (1997).
- [2] Jin Zhao, Niko Pontius, Aimo Winkelmann, Vahit Sametoglu, Atsushi Kubo, Andrei G. Borisov, Daniel Sánchez-Portal, V. M. Silkin, Eugene V. Chulkov, Pedro M. Echenique, and Hrvoje Petek. Electronic Potential of a Chemisorption Interface. *Phys. Rev. B*, 78:085419, (2008).
- [3] Hrvoje Petek, Miles J. Weida, Hisashi Nagano, and Susumu Ogawa. Real-Time Observation of Adsorbate Atom Motion Above a Metal Surface. *Science*, 288:1402–1404, (2000).
- [4] Michael Meyer, Ishita Agarwal, Martin Wolf, and Uwe Bovensiepen. Ultrafast Electron Dynamics at Water Covered Alkali Adatoms Adsorbed on Cu(111). *Phys. Chem. Chem. Phys.*, 17:8441–8448, (2015).
- [5] Humphry Davy. XXIII. Electro-Chemical Researches, on the Decomposition of the Earths; with Observations on the Metals Obtained from the Alkaline Earths, and on the Amalgam Procured from Ammonia. *Philosophical Transactions of the Royal Society of London*, 98:333–370, (1808).
- [6] Edwin J. Hart and J. W. Boag. Absorption Spectrum of the Hydrated Electron in Water and in Aqueous Solutions. *Journal of the American Chemical Society*, 84:4090–4095, (1962).
- [7] David Luckhaus, Yo ichi Yamamoto, Toshinori Suzuki, and Ruth Signorell. Genuine Binding Energy of the Hydrated Electron. *Science Advances*, 3(4):e1603224, (2017).
- [8] Yo-ichi Yamamoto, Yoshi-Ichi Suzuki, Gaia Tomasello, Takuya Horio, Shutaro Karashima, Roland Mitríc, and Toshinori Suzuki. Time- and Angle-Resolved Photoemission Spectroscopy of Hydrated Electrons Near a Liquid Water Surface. *Phys. Rev. Lett.*, 112:187603, (2014).
- [9] Marc P. Coons, Zhi-Qiang You, and John M. Herbert. The Hydrated Electron at the Surface of Neat Liquid Water Appears to be Indistinguishable from the Bulk Species. *Journal of the American Chemical Society*, 138(34):10879–10886, (2016).

- [10] Richard M. Forck, Ingo Dauster, Yasmin Schieweck, Thomas Zeuch, Udo Buck, Milan Ončák, and Petr Slavíček. Communications: Observation of Two Classes of Isomers of Hydrated Electrons in Sodium-Water Clusters. *The Journal of Chemical Physics*, 132(22):221102, (2010).
- [11] Arthur E. Bragg, William J. Glover, and Benjamin J. Schwartz. Watching the Solvation of Atoms in Liquids One Solvent Molecule at a Time. *Phys. Rev. Lett.*, 104:233005, (2010).
- [12] Ricardo Pérez de Tudela, Paul Martini, Marcelo Goulart, Paul Scheier, Fernando Pirani, Javier Hernández-Rojas, José Bretón, Josu Ortiz de Zárate, Massimiliano Bartolomei, Tomás González-Lezana, Marta I. Hernández, José Campos-Martínez, and Pablo Villarreal. A Combined Experimental and Theoretical Investigation of Cs<sup>+</sup> Ions Solvated in HeN Clusters. *The Journal of Chemical Physics*, 150:154304, 2019.
- [13] C. Gahl, U. Bovensiepen, C. Frischkorn, and M. Wolf. Ultrafast Dynamics of Electron Localization and Solvation in Ice Layers on Cu(111). *Phys. Rev. Lett.*, 89:107402, (2002).
- [14] Julia Stähler, Jan-Christoph Deinert, Daniel Wegkamp, Sebastian Hagen, and Martin Wolf. Real-Time Measurement of the Vertical Binding Energy During the Birth of a Solvated Electron. *Journal of the American Chemical Society*, 137:3520–3524, (2015).
- [15] Michael Meyer, Mathieu Bertin, Uwe Bovensiepen, Daniel Wegkamp, Marcel Krenz, and Martin Wolf. Ultrafast Dynamics at the Na/D<sub>2</sub>O/Cu(111) Interface: Electron Solvation in Ice Layers and Na<sup>+</sup>-mediated Surface Solvation. *The Journal of Physical Chemistry C*, 115:204–209, (2011).
- [16] Mariana C. O. Monteiro, Federico Dattila, Bellenod Hagedoorn, Rodrigo García-Muelas, Núria López, and Marc T. M. Koper. Absence of CO<sub>2</sub> Electroreduction on Copper, Gold and Silver Electrodes Without Metal Cations in Solution. *Nature Catalysis*, 4:654–662, (2021).
- [17] Grazia Gonella, Ellen H. G. Backus, Yuki Nagata, Douwe J. Bonthuis, Philip Loche, Alexander Schlaich, Roland R. Netz, Angelika Kühnle, Ian T. McCrum, Marc T. M. Koper, Martin Wolf, Bernd Winter, Gerard Meijer, R. Kramer Campen, and Mischa Bonn. Water at Charged Interfaces. *Nature Reviews Chemistry*, 5:466–485, (2021).
- [18] Christian George, Markus Ammann, Barbara D’Anna, D. J. Donaldson, and Sergey A. Nizkorodov. Heterogeneous Photochemistry in the Atmosphere. *Chemical Reviews*, 115:4218–4258, (2015).

- 
- [19] C. W. Spicer, E. G. Chapman, B. J. Finlayson-Pitts, R. A. Plastridge, J. M. Hubbe, J. D. Fast, and C. M. Berkowitz. Unexpectedly High Concentrations of Molecular Chlorine in Coastal Air. *Nature*, 394:353–356, (1998).
- [20] A. R. Ravishankara. Are Chlorine Atoms Significant Tropospheric Free Radicals? *Proceedings of the National Academy of Sciences*, 106:13639–13640, (2009).
- [21] Charles L. Croskey, John D. Mitchell, Martin Friedrich, Klaus M. Torkar, Ulf-Peter Hoppe, and Richard A. Goldberg. Electrical Structure of PMSE and NLC Regions During the DROPPS Program. *Geophysical Research Letters*, 28:1427–1430, (2001).
- [22] M. Petukh and E. Alexov. Ion Binding to Biological Macromolecules. *Asian J Phys.*, 23:735–744, (2014).
- [23] M. I. Panayiotidis, C. D. Bortner, and J. A. Cidlowski. On the Mechanism of Ionic Regulation of Apoptosis: Would the  $\text{Na}^+/\text{K}^+$ -atpase please stand up? *Acta Physiologica*, 187:205–215, (2006).
- [24] Tomas Vondrak, John M. C. Plane, and Stephen R. Meech. Influence of Submonolayer Sodium Adsorption on the Photoemission of the Cu(111)/Water Ice Surface. *The Journal of Chemical Physics*, 125(22):224702, (2006).
- [25] Tomas Vondrak, John M. C. Plane, and Stephen R. Meech. Photoemission from Sodium on Ice: A Mechanism for Positive and Negative Charge Coexistence in the Mesosphere. *The Journal of Physical Chemistry B*, 110(9):3860–3863, (2006).
- [26] Bhupender Pal, Shengyuan Yang, Subramaniam Ramesh, Venkataraman Thangadurai, and Rajan Jose. Electrolyte Selection for Supercapacitive Devices: a Critical Review. *Nanoscale Adv.*, 1:3807–3835, (2019).
- [27] Taiho Park, Saif A. Haque, Robert J. Potter, Andrew B. Holmes, and James R. Durrant. A Supramolecular Approach to Lithium Ion Solvation at Nanostructured Dye Sensitised Inorganic/Organic Heterojunctions. *Chem. Commun.*, pages 2878–2879, (2003).
- [28] Ksenia S. Egorova, Evgeniy G. Gordeev, and Valentine P. Ananikov. Biological Activity of Ionic Liquids and Their Application in Pharmaceuticals and Medicine. *Chemical Reviews*, 117:7132–7189, (2017).
- [29] Fatima Javed, Faheem Ullah, Muhammad Razlan Zakaria, and Hazizan Md. Akil. An Approach to Classification and Hi-Tech Applications of Room-Temperature Ionic Liquids (RTILs): A Review. *Journal of Molecular Liquids*, 271:403–420, (2018).

- [30] Lauren Raguette and Ryan Jorn. Ion Solvation and Dynamics at Solid Electrolyte Interphases: A Long Way from Bulk? *The Journal of Physical Chemistry C*, 122:3219–3232, (2018).
- [31] I. V. Hertel, C. Hüglin, C. Nitsch, and C. P. Schulz. Photoionization of  $\text{Na}(\text{NH}_3)_n$  and  $\text{Na}(\text{H}_2\text{O})_n$  clusters: A step towards the liquid phase? *Phys. Rev. Lett.*, 67:1767–1770, (1991).
- [32] Miranda J. Baran, Mark E. Carrington, Swagat Sahu, Artem Baskin, Junhua Song, Michael A. Baird, Kee Sung Han, Karl T. Mueller, Simon J. Teat, Stephen M. Meckler, Chengyin Fu, David Prendergast, and Brett A. Helms. Diversity-Oriented Synthesis of Polymer Membranes with Ion Solvation Cages. *Nature*, 592:225–231, (2021).
- [33] Christopher Hardacre, John D. Holbrey, Mark Nieuwenhuyzen, and Tristan G. A. Youngs. Structure and Solvation in Ionic Liquids. *Accounts of Chemical Research*, 40:1146–1155, (2007).
- [34] Haibo Yu, Christopher L. Mazzanti, Troy W. Whitfield, Roger E. Koeppe, Olaf S. Andersen, and Benoît Roux. A Combined Experimental and Theoretical Study of Ion Solvation in Liquid N-Methylacetamide. *Journal of the American Chemical Society*, 132:10847–10856, (2010).
- [35] Wolfgang Wachter, Šarka Fernandez, Richard Buchner, and Glenn Hefter. Ion Association and Hydration in Aqueous Solutions of  $\text{LiCl}$  and  $\text{Li}_2\text{SO}_4$  by Dielectric Spectroscopy. *The Journal of Physical Chemistry B*, 111:9010–9017, (2007).
- [36] S. Schlick, P. A. Narayana, and Larry Kevan. ESR Line Shape Studies of Trapped Electrons in  $\gamma$ -Irradiated 170 Enriched 10M NaOH Alkaline Ice Glass: Model for the Geometrical Structure of the Trapped Electrons. *The Journal of Chemical Physics*, 64:3153–3160, (1976).
- [37] R Leberman and A. K. Soper. Effect of High Salt Concentrations on Water Structure. *Nature*, 378:364–366, (1995).
- [38] Anne Willem Omta, Michel F. Kropman, Sander Woutersen, and Huib J. Bakker. Negligible Effect of Ions on the Hydrogen-Bond Structure in Liquid Water. *Science*, 301:347–349, (2003).
- [39] M. Halder, L. Sanders Headley, P. Mukherjee, X. Song, and J. W. Petrich. Experimental and Theoretical Investigations of Solvation Dynamics of Ionic Fluids: Appropriateness of Dielectric Theory and the Role of DC Conductivity. *The Journal of Physical Chemistry A*, 110:8623–8626, (2006).

- 
- [40] William A. Donald, Ryan D. Leib, Jeremy T. O'Brien, Anne I. S. Holm, and Evan R. Williams. Nanocalorimetry in Mass Spectrometry: A Route to Understanding Ion and Electron Solvation. *Proceedings of the National Academy of Sciences*, 105:18102–18107, (2008).
- [41] Michael J. Tauber and Richard A. Mathies. Structure of the Aqueous Solvated Electron from Resonance Raman Spectroscopy: Lessons from Isotopic Mixtures. *Journal of the American Chemical Society*, 125:1394–1402, (2003).
- [42] H. W. Sarkas, S. T. Arnold, J. G. Eaton, G. H. Lee, and K. H. Bowen. Ammonia cluster anions and their relationship to ammoniated (solvated) electrons: The photoelectron spectra of  $(\text{NH}_3)_{n=41-1100}^-$ . *The Journal of Chemical Physics*, 116:5731–5737, (2002).
- [43] Alejandro Pérez Paz and Angel Rubio. Hydrated Alkali Atoms on Copper(111): A Density Functional Theory Study. *The Journal of Physical Chemistry C*, 125(7):3868–3879, (2021).
- [44] J. Thomas, C. Bertram, J. Daru, J. Patwari, I. Langguth, P. Zhou, D. Marx, K. Morgenstern, and U. Bovensiepen. Competition between Coulomb and van der Waals Interactions in Xe-Cs<sup>+</sup> Aggregates on Cu(111) Surfaces. *Phys. Rev. Lett.*, 127:266802, (2021).
- [45] Toshihiko Mandai, Kazuki Yoshida, Kazuhide Ueno, Kaoru Dokko, and Masayoshi Watanabe. Criteria for Solvate Ionic Liquids. *Phys. Chem. Chem. Phys.*, 16:8761–8772, (2014).
- [46] Rui Shi, Anthony J. Cooper, and Hajime Tanaka. Microscopic Understanding of Ion Solvation in Water, (2021).
- [47] Philippe Hunenberger and Maria Reif. *Single-Ion Solvation*. Theoretical and Computational Chemistry Series. The Royal Society of Chemistry, 2011.
- [48] William J. Glover, Ross E. Larsen, and Benjamin J. Schwartz. Nature of Sodium Atoms/(Na<sup>+</sup>, e<sup>-</sup>) Contact Pairs in Liquid Tetrahydrofuran. *The Journal of Physical Chemistry B*, 114:11535–11543, (2010).
- [49] Joshua A. Snyder and Arthur E. Bragg. Ultrafast Pump–Repump–Probe Photochemical Hole Burning as a Probe of Excited-State Reaction Pathway Branching. *The Journal of Physical Chemistry Letters*, 9:5847–5854, (2018).
- [50] James M. Lisy. Spectroscopy and Structure of Solvated Alkali-Metal Ions. *International Reviews in Physical Chemistry*, 16:267–289, (1997).

- [51] Carl Caleman, Jochen S. Hub, Paul J. van Maaren, and David van der Spoel. Atomistic Simulation of Ion Solvation in Water Explains Surface Preference of Halides. *Proceedings of the National Academy of Sciences*, 108:6838–6842, (2011).
- [52] Katharina Dilchert, Michelle Schmidt, Angela Großjohann, Kai-Stephan Feichtner, Robert E. Mulvey, and Viktoria H. Gessner. Solvation Effects on the Structure and Stability of Alkali Metal Carbenoids. *Angewandte Chemie International Edition*, 60:493–498, 2021.
- [53] Sebastien Kerisit, M. Vijayakumar, Kee Sung Han, and Karl T. Mueller. Solvation Structure and Transport Properties of Alkali Cations in Dimethyl Sulfoxide under Exogenous Static Electric Fields. *The Journal of Chemical Physics*, 142(22):224502, (2015).
- [54] L. H. B. Nguyen, T. Picard, N. Sergent, C. Raynaud, J.-S. Filhol, and M.-L. Doublet. Investigation of Alkali and Alkaline Earth Solvation Structures in Tetraglyme Solvent. *Phys. Chem. Chem. Phys.*, 23:26120–26129, (2021).
- [55] R. Catterall, J. Slater, and M. C. R. Symons. Electron Spin Resonance and Optical Spectra of Solutions of Potassium in Tetrahydrofuran. *The Journal of Chemical Physics*, 52:1003–1004, (1970).
- [56] Fang-Yuan Jou and Gordon R. Freeman. Band Resolution of Optical Spectra of Solvated Electrons in Water, Alcohols, and Tetrahydrofuran. *Canadian Journal of Chemistry*, 57:591–597, (1979).
- [57] W. Weyhmann and F. M. Pipkin. Optical Absorption Spectra of Alkali Atoms in Rare-Gas Matrices. *Phys. Rev.*, 137:A490–A496, (1965).
- [58] GRZEGORZ ŁACH, MAARTEN DEKIEVIET, and ULRICH D. JENTSCHURA. Noble Gas, Alkali and Alkaline Atoms Interacting with a Gold Surface. *International Journal of Modern Physics A*, 25(11):2337–2344, (2010).
- [59] Z. Wu, T. G. Walker, and W. Happer. Spin-Rotation Interaction of Noble-Gas Alkali-Metal Atom Pairs. *Phys. Rev. Lett.*, 54:1921–1924, (1985).
- [60] R. Shaham, O. Katz, and O. Firstenberg. Strong Coupling of Alkali-Metal Spins to Noble-Gas Spins with an Hour-Long Coherence Time. *Nature Physics*, 18:506–510, (2022).
- [61] Lukas An der Lan, Peter Bartl, Christian Leidlmair, Harald Schöbel, Roland Jochum, Stephan Denifl, Tilmann D. Märk, Andrew M. Ellis, and Paul Scheier. The Submersion of Sodium Clusters in Helium Nanodroplets: Identification of the Surface → Interior Transition. *The Journal of Chemical Physics*, 135:044309, (2011).

- 
- [62] Ulrich Boesl. Time-of-Flight Mass Spectrometry: Introduction to the Basics. *Mass Spectrometry Reviews*, 36:86–109, (2017).
- [63] M. Rossi, M. Verona, D. E. Galli, and L. Reatto. Alkali and Alkali-Earth Ions in  $^4\text{He}$  Systems. *Phys. Rev. B*, 69:212510, (2004).
- [64] S. Acosta-Gutiérrez, J. Bretón, J. M. Gomez Llorente, and J. Hernández-Rojas. Optimal Covering of C60 Fullerene by Rare Gases. *The Journal of Chemical Physics*, 137:074306, (2012).
- [65] Eric D. Wachsman and Kang Taek Lee. Lowering the Temperature of Solid Oxide Fuel Cells. *Science*, 334:935–939, (2011).
- [66] Mark K Debe. Electrocatalyst Approaches and Challenges for Automotive Fuel Cells. *Nature*, 486:43–51, (2012).
- [67] NM Marković and PN Ross Jr. Surface Science Studies of Model Fuel Cell Electrocatalysts. *Surface Science Reports*, 45:117–229, (2002).
- [68] Kazuhiko Maeda. Photocatalytic Water Splitting Using Semiconductor Particles: History and Recent Developments. *Journal of Photochemistry and Photobiology C: Photochemistry Reviews*, 12:237–268, (2011).
- [69] Michael G. Walter, Emily L. Warren, James R. McKone, Shannon W. Boettcher, Qixi Mi, Elizabeth A. Santori, and Nathan S. Lewis. Solar Water Splitting Cells. *Chemical Reviews*, 110:6446–6473, (2010).
- [70] Jingrun Ran, Jun Zhang, Jiaguo Yu, Mietek Jaroniec, and Shi Zhang Qiao. Earth-abundant Cocatalysts for Semiconductor-based Photocatalytic Water Splitting. *Chem. Soc. Rev.*, 43:7787–7812, (2014).
- [71] Lihui Ou, Hai Yang, Junling Jin, and Yuandao Chen. Theoretical Insights into the Promotion Effect of Alkali Metal Cations on the Electroreduction Mechanism of CO<sub>2</sub> into C<sub>1</sub> Products at the Cu(111)/H<sub>2</sub>O Interface. *New J. Chem.*, 45:15582–15593, (2021).
- [72] H. Helmholtz. Ueber einige Gesetze der Vertheilung elektrischer Ströme in körperlichen Leitern mit Anwendung auf die thierisch-elektrischen Versuche. *Annalen der Physik*, 165(6):211–233, (1853).
- [73] M Gouy. Sur la constitution de la charge électrique à la surface d’un électrolyte. *J. Phys. Theor. Appl.*, 9(1):457 – 468, (1910).

- [74] David Leonard Chapman. A Contribution to the Theory of Electrocapillarity. *The London, Edinburgh, and Dublin Philosophical Magazine and Journal of Science*, 25(148):475–481, (1913).
- [75] P. Debye and Hückel E. Zur Theorie der Elektrolyte. *Physikalische Zeitschrift*, 9:185–206, (1923).
- [76] Otto Stern. zur Theorie der Elektrolytischen Doppelschicht. *Zeitschrift für Elektrochemie und angewandte physikalische Chemie*, 30:508–516, (1924).
- [77] David C. Grahame. The Electrical Double Layer and the Theory of Electrocapillarity. *Chemical Reviews*, 41(3):441–501, (1947).
- [78] B. E. Conway, J. O'M. Bockris, and I. A. Ammar. The Dielectric Constant of the Solution in the Diffuse and Helmholtz Double Layers at a Charged Interface in Aqueous Solution. *Trans. Faraday Soc.*, 47:756–766, (1951).
- [79] J. O'm. Bockris, M. A. V. Devanathan, K. Müller, and John Alfred Valentine Butler. On the Structure of Charged Interfaces. *Proceedings of the Royal Society of London. Series A. Mathematical and Physical Sciences*, 274(1356):55–79, (1963).
- [80] Matthias M. Waegle, Charuni M. Gunathunge, Jingyi Li, and Xiang Li. How Cations Affect the Electric Double Layer and the Rates and Selectivity of Electrocatalytic Processes. *The Journal of Chemical Physics*, 151(16):160902, (2019).
- [81] Alex G. F. de Beer, R. Kramer Campen, and Sylvie Roke. Separating Surface Structure and Surface Charge with Second-Harmonic and Sum-Frequency Scattering. *Phys. Rev. B*, 82:235431, (2010).
- [82] Shaowei Ong, Xiaolin Zhao, and Kenneth B. Eisenthal. Polarization of Water Molecules at a Charged Interface: Second Harmonic Studies of the Silica/Water Interface. *Chemical Physics Letters*, 191(3):327–335, (1992).
- [83] Matthew A. Brown, Zareen Abbas, Armin Kleibert, Richard G. Green, Alok Goel, Sylvio May, and Todd M. Squires. Determination of Surface Potential and Electrical Double-Layer Structure at the Aqueous Electrolyte-Nanoparticle Interface. *Phys. Rev. X*, 6:011007, (2016).
- [84] Marco Favaro, Beomgyun Jeong, Philip N. Ross, Junko Yano, Zahid Hussain, Zhi Liu, and Ethan J. Crumlin. Unravelling the Electrochemical Double Layer by Direct Probing of the Solid/Liquid Interface. *Nature Communications*, 7:12695, (2016).
- [85] Takeshi Fukuma, Yasumasa Ueda, Shunsuke Yoshioka, and Hitoshi Asakawa. Atomic-Scale Distribution of Water Molecules at the Mica-Water Interface Visualized by Three-Dimensional Scanning Force Microscopy. *Phys. Rev. Lett.*, 104:016101, (2010).



- 
- [86] T Fukuma, K Onishi, N Kobayashi, A Matsuki, and H Asakawa. Atomic-Resolution Imaging in Liquid by Frequency Modulation Atomic Force Microscopy Using Small Cantilevers with Megahertz-Order Resonance Frequencies. *Nanotechnology*, 23:135706, (2012).
- [87] Naritaka Kobayashi, Hitoshi Asakawa, and Takeshi Fukuma. Nanoscale Potential Measurements in Liquid by Frequency Modulation Atomic Force Microscopy. *Review of Scientific Instruments*, 81(12):123705, (2010).
- [88] Wilhelm Melitz, Jian Shen, Andrew C. Kummel, and Sangyeob Lee. Kelvin Probe Force Microscopy and its Application. *Surface Science Reports*, 66:1–27, (2011).
- [89] Kang Xu. Nonaqueous Liquid Electrolytes for Lithium-Based Rechargeable Batteries. *Chemical Reviews*, 104(10):4303–4418, (2004).
- [90] Kang Xu. Electrolytes and Interphases in Li-Ion Batteries and Beyond. *Chemical Reviews*, 114:11503–11618, (2014).
- [91] Naoki Nitta, Feixiang Wu, Jung Tae Lee, and Gleb Yushin. Li-ion Battery Materials: Present and Future. *Materials Today*, 18(5):252–264, (2015).
- [92] Taehoon Kim, Wentao Song, Dae-Yong Son, Luis K. Ono, and Yabing Qi. Lithium-ion Batteries: Outlook on Present, Future, and Hybridized Technologies. *J. Mater. Chem. A*, 7:2942–2964, (2019).
- [93] Arumugam Manthiram. A Reflection on Lithium-ion Battery Cathode Chemistry. *Nature Communications*, 11:1550, (2020).
- [94] James Marcicki, A.T. Conlisk, and Giorgio Rizzoni. A Lithium-Ion Battery Model Including Electrical Double Layer Effects. *Journal of Power Sources*, 251:157–169, (2014).
- [95] Weili Zhang, Yang Lu, Lei Wan, Pan Zhou, Yingchun Xia, Shuaishuai Yan, Xiaoxia Chen, Hangyu Zhou, Hao Dong, and Kai Liu. Engineering a Passivating Electric Double Layer for High Performance Lithium Metal Batteries. *Nature Communications*, 13:2029, (2022).
- [96] Takashi Tsuchiya, Makoto Takayanagi, Kazutaka Mitsuishi, Masataka Imura, Shigenori Ueda, Yasuo Koide, Tohru Higuchi, and Kazuya Terabe. The Electric Double Layer Effect and its Strong Suppression at Li<sup>+</sup> Solid Electrolyte/Hydrogenated Diamond Interfaces. *Communications Chemistry*, 4:117, (2021).
- [97] Jessica Lück and Arnulf Latz. The Electrochemical Double Layer and its Impedance Behavior in Lithium-Ion Batteries. *Phys. Chem. Chem. Phys.*, 21:14753–14765, (2019).

- [98] Nataliia Mozhzhukhina, Eibar Flores, Robin Lundström, Ville Nyström, Paul G. Kitz, Kristina Edström, and Erik J. Berg. Direct Operando Observation of Double Layer Charging and Early Solid Electrolyte Interphase Formation in Li-Ion Battery Electrolytes. *The Journal of Physical Chemistry Letters*, 11:4119–4123, (2020).
- [99] Irving Langmuir and K. H. Kingdon. Thermionic Effects Caused by Alkali Vapors in Vacuum Tubes. *Science*, 57:58–60, (1923).
- [100] I. Langmuir and D. S. Villars. Oxygen Films on Tungsten. I. A Study of Stability by Means of Electron Emission in Presence of Cesium Vapor. *Journal of the American Chemical Society*, 53:486–497, (1931).
- [101] H.P. Bonzel. Alkali Metal Affected Adsorption of Molecules on Metal Surfaces. *Surface Science Reports*, 8:43–125, (1988).
- [102] M.I. Trioni, S. Achilli, and E.V. Chulkov. Key Ingredients of the Alkali Atom – Metal Surface Interaction: Chemical Bonding Versus Spectral Properties. *Progress in Surface Science*, 88:160–170, (2013).
- [103] M. Bauer, S. Pawlik, and M. Aeschlimann. Decay Dynamics of Photoexcited Alkali Chemisorbates: Real-Time Investigations in the Femtosecond Regime. *Phys. Rev. B*, 60:5016–5028, (1999).
- [104] A. G. Borisov, V. Sametoglu, A. Winkelmann, A. Kubo, N. Pontius, J. Zhao, V. M. Silkin, J. P. Gauyacq, E. V. Chulkov, P. M. Echenique, and H. Petek.  $\pi$  Resonance of Chemisorbed Alkali Atoms on Noble Metals. *Phys. Rev. Lett.*, 101:266801, (2008).
- [105] A.G. Borisov, A.K. Kazansky, and J.P. Gauyacq. Stabilisation of Alkali Adsorbate Induced States on Cu(111) Surfaces. *Surface Science*, 430:165–175, (1999).
- [106] J.P. Gauyacq, A.G. Borisov, and M. Bauer. Excited States in the Alkali/noble Metal Surface Systems: A Model System for the Study of Charge Transfer Dynamics at Surfaces. *Progress in Surface Science*, 82:244–292, (2007).
- [107] Dominik Kröner, Tillmann Klamroth, Mathias Nest, and Peter Saalfrank. Laser-Induced Charge Transfer and Photodesorption of Cs/Cu(111): Quantum Dynamical Model Simulations. *Applied Physics A*, 88:535–546, (2007).
- [108] N.-H. Ge, C. M. Wong, R. L. Lingle, J. D. McNeill, K. J. Gaffney, and C. B. Harris. Femtosecond Dynamics of Electron Localization at Interfaces. *Science*, 279:202–205, (1998).
- [109] M. Wolf, E. Knoesel, and T. Hertel. Ultrafast Dynamics of Electrons in Image-Potential States on Clean and Xe-covered Cu(111). *Phys. Rev. B*, 54:R5295–R5298, (1996).

- 
- [110] A. Hotzel, M. Wolf, and J. P. Gauyacq. Phonon-Mediated Intraband Relaxation of Image-State Electrons in Adsorbate Overlayers:  $\text{N}_2/\text{Xe}/\text{Cu}(111)$ . *The Journal of Physical Chemistry B*, 104:8438–8455, (2000).
- [111] W Berthold, U Höfer, P Feulner, and D Menzel. Influence of Xe Adlayer Morphology and Electronic Structure on Image-Potential State Lifetimes of  $\text{Ru}(0001)$ . *Chemical Physics*, 251:123–132, (2000).
- [112] F. Berthold, W. and Rebentrost, P. Feulner, and U. Höfer. Influence of Ar, Kr, and Xe Layers on the Energies and Lifetimes of Image-Potential States on  $\text{Cu}(100)$ . *Applied Physics A*, 78:131–140, (2003).
- [113] J. Stähler, M. Mehlhorn, U. Bovensiepen, M. Meyer, D. O. Kusmirek, K. Morgenstern, and M. Wolf. Impact of Ice Structure on Ultrafast Electron Dynamics in  $\text{D}_2\text{O}$  Clusters on  $\text{Cu}(111)$ . *Phys. Rev. Lett.*, 98:206105, (2007).
- [114] C. Gahl, K. Ishioka, Q. Zhong, A. Hotzel, and M. Wolf. Structure and Dynamics of Excited Electronic States at the Adsorbate/Metal Interface:  $\text{C}_6\text{F}_6/\text{Cu}(111)$ . *Faraday Discuss.*, 117:191–202, (2000).
- [115] Q Zhong, C Gahl, and M Wolf. Two-photon Photoemission Spectroscopy of Pyridine Adsorbed on  $\text{Cu}(111)$ . *Surface Science*, 496(1):21–32, (2002).
- [116] Gregory Dutton, Jingzhi Pu, Donald G. Truhlar, and X.-Y. Zhu. Lateral Confinement of Image Electron Wave Function by an Interfacial Dipole lattice. *The Journal of Chemical Physics*, 118(10):4337–4340, (2003).
- [117] John M. Herbert and Marc P. Coons. The Hydrated Electron. *Annual Review of Physical Chemistry*, 68(1):447–472, (2017).
- [118] B. Abel, U. Buck, A. L. Sobolewski, and W. Domcke. On the Nature and Signatures of the Solvated Electron in Water. *Phys. Chem. Chem. Phys.*, 14:22–34, (2012).
- [119] Ross E. Larsen, William J. Glover, and Benjamin J. Schwartz. Does the Hydrated Electron Occupy a Cavity? *Science*, 329(5987):65–69, (2010).
- [120] Madeline H. Elkins, Holly L. Williams, Alexander T. Shreve, and Daniel M. Neumark. Relaxation Mechanism of the Hydrated Electron. *Science*, 342(6165):1496–1499, (2013).
- [121] Laszlo Turi. Hydrated Electrons in Water Clusters: Inside or Outside, Cavity or Noncavity? *Journal of Chemical Theory and Computation*, 11(4):1745–1755, (2015).

- [122] Thomas Fauster and Wulf Steinmann. Chapter 8 - Two-Photon Photoemission Spectroscopy of Image States. In *Photonic Probes of Surfaces*, Electromagnetic Waves: Recent Developments in Research, pages 347–411. Elsevier, (1995).
- [123] U. Höfer, I. L. Shumay, Ch. Reuß, U. Thomann, W. Wallauer, and Th. Fauster. Time-Resolved Coherent Photoelectron Spectroscopy of Quantized Electronic States on Metal Surfaces. *Science*, 277:1480–1482, (1997).
- [124] R. A. Marcus. On the Theory of Oxidation-Reduction Reactions Involving Electron Transfer-I. *The Journal of Chemical Physics*, 24:966–978, (1956).
- [125] R.A. Marcus and Norman Sutin. Electron Transfers in Chemistry and Biology. *Biochimica et Biophysica Acta (BBA) - Reviews on Bioenergetics*, 811:265–322, (1985).
- [126] W. Berthold, P. Feulner, and U. Höfer. Decoupling of Image-Potential States by Ar Mono- And Multilayers. *Chemical Physics Letters*, 358:502–508, (2002).
- [127] D. C. Marinica, C. Ramseyer, A. G. Borisov, D. Teillet-Billy, J. P. Gauyacq, W. Berthold, P. Feulner, and U. Höfer. Effect of an Atomically Thin Dielectric Film on the Surface Electron Dynamics: Image-Potential States in the Ar/Cu(100) System. *Phys. Rev. Lett.*, 89:046802, (2002).
- [128] S. Vijayalakshmi, A. Föhlisch, F. Hennies, A. Pietzsch, M. Nagasono, W. Wurth, A.G. Borisov, and J.P. Gauyacq. Surface Projected Electronic Band Structure and Adsorbate Charge Transfer Dynamics: Ar Adsorbed on Cu(111) and Cu(100). *Chemical Physics Letters*, 427:91–95, (2006).
- [129] A. Damm, K. Schubert, J. Güdde, and U. Höfer. Observation of the Transition from Image-Potential States to Resonances on Argon-Covered Cu(111) and Ag(111) by Time-Resolved Two-Photon Photoemission. *Phys. Rev. B*, 80:205425, (2009).
- [130] B. J. Hinch and L. H. Dubois. Stable and Metastable Phases of Water Adsorbed on Cu(111). *The Journal of Chemical Physics*, 96:3262–3268, (1992).
- [131] C. Gahl, U. Bovensiepen, C. Frischkorn, K. Morgenstern, K.-H. Rieder, and M. Wolf. Ultrafast Electron Solvation Dynamics in D<sub>2</sub>O/Cu(111): Influence of Coverage and Structure. *Surface Science*, 532-535:108–112, (2003).
- [132] U. Bovensiepen, C. Gahl, J. Stähler, M. Bockstedte, M. Meyer, F. Baletto, S. Scandolo, X.-Y. Zhu, A. Rubio, and M. Wolf. A Dynamic Landscape from Femtoseconds to Minutes for Excess Electrons at Ice–Metal Interfaces. *The Journal of Physical Chemistry C*, 113(3):979–988, (2009).

- 
- [133] Michael Meyer, Julia Stähler, Daniela O. Kusmirek, Martin Wolf, and Uwe Bovensiepen. Determination of the Electron's Solvation Site on D<sub>2</sub>O/Cu(111) Using Xe Overlayers and Femtosecond Photoelectron Spectroscopy. *Phys. Chem. Chem. Phys.*, 10:4932–4938, (2008).
- [134] Julia Stähler, Uwe Bovensiepen, Michael Meyer, and Martin Wolf. A Surface Science Approach to Ultrafast Electron Transfer and Solvation Dynamics at Interfaces. *Chem. Soc. Rev.*, 37:2180–2190, (2008).
- [135] Julia Stähler, Uwe Bovensiepen, Michael Meyer, and Martin Wolf. A Surface Science Approach to Ultrafast Electron Transfer and Solvation Dynamics at Interfaces. *Chem. Soc. Rev.*, 37:2180–2190, (2008).
- [136] J. Güdde and U. Höfer. Review on Femtosecond Time-Resolved Studies of Image-Potential States at Surfaces and Interfaces of Rare-Gas Adlayers. *Progress in Surface Science*, 80:49–91, (2005).
- [137] Philipp Auburger, Ishita Kemeny, Cord Bertram, Manuel Ligges, Michel Bockstedte, Uwe Bovensiepen, and Karina Morgenstern. Microscopic Insight into Electron-Induced Dissociation of Aromatic Molecules on Ice. *Phys. Rev. Lett.*, 121:206001, (2018).
- [138] Julia Stähler, Cornelius Gahl, Uwe Bovensiepen, and Martin Wolf. Ultrafast Electron Dynamics at Ice–Metal Interfaces: Competition Between Heterogeneous Electron Transfer and Solvation. *The Journal of Physical Chemistry B*, 110(19):9637–9644, (2006).
- [139] Tomas Vondrak, Stephen R. Meech, and John M. C. Plane. Photoelectric Emission from the Alkali Metal Doped Vacuum-ice Interface. *The Journal of Chemical Physics*, 130(5):054702, (2009).
- [140] Christopher Penschke, John Thomas, Cord Bertram, Angelos Michaelides, Karina Morgenstern, Peter Saalfrank, and Uwe Bovensiepen. Hydration at Highly Crowded Interfaces. *Phys. Rev. Lett.*, 130:106202, (2023).
- [141] A. Einstein. Über einen die Erzeugung und Verwandlung des Lichtes betreffenden heuristischen Gesichtspunkt. *Annalen der Physik*, 322:132–148, (1905).
- [142] M. P. Seah and W. A. Dench. Quantitative Electron Spectroscopy of Surfaces: A Standard Data Base for Electron Inelastic Mean Free Paths in Solids. *Surface and Interface Analysis*, 1:2–11, (1979).
- [143] Stephan Hüfner. *Photoelectron Spectroscopy, Principles and Applications*. Springer, Berlin, Heidelberg, Heidelberg, (2003).

- [144] SPECS Surface Nano Analysis. Inverse Photoelectron Spectroscopy (IPES) or Bremsstrahlung Isochromate Spectroscopy (BIS). <https://www.specs-group.com/nc/specsgroup/knowledge/methods/detail/ipes-bis/>, (2022).
- [145] M. Wolf, A. Hotzel, E. Knoesel, and D. Velic. Direct and Indirect Excitation Mechanisms in Two-photon Photoemission Spectroscopy of Cu(111) and CO/Cu(111). *Phys. Rev. B*, 59:5926–5935, (1999).
- [146] H. Ueba and Branko Gumhalter. Theory of Two-photon Photoemission Spectroscopy of Surfaces. *Progress in Surface Science*, 82:193–223, (2007).
- [147] Ken Onda, Bin Li, and Hrvoje Petek. Two-photon Photoemission Spectroscopy of TiO<sub>2</sub> (110) Surfaces Modified by Defects and O<sub>2</sub> or H<sub>2</sub>O Adsorbates. *Phys. Rev. B*, 70:045415, (2004).
- [148] Uwe Bovensiepen Hrvoje Petek and Martin Wolf. *Dynamics at Solid State Surfaces and Interfaces, Vol. 2*. Wiley-VCH Verlag and Co. KGaA, Boschstr. 12, 69496 Weinheim, Germany, (2012).
- [149] Rodney Loudon. *The Quantum Theory of Light, 3rd Edition*. Oxford University Press, Great Clarendon Street, Oxford ox2 6DP, (2000).
- [150] John Weiner and P. T. Ho. *Light—Matter Interaction*. John Wiley and Sons, Ltd, Hoboken, New Jersey, (2003).
- [151] B.N. Sanchez and T. Brandes. Matrix Perturbation Theory for Driven Three-level Systems with Damping. *Annalen der Physik*, 13:569–594, (2004).
- [152] Cornelius Gahl. *Elektronentransfer- und Solvatisierungsdynamik in Eis adsorbiert auf Metalloberflächen*. PhD thesis, Freie University Berlin, (2004).
- [153] Martin Julius Lisowski. *Elektronen- und Magnetisierungsdynamik in Metallen untersucht mit zeitaufgelöster Photoemission*. PhD thesis, Freie University Berlin, (2005).
- [154] Julia Stähler. *Freezing Hot Electrons - Electron Transfer and Solvation Dynamics at D<sub>2</sub>O and NH<sub>3</sub>- Metal Interfaces*. PhD thesis, Freie University Berlin, (2007).
- [155] Patrick S. Kirchmann. *Ultrafast Electron Dynamics in Low-Dimensional Materials*. PhD thesis, Freie University Berlin, (2008).
- [156] Arthur Hotzel. *Femtosekunden-Elektronendynamik der Adsorbat-bedeckten Cu(111)-Oberfläche*. PhD thesis, Freie University Berlin, (1999).
- [157] Wibke Bronsch. *Molecular Exciton Related Phenomena Studied by Two-Photon Photoemission*. PhD thesis, Freie University Berlin, (2018).

- 
- [158] Coherent. *Operator's Manual: Micra-5 Modelocked Titanium: Sapphire Laser system*. Technical report, Coherent Inc., (2009).
- [159] Jean-Claude Diels and Wolfgang Rudolph. *Ultrashort Laser Pulse Phenomena*. Academic Press, Inc, California, (1996).
- [160] Claude Rulliere. *Femtosecond Laser Pulses*. Springer Science+Business Media, Inc, New York, (2005).
- [161] Donna Strickland and Gerard Mourou. Compression of Amplified Chirped Optical Pulses. *Optics Communications*, 56:219–221, (1985).
- [162] Press release. The Nobel Prize in Physics 2018. <https://www.nobelprize.org/prizes/physics/2018/press-release/>, (2018).
- [163] Klaas Wynne, Gavin D. Reid, and Robin M. Hochstrasser. Regenerative Amplification of 30-fs Pulses in Ti:sapphire at 5 kHz. *Optics Letters*, 19:895–897, (1994).
- [164] Rüdiger Paschotta. Regenerative Amplifiers in the RP Photonics Encyclopedia. [https://www.rp-photonics.com/regenerative\\_amplifiers.html](https://www.rp-photonics.com/regenerative_amplifiers.html), (2018).
- [165] Coherent. *Operator's Manual: RegA Model 9000*. Technical report, Coherent Inc., (2009).
- [166] Newport. The Effect of Dispersion on Ultrashort Pulses. <https://www.newport.com/n/the-effect-of-dispersion-on-ultrashort-pulses>, (2022).
- [167] Hans Lüth. *Solid Surfaces, Interfaces and Thin Films*. Springer Science+Business Media, Inc, New York, (2010).
- [168] Q.B. Lu, D.J. O'Connor, B.V. King, and R.J. MacDonald. Local Electrostatic Potential Determination of Cs/Cu(111) Surfaces by Negative Ion Spectroscopy. *Surface Science*, 347:L61–L65, (1996).
- [169] Michael Meyer. *Ultrafast Electron Dynamics at Alkali/Ice Structures Adsorbed on a Metal Surface*. PhD thesis, Freie University Berlin, (2011).
- [170] Uwe Bovensiepen, Cornelius Gahl, and Martin Wolf. Solvation Dynamics and Evolution of the Spatial Extent of Photoinjected Electrons in D<sub>2</sub>O/Cu(111). *The Journal of Physical Chemistry B*, 107:8706–8715, (2003).
- [171] G. Held and D. Menzel. Isotope Effects in Structure and Kinetics of Water Adsorbates on Ru(001). *Surface Science*, 327:301–320, (1995).

- [172] Uwe Bovensiepen, Cornelius Gahl, and Martin Wolf. Solvation Dynamics and Evolution of the Spatial Extent of Photoinjected Electrons in  $D_2O/Cu(111)$ . *The Journal of Physical Chemistry B*, 107:8706–8715, (2003).
- [173] Th. von Hofe, J. Kröger, and R. Berndt. Adsorption Geometry of  $Cu(111)$ –Cs Studied by Scanning Tunneling Microscopy. *Phys. Rev. B*, 73:245434, (2006).
- [174] Angelos Michaelides and Karina Morgenstern. Ice Nanoclusters at Hydrophobic Metal Surfaces. *Nature Materials*, 6:597–601, (2007).
- [175] Kang Xu and Arthur von Wald Cresce.  $Li^+$  -Solvation/Desolvation Dictates Interphasial Processes on Graphitic Anode in Li Ion Cells. *Journal of Materials Research*, 27:2327–2341, (2012).
- [176] Satoshi Ashihara, Nils Huse, Agathe Espagne, Erik T. J. Nibbering, and Thomas Elsaesser. Ultrafast Structural Dynamics of Water Induced by Dissipation of Vibrational Energy. *The Journal of Physical Chemistry A*, 111:743–746, (2007).
- [177] M. L. Cowan, B. D. Bruner, N. Huse, J. R. Dwyer, B. Chugh, E. T. J. Nibbering, T. Elsaesser, and R. J. D. Miller. Ultrafast Memory Loss and Energy Redistribution in the Hydrogen Bond Network of Liquid  $H_2O$ . *Nature*, 434:199–202, (2005).
- [178] John Weeks. Personal communication with Igor software technical support team led by Mr. John Weeks during the analysis of the data. A similar topic was discussed in the open forum of the Igor software. The link of the discussion given as follows. See the response of the technical help on 23-08-2017, <https://www.wavemetrics.com/forum/general/how-can-i-force-double-exponential-x-offset-asymptote-constant>, June 2021.
- [179] B. Hellsing, D. V. Chakarov, L. Österlund, V. P. Zhdanov, and B. Kasemo. Photoinduced Desorption of Potassium Atoms from a Two Dimensional Overlayer on Graphite. *The Journal of Chemical Physics*, 106(3):982–1002, (1997).
- [180] Peter Nordlander, Claes Holmberg, and John Harris. Physisorption Interaction of  $H_2$  with noble metals. *Surface Science*, 152-153:702–709, (1985).
- [181] S. Fölsch, U. Barjenbruch, and M. Henzler. Atomically Thin Epitaxial Films of NaCl on Germanium. *Thin Solid Films*, 172:123–132, 1989.
- [182] Friederike Matthaei, Sarah Heidorn, Konrad Boom, Cord Bertram, Ali Safiei, Jörg Henzl, and Karina Morgenstern. Coulomb Attraction During the Carpet Growth Mode of NaCl. *Journal of Physics: Condensed Matter*, 24:354006, 2012.



- [183] Th. Seyller, M. Caragiu, R.D. Diehl, P. Kaukasoina, and M. Lindroos. Observation of Top-site Adsorption for Xe on Cu(111). *Chemical Physics Letters*, 291(5):567–572, 1998.
- [184] S. Å. Lindgren, L. Walldén, J. Rundgren, P. Westrin, and J. Neve. Structure of Cu(111) $p(2 \times 2)$ Cs Determined by Low-Energy Electron Diffraction. *Phys. Rev. B*, 28:6707–6712, 1983.
- [185] R. Wallauer, M. Raths, K. Stallberg, L. Münster, D. Brandstetter, X. Yang, J. Gütde, P. Puschnig, S. Soubatch, C. Kumpf, F. C. Bocquet, F. S. Tautz, and U. Höfer. Tracing Orbital Images on Ultrafast Time Scales. *Science*, 371:1056–1059, (2021).



# List of Publications

- **J. Thomas**, C. Bertram, J. Daru, J. Patwari, I. Langguth, P. Zhou, D. Marx, K. Morgenstern, and U. Bovensiepen. Competition between Coulomb and van der Waals Interactions in Xe–Cs<sup>+</sup> Aggregates on Cu(111) Surfaces, *Phys. Rev. Lett.*, 127:266802, (2021).
- Christopher Penschke, **John Thomas**, Cord Bertram, Angelos Michaelides, Karina Morgenstern, Peter Saalfrank, and Uwe Bovensiepen. Solvation at highly crowded interfaces. *Phys. Rev. Lett.*, 130:106202, (2023).
- **J. Thomas et al.**, Ultrafast solvation dynamics of Cs-water clusters at interfaces. Under preparation, (2023).



## Competition between Coulomb and van der Waals Interactions in Xe-Cs<sup>+</sup> Aggregates on Cu(111) Surfaces

J. Thomas<sup>1</sup>, C. Bertram<sup>1,2</sup>, J. Daru<sup>3,\*</sup>, J. Patwari<sup>1,2</sup>, I. Langguth<sup>2</sup>, P. Zhou<sup>1</sup>, D. Marx<sup>3</sup>,  
K. Morgenstern<sup>2</sup> and U. Bovensiepen<sup>1,†</sup>

<sup>1</sup>*Fakultät für Physik and Center for Nanointegration (CENIDE), Universität Duisburg-Essen,  
Lotharstrasse 1, 47057 Duisburg, Germany*

<sup>2</sup>*Lehrstuhl für Physikalische Chemie I, Ruhr-Universität Bochum, Universitätsstrasse 150, 44801 Bochum, Germany*

<sup>3</sup>*Lehrstuhl für Theoretische Chemie, Ruhr-Universität Bochum, Universitätsstrasse 150, 44801 Bochum, Germany*

(Received 19 December 2020; revised 7 July 2021; accepted 19 November 2021; published 23 December 2021)

Microscopic insight into interactions is a key for understanding the properties of heterogenous interfaces. We analyze local attraction in noncovalently bonded Xe-Cs<sup>+</sup> aggregates and monolayers on Cu(111) as well as repulsion upon electron transfer. Using two-photon photoemission spectroscopy, scanning tunneling microscopy, and coupled cluster calculations combined with an image-charge model, we explain the intricate impact Xe has on Cs<sup>+</sup>/Cu(111). We find that attraction between Cs<sup>+</sup> and Xe counterbalances the screened Coulomb repulsion between Cs<sup>+</sup> ions on Cu(111). Furthermore, we observe that the Cs 6s electron is repelled from Cu(111) due to xenon's electron density. Together, this yields a dual, i.e., attractive or repulsive, response of Xe depending on the positive or negative charge of the respective counterparticle, which emphasizes the importance of the Coulomb interaction in these systems.

DOI: 10.1103/PhysRevLett.127.266802

Properties of heterogenous interfaces are determined by covalent, Coulomb, and van der Waals interactions at an extent which is specific to the particular interface system. Competition or cooperation are decisive, as is highlighted, for example, by a doping-induced, reentrant metal-insulator-metal phase transition in alkali doped K<sub>x</sub>C<sub>60</sub> adsorbed on a Au(111) surface [1–3]. While the individual fullerenes are interacting among each other and with the substrate by van der Waals interaction, the electrons donated by the alkalis determine the electronic properties of the interface by exchange and Coulomb interaction [3,4]. A similarly promising, yet unexplored, pathway might be to prepare aggregates consisting of atoms as building blocks which allow a modification of the effective overall interaction by a variation of the atomic interactions. In this Letter, we lay the foundations of this approach. We demonstrate a modification of the local interaction by coadsorbing Xe to Cs/Cu(111).

On metal surfaces, the adsorption of noble gases like Xe is governed by an interplay of van der Waals attraction and Pauli repulsion [5,6]. Alkali atoms like Cs transfer, upon adsorption, their single valence electron to the metal surface [7–10]. They are, in a good approximation, cations Cs<sup>+</sup> dominated by Coulomb interaction. The resulting surface dipole lowers the work function [11–13]. The investigation of coadsorbed Cs and Xe promises novel insights regarding competition (or cooperation) of these interactions. Such understanding is highly relevant from a fundamental viewpoint because local Coulomb interactions are essential in understanding structural order, electronic properties, and

the elementary processes at heterogeneous interfaces. Those local effects and a potential control of the interactions are interesting for sensor design and energy conversion [14,15], among other applications. So far, electronic and ionic interactions in multicomponent adsorbate systems are unknown on the single-particle scale.

Few percents of a monolayer (ML) Cs<sup>+</sup> form on Cu(111) a hexagonal alkali lattice due to mutual Coulomb repulsion of adjacent alkali ions observed in scanning tunneling microscopy (STM) [16]. The missing valence electron of the adsorbed alkalis induces an unoccupied electronic state observed in inverse photoemission [17] and two-photon photoemission (2PPE) [11,18]. The antibonding character of this Cs 6s state manifests itself in an ultrafast energy shift due to the propagation of a nuclear wave packet along the Cu–Cs<sup>+</sup> coordinate [19].

Adsorption of noble gas layers on metal surfaces increases the lifetime of electrons in image potential states (IPs) in front of the surface [20,21] since their dielectric response repels the electronic wave function reducing the wave function overlap with electronic states of the substrate [22,23]. Though well established in two dimensions, this phenomenon remains to be explored for structures of lower dimensionality. This holds even more since the highly polarizable Xe is considered as a nonpolar solvent in the presence of cations [24]. The fundamental question of interest, here, is how Xe affects the structural and electronic properties of alkali ions on surfaces.

In this Letter, we unveil that Xe mediates an effective, attractive interaction between Cs<sup>+</sup> on the surface

and enhances attraction between  $\text{Cs}^+$  and  $\text{Cu}(111)$ . Furthermore, Xe induces a repulsion of the Cs 6s electron from  $\text{Cu}(111)$ . We trace this dual impact of Xe back to its polarization of opposite sign induced by cations and electrons. This was achieved by using STM and 2PPE as complementary tools which probe  $\text{Cs}^+$  and Cs, respectively, on a wetting Xe ML with  $\text{Cs}^+$  on  $\text{Cu}(111)$ , supplemented by aggregates at sub-ML Xe. Supported by coupled cluster calculations in conjunction with image-charge modeling of the screened Coulomb repulsion, we showcase the impact of the dominant Coulomb interaction locally.

The experiments were performed in two separate ultra-high vacuum systems at a base pressure of  $4 \times 10^{-10}$  mbar. STM was carried out at  $T \leq 8$  K. 2PPE spectra were measured at  $T = 30$  K using two time-delayed laser pulses of 3.1 eV photon energy, 40 fs pulse duration at an incident fluence of  $1 \text{ mJ}/\text{cm}^2$  [25]. The  $\text{Cu}(111)$  surfaces were prepared by sputter-anneal cycles. The Cs atoms were deposited at  $T = 200$  K from commercial Cs dispensers (SAES getters). The alkali coverage was determined by counting the ions on  $\text{Cu}(111)$  using STM and an analysis of the work function in 2PPE [11,12]. Xenon was deposited from a background pressure of  $2 \times 10^{-6}$  mbar in the STM and exposed to a Xe beam in the 2PPE setup. The Xe coverage was determined from temperature programmed desorption calibrated by desorbing the first ML from  $\text{Cu}(111)$ . All electronic structure calculations have been performed using the ORCA package. The energies were computed using canonical CCSD(T) theory employing complete basis set (CBS) extrapolation [26].

After Cs deposition, protrusions cover the surface randomly at an apparent coverage of  $7 \times 10^{-4}$  ML, which are identified as  $\text{Cs}^+$ , Fig. 1(a).  $\text{Cs}^+$  is partially pinned at defects and partially mobile, leading to a striped appearance. After Xe adsorption,  $\text{Cs}^+$  ions are trapped in Xe- $\text{Cs}^+$  aggregates, Figs. 1(b) and 1(c). The flat parts of the aggregates exhibit the same  $R30^\circ - \sqrt{3} \times \sqrt{3}$  hexagonal superstructure as pure Xe/ $\text{Cu}(111)$ , see insets in Figs. 1(a) and 1(b). Thus, we assign the flat parts of the aggregates to single Xe layers. The aggregates exhibit protrusions at the border and in the center that do not exist for pure Xe layers, Fig. 1(b) inset. The Laplace filtered image in panel (c) identifies two causes. For some, marked by yellow arrows in Fig. 1(c), a small feature with the lateral size of a  $\text{Cs}^+$  is surrounded laterally by Xe atoms, which are imaged at a larger apparent height than other Xe atoms. For other protrusions, marked by black arrows in (c), the lateral size of all features is similar. We assign these latter protrusions to  $\text{Cs}^+$  covered by Xe. Both cases represent 2D solvation of  $\text{Cs}^+$ , but of different coordination. In the aggregate center, one  $\text{Cs}^+$  is fully solvated, showing up in the Laplace-filtered image as a Xe heptamer. Such heptamers are the dominant species in STM images of 1 ML Xe/0.16 ML  $\text{Cs}^+$ / $\text{Cu}(111)$  in Fig. 1(e). Their number reflects the  $\text{Cs}^+$

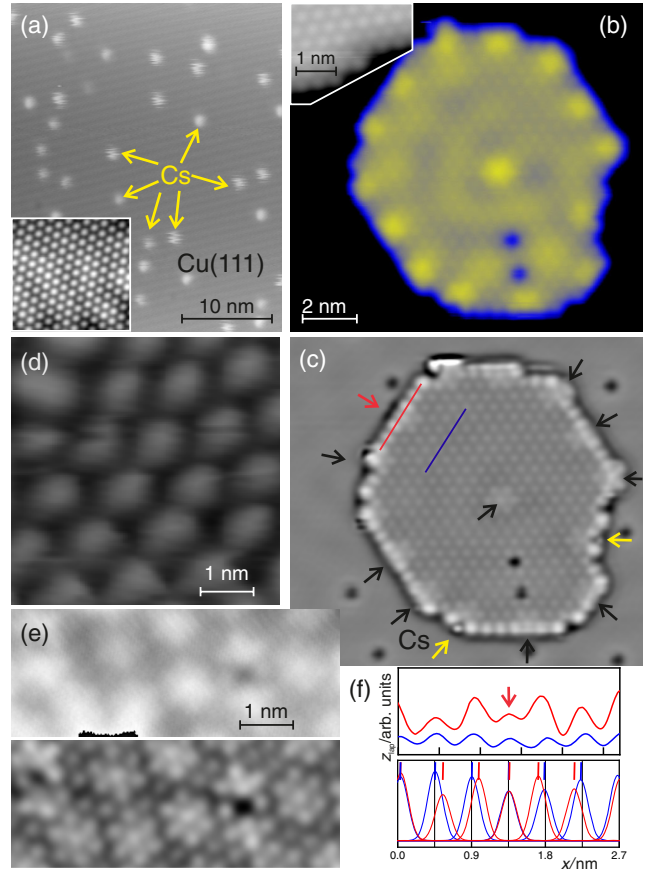


FIG. 1. STM images (a) of  $\text{Cs}^+$ / $\text{Cu}(111)$ ,  $-500$  mV,  $10$  pA, and (b) of a Xe- $\text{Cs}^+$  aggregate on  $\text{Cu}(111)$  using a false-color scale,  $10$  pA,  $-25$  mV. Insets in (a),(b) show  $1$  ML Xe/ $\text{Cu}(111)$ , recorded at  $1.2$  nA,  $100$  mV on a wetting ML and at an aggregate perimeter,  $44$  pA,  $7$  mV, respectively. (c) Laplace-filtered image of (b). The Xe: $\text{Cs}^+$  ratio in (b),(c) is  $40:1$ . (d)  $0.16$  ML  $\text{Cs}^+$ / $\text{Cu}(111)$ ,  $10$  pA,  $250$  mV; (e) Original (top) and Laplace-filtered image (bottom) of  $1$  ML Xe on top of  $0.16$  ML  $\text{Cs}^+$ / $\text{Cu}(111)$ ,  $89$  pA,  $250$  mV, (f) apparent height profiles (top) along the lines marked in panel (c) in identical colors and their Gaussian fits with maxima marked (bottom).

coverage. The uniformity of the solvatomers facilitates an analysis by a space averaging method like 2PPE reported below. We explain the observed structure by a carpetlike growth [36,37] of the Xe layer across  $\text{Cs}^+$  which is facilitated by the larger size of Xe ( $r_{\text{Xe}} = 216$  pm vs  $r_{\text{Cs}^+} = 174$  pm) and its larger physisorption distance of  $360$  pm [38] compared to the chemisorption distance of  $\text{Cs}^+$  of  $301$  pm [39].

Height profiles across a row of Xe atoms in the interior of the aggregate reflect the regular distance between two Xe of  $0.45$  nm, blue line in Fig. 1(f). The distances between the maxima in the height profile across a Xe-covered  $\text{Cs}^+$  are less regular and indicate a nearest neighbor  $\text{Cs}^+$ -Xe distance which is shorter by  $\sim 50$  pm, red line and vertical markers in Fig. 1(f), better observed in the Gaussian fits to the height profiles (bottom). This leads to a larger distance

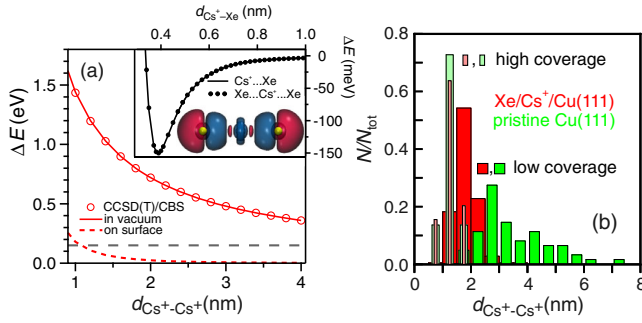


FIG. 2.  $\text{Cs}^+-\text{Cs}^+$  distances in  $\text{Xe}-\text{Cs}^+$  aggregates: (a) Repulsive interactions between two  $\text{Cs}^+$  without (solid line) and with contact to a metal (red dashed line) as a function of the  $\text{Cs}^+-\text{Cs}^+$  distance. Circles represent the CCSD(T)/CBS reference. Inset: Attractive interactions between  $\text{Cs}^+$  and one (or two) Xe atoms per Xe obtained from CCSD(T)/CBS calculations as a function of  $\text{Cs}^+-\text{Xe}$  (equi)distance; the resulting attraction of 150 meV per nearest-neighbor Xe atom provides the gray dashed line in the main panel. The blue and red isosurfaces of the charge density difference visualize charge accumulation and depletion, respectively, of  $\text{Xe}-\text{Cs}^+-\text{Xe}$  at the optimized equidistance of 0.39 nm. Xe cores are yellow [26]. (b) Nearest-neighbor distance histogram of  $\text{Cs}^+$  on Cu(111) in green and in  $\text{Xe}-\text{Cs}^+$  aggregates in red normalized to the number of distances  $N_{\text{tot}}$  in STM images for  $\Theta_{\text{Cs}^+} = 7 \times 10^{-4}$  ML (low) and 0.16 ML (high).

to the next nearest neighbor to maintain registry with the Xe environment [40].

The formation of such aggregates is surprising as aggregates containing multiple positive ions are expected to break up into smaller ones due to Coulomb repulsion. We shed light on this paradox by CCSD(T)/CBS calculations to compare the  $\text{Cs}^+-\text{Xe}$  attraction to the  $\text{Cs}^+-\text{Cs}^+$  repulsion in the absence and presence of screening by a metal surface, see Fig. 2(a). At the preferred  $\text{Cs}^+-\text{Xe}$  distance of 0.4 nm, which is in accord with the measured distances, see Fig. 1(f), the attractive interactions between  $\text{Cs}^+$  and Xe amounts to  $\sim 150$  meV in vacuum, see Fig. 2(a), inset. We conclude that, although this  $\text{Cs}^+-\text{Xe}$  attraction features significant electronic polarization as demonstrated by our charge density difference analysis, Fig. 2(a) inset, in addition to dispersion, it is one order of magnitude smaller than the unscreened Coulomb repulsion between two  $\text{Cs}^+$  at observed separations of  $d_{\text{Cs}^+-\text{Cs}^+} \approx 1-2$  nm in the aggregates, see Fig. 2(b). Thus, without a metal support,  $\text{Xe}-\text{Cs}^+$  aggregates should disperse into smaller ones in contrast to our observations.

To scrutinize the role of Cu(111), we have factored in image charges [41,42]. Having shown that the Coulomb repulsion between point charges represents the  $\text{Cs}^+-\text{Cs}^+$  interactions as given by explicit electronic structure calculations faithfully at the experimentally relevant distances [compare solid line to circles in Fig. 2(a)], we discuss the impact of image charges at the metal surface on equal footing [26]. As evidenced by Fig. 2(a), the screening effect is enormous at 1.5 nm: The Coulomb repulsion is decreased

from  $\approx 1$  eV (solid line) to  $\approx 50$  meV (red dashed line), which is much smaller than the  $\text{Cs}^+-\text{Xe}$  attraction of 150 meV per Xe atom (gray dashed line).

The distances between two  $\text{Cs}^+$  have been analyzed for low and high  $\text{Cs}^+$  coverage  $\Theta_{\text{Cs}^+}$  in the absence (presence) of Xe yielding the green (red) data in Fig. 2(b). For low  $\Theta_{\text{Cs}^+}$ , a sharp distribution of  $\text{Cs}^+-\text{Cs}^+$  pairs at short distances of about 1–2 nm is observed within  $\text{Xe}-\text{Cs}^+$  aggregates for different Xe coverages [26]. In this limit, the screened Coulomb repulsion between two  $\text{Cs}^+$  on Cu(111) is overcompensated by the attractive interaction between  $\text{Cs}^+$  and Xe, as revealed by the calculations. Phenomenologically, an effective attraction between cations on Xe/Cu(111) with reference to the pristine Cu(111) surface is obtained. The picture extracted is that individual  $\text{Cs}^+/\text{Cu}(111)$  prefer to reside at Xe aggregates given their favorable interactions with Xe. Being bound to the rim, the remaining weak repulsion between any two such cations leads to similar  $\text{Cs}^+-\text{Cs}^+$  distances along the perimeter.

At higher  $\Theta_{\text{Cs}^+}$ , a regular superstructure forms with an average  $\text{Cs}^+-\text{Cs}^+$  distance of  $(1.25 \pm 0.22)$  nm, which is smaller than the distance reported for the aggregates, Figs. 1(d), 2(b). Xe adsorption leads to a regular array of heptamers, also found in the aggregate center in Fig. 1(c), with the same distance of  $(1.28 \pm 0.28)$  nm, Figs. 1(e), 2(b). As for low  $\Theta_{\text{Cs}^+}$ , the Xe overgrows the  $\text{Cs}^+$  like a carpet, Fig. 1(e). Within the carpet, the  $\text{Xe}-\text{Cs}^+$  interaction also modifies the adjacent Xe-Xe distance, but the larger Coulomb energy at the shorter  $\text{Cs}^+-\text{Cs}^+$  distance is not overcompensated so that the distance histogram remains unaltered [40]. These are the surfaces that were investigated by time-resolved 2PPE to provide insight in the response of the environment to this local excitation [9,43]. As sketched in Fig. 3, the photon energy is set for resonant electron attachment from Cu(111) to the Cs 6s state [18,19]. Adsorption of 1 ML Xe increases the work function of 0.14 ML  $\text{Cs}^+/\text{Cu}(111)$  by  $(100 \pm 15)$  meV, while the energy of the Cs 6s feature changes by  $(120 \pm 15)$  meV. As discussed in [26], this behavior suggests a Xe-induced decoupling of the Cs 6s electron from Cu(111), contrary to the effective attraction Xe mediates on the metal surface between two  $\text{Cs}^+$  reported above.

Time-resolved 2PPE provides microscopic insights into this decoupling. Figure 3(a) shows the 2PPE intensity autocorrelation as a function of time delay  $\Delta t$  between two identical laser pulses. The Cs 6s feature occurs at time zero at  $E-E_F = 2.6$  eV and relaxes to lower energy with increasing  $\Delta t$  due to the progression of the nuclear wave packet on the antibonding potential energy surface [19]. Two effects of Xe are identified. First, the Cs 6s electron relaxation time  $\tau$  is increased by a factor of 6 from 13 to 80 fs, Fig. 3(b) and [44]. Since such a pronounced increase in  $\tau$  represents a substantial reduction in the overlap of the Cs 6s wave function with Cu(111) states [9], we conclude that Xe coadsorption induces a decoupling of the Cs 6s

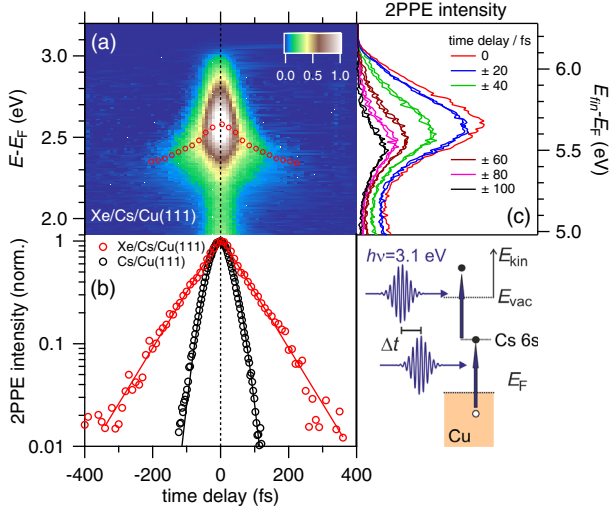


FIG. 3. 2PPE intensity (a) of 1 ML Xe/0.16 ML Cs<sup>+</sup>/Cu(111) recorded at  $T = 30$  K in false color as a function of intermediate energy  $E - E_F$  (left), final state energy (right), and time delay. The time-dependent energy of the Cs 6s feature is indicated by circles. (b) Autocorrelation traces of the Cs 6s state (circles), obtained by integrating the intensity within 200 and 150 meV for Cs/Cu(111) (black) and Xe/Cs/Cu(111) (red), respectively. Relaxation times of  $(13 \pm 3)$  and  $(80 \pm 10)$  fs for Cs/Cu(111) and Xe/Cs/Cu(111), respectively, are obtained by fits of single exponential decays convolved with the autocorrelation of the laser pulse (solid lines) [44]. (c) 2PPE spectra at the indicated time delays.

wave function from Cu(111). Second, while the observed transient energy gain is 0.24 eV, similar to Cs/Cu(111) [19], Xe influences the time dependent energy changes  $\Delta E$ , Fig. 4(a). Following [19], we estimate the potential along the surface normal direction from  $\Delta E(\Delta t)$ . We convert the

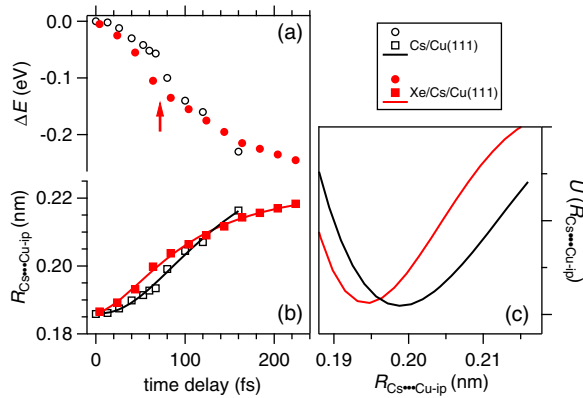


FIG. 4. Time-dependent change of intermediate state energy  $\Delta E$  (a) plotted for Xe/Cs<sup>+</sup>/Cu(111) from Fig. 3 and for bare Cs<sup>+</sup>/Cu(111) using data from [19]. The respective distances  $R_{\text{Cs}\dots\text{Cu-ip}}$  and the excited state potential energy surface  $U(R_{\text{Cs}\dots\text{Cu-ip}})$  are determined with (red) and without (black) coadsorbed Xe. Note that the absolute energy difference between the two potentials in (c) is not known.

energy to the distance  $R_{\text{Cs}\dots\text{Cu-ip}}$  between Cs and the image-plane of the Cu(111) interface using previous calculations [45]. We fit the values by an analytical function, Fig. 4(b), under the assumption of the same  $R_{\text{Cs}\dots\text{Cu-ip}}(E)$  because Xe has a minor effect on the Cs 6s energy. An inflection point identified in  $\Delta E$  for Xe/Cs/Cu(111) at  $\Delta t = 70$  fs, see arrow in panel (a), is not evident for Cs/Cu(111), but appears in Fig. 4(b) at later delays than for Xe/Cs/Cu(111). Using  $\partial^2 R^2 / \partial \Delta t^2$ , which defines the force  $F$  acting on the Cs ion core, we determine the excited state potential  $U(R_{\text{Cs}\dots\text{Cu-ip}}) = -\int F dR_{\text{Cs}\dots\text{Cu-ip}}$ . The minimum in  $U$  shifts  $(4.0 \pm 1.5)$  pm toward Cu(111) upon adding Xe, resembling the attraction Xe mediates among two Cs<sup>+</sup> concluded above, Fig. 4(c).

Our analysis establishes that adding Xe to Cs<sup>+</sup>/Cu(111) compensates for the repulsive interaction in the surface plane between adjacent Cs<sup>+</sup> and enhances the binding of Cs<sup>+</sup> to Cu(111) along the surface normal. The observed increase in Cs 6s electron lifetime upon adding Xe is explained by a decrease in wave function overlap with the states of Cu(111), which implies that the respective Cs wave function  $\Psi_{6s}$  is repelled by Xe from Cu(111) to the vacuum. Such repulsion has been previously concluded from an increase in electronic lifetimes of IPSs upon adsorbing a closed noble gas layer on metal surfaces [20–23]. It is based on the dielectric polarization response of the noble gas electron density to the transient IPS population. In the present case, Cs<sup>+</sup> is surrounded by Xe (Fig. 1). Since  $\Psi_{6s}$  extends laterally over several Cu lattice constants [9] and affects the appearance of adjacent Xe atoms in STM images (Fig. 1), we explain the repulsion of  $\Psi_{6s}$  by the part of the Xe electron density that is beneath Cs<sup>+</sup> which reduces the overlap of  $\Psi_{6s}$  with Cu(111) states. While on homogenous surfaces in two spatial dimensions, 1 ML of Xe doubles the IPS lifetime [23], the larger, sixfold increase in  $\tau$ , see Fig. 3(b), is explained by the localized nature of  $\Psi_{6s}$ . The lifetime increase for Xe/Cs/Cu(111) is attributed to the reduced dimension where seven Xe atoms modify a single Cs<sup>+</sup>, while for the two-dimensional layers, the homogenous electron density acts and provides less electron density for screening.

In conclusion, we have investigated the mutual influence of Xe and Cs<sup>+</sup> on a Cu(111) surface and discovered two-dimensional, nanostructured Xe-Cs<sup>+</sup> aggregates. Weak interactions with Xe outperform the Coulomb repulsion between cations due to screening by the metallic surface. A proposed electron repulsion between the Xe electron density and the Cs 6s wave function corroborates the dominant character of the local Coulomb interaction. We believe that our results are of general nature. Since alkali and noble gases represent groups in the periodic table, systematic variation of the described local interactions could become feasible by changing the atomic polarizability via the noble gas and the different surface dipoles via alkalis. Extension to earth alkalis and halogens bears



additional potential. Since the interfacial electronic structure and the electron affinity of the constituents contribute as well [23], further means for modification exist. The atomic-scale understanding established here provides opportunities to tune local, noncovalent interactions and opens the doorway toward establishing novel nanostructuring strategies of heterogenous interfaces.

This work was supported by the European Union's Horizon 2020 research and innovation program under the Marie Skłodowska-Curie Grant Agreement No. 801459—FP-RESOMUS, by the Deutsche Forschungsgemeinschaft (DFG, German Research Foundation) under Germany's Excellence Strategy—Grant No. EXC 2033—390677874—RESOLV, GRK 2376/331085229, and Project ID No. 278162697—SFB 1242.

\*janos.daru@ttk.elte.hu

Eötvös Loránd University, Department of Organic Chemistry Budapest, Hungary.

†uwe.bovensiepen@uni-due.de

- [1] A. Wachowiak, R. Yamachika, K. H. Khoo, Y. Wang, M. Grobis, D.-H. Lee, S. G. Louie, and M. F. Crommie, *Science* **310**, 468 (2005).
- [2] Y. Wang, R. Yamachika, A. Wachowiak, M. Grobis, K. H. Khoo, D.-H. Lee, S. G. Louie, and M. F. Crommie, *Phys. Rev. Lett.* **99**, 086402 (2007).
- [3] M. Feng, J. Zhao, and H. Petek, *Science* **320**, 359 (2008).
- [4] X. Cui, D. Han, H. Guo, L. Zhou, J. Qiao, Q. Liu, Z. Cui, Y. Li, C. Lin, L. Cao, W. Ji, H. Petek, and M. Feng, *Nat. Commun.* **10**, 3374 (2019).
- [5] P. S. Bagus, V. Staemmler, and C. Wöll, *Phys. Rev. Lett.* **89**, 096104 (2002).
- [6] J. L. F. Da Silva, C. Stampfl, and M. Scheffler, *Phys. Rev. Lett.* **90**, 066104 (2003).
- [7] I. Langmuir, *J. Am. Chem. Soc.* **54**, 2798 (1932).
- [8] M. Scheffler, Ch. Droste, A. Fleszar, F. Maca, G. Wachutka, and G. Barzel, *Physica (Amsterdam)* **172B**, 143 (1991).
- [9] J. P. Gauyacq, A. G. Borisov, and M. Bauer, *Prog. Surf. Sci.* **82**, 244 (2007).
- [10] A. Politano, G. Chiarello, G. Benedek, E. V. Chulkov, and P. M. Echenique, *Surf. Sci. Rep.* **68**, 305 (2013).
- [11] N. Fischer, S. Schuppler, Th. Fauster, and W. Steinmann, *Surf. Sci.* **314**, 89 (1994).
- [12] Q. B. Lu, D. J. O'Connor, B. V. King, and R. J. MacDonald, *Surf. Sci.* **347**, L61 (1996).
- [13] D. M. Riffe, G. K. Wertheim, and P. H. Citrin, *Phys. Rev. Lett.* **64**, 571 (1990).
- [14] K. Xu, N. Li, D. Zeng, S. Tian, S. Zhang, D. Hu, and C. Xie, *ACS Appl. Mater. Interfaces* **7**, 11359 (2015).
- [15] R. Schlögl, *Angew. Chem. Int. Ed.* **54**, 3465 (2015).
- [16] T. von Hofe, J. Kröger, and R. Berndt, *Phys. Rev. B* **73**, 245434 (2006).
- [17] W. Jacob, E. Bertel, and V. Dose, *Phys. Rev. B* **35**, R5910 (1987).
- [18] M. Bauer, S. Pawlik, and M. Aeschlimann, *Phys. Rev. B* **55**, 10040 (1997).
- [19] H. Petek, M. J. Weida, H. Nagano, and S. Ogawa, *Science* **288**, 1402 (2000).
- [20] J. D. McNeill, R. L. Lingle, Jr., N.-H. Ge, C. M. Wong, R. E. Jordan, and C. B. Harris, *Phys. Rev. Lett.* **79**, 4645 (1997).
- [21] M. Wolf, E. Knoesel, and T. Hertel, *Phys. Rev. B* **54**, R5295 (1996).
- [22] A. Hotzel, G. Moos, K. Ishioka, M. Wolf, and G. Ertl, *Appl. Phys. B* **68**, 615 (1999).
- [23] W. Berthold, F. Rebenrost, P. Feulner, and U. Höfer, *Appl. Phys. A* **78**, 131 (2004).
- [24] P. M. Rentzepis and D. C. Douglass, *Nature (London)* **293**, 165 (1981).
- [25] M. Sandhofer, I. Yu. Sklyadnev, V. Sharma, V. Mikšić Trontl, P. Zhou, M. Ligges, R. Heid, K.-P. Bohnen, E. V. Chulkov, and U. Bovensiepen, *J. Electron Spectrosc. Relat. Phenom.* **195**, 278 (2014).
- [26] See Supplemental Material at <http://link.aps.org/supplemental/10.1103/PhysRevLett.127.266802> for STM images on Xe-Cs<sup>+</sup> aggregates on Cu(111) with three to five ions, results of static 2PPE spectroscopy as a function of Xe coverage, and computational details of the calculations, which includes Refs. [27–35].
- [27] F. Neese, *Comput. Mol. Sci.* **8**, e1327 (2018).
- [28] F. Neese and E. F. Valeev, *J. Chem. Theory Comput.* **7**, 33 (2011).
- [29] F. Weigend and R. Ahlrichs, *Phys. Chem. Chem. Phys.* **7**, 3297 (2005).
- [30] F. Weigend, *Phys. Chem. Chem. Phys.* **8**, 1057 (2006).
- [31] A. Hellweg, C. Hättig, S. Höfener, and W. Klopper, *Theor. Chem. Acc.* **117**, 587 (2007).
- [32] K. A. Peterson, D. Figgen, E. Goll, H. Stoll, and M. Dolg, *J. Chem. Phys.* **119**, 11113 (2003).
- [33] T. Leininger, A. Nicklass, W. Kuechle, H. Stoll, M. Dolg, and A. Bergner, *Chem. Phys. Lett.* **255**, 274 (1996).
- [34] M. M. Taddei, T. N. C. Mendes, and C. Farina, *Eur. J. Phys.* **30**, 965 (2009).
- [35] A. G. Borisov, J. P. Gauyacq, A. K. Kazansky, E. V. Chulkov, V. M. Silkin, and P. M. Echenique, *Phys. Rev. Lett.* **86**, 488 (2001).
- [36] S. Fölsch, U. Barjenbruch, and M. Henzler, *Thin Solid Films* **172**, 123 (1989).
- [37] F. Matthaei, S. Heidorn, K. Boom, C. Bertram, A. Safiei, J. Henzl, and K. Morgenstern, *J. Phys. Condens. Matter* **24**, 354006 (2012).
- [38] Th. Seyller, M. Caragiua, R. D. Diehl, P. Kaukasoin, and M. Lindroos, *Chem. Phys. Lett.* **291**, 567 (1998).
- [39] S. A. Lindgren, L. Wallden, J. Rundgren, P. Westrin, and J. Neve, *Phys. Rev. B* **28**, 6707 (1983).
- [40] In the 1 ML Xe/0.16 ML Cs<sup>+</sup> case, this Cs<sup>+</sup>-induced shortening of the Xe-Xe distance is particularly visible for adjacent heptamers. The shortened distance within the heptamers leads to a larger distance between the Xe of adjacent heptamers, visible as a dark rim around them, see Fig. 1(e).
- [41] M. L. Perrin, C. J. O. Verzijl, C. A. Martin, A. J. Shaikh, R. Eelkema, J. H. van Esch, J. M. van Ruitenbeek, J. M. Thijssen, H. S. J. van der Zant, and D. Dulic, *Nat. Nanotechnol.* **8**, 282 (2013).
- [42] I. L. Geada, H. Ramezani-Dakhel, T. Jamil, M. Sulpizi, and H. Heinz, *Nat. Commun.* **9**, 716 (2018).

- [43] J. Zhao, N. Pontius, A. Winkelmann, V. Sametoglu, A. Kubo, A. G. Borisov, D. Sánchez-Portal, V. M. Silkin, E. V. Chulkov, P. M. Echenique, and H. Petek, *Phys. Rev. B* **78**, 085419 (2008).
- [44] The obtained times are for  $\text{Cs}^+/\text{Cu}(111)$  numerically shorter than those reported in previous studies [9,18] since a single exponential decay is considered here contrary to a microscopic model based on optical Bloch equations used in literature to distinguish elastic and inelastic relaxation.
- [45] A. G. Borisov, A. K. Kazansky, and J. P. Gauyacq, *Surf. Sci.* **430**, 165 (1999).

## Hydration at Highly Crowded Interfaces

Christopher Penschke<sup>1,\*</sup>, John Thomas<sup>2</sup>, Cord Bertram<sup>2,3</sup>, Angelos Michaelides<sup>4</sup>, Karina Morgenstern<sup>3</sup>, Peter Saalfrank<sup>1,5</sup> and Uwe Bovensiepen<sup>2,†</sup>


<sup>1</sup>*Department of Chemistry, University of Potsdam, Karl-Liebknecht-Strasse 24-25, D-14476 Potsdam-Golm, Germany*

<sup>2</sup>*Faculty of Physics and Center for Nanointegration (CENIDE), University of Duisburg-Essen, D-47048 Duisburg, Germany*

<sup>3</sup>*Department of Chemistry and Biochemistry, Ruhr-Universität Bochum, Universitätsstraße 150, D-44801 Bochum, Germany*

<sup>4</sup>*Yusuf Hamied Department of Chemistry, University of Cambridge, Lensfield Road, Cambridge CB2 1EW, United Kingdom*

<sup>5</sup>*Department of Physics and Astronomy, University of Potsdam, Karl-Liebknecht-Strasse 24-25, D-14476 Potsdam-Golm, Germany*

 (Received 24 June 2022; revised 8 October 2022; accepted 5 February 2023; published 8 March 2023)

Understanding the molecular and electronic structure of solvated ions at surfaces requires an analysis of the interactions between the surface, the ions, and the solvent environment on equal footing. Here, we tackle this challenge by exploring the initial stages of Cs<sup>+</sup> hydration on a Cu(111) surface by combining experiment and theory. Remarkably, we observe “inside-out” solvation of Cs<sup>+</sup> ions, i.e., their preferential location at the perimeter of the water clusters on the metal surface. In addition, water-Cs complexes containing multiple Cs<sup>+</sup> ions are observed to form at these surfaces. Established models based on maximum ion-water coordination and conventional solvation models cannot account for this situation, and the complex interplay of microscopic interactions is the key to a fundamental understanding.

DOI: [10.1103/PhysRevLett.130.106202](https://doi.org/10.1103/PhysRevLett.130.106202)

The interplay of screening local charge accumulation and high electronic density of states at metal surfaces is decisive for understanding the fundamental aspects of surface reconstruction and reactions [1]. This is particularly pronounced for, but not limited to, metal-electrolyte interfaces, because screening and local reorganization occurs in this situation not only in the metal, but in the electrolyte as well [2]. Prominent examples of such interfaces include alkali ions in aqueous solution approaching metal surfaces [3,4]. In the presence of water, either as a reactant or as part of the environment, hydration of adsorbates may occur even without an extensive liquid phase due to its local character on the molecular scale of the solvent. Thus, hydrated ions at interfaces are relevant in many fields, for example, atmospheric aerosols, corrosion, and aggregation of biomolecules [5], which also results in a multifaceted landscape of potential applications. However, the complexity of the different types of interactions (ion-surface, ion-solvent, solvent-surface, solvent-solvent, ion-ion) also impedes understanding of such interfaces, and fundamental questions like the effect of ions on the structure of interfacial water are of considerable current interest [6,7].

Surface science studies at defined model systems provide a well-established approach to analyze the fundamental, microscopic interactions since they promise insights regarding competing or cooperative effects in general [8]. One such model system is Cs on Cu(111) [9–14], which has been investigated for a range of catalytic conversions, including reactions involving water (e.g., the water-gas shift reaction).

The interaction between adsorbate and metal surface affects both the geometric and the electronic structure at the

interface [15]. It is well known that the most stable clusters in bulk water consist of single alkali ions surrounded by four (Li<sup>+</sup>) to eight (Rb<sup>+</sup>, Cs<sup>+</sup>) water molecules [16]. Close to a transition metal surface, the solvation structures may be entirely different [17,18]. Model systems with reduced complexity (i.e., adsorption at submonolayer coverage under ultrahigh vacuum conditions) provide valuable contributions to understanding the interface and the fundamental interactions determining its structure. In addition, such model studies can also reveal changes in the electronic structure of the surface [19]. The formation of alkali ions upon adsorption of neutral alkali atoms is due to an electron transfer to the surface accompanied by the formation of unoccupied, short-lived resonances, which are decisive for the occurrence or nonoccurrence of photoreactions [20]. For example, photoexcitation into the Cs 6s resonance on Cu(111) leads to an increase of the Cs-Cu bond distance [21], but photodesorption is unlikely because of the low cross section under experimental conditions [22,23]. While changes in energy and lifetime of the alkali resonances on Cu(111) by solvation were experimentally detected [24,25], a microscopic understanding of the complex interactions of water and alkali ions on metal surfaces remains elusive.

In this Letter, we investigate the relationship between the geometric and electronic structure of Cs<sup>+</sup> ions coadsorbed with water on a Cu(111) surface. Combining density functional theory (DFT), scanning tunneling microscopy (STM), and two-photon photoelectron emission (2PPE), we show how the relative strengths of water-ion and water-water interactions lead to coverage-dependent changes in the structure of the coadsorbates. We find that clusters

crowded with ions form with the ions solvated at the perimeter of the water clusters. The results also suggest that the local ion and water concentration causes pronounced energetic shifts and splitting of the Cs resonance, which may significantly affect the properties of the interface. While this Letter focuses on the fundamental aspects of such interfaces, the results may be relevant in diverse fields such as ion hydration, catalysis, and atmospheric science.

To calculate the Cs<sup>+</sup>-water clusters on Cu(111) for different Cs<sup>+</sup> and H<sub>2</sub>O coverage, we used the exchange-correlation functional by Perdew *et al.* [26] together with the D3 dispersion correction [27,28] as implemented in VASP [29,30]. The Cu(111) surface was modeled by 5 × 5 surface unit cells, in which the different clusters are placed individually. Thus, the clusters are defined by the number of Cs<sup>+</sup> ions (one to three) and water molecules (zero to six) per unit cell. One Cs<sup>+</sup> per unit cell corresponds to a coverage of 0.16 monolayers (ML) defined with respect to a closed-packed (2 × 2) monolayer. The water coverage is given in fractions of a bilayer (BL), which is a closed hexagonal layer with two water molecules per three surface atoms [15]. See the Supplemental Material for more details [31].

The Cs<sup>+</sup>-water and the water-water interactions are of comparable strength. For instance, the agglomeration energy of a Cs<sup>+</sup> ion and a water molecule on Cu(111) is −0.36 eV, compared to a value of −0.28 eV for two water molecules. This competition between ion-water and water-water interactions has been discussed in the context of gas-phase Cs<sup>+</sup>-water clusters [39]. In contrast to the typically three-dimensional gas-phase clusters with many Cs-water bonds, flat structures are more favorable on Cu(111) due to the strong adsorbate-surface bonds. Because of the large size of Cs<sup>+</sup>, it is difficult to build flat clusters with both many Cs<sup>+</sup>-water and many hydrogen bonds. Remarkably, we find that the most stable structures are hydrogen-bonded water clusters with Cs<sup>+</sup> located at the perimeter or as part of a ring; see Fig. 1(a). We emphasize that structures with Cs<sup>+</sup> in the center of surrounding water with maximal coordination on Cu(111), which were analyzed in Ref. [40], are found to be less stable; see Supplemental Material [31].

Increasing the amount of water per Cs changes the electronic structure. Up to four water molecules per Cs<sup>+</sup> ion, the work function increases by 1 eV [see Fig. 1(b)], and the band center of the unoccupied Cs<sup>+</sup> 6s states shifts to higher energies by 0.8 eV; see Fig. 1(c). For a more detailed depiction of the computed band centers, we refer to the Supplemental Material [31], Fig. S4. We also investigated clusters with multiple Cs<sup>+</sup> ions. The cluster structures are similar to those with one Cs<sup>+</sup> ion; i.e., Cs<sup>+</sup> is located at the perimeter of water clusters or part of a ring. The Cs-Cs distances are 50 to 150 pm shorter in the presence of water. Increasing the Cs<sup>+</sup> coverage from 0.16 to 0.48 ML at a given water coverage reduces both the work function and the Cs<sup>+</sup>6s energy, as shown in Figs. 1(b) and 1(c). A computed phase diagram (see Fig. S10 in the

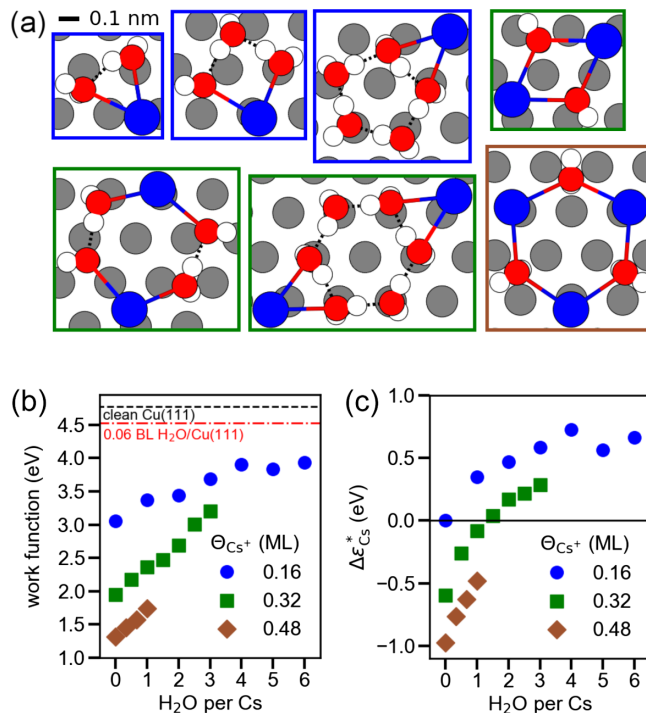


FIG. 1. (a) Clusters of one Cs<sup>+</sup> ion with two, three, and five water molecules, two Cs<sup>+</sup> ions with two, four, and six water molecules, and three Cs<sup>+</sup> ions with three water molecules obtained by DFT calculations. Cs, Cu, O, and H are depicted in blue, gray, red, and white, respectively. A complete overview of the structures is available in the Supplemental Material [31]; see Figs. S5–S7. (b) Computed work function as a function of the number of water molecules per Cs<sup>+</sup>, for adsorbed clusters containing one (blue circles), two (green squares), and three (brown diamonds) Cs<sup>+</sup> ions, which correspond to coverages of 0.16, 0.32, and 0.48 ML, respectively. The work function of clean Cu(111) and 0.06 BL H<sub>2</sub>O/Cu(111) (one adsorbed water molecule per 5 × 5 unit cell) is indicated by black and red lines, respectively. (c) Computed band center shift of the unoccupied Cs 6s states, Δε<sub>Cs</sub><sup>\*</sup>, relative to a single adsorbed Cs<sup>+</sup> ion (0.16 ML); see Supplemental Material [31].

Supplemental Material [31]) shows the most stable clusters. It demonstrates that small changes in concentration affect the cluster size, suggesting that the cluster structure changes depending on the local concentration of Cs<sup>+</sup> and water, which complements the changes in the electronic structure discussed above.

To verify the calculated cluster structures, we used STM; see Supplemental Material for details [31]. Starting with Cs deposited without water, a hexagonal superstructure forms [see the inset of Fig. 2(a)] at a coverage of 0.2 ML Cs<sup>+</sup>, in agreement with Ref. [41]. With a distance of (1.55 ± 0.07) nm between the protrusions, this corresponds to a (6 × 6) superstructure with respect to the hexagonal Cu(111) surface, suggesting long-range interaction between individual Cs<sup>+</sup>, which was attributed to electrostatic repulsion [41]. The striped appearance of some ions within the Cs<sup>+</sup> layer reflects their mobility even at T = 7 K; cf. Supplemental Material

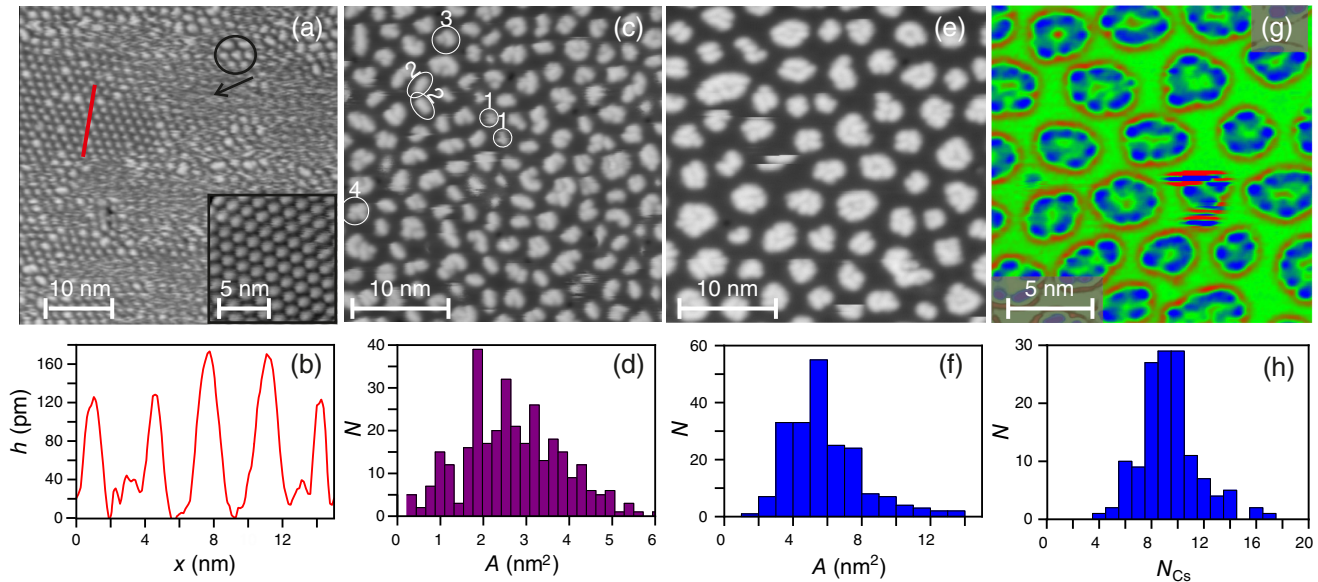


FIG. 2. Scanning tunneling microscopy of  $\text{Cs}^+$  ions coadsorbed on Cu(111) with  $\text{D}_2\text{O}$ . (a) Initial hydration; circle surrounds some of the larger clusters; arrow points to a diffusive region. Inset:  $\text{Cs}^+$  only. (b) Height profile along the line in (a). (c),(d) STM image and area histogram of hydration at approximately ten  $\text{D}_2\text{O}$  molecules per  $\text{Cs}^+$  ion, with some clusters marked with the number of their subunits. (e)–(h) Ten  $\text{D}_2\text{O}$  molecules per  $\text{Cs}^+$  ion annealed at 50 K for 15 min. (e),(g) STM images on gray and Laplace filtered on false-color scale (cf. Fig. S1 in the Supplemental Material [31]). (f) Area histogram; (h) histogram of estimated number  $N_{\text{Cs}}$  per cluster. Tunneling parameters: (a)  $-250$  mV, 10 pA; (c) 53 mV, 7.5 pA; (e) 40 mV, 7.5 pA; (g) 100 mV, 10 pA.

Fig. S2 [31]. For an incompletely hydrated layer, parts of the surface are still covered by the hexagonal layer; upper left in Fig. 2(a). Here, protrusions in the hexagonal array are imaged broader, at an area of  $(0.34 \pm 0.08)$   $\text{nm}^2$  as compared to  $(0.83 \pm 0.09)$   $\text{nm}^2$ , and higher, at 170 pm instead of 125 pm; Fig. 2(b). Their distinct size suggests that only one water molecule is attached to a single ion. On other parts of the surface, wider clusters exist; see circle in Fig. 2(a). Here, the distance between the clusters is larger than in the hexagonal array. These regions are surrounded by some diffusive layer, indicative of mobile  $\text{Cs}^+$ . Such a mobility is possible if there is more than one  $\text{Cs}^+$  ion bound in each cluster, and each ion occupies less space than before solvation. For such an approach of  $\text{Cs}^+$  ions, the water needs to screen the ions and compensate their repulsive Coulomb interaction by bonding.

At higher water coverages of approximately ten water molecules per  $\text{Cs}^+$ , all  $\text{Cs}^+$  ions are bound within  $\text{D}_2\text{O}$ - $\text{Cs}^+$  clusters; see Fig. 2(c). The considerably decreased number of  $\text{D}_2\text{O}$ - $\text{Cs}^+$  clusters as compared to the original number of  $\text{Cs}^+$  ions confirms that more than one  $\text{Cs}^+$  is bound within each cluster; on average, we identify four to five. Elongated clusters are frequent and are marked by ellipsoids “2.” These lead to a distinct maximum at an area of  $(1.9 \pm 0.2)$   $\text{nm}^2$  in the area histogram in Fig. 2(d), which suggests clusters of around half and 1.5 times this size. Their apparent size in the STM image as compared to sizes of pure water clusters is consistent with ten water molecules per  $\text{Cs}^+$  ion [42], suggesting that these smallest units contain one  $\text{Cs}^+$  ion. The smallest clusters thereby show the

characteristic stripes of a mobile species marked by circles “1” in Fig. 2(c). This is in contrast to immobile, larger clusters which consist of subunits of this size, leading to distinct multiples in the area histogram. Thereby, clusters with three protrusions are triangular and those with four protrusions rectangular. Larger clusters are far from being uniform in shape.

Similar structures were found after increasing the temperature. Upon annealing at 50 K, the cluster size increases; Fig. 2(e). The mean area doubles from  $(2.7 \pm 1.2)$  to  $(5.9 \pm 2.3)$   $\text{nm}^2$ ; see Fig. 2(f). The cluster size is far from uniform, but all clusters seem to consist of subunits that align along their perimeter. These subunits are enhanced in visibility by color coding a Laplace-filtered image in Fig. 2(g) (see also Fig. S1 in the Supplemental Material [31] for a comparison of regular and filtered images). Assuming that each of the circular blue dots of smallest height contains one  $\text{Cs}^+$  ion and that the elongated or the higher protrusions contain two  $\text{Cs}^+$  ions leads to a number of  $\text{Cs}^+$  ions per area equivalent to the deposited value. The corresponding histogram reveals that 85% of the clusters contain eight to ten  $\text{Cs}^+$  ions, a rather uniform distribution. Thus, the STM results at high water coverage confirm the structure found by DFT. Instead of a central ion with a solvation shell, we observe water clusters with multiple ions at the perimeter, an arrangement which we term “inside-out hydration.”

Having established a good agreement between calculated and experimental cluster structures, we turn now to the electronic structure. Experimentally, this was studied by

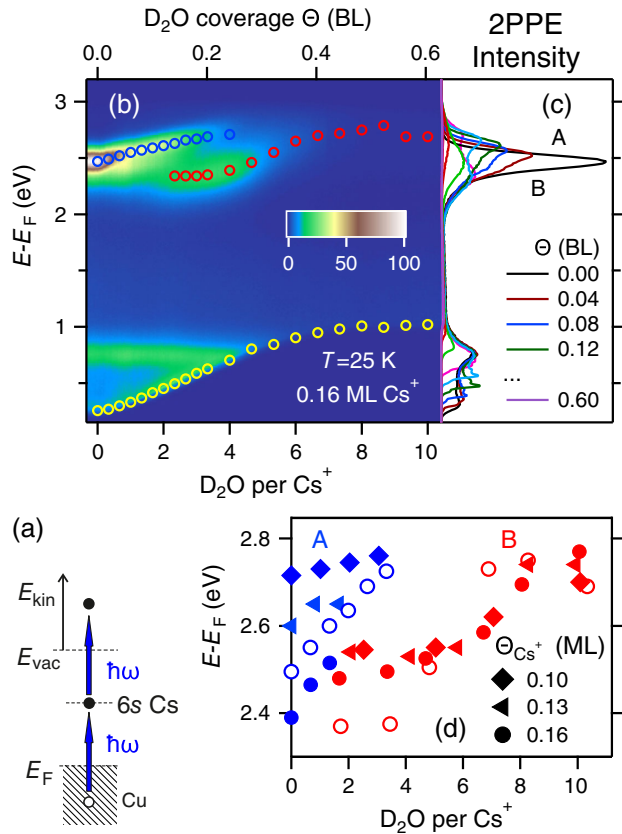


FIG. 3. (a) Schematic of 2PPE on  $\text{Cs}^+/\text{Cu}(111)$ . (b) False color map of 2PPE intensity as a function of the  $\text{D}_2\text{O}$  coverage and  $E - E_F$ . The  $\text{D}_2\text{O}$  coverage is given in bilayers (top axis) and as the number of molecules  $\text{D}_2\text{O}$  per  $\text{Cs}^+$  (bottom axis); see Supplemental Material for details [31]. The Cs  $6s$  states dressed with  $\text{D}_2\text{O}$  until  $2.7 \text{ D}_2\text{O}/\text{Cs}^+$ , for  $\Theta > 0.16 \text{ BL}$  or  $2.7 \text{ D}_2\text{O}/\text{Cs}^+$ , and the change in work function are depicted by blue, red, and yellow circles, respectively. (c) 2PPE spectra at selected  $\Theta$ . (d) The change in energy of the two states (at low water coverage, A, in blue, and at high water coverage, B, in red) as a function of  $\text{D}_2\text{O}/\text{Cs}^+$  for different  $\text{Cs}^+$  coverage  $\Theta_{\text{Cs}^+}$  and  $T = 25$  and  $80 \text{ K}$  depicted by open and closed symbols, respectively.

2PPE, for which we employ femtosecond laser pulses of photon energy  $\hbar\omega = 3.1 \text{ eV}$  [25,43]. In 2PPE, the first photon  $\hbar\omega$  excites resonant electron transfer from  $\text{Cu}(111)$  to the unoccupied Cs  $6s$  state. A second photon generates the photoelectron analyzed in a spectrometer [43]; see Fig. 3(a). To study the interaction of  $\text{D}_2\text{O}$  with  $\text{Cs}^+$ , we acquired 2PPE spectra while adsorbing  $\text{D}_2\text{O}$  on  $\text{Cs}^+/\text{Cu}(111)$  at  $25 \text{ K}$  as shown in Figs. 3(b) and 3(c). The peaks at energies  $E - E_F = 2.47$  and  $0.75 \text{ eV}$  observed for bare  $\text{Cs}^+/\text{Cu}(111)$  are assigned to the unoccupied Cs  $6s$  state [44] and the occupied  $3d$  band of the  $\text{Cu}(111)$  substrate, respectively. Here,  $E_F$  is the Fermi energy of  $\text{Cu}(111)$ . The energy of the Cs  $6s$  state increases during the adsorption of  $\text{D}_2\text{O}$  by  $240 \text{ meV}$ ; see Fig. 3(b). The intensity of the Cs  $6s$  state decreases with  $\text{D}_2\text{O}$  coverage and vanishes at four  $\text{D}_2\text{O}$  molecules per ion. Slightly below

this coverage, a new state appears at  $2.34 \text{ eV}$ . Its energy increases with  $\text{D}_2\text{O}$  coverage as well; see red circles. This state may be solvent dependent, as it was not observed for  $\text{Cs}^+/\text{Xe}$  on  $\text{Cu}(111)$  [25]. The change in the work function of the surface is manifested as a change in the low-energy cutoff of spectra; see yellow circles.

Figure 3(d) compiles energies for different  $\text{Cs}^+$  coverages  $\Theta_{\text{Cs}^+}$  and at two water adsorption temperatures,  $T = 25$  and  $80 \text{ K}$ . In agreement with Ref. [44], the energy of the Cs  $6s$  state for bare  $\text{Cs}^+/\text{Cu}(111)$  decreases with increasing  $\Theta_{\text{Cs}^+}$ . The unoccupied Cs  $6s$  state dressed with  $\text{D}_2\text{O}$  is designated as A (blue markers). The unoccupied Cs  $6s$  derived state observed for more water is denoted as B (red markers). Upon adsorption of  $\text{D}_2\text{O}$ , the energy of the A state increases. Remarkably, the energy of the B state is independent of the  $\text{Cs}^+$  coverage but increases with  $\text{D}_2\text{O}$  coverage by more than  $200 \text{ meV}$ . At  $T = 25 \text{ K}$ , the energy of the B state is nearly constant below four  $\text{D}_2\text{O}/\text{Cs}^+$  and above seven  $\text{D}_2\text{O}/\text{Cs}^+$ , and the increase in energy occurs via a jump at around six to seven  $\text{D}_2\text{O}/\text{Cs}^+$ . This is in contrast to the weaker, more gradual increase at  $T = 80 \text{ K}$ , which indicates limited mobility of Cs-water clusters at the lower temperature.

These results agree qualitatively with our DFT calculations, but the latter overestimate the observed shifts by a factor of 2; cf. Figs. 1 and 3. The appearance of two different resonance states at water coverages around one  $\text{D}_2\text{O}/\text{Cs}^+$  suggests that different clusters coexist, in agreement with the STM results. To test this hypothesis, we performed calculations using a larger  $7 \times 7$  unit cell. This enables us to investigate the electronic structures of different clusters within one unit cell. As shown in Fig. S6 of the Supplemental Material [31], the maxima of the unoccupied Cs  $6s$  bands of  $\text{Cs}^+$  ions in different clusters have different energies.

This agreement among experiment and theory allows us to propose a scheme for the hydration of  $\text{Cs}^+$  on  $\text{Cu}(111)$ . At low water coverage ( $\leq 1$  water molecule per  $\text{Cs}^+$ ),  $\text{Cs}^+$  ions are dispersed on the surface in a hexagonal array and are bonded to at most one water molecule. Adding water leads to the formation of small clusters with low water: $\text{Cs}^+$  ratio (up to ca. 3:1), which shifts the  $6s$  state to higher energies. At a coverage of three water molecules per  $\text{Cs}^+$  ion, larger clusters with multiple  $\text{Cs}^+$  ions start to dominate. They show a new lower-energy  $6s$  state due to the higher local  $\text{Cs}^+$  coverage. Adding water shifts this state to higher energies.

The hydration structure of  $\text{Cs}^+$  on  $\text{Cu}(111)$  is markedly different compared to bulk water or the gas phase. Because of adsorbate-surface interactions, two-dimensional clusters are energetically preferred. Together with the large size of  $\text{Cs}^+$  ions, this leads to a competition between  $\text{Cs}^+$ -water bonds and hydrogen bonds. The latter dominate in the most stable cluster structures, leading to a preference for water clusters with  $\text{Cs}^+$  ions at their perimeter.

As demonstrated here for a highly crowded situation, the relationship between coverage, cluster structure, and unoccupied electronic states may have important consequences for the reactivity of solvated alkali or metal interfaces. Such an understanding of the elementary interactions that determine the structures of ion-solvent clusters may also provide useful input for an advanced model description of electrode-electrolyte interfaces. While the peculiar inside-out solvation structure may not be visible at high water coverages, the balance of the fundamental interactions shown could still play an important role in the chemistry and physics of solvated alkali ions at the metal-liquid interface.

Funded by the Deutsche Forschungsgemeinschaft (DFG, German Research Foundation) under Germany's Excellence Strategy, Grant No. EXC 2033-390677874 RESOLV (C. B., U. B., K. M., J. T.) as well as Grant No. EXC 2008/1-390540038, UniSysCat (C. P. and P. S.). The DFG is furthermore acknowledged for funding within Project ID No. 278162697-SFB 1242 (U. B. and J. T.). C. P. is grateful to the Alexander von Humboldt Foundation for financial support within the Feodor Lynen Program. We thank M. Meyer for experimental support, as well as M. Wolf and A. Rubio for fruitful discussions.

\*penschke@uni-potsdam.de

†uwe.bovensiepen@uni-due.de

- [1] A. Zangwill, *Physics at Surfaces* (Cambridge University Press, Cambridge, England, 1988).
- [2] G. Gonella, E. H. G. Backus, Y. Nagata, D. J. Bonthuis, P. Loche, A. Schlaich, R. R. Netz, A. Kühnle, I. T. McCrum, M. T. M. Koper, M. Wolf, B. Winter, G. Meijer, R. K. Campen, and M. Bonn, *Nat. Rev. Chem.* **5**, 466 (2021).
- [3] W. Schmickler, G. Belletti, and P. Quaino, *Chem. Phys. Lett.* **795**, 139518 (2022).
- [4] C. Xi, F. Zheng, G. Gao, M. Ye, C. Dong, X.-W. Du, and L.-W. Wang, *J. Mater. Chem. A* **8**, 24428 (2020).
- [5] P. Jungwirth and D. J. Tobias, *Chem. Rev.* **106**, 1259 (2006).
- [6] J. Hunger, J. Schaefer, P. Ober, T. Seki, Y. Wang, L. Prädell, Y. Nagata, M. Bonn, D. J. Bonthuis, and E. H. G. Backus, *J. Am. Chem. Soc.* **144**, 19726 (2022).
- [7] B. Rehl and J. M. Gibbs, *J. Phys. Chem. Lett.* **12**, 2854 (2021).
- [8] D. M. Kolb, *Angew. Chem., Int. Ed. Engl.* **40**, 1162 (2001).
- [9] C. T. Campbell and B. E. Koel, *Surf. Sci.* **186**, 393 (1987).
- [10] J. Gauyacq, A. Borisov, and M. Bauer, *Prog. Surf. Sci.* **82**, 244 (2007).
- [11] T. K. Shimizu, J. Jung, H. Imada, and Y. Kim, *Angew. Chem. Int. Ed.* **53**, 13729 (2014).
- [12] J. Resasco, L. D. Chen, E. Clark, C. Tsai, C. Hahn, T. F. Jaramillo, K. Chan, and A. T. Bell, *J. Am. Chem. Soc.* **139**, 11277 (2017).
- [13] M. C. O. Monteiro, F. Dattila, B. Hagedoorn, R. García-Muelas, N. López, and M. T. M. Koper, *Nat. Catal.* **4**, 654 (2021).
- [14] R. C. E. Hamlyn, M. Mahapatra, I. Orozco, I. Waluyo, A. Hunt, J. A. Rodriguez, M. G. White, and S. D. Senanayake, *J. Phys. Chem. C* **124**, 3107 (2020).
- [15] M. Henderson, *Surf. Sci. Rep.* **46**, 1 (2002).
- [16] J. Mähler and I. Persson, *Inorg. Chem.* **51**, 425 (2012).
- [17] I. Weber, N. Gerrard, A. Hodgson, and K. Morgenstern, *J. Phys. Chem. C* **123**, 6861 (2019).
- [18] K. Lucht, I. Trosien, W. Sander, and K. Morgenstern, *Angew. Chem., Int. Ed. Engl.* **57**, 16334 (2018).
- [19] S. Dahl, A. Logadottir, C. J. Jacobsen, and J. K. Nørskov, *Appl. Catal., A* **222**, 19 (2001).
- [20] H. Petek and S. Ogawa, *Annu. Rev. Phys. Chem.* **53**, 507 (2002).
- [21] S. Ogawa, H. Nagano, and H. Petek, *Phys. Rev. Lett.* **82**, 1931 (1999).
- [22] H. Petek, M. J. Weida, H. Nagano, and S. Ogawa, *Science* **288**, 1402 (2000).
- [23] D. Kröner, T. Klamroth, M. Nest, and P. Saalfrank, *Appl. Phys. A* **88**, 535 (2007).
- [24] M. Meyer, I. Agarwal, M. Wolf, and U. Bovensiepen, *Phys. Chem. Chem. Phys.* **17**, 8441 (2015).
- [25] J. Thomas, C. Bertram, J. Daru, J. Patwari, I. Langguth, P. Zhou, D. Marx, K. Morgenstern, and U. Bovensiepen, *Phys. Rev. Lett.* **127**, 266802 (2021).
- [26] J. P. Perdew, K. Burke, and M. Ernzerhof, *Phys. Rev. Lett.* **77**, 3865 (1996).
- [27] S. Grimme, J. Antony, S. Ehrlich, and H. Krieg, *J. Chem. Phys.* **132**, 154104 (2010).
- [28] S. Grimme, S. Ehrlich, and L. Goerigk, *J. Comput. Chem.* **32**, 1456 (2011).
- [29] G. Kresse and J. Furthmüller, *Comput. Mater. Sci.* **6**, 15 (1996).
- [30] G. Kresse and J. Furthmüller, *Phys. Rev. B* **54**, 11169 (1996).
- [31] See Supplemental Material at <http://link.aps.org/supplemental/10.1103/PhysRevLett.130.106202> for details on sample preparation and characterization, scanning tunneling microscopy, and density functional theory calculations, which includes Refs. [32–38].
- [32] P. E. Blöchl, *Phys. Rev. B* **50**, 17953 (1994).
- [33] Q. Lu, D. O'Connor, B. King, and R. MacDonald, *Surf. Sci.* **347**, L61 (1996).
- [34] G. Kresse and D. Joubert, *Phys. Rev. B* **59**, 1758 (1999).
- [35] K. Reuter and M. Scheffler, *Phys. Rev. B* **65**, 035406 (2001).
- [36] U. Bovensiepen, C. Gahl, and M. Wolf, *J. Phys. Chem. B* **107**, 8706 (2003).
- [37] S. Maintz, V. L. Deringer, A. L. Tchougréeff, and R. Dronskowski, *J. Comput. Chem.* **34**, 2557 (2013).
- [38] S. Maintz, V. L. Deringer, A. L. Tchougréeff, and R. Dronskowski, *J. Comput. Chem.* **37**, 1030 (2016).
- [39] M. Kołaski, H. M. Lee, Y. C. Choi, K. S. Kim, P. Tarakeshwar, D. J. Miller, and J. M. Lisy, *J. Chem. Phys.* **126**, 074302 (2007).
- [40] A. Pérez Paz and A. Rubio, *J. Phys. Chem. C* **125**, 3868 (2021).
- [41] T. von Hofe, J. Kröger, and R. Berndt, *Phys. Rev. B* **73**, 245434 (2006).
- [42] A. Michaelides and K. Morgenstern, *Nat. Mater.* **6**, 597 (2007).

- [43] M. Sandhofer, I. Sklyadneva, V. Sharma, V. M. Trontl, P. Zhou, M. Ligges, R. Heid, K.-P. Bohnen, E. Chulkov, and U. Bovensiepen, *J. Electron Spectrosc. Relat. Phenom.* **195**, 278 (2014).
- [44] J. Zhao, N. Pontius, A. Winkelmann, V. Sametoglu, A. Kubo, A. G. Borisov, D. Sánchez-Portal, V. M. Silkin, E. V. Chulkov, P. M. Echenique, and H. Petek, *Phys. Rev. B* **78**, 085419 (2008).



**The curriculum vitae is not included in the online version  
for data protection reasons.**

# DuEPublico

Duisburg-Essen Publications online

UNIVERSITÄT  
DUISBURG  
ESSEN

*Offen im Denken*

ub | universitäts  
bibliothek

Diese Dissertation wird via DuEPublico, dem Dokumenten- und Publikationsserver der Universität Duisburg-Essen, zur Verfügung gestellt und liegt auch als Print-Version vor.

**DOI:** 10.17185/duepublico/77878

**URN:** urn:nbn:de:hbz:465-20230523-150607-4



Dieses Werk kann unter einer Creative Commons Namensnennung - Nicht-kommerziell - Weitergabe unter gleichen Bedingungen 4.0 Lizenz (CC BY-NC-SA 4.0) genutzt werden.